THE UNIVERSITY *of* EDINBURGH

Discrete Element Modelling of Cementitious Materials

Nicholas John Brown

Doctor of Philosophy

The University of Edinburgh

January 2013

Declaration

This thesis entitled “Discrete Element Modelling of Cementitious Materials” is submitted to the University of Edinburgh for the degree of Doctor of Philosophy. The research work described and reported in this thesis has been completed solely by Nicholas Brown under the supervision of Professor Jin Y. Ooi and Dr Jian-Fei Chen. Where other sources are quoted full references are given.

Nicholas Brown

January 2013

Publications based on this thesis:

Brown, N.J., Chen, J.F. and Ooi, J.Y. (2012) “A bond model for DEM simulation of bonded particles and deformable boundaries” *Proceedings of seventh International Conference for Conveying and Handling of Particulate Solids (CHoPS 2012), September 10th-13th 2012*. Friedrichshafen, Germany

Brown, N.J., Ooi, J.Y. and Chen, J.F. (2012) “DEM modelling of cementitious materials”. Poster presentation. *The Royal Society of Edinburgh, November 20th 2012*. Edinburgh, Scotland

Brown, N.J., Ooi, J.Y. and Chen, J.F. (2011) “Bond models in EDEM: The suitability of new and existing inter-particle bond models for the prediction of concrete behaviour”. Poster presentation. *EDEM User Conference 2011, March 31st – April 1st 2011*. Edinburgh, Scotland

Brown, N.J., Ooi, J.Y. and Chen, J.F. (2009) “Validation of the Hertz-Mindlin with bonding contact model in EDEM”. Poster presentation. *EDEM User Conference 2009, August 13th-14th 2009*. Edinburgh, Scotland

Abstract

This thesis presents a new bonded particle model that accurately predicts the wide-ranging behaviour of cementitious materials. There is an increasing use of the Discrete Element Method (DEM) to study the behaviour of cementitious materials such as concrete and rock; the chief advantage of the DEM over continuum-based techniques is that it does not predetermine where cracking and fragmentation initiate and propagate, since the system is naturally discontinuous. The DEM's ability to produce realistic representations of cementitious materials depends largely on the implementation of an inter-particle bonded-contact model. A new bonded-contact model is proposed, based on the Timoshenko beam theory which considers axial, shear and bending behaviour of inter-particle bonds. The developed model was implemented in the commercial EDEM code, in which a thorough verification procedure was conducted.

A full parametric study then considered the uni-axial loading of a concrete cylinder; the influence of the input parameters on the bulk response was used to produce a calibrated model that has been shown to be capable of producing realistic predictions of a wide range of behaviour seen in cementitious materials. The model provides useful insights into the microscopic phenomena that result in the bulk loading responses observed for cementitious materials such as concrete.

The new model was used to simulate the loading of a number of deformable structural elements including beams, frames, plates and rings; the numerical results produced by the model provided a close match to theoretical solutions.

Acknowledgements

I would like to first and foremost thank Professor Jin Ooi and Dr Jian-Fei Chen for their excellent supervision and support throughout this project. I would also like to thank EPSRC and DEM Solutions Ltd for the funding and sponsorship. I am also grateful for the assistance from DEM Solutions Ltd, especially through discussion with Stephen Cole, Mark Cook, David Curry and Richard LaRoche.

I would like to thank everyone in the Silos and Granular solids group at Edinburgh University and all of the residents of AGB 3.13, especially Mical Johnstone, J.P. Morrisey and Carlos Labra.

I would also like to thank Josh, Chuck, Andy and John, who kept me smiling during the good times and the bad.

There is always friendship in The Banana Stand.

I would like to thank my Mum and Dad, and my brother Mark. They all provided me with unwavering support and love during my study.

Last but by no means least I would like to thank my wife Katie, there is no doubt that without her I never would have made it this far.

This thesis is dedicated to my father, the smartest and most patient person I know.

Contents

List of figures

List of tables

Nomenclature

Roman characters

A	Area
A_{ratio}	Height to diameter aspect ratio
b_d	Damping ratio
B	Number of bonds connected to a particle
cr	Contact radius
d	Translational displacement
d_f	Dispersion factor
D	Specimen diameter
D_m	Particle damage
e	Coefficient of restitution
E	Young's modulus
E^*	Equivalent Young's modulus
$f_{c'}$	Ultimate cylinder compressive strength
f_s	Form factor for shear
F	Force
G	Shear modulus
G^*	Equivalent shear modulus
h	Height of the specimen
I	Second moment of area
K	Stiffness matrix
L_b	Bond length

Lr	Loading rate
m	Particle mass
m^*	Equivalent mass
M	Moment
n	Porosity
n_p	Total number of particles
P	Particle position
Q	Shear force
r	Particle radius
r_b	Bond radius
S_n	Normal stiffness
S_t	Tangential stiffness
S_C	Mean bond compressive strength
S_S	Mean bond tensile strength
S_T	Mean bond shear strength
u	Displacement vector
V	Translational velocity
$\overline{X}_{Co}$	Average number of bonds per particle

Greek characters

γ	Transformation matrix
δ	Overlap
Δt	Time step

Δt_{crit}	Critical time step
ε	Axial strain of specimen
ε_r	Radial strain of specimen
η	Contact radius multiplier
θ	Rotational displacement
ι_d	Global damping coefficient
κ	Shear correction coefficient
λ	Bond radius multiplier
μ_s	Coefficient of static friction
μ_r	Coefficient of rolling friction
ν	Poisson's ratio
$\nu_{c(0.4)}$	Bulk Poisson's ratio
ξ	Time step factor
ρ_p	Particle density
σ	Macroscopic stress
σ_C	Bond compressive strength
$\sigma_{C\,MAX}$	Maximum compressive stress in a bond
σ_T	Tensile strength of a bond
$\sigma_{T\,MAX}$	Maximum tensile stress in a bond
ς	Coefficient of variation for all bond strength components
ς_C	Coefficient of variation of bond compressive strength
ς_T	Coefficient of variation of bond tensile strength
ς_S	Coefficient of variation of bond shear strength
τ	Shear strength of a bond

τ_{MAX}	Maximum shear stress in a bond
Φ	Timoshenko shear coefficient
ω	Angular velocity

Chapter 1 Introduction

1.1 Background

Cementitious materials such as rock (natural) and concrete (man-made) have been used in construction for centuries. Concrete is currently the most commonly used man-made material in the world; this is in part due to its high compressive strength to cost ratio, its ease of manufacture and its flexibility. By varying the ratios of the four main constituents: coarse aggregate, fine aggregate, cement and water, the overall strength, durability and workability can be easily modified. Due to its popularity, there has been extensive interest into its behaviour and that of other cementitious materials. These materials exhibit complex heterogeneous and non-linear behaviour caused by distributions of multiple phases at different length scales (Yang et al., 2009). Innovation of new concrete mixes, including using waste materials such as plastic (Ismail and Al-Hashmi, 2008) or recycled aggregates (Xiao et al., 2012) means that there is a continued need for methods to study the behaviour of cementitious materials, especially their response to load.

Research into the behaviour of cementitious materials broadly follows one of three approaches: analytical, physical testing, or numerical techniques. Each has its advantages, but as computational power increases with time, numerical modelling becomes more attractive as investigations into massive structures or the material microstructure can be represented without an unreasonable computational cost. One of the advantages of numerical techniques is that the stresses inside a specimen can be determined directly and at any time rather than estimated from boundary conditions, as is the case with physical experiments Cundall and Strack (1979). Analytical models lack the flexibility of numerical models where loading configurations, particle sizes, size distributions and physical properties of the particles can all be easily modified Cundall and Strack (1979). It is relatively easy to

compare the failure process predicted by numerical models against experimental observations. These methods can then be used to investigate phenomena that cannot be seen or recorded in experiments. Potapov and Campbell (1997) add “The great advantage of the computer simulation is that it allows precise control of the material properties and the breakage parameters. Furthermore, it permits the breakage process to be carefully observed as it progresses, which is very difficult to replicate experimentally as the actual process occurs very rapidly”.

Numerical models are generally based on the concept that the material is either represented as a continuum or as discrete elements. There are also some hybrid methods combining these concepts (e.g. Breugnot et al., 2010). The modelling of continua (e.g. dams in civil engineering applications, or engine castings in mechanical applications) is clearly better treated by using a continuum basis for the technique, such as finite elements e.g. Zienkiewicz et al., 2005; Crisfield, 1997. Materials that are clearly particulate in nature are better suited to a discrete approach, which has been used in the modelling of free-flowing granular solids e.g. Rotter et al., 1998; Langston et al., 1995.

Cementitious materials provide a challenge for either continuous or discrete models. These materials are often treated as continuous on the macroscopic scale, but are naturally heterogeneous at the microscopic scale. Kim and Buttlar (2009) stated that “the fracture of heterogeneous solids is a difficult problem to solve numerically, due to the creation and continuous motion of new surfaces”. Continuum methods, especially those based on continuum damage mechanics, may require an extension to deal with the fracture of these materials (D’Addetta and Ramm, 2006). Additional processes, such as remeshing of lattices, are not required with discrete methods where contact types can be changed easily with mass conservation (Kim and Buttlar, 2009).

This means that continuous models are challenged because of the need to introduce this lack of homogeneity at the geometric level and often only describe the material behaviour in an average sense (Kuhl et al., 2000). This has been done but demands a

particularly high level of technology and is often computationally expensive. Nevertheless, accurate models can be created, such as those described by Caballero et al., (2006) and Yang and Xu (2008)

Discrete modelling of cementitious materials has the advantage that the representation is naturally discrete, and can provide this lack of homogeneity more readily by approximating the different distributions of size and shape of the particles within the mass e.g. Cho et al., 2007; Schneider et al., 2010. However, the interconnection of the particles, generally achieved using contact models, provides a challenging aspect. Unlike continuum techniques, discrete particle models naturally simulate the formation and development of cracks, which are so crucial to the overall behaviour, relating complex behaviour at the microscopic scale to that on the macroscopic scale.

Generally, discrete methods have been computationally expensive and become unreasonable when modelling large-scale problems, although the importance of this limitation is diminishing with increasing computing power. This study is primarily interested in using a discrete method to study the fracture mechanics of concrete, which considers the discontinuous phenomena of micro-crack initiation and growth and ultimately its effect on the material's macrostructure.

One popular numerical method for studying the behaviour of cementitious materials is the Discrete (or Distinct) Element Method (DEM), which was first proposed by Cundall (1971) for the study of rock mechanics and later expanded for modelling granular materials by Cundall and Strack (1979). The potential use of this method provides the framework for the thesis that follows.

1.2 Objectives and scope of this research

This project sets out to examine the suggestion that the Discrete Element Method can be used to reproduce the constitutive and failure behaviour of cementitious materials

such as concrete. This thesis aims to advance the understanding of DEM modelling of cementitious materials and provide a model which can be used for this purpose.

To achieve this aim either an existing contact model will be adopted or a new one developed which is capable of replicating the behaviour of cementitious materials. This model will be implemented into appropriate software and verified to ensure that the fundamental mathematical basis for the model matches the described behaviour.

After the model has been verified it will be used to investigate the response of cementitious materials to load. A parametric study will be conducted which will consider the uni-axial loading of a concrete cylinder as a benchmark in order to determine the influence of the model's input parameters on the bulk response. With these influences understood, relationships can be drawn between them, leading to the formation of a calibrated model capable of predicting a realistic range of concrete behaviour. The model can then be extended to modelling materials beyond the uni-axial compression of concrete cylinders.

1.3 Structure of thesis

This thesis is presented in eight chapters (including this introductory chapter); a brief summary of the contents of each is given below:

Chapter 2 presents a review of the literature relevant to this thesis. Emphasis is placed on the methods and limitations of existing bonded particle models using the DEM. The current bond model available in the code EDEM is discussed in depth, as this is the software that will be used in the rest of this study.

Chapter 3 describes the background and development of a new bonded particle model. The theory behind the bonded part of the model is described, as is the implementation into the DEM software EDEM. The implemented model is then verified to ensure that the model's code matches the theory upon which the model is based.

Chapters 4 and 5 present a parametric study which is conducted to determine the influence of the many input parameters on the macroscopic response of a specimen of concrete under uni-axial compression. The responses are compared with the Eurocode stress-strain prediction.

Chapter 6 focuses on calibrating the model, using the results from the parametric study, so that a range of concrete behaviour can be reproduced on demand.

Chapter 7 shows how the developed model can be used to study a range of structural problems, through the demonstration of simple structures including beams, frames and plates. Applications of the model to additional cementitious situations are also discussed, as well as how the developed model can be used to study the interaction of more complex materials such as fibre-reinforced polymers and concrete.

Chapter 8 summarises the general conclusions that can be drawn from this thesis, recommendations for future work are also given.

Chapter 2 Literature review

2.1 A brief review of Discrete Element Method

In the Discrete Element Method, the subject material can be discretised into a finite number of independent, or discrete, non-deformable elements (particles). These elements contain all the mass of the system and interact with each other at soft contacts where interpenetration (overlap) is always allowed but not required. In some instances, such as when modelling cementitious materials, a contact can still exist between two elements even if there is no physical overlap between them. The overlap of elements represents the deformation of surfaces that occurs when grains come into contact in the physical material. It is assumed that this overlap area is relatively small compared to the dimensions of the corresponding elements. Cundall and Hart (1992) proposed that a code could be named a Discrete Element Method if it allows finite displacements and rotations of discrete bodies, and it recognises new contacts automatically as the calculation progresses. There are many different codes available for commercial software such as: EDEM (DEM.Solutions, 2010), PFC (Itasca, 2001) and DEMpack (CIMNE, 2010).

Traditionally DEM provides a three-stage calculation cycle which resolves the dynamic interaction of elements. The three stages are: contact detection, calculation of interaction forces and numerical time integration. The process flow chart in Figure 2.1 shows this three-stage calculation process.

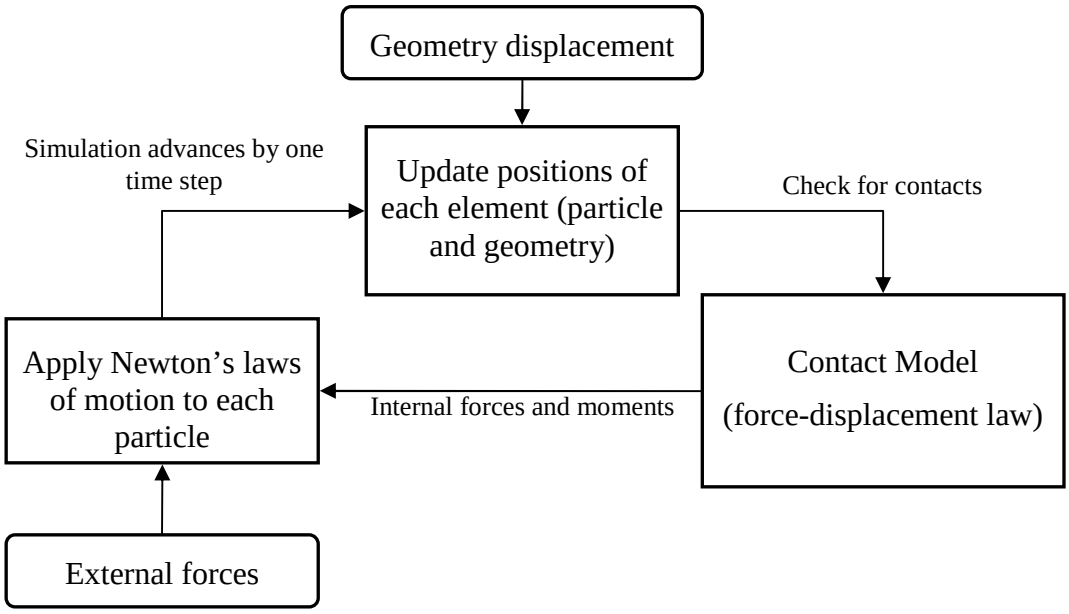

Figure 2.1 An example of the DEM calculation cycle

Internal forces resulting from element interactions are determined using force-displacement laws contained within contact models. Newton's second law of motion is then used to provide an acceleration term for each element, based on the summation of internal and external forces. By considering a progression in time, the position of each element can be updated and a new list of contacts formed. This time marching calculation cycle continues until a precondition is reached, usually when a specified number of calculation cycles have been completed.

By only allowing small time steps (the increase in time between calculation cycles) the numerical stability of the model improves and only relatively small element overlaps are obtained; most importantly the resultant forces acting on an individual element come exclusively from its interactions with elements it is in contact with (Cundall and Strack, 1979). The speed at which disturbances can propagate depends on the physical properties of the system such as the distribution of mass and stiffness; therefore the time step should be related to these physical properties to ensure no elements can interact with another element it is not in contact with and to satisfy the above conditions (Potyondy and Cundall, 2004).

Whilst the manner in which the update of element position and application of Newton's laws of motion will be similar for each DEM simulation, the types of interaction that the contact model must represent can vary greatly, such as cohesion or electrostatics. To accommodate this variation, different contact models can be implemented into a DEM code. Even the most advanced models are designed for one job, but most materials and phenomena are very complicated so it would be unreasonable to expect a single model to be able to cope with all types of contacts (Dolado and van Breugel, 2011). As a result, contact models can be broadly divided into three categories depending on their application; contact-stiffness models, slip models, and bonded models.

This study examines the use of DEM models, with special reference to bonded particle models as only they are capable of representing the connecting joints that exist between grains in cementitious materials. At the microscopic scale, materials such as concrete (man-made) and rock (natural) are composed of relatively small grains cemented together to form a much larger bulk solid on the macroscopic scale. In concrete aggregate grains are cemented together by hardened cement paste, while in rocks either a true cement paste is present (sedimentary rock sandstone) or an approximation of cement is present (crystalline rock granite) where granular interlocking exists (Potyondy and Cundall, 2004). The representation of the cement joint in these materials is usually achieved by inserting a bond between particle elements, which is capable of resisting the relative displacement of the two particles in at least one degree of freedom. By introducing bonds between elements, a collection of particles can be transformed into a heterogeneous macroscopic granular solid (Ergenzinger et al., 2011).

By providing failure criterion for each bond, material damage can be represented through the overall breakage of bonds. The more bonds break, the more granular in nature the material becomes; "the mechanical behaviour of rock is governed by the formation, growth and eventual interaction of micro-cracks" (Potyondy and Cundall, 2004). This means that all bonded particle models must be able to replicate this behaviour.

There appears to be no standard term in the literature to describe materials such as concrete and rock. A few of the common terms include: cemented granular materials (Potyondy and Cundall, 2004), brittle geo-materials (Hentz et al., 2004b), cohesive frictional granular materials (D'Addetta et al., 2002; Kuhl et al., 2000), cohesive materials (Camborde et al., 2000), brittle and cohesive materials (Groh et al., 2011) and cementitious materials (He et al., 2009). For the purposes of this study these materials will be referred to as cemented granular materials or cementitious materials. The term "cohesive" should not be applied to cemented granular materials. If the cement joint between two grains breaks then no tensile forces can be carried at the contact. If the two grains were then compressed together the cement joint would not reform; the term cohesive suggests that reformation would be possible, as occurs in truly cohesive materials such as limestone powder and kaolin clay.

2.2 Bonded particle models in DEM

There have been many bonded particle models e.g. those proposed by Schneider et al. (2010) and Potyondy and Cundall (2004) which have been developed and implemented in various DEM software e.g. EDEM (DEM.Solutions, 2010), PFC (Itasca, 2001), and DEMPack (CIMNE, 2010). Most share four features which influence the way in which the material is modelled. They are:

- *Discretization of the subject material*: this process creates the elements that will be representing the subject material. There are many particle generation techniques and different element representations.
- *Initialization of bonds*: most bonded particle models have criteria which must be met in order for a bond to form between two elements. These bonded contacts can then be treated in a different manner to non-bonded contacts.
- *Contact law*: within the heart of each bonded particle model is a constitutive relation that describes the behaviour at bonded contacts, based on the displacements of the two interacting elements.

- *Bond failure*: bonded particle models also contain breakage criteria which are used to determine if a bonded contact has broken. These criteria are normally based on either stress or strain limits. Bond breakage represents the process that occurs in cementitious materials under loading where they degrade from macroscopic solids to being more particulate in nature.

Each of these features will be briefly discussed in order to demonstrate precisely how cemented granular materials have been modelled using the DEM.

2.2.1 Discretization of the subject material

"The generation of a suitable initial configuration is the first step of every DEM simulation" (Ergenzinger et al., 2011). It is very important when conducting any DEM modelling that the particle packing generated is representative of the problem that is to be solved and to ensure good assemblies that do not include preferable crack paths (Carmona et al., 2008) with macroscopic isotropy being obtained.

The microscopic grain structures of cementitious materials are highly inhomogeneous, often including pores or inclusions which provide natural weaknesses. Due to the wide range in grain size, especially in concrete where sand grains can be of an order of magnitude smaller than the aggregate, DEM representations do not necessarily model every individual grain; assumptions have to be made, and larger elements are often used to represent a portion of the sample. The elements at the meso-scopic scale incorporate properties of the microstructure and directly affect the properties of the bulk solids. The discretization should be taken into account when considering the calibration of the model, as the particle packing directly affects the properties of the macrostructure.

Although there are a number of ways the material is represented, there are four key variables. They are:

- Spatial distribution and orientation of elements
- Number of component phases
- Size and distribution of size of the elements
- Shape of the elements

2.2.1.1 Spatial distribution of elements

In real concrete, the proportion of the constituent parts has an important effect on the bulk behaviour. Packing more aggregate into a sample leads to a cheaper but weaker material; the reverse is also true, as a sample with more cement will be stronger but more expensive as cement is the costly element. A number of methods can be used to determine proportions and the distribution of the grains inside a specimen of cementitious material. Groh et al. (2011) suggest the following methods: sieve analysis (for size alone), 3D laser scanning (shape), computerized particle analysis, tomography, thin section analysis, and surface analysis. The use of X-ray computerized tomography has been used more and more since the late 90's to characterise the internal structures of concrete (Wang, 2004). One of the advantages of X-ray computerized tomography is that it is non-destructive, meaning that the influence of a specific initial particle packing arrangement on the crack initiation and propagation can be monitored. The results also give precise aggregate shapes in three dimensions.

Because of their influence on the macroscopic behaviour, the initial particle packing is very important. Because of this importance, many authors have proposed different methods for achieving different particle assemblies. It is often desirable to produce dense particle assemblies as they can be said to better represent cementitious materials. Particle generation methods can be divided into two categories dynamic techniques and constructive techniques (Bagi, 2005; Jerier et al., 2009; Labra and Eugenio, 2009).

Bagi (2005) provides a thorough overview of these methods, however a short summary is provided here. Dynamic techniques involve an iterative process which often occurs within the DEM framework. These techniques are characterised by a change in the particle position and/or radius, either caused by an algorithm or by external forces (either through boundary conditions or gravity). There are a number of methods that fall into this category, including: particle expansion, isotropic compression, gravitational deposition and collective rearrangement techniques (this last technique is used in this thesis and is discussed further in Chapter 4).

Two examples from the range of particle generation techniques available are provided. Carmona et al. (2008) created a large volume of random particles, and then added gravity to a central point to create a sphere of particles. These spheres are then bonded together with an increasing stiffness. This means that the particles end up not touching and the gravitational field is turned off, so there is no gravity during the testing. Stroeven et al. (2011) have dilute packing which is then pushed together using a particular geometry. They monitor the forces on the geometry to decide when a jammed state is reached. Stroeven et al. (2011) warns, however, that using vibration techniques to get denser particle packing may lead to the "brazil nut effect", where larger particles rise to the top from vertical vibration.

Constructive algorithms create particle assemblies purely using geometrical calculations (Bagi, 2005). Particles are placed one after another depending on a given rule, e.g. a new particle cannot be placed into contact with another element. Examples of constructive algorithms include regular arrangements, sequential inhibition models, sedimentation techniques, closed front techniques and inwards packing algorithms (Bagi, 2005) . The advantage of using constructive algorithms is that they are often cheap computationally, and can act as a good starting point for further dynamic techniques.

2.2.1.2 Number of component phases

The number of component phases into which the material is discretised depends greatly on the material being modelled and the modelling approach, i.e. at what scale the model is looking to predict behaviour. Rock can generally be treated as a single phase material, i.e. all particles are of the same type. Concrete is a composite material, the structure being composed of aggregate which is bound in a hardened cement paste. On the meso-scopic scale the structure itself can be divided into three distinct phases: aggregate, hardened cement paste, and an interfacial transition zone which is a very thin weak area between the other two phases.

The literature presents varying approaches to modelling the different phases. Some models represent all three phases separately; these models are advanced, as they are modelling at the microscopic scale, and as this is very computationally expensive they remain mostly in only two dimensions. For concrete modelling there are many models that use two-phase representation (Khanal et al., 2005; Qin and Zhang, 2011; Schneider et al., 2010), which represents aggregate and hardened cement paste as separate elements. Finally, many models use only a single phase (Camborde et al., 2000; D'Addetta et al., 2002). These models are most common with modelling of rock (Potyondy and Cundall, 2004), so that all the elements in the system have the same material properties and will solely be representing sections of the material that is being modelled.

2.2.1.3 Size and distribution of size of the elements

It is important to ensure that the size of the elements used allows the key phenomena of interest to be studied. Usually not all of the grains are represented like-for-like, and it is often more important that there is a sufficient number of elements in a simulation to ensure there is a high enough resolution to study fracture. The choice of size, and distribution of the elements used, determines the resolution to which results can be obtained. In the case of cementitious materials, this will relate to the size of cracks that can develop.

The particle size distribution (when using spherical particles) can be divided into three categories. They are: mono disperse, which uses one size of particle for the whole sample, e.g. Magnier and Donze (1998); bi-disperse, which uses two sizes of particle for the whole sample, e.g. Carmona et al. (2008); and poly-disperse, which uses multiple sizes of particle for the whole sample e.g. Rojek et al. (2012).

2.2.1.4 Shape of the elements

The grains found in cementitious materials, especially concrete, often have irregular shapes; this means that defining the shape of the DEM elements is not straightforward and some assumptions will have to be made. There are a number of element shapes that have been used in both two and three dimensions: circles and spheres, ellipses and ellipsoids, and polygons (2D and 3D). Circles and spheres have an advantage in that the contact detection algorithms are very simple and they can be defined with only two parameters (centre and radius). Using spheres provides a simple method for branching into 3D-modelling. In order to form more complex particle shapes with spheres, an element can be built from many spheres. There are no forces between sub-spheres, i.e. the distance between the centres is maintained. There is, however, a limit to the solid fraction that can be achieved when using these relatively simple shapes. D'Addetta et al. (2002) use polygons in 2D; this creates a zero porosity system. The problem with this is that the structure of cementitious materials includes natural pores that collapse under load; when the representation has a low or zero porosity, this effect must be added separately.

Another more advanced method is to use a cluster technique, e.g. Ergenzinger et al. (2011). In this manner, simple base elements (e.g. circles or spheres) are held together with relatively strong bonds to form meta-particles. These meta-particles are either composed of particles that are overlapping and fixed relative to one another, or not overlapping and bonded together. Making a cluster out of bonded particles allows intra-meta-particle breakage to occur, and small clusters of particles are able to break off; this is a phenomenon often seen in tensile splitting tests. In simulations by Qin and Zhang (2011), non-overlapping circular disks are placed adjacent to each other to

create a larger particle; Groh et al. (2011) used ellipsoidal-shaped clusters made of spheres.

2.2.2 Initialization of bonds

Bond models designed to simulate the behaviour of cementitious materials differ from other models by the inclusion of a mechanism that represents the cement joint between grains found in those materials. In most cases, this mechanism is represented by a bonded contact which is capable of resisting the separation of the particles it connects. An initialization procedure is required to determine which elements are considered bonded and which are not. For most bond models, a criterion exists which must be met in order for two particles to be considered bonded; this is often related to the proximity of two elements.

Most commonly, a parameter is included in the model that extends the contact search radius for each particle e.g. Bazant et al. (1991); Hentz et al. (2004a); Tavarez and Plesha (2007). This means that particles which are not in physical contact can still be bonded together. As the value of the parameter that extends the contact radius is reduced, the number of bonds will reduce and so the material being represented becomes more granular in nature. If the contact search radius for each particle was reduced to the same as the physical radius, then the elements would have to be in direct physical contact for a bond to form between them; this is seen in the model presented by Ergenzinger et al. (2011).

The literature reports that the force-displacement law for a single bond between two elements often requires the geometric dimensions of the bond to be defined. When using spherical particles, the bond is either assumed to be a cylinder of uniform or non-uniform cross section (Rojek et al., 2012). The length of the bond is taken as the straight line distance between particle centres. There are a number of ways in which the radius of the bond can be determined, although it is almost always related to the radii of the two particles connected by the bond. When a uniform cylinder is considered, the radius of the bond is either determined to be the arithmetic mean of

the two connecting particles as shown in Figure 2.2(a), used in (Potyondy and Cundall, 2004), or a proportion of the smallest radius of the two connecting particles as shown in Figure 2.2(b), used by DEM Solutions (2008), Bazant (1990) and Hentz, et al. (2004a). When a non-uniform cylinder is considered, the bond radius is calculated using the harmonic mean of the radii of the two connecting particles, as shown in Figure 2.2(c), which is used by Rojek et al. (2012). It should be noted that some models such as the one proposed by Potyondy and Cundall (2004) use the arithmetic mean when determining the radius for bond stiffness, but the minimum when determining it for bond strength. This is because the smaller radius will act as the weakest link in the structure; this is an analogy of the Weibull weakest link model (Bažant et al., 2004).

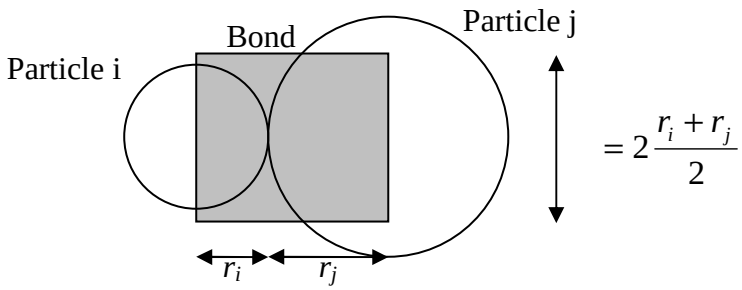

(a) Arithmetic mean of particle radii

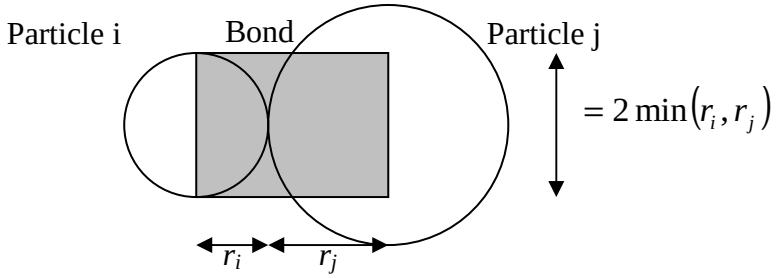

(b) Minimum particle radius

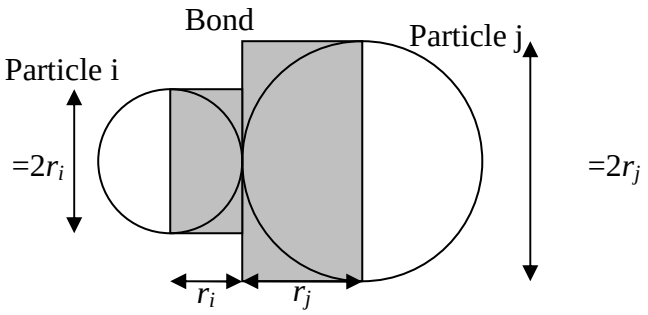

(c) Harmonic mean of particle radii

Figure 2.2 Determining the cross sectional geometry of a bond

2.2.3 Contact law

In the DEM, elements interact through contact forces. The resolution of these forces, and thus the interaction, is determined using a contact law which describes the material's constitutive behaviour (Antonyuk et al., 2006). These laws can be seen as the formulation of the material model on the microscopic level (Labra, 2012) and are probably the most important part of the model (Kuhl et al. 2000). Models designed for simulating cementitious materials are similar in the way that they assume that the

discrete elements are bonded together; these bonds are normally massless with mass assigned to the discrete elements. Sawamoto et al. (1998) suggest that two possible states are defined for each interaction between elements, depending on the status of the contact. In the first state (the initial state) the constitutive law allows either compression, shear or tension forces to be generated between particles. Failure conditions can then be applied, and if met, the interaction can be changed. The status can then become defined by a second state, in which the contact only has compressive or shear forces and can no longer resist tensile forces. Ergenzinger et al. (2011) suggest that contact models should be as simple as possible whilst still capturing the important mechanisms. This saves computational effort and the number of free parameters that must be estimated.

There are a number of different approaches which have been developed to represent the cement mechanism; in the most simplistic fashion they can either be linear or non-linear.

One of these representations assumes that particles are connected by a point of glue, such as in the contact bond model as described by (Cho et al., 2007). The glue represents a pair of elastic springs with a constant normal and shear stiffness. These connections are unable to carry moments and are relatively simple. Cho et al. (2007) points out that the “contact stiffness is still active even after bond breakage as long as particles are kept in contact. This implies that in the contact bond model, if particle contact is maintained, bond breakage may not significantly affect the macro stiffness, which is unlikely for rocks”.

An alternative to the contact bond model is the improved parallel bond model (Potyondy and Cundall, 2004), which has been used by many authors including Su and Ali-Akcin (2011) and Cho et al. (2007). The parallel bond model can be considered as “a set of elastic springs uniformly distributed over a rectangular cross section with a constant normal bond stiffness and shear bond stiffness lying on the contact plane and centred at the contact point” Cho et al. (2007). In addition to normal and shear forces, the parallel bond is also able to transmit moments.

Another bond representation is the use of beam elements, which are assumed to link the centres of particles in a bonded contact e.g. Schneider et al. (2010); André et al. (2012); Carmona et al. (2008) and D'Addetta et al. (2002). When using beams, the elastic behaviour can be described simply using the following: radius, length, Young's modulus and Poisson's ratio. The contact laws can be based on Euler-Bernoulli or Timoshenko beam theory, and the elements are able to resist tensile force and moments. Schneider et al. (2010) highlighted that beam models provides a good compromise between computational time and accuracy.

In some cases, the bond between elements can be considered as a series of springs across the interface of two elements (Schneider et al., 2010). The use of interface elements is borrowed from the finite element method; D'Addetta and Ramm (2006) provide a detailed description of this bond type.

It should be remembered that models used to mimic the behaviour of cementitious materials need to include a contact law that deals with non-bonded contacts as well as bonded contacts. These non-bonded contacts may arise either through the breakage of bonds or when two elements come into contact after the bond initialization procedure.

It is the behaviour at the contact level which influences the overall mechanical behaviour. One of the main concerns when using the DEM is to ensure that the appropriate contact laws and microscopic parameters are used to represent the subject material on the macroscopic scale (Rojek et al., 2012).

Determining the micromechanical parameters becomes harder when modelling concrete as a two phase material (Schneider et al., 2010). In this instance, although the elements representing the aggregates and cement matrix have different physical properties, the bonds between them are also given different stiffness and strength properties to represent those found in concrete. In the two phase representation presented by Schneider et al. (2010) the bonds between aggregates are the stiffest and strongest, then it is the bonds between the matrix particles and then the lowest

stiffness and weakest are the bonds between matrix and aggregate particles. The use of multiple bond types is compounded by the fact that micro-properties are unknown.

2.2.4 Bond failure criteria

Under loading, a cementitious material represented with a bond model will fail when enough bonds have been broken so that the specimen becomes unable to sustain the load. In this manner, bonds can fail at any location in the material. Therefore, there is no need to artificially initiate cracks as is sometimes required in Finite Element Methods (Ergenzinger et al., 2011).

Bonded particle models require a method through which the inter-particle bonds can fail; this failure represents the fracture and progression of damage in the granular solid. Most bonded particle models reported in the literature compare the state of each bond to a predefined failure criteria; these criteria are based on limits of force (Magnier and Donze, 1998), strain (Carmona et al., 2008; D'Addetta et al., 2002; Schneider et al., 2010), stress (Cho et al., 2007), or energy release rate (Tavarez and Plesha, 2007).

2.2.5 Calibration and estimation of the bond model parameters

Magnier and Donze, (1998) highlighted that "because of the geometrical disorder in the model, explicit relationships between local parameters and macroscopic parameters are difficult to determine". Most models require some form of calibration procedure or estimation of the microscopic parameters; in this, relationships are established between the microscopic parameters and the bulk response with the aim of matching this to a set of desired behaviour. Camborde et al. (2000) suggest that uni-axial compression tests are an appropriate method for this calibration. If loading of these tests is strain-rate controlled, then the post-peak behaviour can also be matched (Ergenzinger et al., 2011). Many authors, including André et al. (2012); Magnier and Donze, (1998) and Su and Ali-Akcin (2011) use the uni-axial compression test to calibrate their models for cementitious materials.

There are some drawbacks to only using one test to estimate the parameters for the model. Diederich (2000) cited by Cho et al. (2007) found that the tensile strength was over-predicted when the 2D bonded particle model (Potyondy and Cundall, 2004) was calibrated to the uni-axial compressive strength. Cho et al. (2007) found that it was not clear if the same model was being calibrated for modelling any problem with that material, or just a uni-axial compression test. In order to be sure that a model is correctly calibrated, Cho et al. (2007) suggest using uni-axial, tri-axial and Brazilian tests. This is clearly more accurate, but could be considered too time consuming if a simpler model were available.

2.3 Application of bonded models for predicting the behaviour of cementitious materials

A variety of work has been conducted that uses bonded particle models to simulate the behaviour of cementitious materials under different loading conditions. Most of the work has looked at cementitious materials under quasi-static uni-axial loading, of rock in 2D (Cho et al., 2007) and 3D (Potyondy and Cundall, 2004), and also concrete in 2D (Azevedo et al., 2008) and 3D (André et al., 2012).

In addition to this a number of authors have looked into the influence of strain rate on behaviour and dynamic loading (Camborde et al., 2000; Hentz et al., 2004b; Qin and Zhang, 2011) including the impact of missiles on concrete beams studied in 2D by Magnier and Donze (1998). Sawamoto et al. (1998) used a bonded particle model to examine the dynamic impact of deformable missiles on reinforced concrete.

Advances in imaging technology mean more complex physical behaviour of cementitious materials can be compared to numerical results; Carmona et al. (2008) used high-speed cameras to capture the fragmentation process of comminution of concrete specimens. Bonded particle models have been used to study the behaviour of impact breakage and comminution of materials – in these cases meta-particles are formed, consisting of a number of individual discrete elements which are bonded together. This technique has been successfully employed for looking at the impact

breakage of granules of different materials at different velocities on a plane surface (Antonyuk et al., 2006). This work was limited to 2D, but clearly showed how the material fragments and how cracks grow.

Another area of interest is rock cutting, whereby the interaction between a cutting element and a DEM-simulated rock material is assessed. This has been looked at in 3D by Su and Ali-Akcin (2011) and also by Labra (2012).

Groh et al. (2011) state: “DEM was already widely applied to simulate damage and crack development but these simulations are restricted in all or at least some ... aspects”. They flagged restrictions such as the following: simulations consider 2D problems only, only quasi-homogeneous material is considered, there is no consideration and distinction between intra-granular and inter-granular breakage and there is no explicit consideration of shape, orientation and space distribution of grains.

2.3.1 Application of EDEM’s Hertz-Mindlin with bonding model

The simulations in this study will be carried out using the DEM software EDEM (DEM.Solutions, 2010). EDEM contains its own bonded particle model called the “Hertz-Mindlin with bonding model”; this is a modification of the bonded particle model presented by Potyondy and Cundall (2004). In the Hertz-Mindlin with bonding model, particles are joined by finite-sized glue which is capable of resisting normal and tangential displacements at bonded contacts. Breakage of bonds occurs when normal or tangential stress limits are exceeded; after bond breakage, particles can interact using the regular Hertz-Mindlin model, which is described in more detail in Chapter 3.

There appears to be no published works which have validated the use of this model for cementitious materials, so to see if this model would be suitable for use in this project, extensive verification and validation processes were conducted. This review concluded that there are a number of deficiencies with the Hertz-Mindlin with bonding model which make it unsuitable for use in this project. Some of these

deficiencies include the fact that the bending moment is calculated based on the relative rotation of the particles at each end of each bond. One consequence is that the two particles can rotate at the same speed without causing any moment in the bond; such a mechanism is not physical in a bonded assembly. This moment is also not fed back to the particles, meaning that there are no moments resisting the rotations of the particles included in the model.

In the Hertz-Mindlin with bonding model, if there is a relative displacement (normal to the bond axis) between the two particles with no relative rotation, the model predicts a pure shear without any bending moment. This violates the engineering bending theory and can cause significant errors.

As discussed above, the bonds in a complex assembly of particles have different lengths and radii. The Hertz-Mindlin with bonding model does not reflect this, as it has a constant normal stiffness and constant shear stiffness irrespective of bond geometry. The cross sectional area of each bond is calculated irrespective of the radii of the particles it connects.

From fundamental mechanics, one may either use a strut model or a beam model for the bond. A strut model only resists axial forces, which is simple to implement and fast for computation. A beam model is more realistic, but is more complex and computationally more intensive. The current EDEM Hertz-Mindlin with bonding model includes components from both strut models and beam models however, as some critical components are missing it cannot be classified as either.

2.4 Summary

The literature review reveals that many differing approaches have been taken to the modelling of cementitious materials using a DEM approach. From this review it is clear that although the application of the method is varied, the models share many core principles.

The key issues identified herein include the nature and packing of particles, the definition of the bonded contacts, and their constitutive relations (including failure criteria to remove bonded contacts). These issues are addressed in the following chapters, where a novel bonded particle model is developed and a parametric study adds to the understanding of the issues raised here.

Chapter 3 The development of a new bonded particle model

3.1 Introduction

This chapter presents a new bonded particle model, developed to study the behaviour of cementitious materials. It first presents the theory of the bonded contact model and then the main operating procedures for the implementation of the model. The results from a verification procedure conducted to ensure the correct implementation of the theory are also included.

The primary aim of this study is to investigate the response of cementitious materials to load. The literature review in Chapter 2 revealed that bonded particle models implemented in the Discrete Element Method (DEM) provide an effective tool for this purpose; this is due to the discrete inhomogeneous nature of these materials. Whilst a range of bond models have been reported, the literature review has shown that some limitations still exist.

The failure of cementitious materials is highly influenced by the initiation and propagation of cracks that occur at cemented grain interfaces. The ability of bonded particle models to produce a realistic representation of a cemented granular material depends largely on the constitutive relationship used to describe the behaviour of bonded contacts between particles, which can be used to represent the interactions in the physical material. There are many derivations for these constitutive relationships, but from fundamental mechanics either a strut model or a beam model may be used. A strut model only resists axial forces, but is simple to implement and fast for computation; beam models are more computationally expensive but tend to provide a more realistic representation of the bond mechanism as they take into account all

potential loading actions at a cemented joint (Carmona et al., 2008; D'Addetta et al., 2002; Schneider et al., 2010).

A new bonded particle model, referred to hereafter as the Edinburgh Bonded Particle Model (EBPM), is proposed. In this model cementitious materials are idealised as a dense assembly of spherical, non-deformable discrete elements (particles) connected by bonds. The objective of this new approach is to provide a realistic mechanics-based representation of the interaction between particles.

It should be noted that it is often the case when using the DEM to model granular materials that each particle will represent a single grain of the subject material. Although the possibility of modelling solid materials, such as concrete, grain for grain is not excluded each DEM particle may instead represent a portion of the subject material incorporating a mixture of aggregates and hardened cement paste. In this manner the subject material could be discretized into any number of particles of any size rather than there being a direct grain for grain representation. In a similar way the bonds between particles do not necessarily directly represent a physical "glue" between grains but rather provide a virtual network which describes the interactions of particles and can transmit forces between them. As the bonds are not physical they contain no mass and cannot have external forces applied to them directly (this is discussed in more detail below); the mass of the subject material is entirely represented by the mass of the particles.

In the implementation of the model presented in this study the meso-structure of concrete is directly considered with the material being represented in a single phase where each particle represents a portion of the material (as described above). Behaviour and properties at the microscopic level are incorporated into the model response which is then projected onto the macroscopic level.

3.2 The Edinburgh Bonded Particle Model

The particles in the Edinburgh Bonded Particle Model interact at either bonded or non-bonded contacts. Only one contact can exist between any two particles due to their spherical nature:

- At a *bonded contact* a virtual bond element is considered to exist between the particles cementing them together. The constitutive behaviour of the bond is described in the Timoshenko Beam Bonded-Contact Model (TBBM), which is presented in this chapter and is based on the Timoshenko beam theory (Timoshenko, 1922).
- At a *non-bonded contact* a spring-dashpot configuration is assumed. The constitutive behaviour of this configuration is described using the popular Hertz-Mindlin Contact Model (HMCM), the components of which are described in Johnson (1987).

Both contact types resist compressive and shear forces, but bonded contacts may also resist tensile forces and bending moments. Material damage is represented directly through the breakage of bonds. In this manner failure mechanisms which occur in the microstructure of the subject material are included but not necessarily represented directly. This enables the response of the material to load to be studied as damage develops in the system.

3.2.1 The Timoshenko Beam Bonded-Contact Model

The TBBM forms the core section of the EBPM and is described here in full. In the TBBM model, each bond is assumed to behave as a cylindrical beam that connects the centres of two bonded particles. The connection between each end of the bond and the centre of the corresponding particle is considered to be rigid; therefore each end of the bond shares the same six degrees of freedom as the particle. A single beam can be considered to exist between particles *A* and *B* as shown in Figure 3.1.

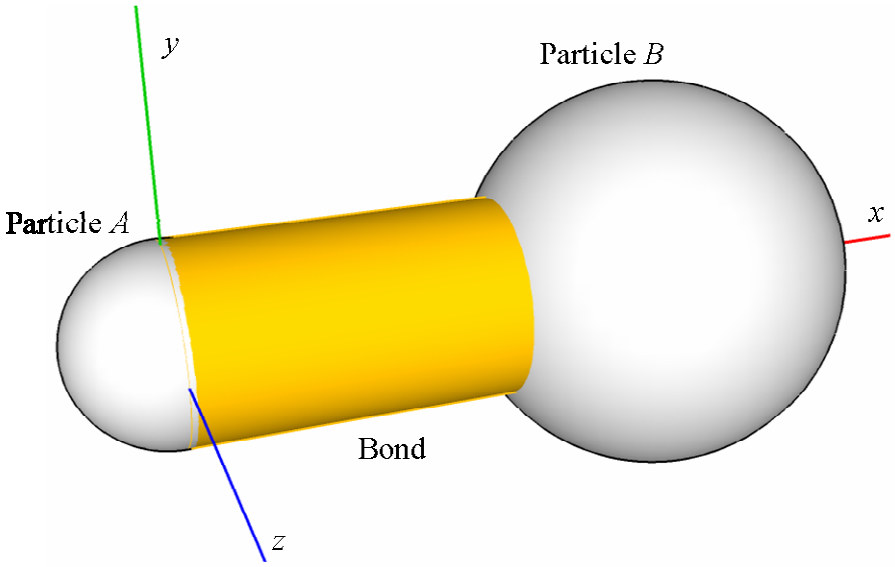

(a) Full view

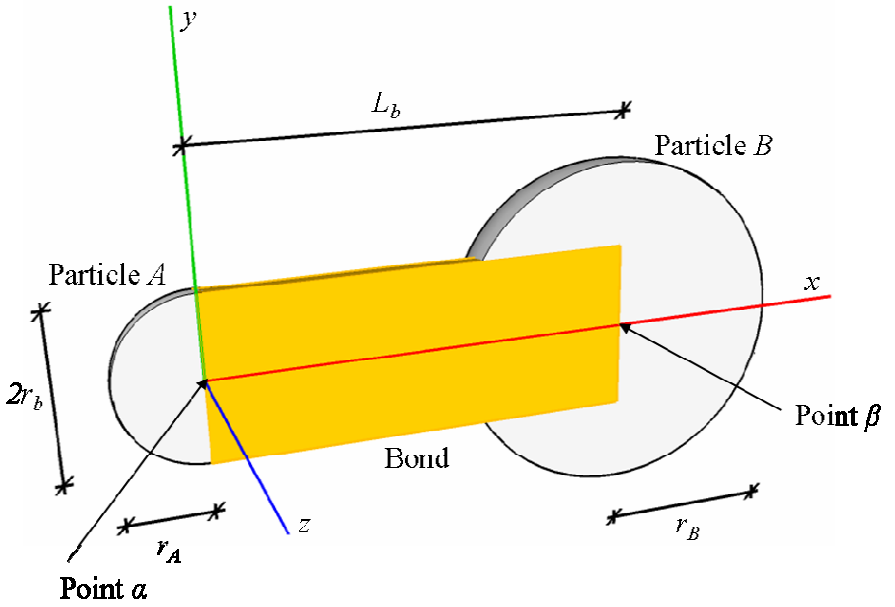

(b) View cutting through the centre of the bond

Figure 3.1 A single bond connecting particles *A* and *B*

The position *P* of each particle is defined as the location of its centre in the global Cartesian co-ordinate system (*X*, *Y*, *Z*); in the example shown in Figure 3.1 points α and β are the centres of particles *A* and *B* respectively. In addition to the global co-ordinate system, each bond has its own local co-ordinate system (*x*, *y*, *z*) as shown in

Figure 3.1. The local co-ordinate system is required to determine the forces acting on the bond, as described later in this chapter.

The geometric properties of a bond are influenced by the locations and properties of the particles it connects. A bond's length L_b can be determined from the distance between its two ends, which is the same as the distance between particle centres:

$$L_b = \|P_B - P_A\| = \sqrt{(X_B - X_A)^2 + (Y_B - Y_A)^2 + (Z_B - Z_A)^2} \tag{3.1}$$

The literature reports many different ways in which the bond radius can be determined, for example either using the arithmetic or harmonic means of the two particles' radii (Rojek et al., 2012). For the purposes of this thesis, the radius for each bond r_b is assumed to be:

$$r_b = \lambda \cdot \min(r_A, r_B) \tag{3.2}$$

where r_A and r_B are the radii of particles A and B respectively. The numerical parameter λ is henceforth termed the bond radius multiplier; this parameter introduces flexibility into the way the bond radius is determined. By including a multiplier, the geometric parameters of the assembly (e.g. porosity) can be taken into consideration. Similar bulk responses can be generated for different particle assemblies by modifying the value of bond radius multiplier. A default value for the bond radius multiplier of one is recommended.

Bonds are virtual elements with no mass or volume. However, bonds are subjected to internal forces caused by the displacements and rotations of the particles they connect. As the bonds are assumed to behave like beams, these internal forces can be determined using one of the beam theories.

An assumption of the most common beam theory, the Euler-Bernoulli beam theory (Bauchau and Craig, 2009), is that after deflection, cross sections perpendicular to the neutral axis of the beam remain both plane and perpendicular – the well-known plane section assumption. This means that the shear deformation is neglected. Whilst this is acceptable for slender beams, the shear deformation can be significant in stocky beams such as those concerned in this study. The Timoshenko beam theory, which includes the shear deformation, is therefore more appropriate here (Timoshenko, 1922).

The Timoshenko beam theory can be used to describe the response of a deep beam to loading actions. If a pair of transverse shear forces of magnitude Q and a pair of bending moments of magnitude M are considered to act on a single cylindrical beam (as shown in Figure 3.2), such that only transverse deflections are considered, then the rotation of a deformed cross section ψ can be determined using the Timoshenko beam theory, as shown in Equation (3.3):

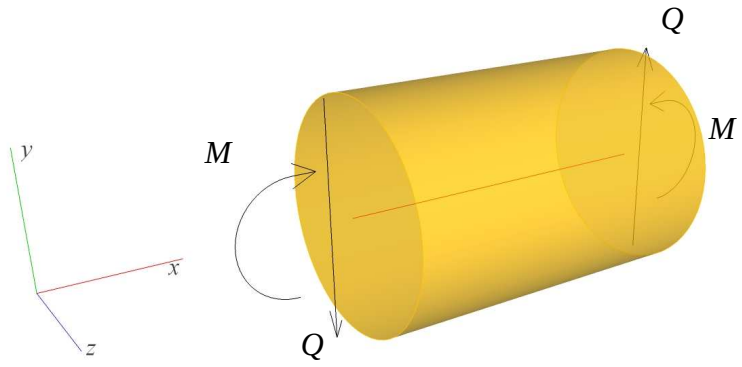

Figure 3.2 Shear forces and bending moments acting on a cylindrical beam

$$\psi = \frac{dz}{dx} + \frac{dz_s}{dx} \tag{3.3}$$

where dz/dx is the slope of the deformed neutral axis and dz_s/dx is the rotation of the cross section due to shear deformation, which is approximately equal to the shear strain at the neutral axis, so that:

$$\frac{dz_s}{dx} = -\frac{Q}{\kappa GA} \tag{3.4}$$

where G is the shear modulus of elasticity of the beam, A is the cross sectional area of the beam and κ is a shear correction coefficient which takes into account the difference between the actual and assumed uniform distribution of shear stress across the depth of the beam; this is still an approximation, as the real distribution is not linear. The value of the shear correction coefficient is related to the Poisson's ratio v of the beam and the cross sectional shape. Values of κ from experiments conducted by Kaneko (1978) match the theoretical solution derived from Timoshenko's original paper (Timoshenko, 1921), and have been confirmed more recently by Hutchinson (2001). For a circular cross section, the shear correction factor is:

$$\kappa = \frac{6+12\nu+6\nu^2}{7+12\nu+4\nu^2} \tag{3.5}$$

The stiffness parameters for a Timoshenko beam are derived from the governing equations for the transverse deflections, which are:

$$M = -EI\frac{d\psi}{dx} \tag{3.6}$$

$$\frac{dz}{dx} - \psi = -\frac{Qf_s}{GA} \tag{3.7}$$

where M is the applied moment, EI the flexural rigidity of the beam and GA/f_s the shearing rigidity of the beam; f_s is the form factor for shear, which can be equated to the inverse of the shear correction coefficient κ when determined from the method of virtual work. Wang (1995) put the Timoshenko deflection and stress resultants in terms of their Euler-Bernoulli counterparts for easy comparison.

Equations 3.6 and 3.7 are used in part to determine the 12 internal forces and moments in a bond. The location and positive direction of these forces and moments are shown in Figure 3.3.

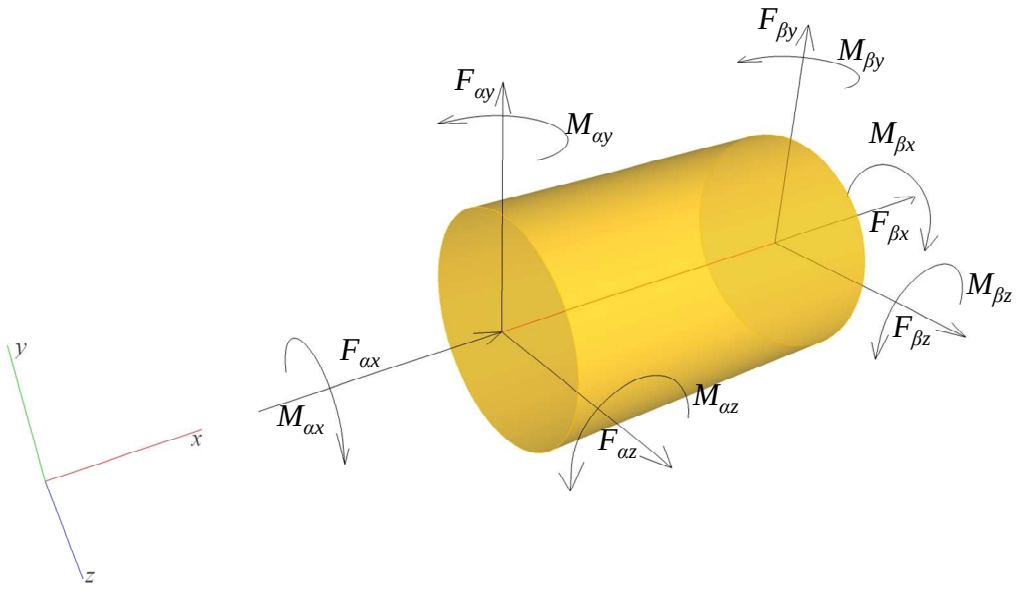

Figure 3.3 The six forces and six moments acting on a bond in the local co-ordinate system

In Figure 3.3, M and F represent the moments and forces acting on the bond respectively, the subscripts α and β denote the two ends of the bond, and subscripts x, y and z denote the local coordinate system of the bond (i.e., $F_{\alpha x}$ is the internal force acting at the point where the x axis of the bond meets the α end of the bond). The forces and moments acting on the bond can be broken down as follows: axial forces $F_{\alpha x}$ and $F_{\beta x}$, shear forces $F_{\alpha y}$, $F_{\alpha z}$, $F_{\beta y}$ and $F_{\beta z}$, twisting moments $M_{\alpha x}$ and $M_{\beta x}$, and bending moments $M_{\alpha y}$, $M_{\alpha z}$, $M_{\beta y}$ and $M_{\beta z}$. Using the Timoshenko beam theory, the

relationship between the end displacement loading and resulting forces for a bond can be expressed as:

$$\{F\} = [K] \cdot \{u\} \tag{3.8}$$

where $\{F\}$ is the force vector containing the 12 forces and moments (Equation (3.9)), $\{u\}$ is the corresponding displacement (rotation) vector in which d and θ are the displacements and rotations of the two ends of the bond (Equation (3.10)), and $[K]$ is a 12×12 stiffness matrix, of which the general form is derived from the differential equations for beam displacement using the unit displacement theory for a Timoshenko beam, as presented by Przemieniecki (1968) (Equation (3.11)).

$$\{F\} = \begin{Bmatrix} F_{\alpha x} \\ F_{\alpha y} \\ F_{\alpha z} \\ M_{\alpha x} \\ M_{\alpha y} \\ M_{\alpha z} \\ F_{\beta x} \\ F_{\beta y} \\ F_{\beta z} \\ M_{\beta x} \\ M_{\beta y} \\ M_{\beta z} \end{Bmatrix} \tag{3.9}$$

$$\{u\}=\begin{Bmatrix} d_{\alpha x} \\ d_{\alpha y} \\ d_{\alpha z} \\ \theta_{\alpha x} \\ \theta_{\alpha y} \\ \theta_{\alpha z} \\ d_{\beta x} \\ d_{\beta y} \\ d_{\beta z} \\ \theta_{\beta x} \\ \theta_{\beta y} \\ \theta_{\beta z} \end{Bmatrix} \tag{3.10}$$

(3.11)

$$
[K]=\left[\begin{array}{cccccc|cccccc}
\frac{E_b A_b}{L_b} & & & & & & & & & & & \\
0 & \frac{12E_bI_b}{L_b^3(1+\Phi)} & & & & & & & & & & \\
0 & 0 & \frac{12E_bI_b}{L_b^3(1+\Phi)} & & & & & & & & & \\
0 & 0 & 0 & \frac{E_bI_b}{(1+\nu_b)L_b} & & & & & & & & \\
0 & 0 & \frac{-6E_bI_b}{L_b^2(1+\Phi)} & 0 & \frac{(4+\Phi)E_bI_b}{L_b(1+\Phi)} & & & & & & & \\
0 & \frac{6E_bI_b}{L_b^2(1+\Phi)} & 0 & 0 & 0 & \frac{(4+\Phi)E_bI_b}{L_b(1+\Phi)} & & & & & & \\
\hline
\frac{-E_bA_b}{L_b} & 0 & 0 & 0 & 0 & 0 & \frac{E_bA_b}{L_b} & & & & & \\
0 & \frac{-12E_bI_b}{L_b^3(1+\Phi)} & 0 & 0 & 0 & \frac{-6E_bI_b}{L_b^2(1+\Phi)} & 0 & \frac{12E_bI_b}{L_b^3(1+\Phi)} & & & & \\
0 & 0 & \frac{-12E_bI_b}{L^3(1+\Phi)} & 0 & \frac{6E_bI_b}{L_b^2(1+\Phi)} & 0 & 0 & 0 & \frac{12E_bI_b}{L_b^3(1+\Phi)} & & & \\
\hline
0 & 0 & 0 & \frac{-E_bI_b}{(1+\nu_b)L_b} & 0 & 0 & 0 & 0 & 0 & \frac{E_bI_b}{(1+\nu_b)L_b} & & \\
0 & 0 & \frac{-6E_bI_b}{L_b^2(1+\Phi)} & 0 & \frac{(2-\Phi)E_bI_b}{L_b(1+\Phi)} & 0 & 0 & 0 & \frac{6E_bI_b}{L_b^2(1+\Phi)} & 0 & \frac{(4+\Phi)E_bI_b}{L_b(1+\Phi)} & \\
0 & \frac{6E_bI_b}{L_b^2(1+\Phi)} & 0 & 0 & 0 & \frac{(2-\Phi)E_bI_b}{L_b(1+\Phi)} & 0 & \frac{-6E_bI_b}{L_b^2(1+\Phi)} & 0 & 0 & 0 & \frac{(4+\Phi)E_bI_b}{L_b(1+\Phi)}
\end{array}\right]
\quad \text{Symmetric}
$$

In Equation (3.11), E_b is the bond's Young's modulus, v_b the bond's Poisson's ratio, A_b the bond's cross sectional area, I_b the bond's second moment of area and Φ the Timoshenko shear coefficient, where:

$$I_b = \frac{r_b^4 \pi}{4} \tag{3.12}$$

$$A_b = r_b^2 \pi \tag{3.13}$$

$$\Phi = \frac{f_s 12 E_b I_b}{G_b A_b L_b^2} = \frac{20 r_b^2 (1+v_b)}{3 L_b^2} \tag{3.14}$$

Each bond is assumed to behave in a linear, elastic and brittle manner; a bond will fail if any of the following criteria are met:

$$\sigma_C < \sigma_{C\,MAX} \tag{3.15}$$

$$\sigma_T < \sigma_{T\,MAX} \tag{3.16}$$

$$\tau < \tau_{MAX} \tag{3.17}$$

where σ_{CMAX}, σ_{TMAX} and τ_{MAX} are the maximum compressive, tensile and shear stresses in each bond respectively and σ_C, σ_T and τ are the compressive, tensile and shear strengths of that bond. In the TBBM each strength component is considered independent of the others, i.e. the shear stress has no influence on the tensile failure criterion. Whilst more complex failure criterion, such as Von Mises or Mohr-Coulomb, exist the simplicity of considering them independent is sufficient for the purposes of this study.

In this study tensile stresses are considered positive and compressive stresses negative. The compressive, tensile and shear stress limits are pre-assigned for each bond through a process described in section 3.2.2.

If any of the three failure criteria shown in Equation (3.15), Equation (3.16) and Equation (3.17) are met, the bond fails and cannot reform. If there is a physical contact between the two particles, the contact will be considered to be a non-bonded Hertz-Mindlin contact and contact forces calculated accordingly. If there is no particle overlap, the contact will cease to exist.

The maximum compressive and tensile stresses in a bond occur at the outermost fibre at one end (α or β), depending on the deformation. The axial stress is constant over the cross section, whilst bending stress varies linearly. In the example shown in Figure 3.4, the maximum compressive stress will be greater than the maximum tensile stress due to the direction of the axial stress.

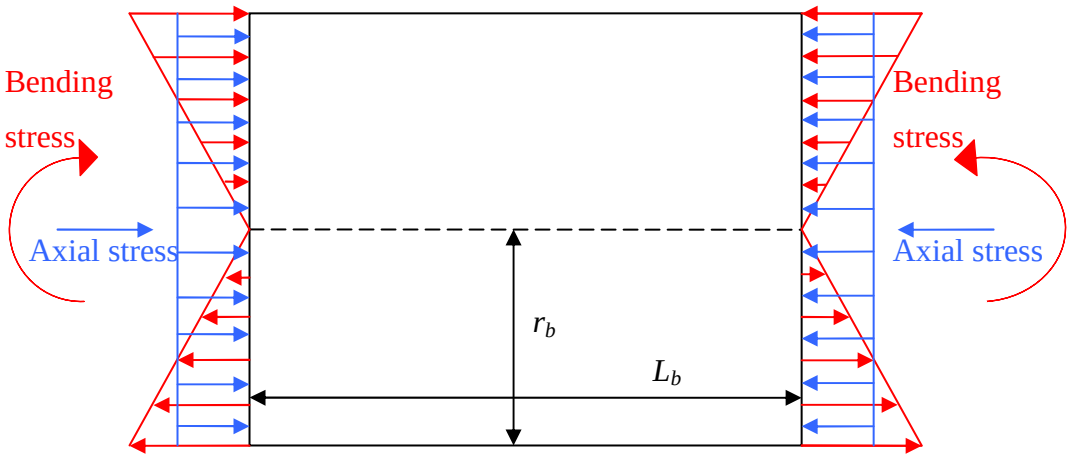

Figure 3.4 Normal stresses in a bond

While the axial stress in the bond will be equal at each end, in Equation (3.18) the axial stress is determined from the β end of the bond. As compressive stress is negative, the maximum compressive stress σ_{CMAX} in a bond will occur when:

$$\sigma_{Ci} = \left(\frac{F_{\beta x}}{A_b} - \frac{r_b \sqrt{M_{iy}^2 + M_{iz}^2}}{I_b} \right) \quad i = \alpha, \beta \tag{3.18}$$

$$\sigma_{C\,MAX} = -\min\left(\sigma_{C\alpha}, \sigma_{C\beta}\right) \tag{3.19}$$

This provides a positive value for use in the failure criteria, Equation (3.15). The maximum tensile stress σ_{TMAX} is calculated in a similar manner to the compressive stress.

$$\sigma_{Ti} = \left(\frac{F_{\beta x}}{A_b} + \frac{r_b \sqrt{M_{iy}^2 + M_{iz}^2}}{I_b} \right) \quad i = \alpha, \beta \tag{3.20}$$

$$\sigma_{T\,MAX} = \max\left(\sigma_{T\alpha}, \sigma_{T\beta}\right) \tag{3.21}$$

As the twisting moments and shear forces are equal and opposite at the two ends of the bond, the maximum shear stress can be determined at either end; here the maximum shear stress is calculated at the α end. The maximum shear stress occurs at the outermost fibre as this is where the contribution from the torsion stress is greatest and compliments the shear stress, which does not increase with distance from the centroid.

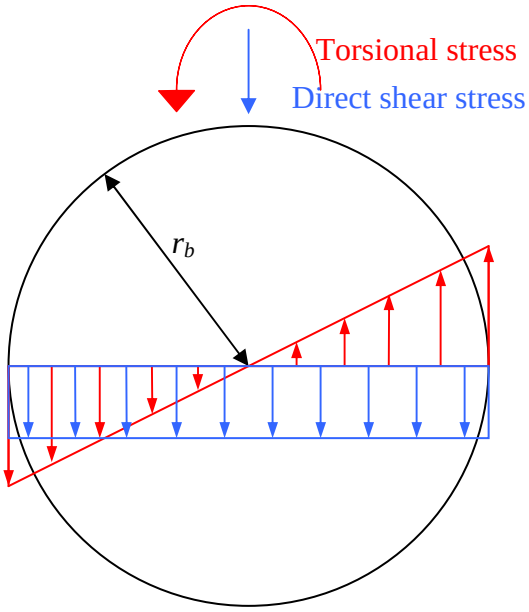

Figure 3.5 Shear stresses in a bond

$$\tau_{MAX} = \frac{|M_{\alpha x}| r_b}{2I_b} + \frac{4\sqrt{F_{\alpha y}{}^2 + F_{\alpha z}{}^2}}{3A_b} \tag{3.22}$$

If the failure criteria are not met, then forces equal and opposite to the internal forces $\{F\}$ are applied to the two particles to act as restoring forces resisting the displacements and rotations.

3.2.2 Failure criteria of bonds

In the Timoshenko Beam Bonded-Contact Model, each bond is assigned a compressive stress limit σ_C, a tensile stress limit σ_T and a shear stress limit τ; these limits define the maximum stresses that the bond can withstand before failing. The stress limits are calculated for each bond, such that:

$$\sigma_C = S_C \cdot ((\varsigma_C \cdot N) + 1) \tag{3.23}$$

$$\sigma_T = S_T \cdot ((\varsigma_T \cdot N) + 1) \tag{3.24}$$

$$\tau = S_S \cdot ((\varsigma_S \cdot N) + 1) \tag{3.25}$$

where S_C is the mean bond compressive strength, S_T is the mean bond tensile strength, S_S is the mean bond shear strength, ς_C is the coefficient of variation of compressive strength, ς_T is the coefficient of variation of tensile strength, ς_S is the coefficient of variation of shear strength (it should be noted that the acronym CoV is used in this thesis to mean coefficient of variation), and N is a random number. Whilst other statistical distributions are possible, the value for N is drawn from a normal distribution with a mean of zero and a standard deviation of one. The value of N is constant in the calculation of all three stress limits for a bond (Equation (3.23), Equation (3.24) and Equation (3.25)) but varies between bonds in a simulation. The value of the bond strengths are capped so that they must fall in a range of between zero and twice the mean strength.

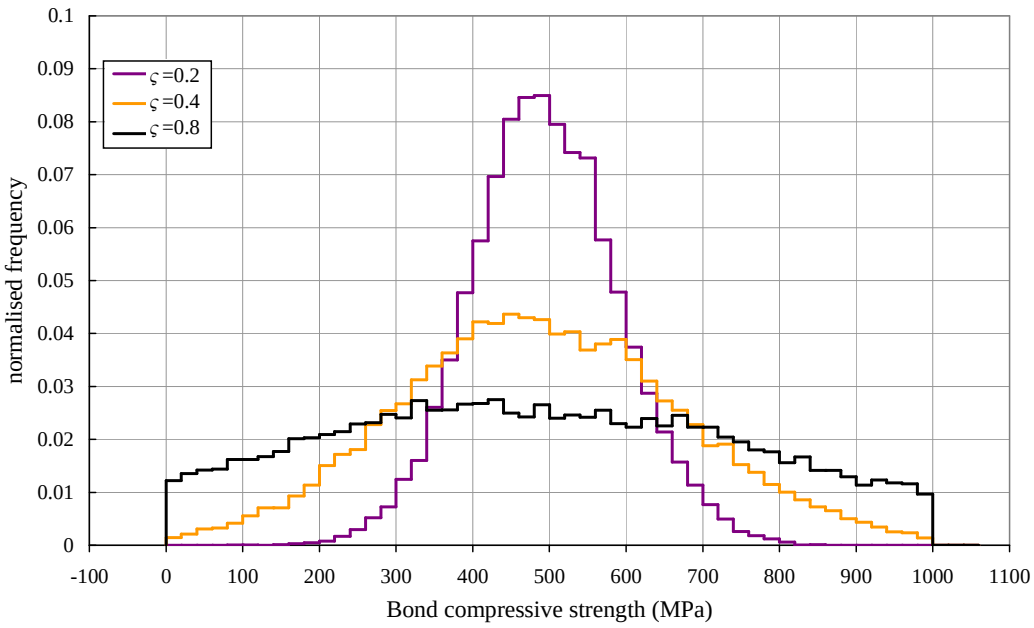

Figure 3.6 Comparing three values for coefficient of variation of strength

In Figure 3.6, three histograms describe the distribution of compressive stress limits for three values of CoV of compressive strength: the purple histogram has a mean strength of 500 MPa and a CoV of 0.2, the yellow histogram has a mean strength of 500 MPa and a CoV of 0.4, and the black histogram also has a mean strength of 500 MPa but a CoV of 0.8.

3.2.3 Coordinate transformation

The TBBM works on the assumption that there is a local co-ordinate system created for each bond; the *x* axis of this co-ordinate system is defined by the centroid axis of the bond, which runs between the centres of the two bonded particles. The other two local axes (*y* and *z*) lie normal to each other and to the centroid axis of the bond; an example of this system is shown in Figure 3.7:

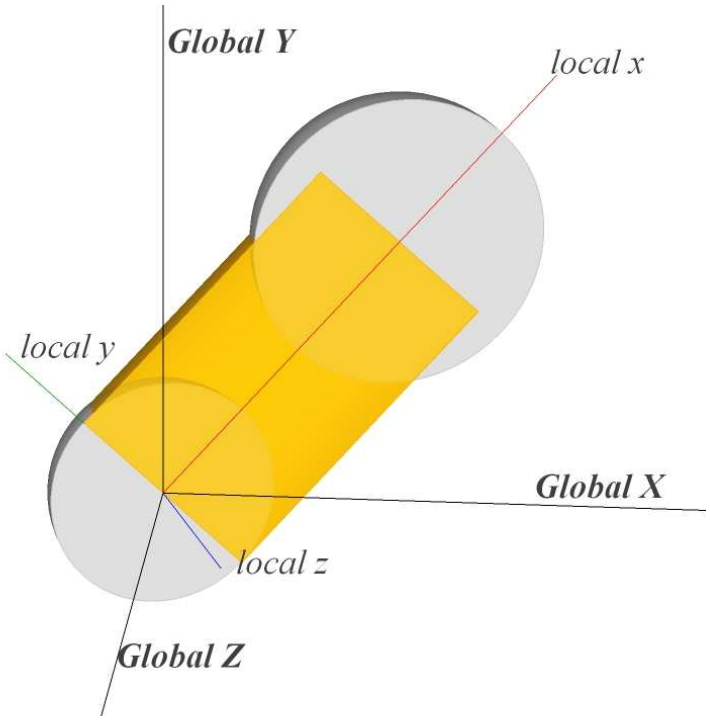

Figure 3.7 A bond with its own local co-ordinate system shown in the global co-ordinate system.

In order to calculate the forces and moments in each bond, the respective displacement loading needs to be determined in terms of that bond's local co-ordinate system. This can be achieved by multiplying the particle displacement vector in the global co-ordinate system $\{u_g\}$ by a transformation matrix $[\gamma]$, so that:

$$\{u\} = [\gamma]\{u_g\} \tag{3.26}$$

As mentioned above, $\{u\}$ is the displacement of the particles in the local co-ordinate system. The transformation matrix $[\gamma]$ contains nine directional cosines, which represent the nine angles between the three vectors defining the axes of the global co-ordinate system and the three vectors defining the axes of the local co-ordinate system.

$$[\gamma] = \begin{bmatrix} x_i & x_j & x_k \\ y_i & y_j & y_k \\ z_i & z_j & z_k \end{bmatrix} \tag{3.27}$$

There is only one set of global axes, the vectors of which are known:

$$\{\hat{X}\} = \{1 \quad 0 \quad 0\}^T \tag{3.28}$$

$$\{\hat{Y}\} = \{0 \quad 1 \quad 0\}^T \tag{3.29}$$

$$\{\hat{Z}\} = \{0 \quad 0 \quad 1\}^T \tag{3.30}$$

Due to the standard nature of the global vectors, the three vectors that define the local co-ordinate system contain the components of the transformation matrix.

$$\{\hat{x}\} = \{x_i \quad x_j \quad x_k\}^T \tag{3.31}$$

$$\{\hat{y}\} = \{y_i \quad y_j \quad y_k\}^T \tag{3.32}$$

$$\{\hat{z}\} = \{z_i \quad z_j \quad z_k\}^T \tag{3.33}$$

The three local axis vectors need to be calculated; as mentioned above, the local *x* axis follows the centroid of the beam, so that:

$$\{\hat{x}\} = \frac{P_\beta - P_\alpha}{L_b} \tag{3.34}$$

where P_α and P_β are the positions of the ends of the bond in the global co-ordinate system:

$$P_i = \lfloor X_i \quad Y_i \quad Z_i \rfloor \quad i = \alpha, \beta \tag{3.35}$$

The order in which the *y* and *z* axis of the bond's local co-ordinate system is defined does not matter; here the *y* axis is calculated first using the cross product of the local *x* axis vector, calculated in equation (3.34), and the global *Z* axis vector. The angle between *x* and *y* axes is 90 degrees. The normalised y axis can be determined as:

$$\{\hat{y}\} = \frac{\hat{Z} \times \hat{x}}{\left|\hat{Z}\right| \left|\hat{x}\right|} \tag{3.36}$$

Equation (3.36) will always produce a local *y* axis, unless the vectors *Z* and *x* are collinear; if they are, then the vector defining the local *y* axis is described as:

$$\{\hat{y}\} = \{0 \quad 1 \quad 0\}^T \tag{3.37}$$

The local *z* axis can then be determined as the cross product of the local *x* axis vector and the local *y* axis vector, such that:

$$\{\hat{z}\} = \frac{\hat{x} \times \hat{y}}{|\hat{x}|\,|\hat{y}|} \tag{3.38}$$

The bond end nodes α and β are always assumed to occupy the same positions in global space as the centres of the two particles *A* and *B*. This means that any global displacement and rotation of the particle centres is exactly equal to the global displacement and rotation of the corresponding node.

3.2.4 The Hertz-Mindlin Contact Model

The Hertz-Mindlin Contact Model (HMCM) is used to describe the force displacement relationship at non-bonded contacts; non-bonded contacts occur either through the breakage of bonds, or from two elements coming into contact for the first time (forming a new contact). The HMCM is made from an amalgamation of work and theories by many authors, and a summary can be found in (Johnson, 1987); a brief overview is presented here. The HMCM assumes that a spring-dashpot configuration exists with two directions, normal and tangential, taking into account the full 3D interaction of two elements.

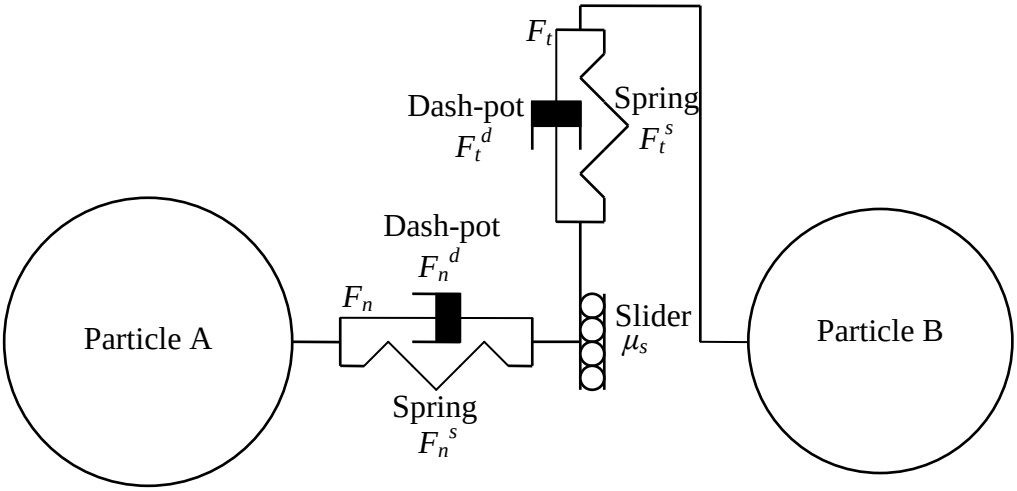

Figure 3.8 A two particle spring dashpot configuration

The normal force model is based on Hertzian contact theory (Johnson, 1987) and the tangential force model is based on the work of Mindlin and Deresiewicz (Mindlin and Deresiewicz, 1953; Mindlin, 1949). The normal force F_n and tangential force F_t at non-bonded contacts are calculated as the sum of their respective spring forces, F_{ns} or F_{ts} and damping forces F_{nd} or F_{td} so that:

$$F_n = F_{ns} + F_{nd} \tag{3.39}$$

$$F_t = F_{ts} + F_{td} \tag{3.40}$$

where

$$F_{ns} = \frac{4}{3} E^* \sqrt{r^*} \delta_n^{1.5} \tag{3.41}$$

$$F_{nd} = -2\sqrt{\frac{5}{6}} b_d \sqrt{S_n m^*} V_{n,relative} \tag{3.42}$$

$$F_{ts} = -S_t \delta_t \tag{3.43}$$

$$F_{td} = -2\sqrt{\frac{5}{6}} b_d \sqrt{S_t m^*} V_{t,relative} \tag{3.44}$$

in which

$$\frac{1}{E^*} = \frac{1-\nu_A{}^2}{E_A} + \frac{1-\nu_B{}^2}{E_B} \tag{3.45}$$

$$r^* = \frac{r_A \cdot r_B}{r_A + r_B} \tag{3.46}$$

$$m^* = \frac{m_A \cdot m_B}{m_A + m_B} \tag{3.47}$$

$$b_d = \frac{\ln e}{\sqrt{\ln^2 e + \pi^2}} \tag{3.48}$$

where E^* is the equivalent Young's modulus of the two particles, r^* is the equivalent radius, δ_n is the normal overlap, δ_t is the tangential overlap, b_d is a damping ratio related to the coefficient of restitution e (viscous damping is applied through the dashpot system, which means that damping is only applied to elements in contact),

m^* is the equivalent mass, $V_{n,\text{relative}}$ is the normal component of the relative velocity, $V_{t,\text{relative}}$ is the tangential component of the relative velocity. The subscripts A and B represent the two elements in the contact. The tangential force is limited by Coulomb friction $\mu_s F_n$, where μ_s is the coefficient of static friction. The normal stiffness S_n and the tangential stiffness S_t are defined as:

$$S_n = 2E^* \sqrt{r^* \delta_n} \tag{3.49}$$

$$S_t = 8G^* \sqrt{r^* \delta_n} \tag{3.50}$$

$$\frac{1}{G^*} = \frac{1-\nu_A^{\,2}}{G_A} + \frac{1-\nu_B^{\,2}}{G_B} \tag{3.51}$$

where G^* is the equivalent shear modulus. This contact model provides a non-linear relationship between the force and overlap.

The HMCM has been used by many authors in regards to the interaction of granular material (Johnstone, 2010; Misra and Cheung, 1999; Tsuji et al., 1992).

3.3 Implementation of the Edinburgh Bonded Particle Model into EDEM

3.3.1 Overview

For this thesis, the EBPM has been implemented in the three-dimensional discrete element software EDEM (DEM.Solutions, 2010) using an application programming interface (API). By using verified commercial software, the programming requirements of the study are reduced; the focus is then placed on verification, validation and application of the EBPM. The software EDEM has a number of useful

features which allow easy implementation and efficient computation. One such feature is the capability to store custom properties for particles and contacts; utilising this capability, the stiffness matrix and failure criteria for each bond are determined at the bond initialisation time and stored as custom contact properties.

The EBPM implementation contains three separate procedures; in addition to the two contact models, the TBBM for bonded and HMCM for non-bonded contacts, there is an initialisation procedure where bonds are created and an initial equilibrium state is enforced. The flow chart in Figure 3.9 outlines how the EBPM (highlighted in blue) is integrated into the explicit time step cycle used in EDEM 2.3. Internal forces for each contact are determined at each time step using one of the two contact models. A marker is placed on bonded contacts to differentiate them from non-bonded contacts; this marker is removed if the bond fails.

The number and geometric properties of the bonds are highly dependent on the initial packing of particles. The initial packing arrangement of particles can be generated through a number of techniques, as discussed in the literature review. In this study the particle rearrangement technique developed by Labra et al. (2010) has been used to produce a dense assembly of particles. A detailed description of this procedure is included in Section 4.3.

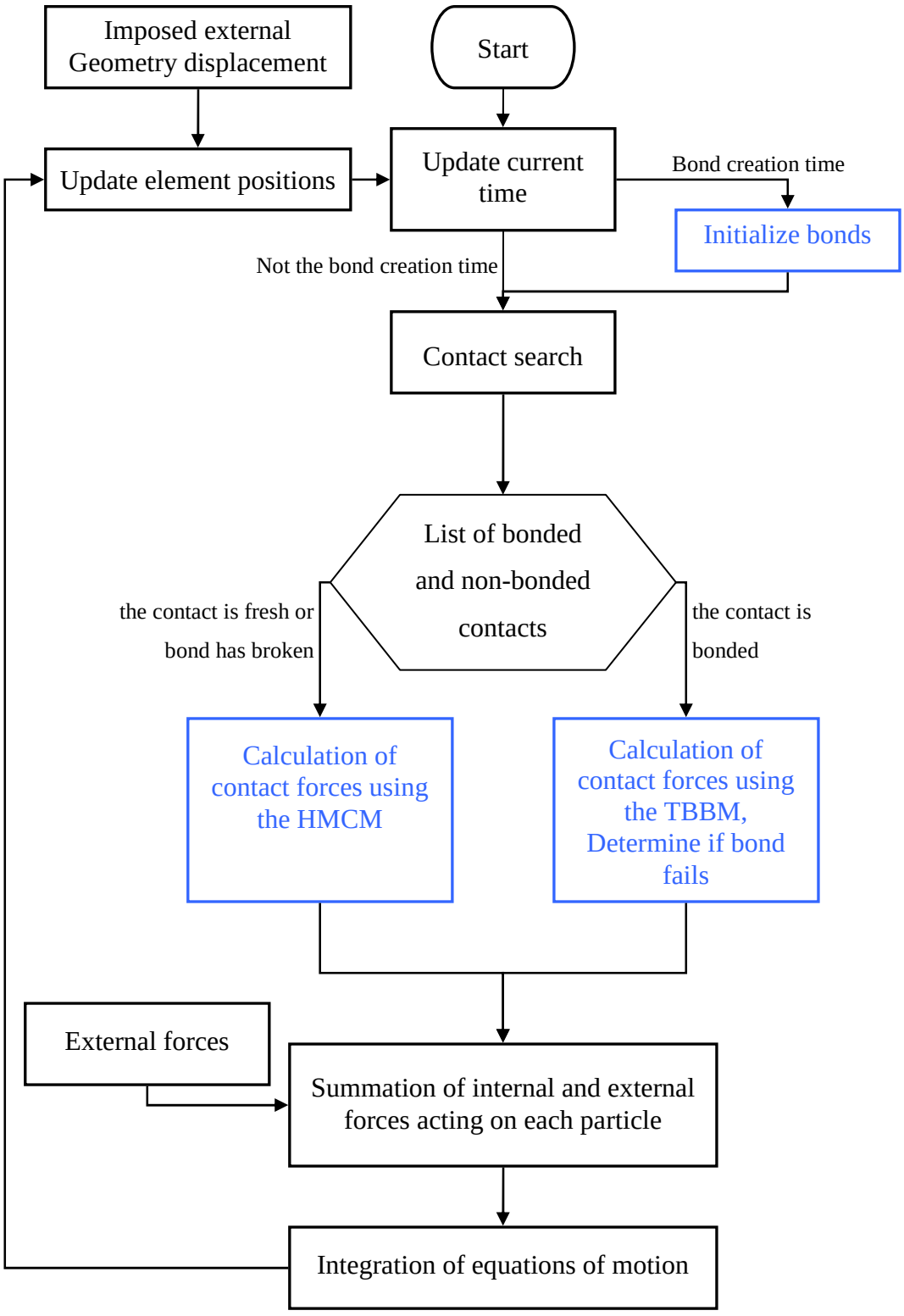

Figure 3.9 Integration of the EBPM (in blue) into the DEM calculation cycle

3.3.2 Initialization of bonded contacts

In the EBPM one time step is predefined as the bond creation time. When the simulation reaches this time step a one off bond initialisation procedure is started, as highlighted in Figure 3.9. At this time, bonds are formed between particles of specific types (in this example labelled *A* and *B*) if the following statement is true:

$$\|P_B - P_A\| \leq cr_A + cr_B \tag{3.52}$$

where

$$cr_i = \eta \times r_i \qquad i = A, B \tag{3.53}$$

where P_A and P_B are the positions of particles (A and B) in the global co-ordinate system, r_A and r_B are the physical radii of the two particles, cr_A and cr_B are the contact radii of the two particles and η is a contact search radius multiplier which is constant for all particles of the same type. By increasing the value of η above 1, bonds can still be formed between particles that are not physically touching.

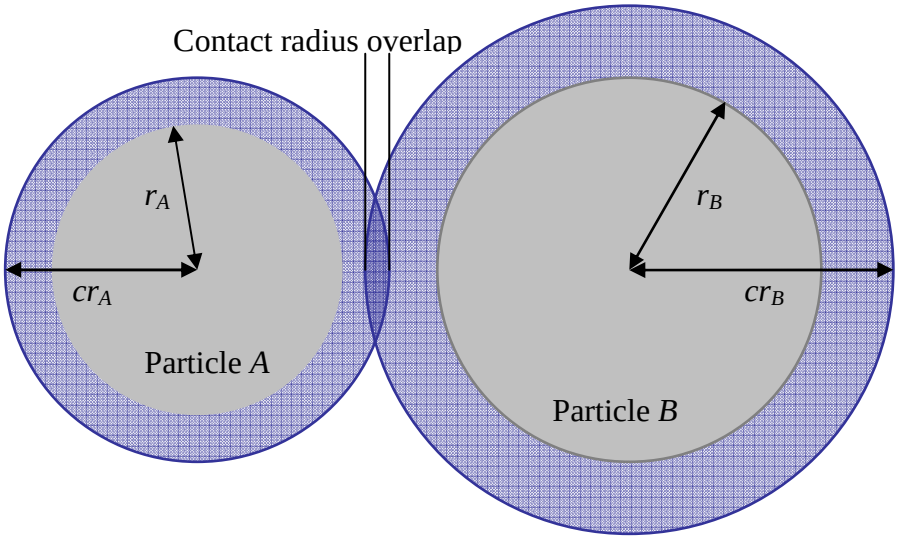

Figure 3.10 Example showing an overlap in the contact radii of particles *A* and *B*

In the example shown in Figure 3.10, there is no physical overlap of particles *A* and *B*, however as their contact radii overlap a bond could be formed between them. In the implementation presented here, there is no nearest neighbour limit for bonding particles; therefore, a bond can be formed between particles even if there is another element between them, such as in the example shown in Figure 3.11. If a nearest neighbour limit was imposed then no bond could form between particles *A* and *C* even though an interaction would be expected.

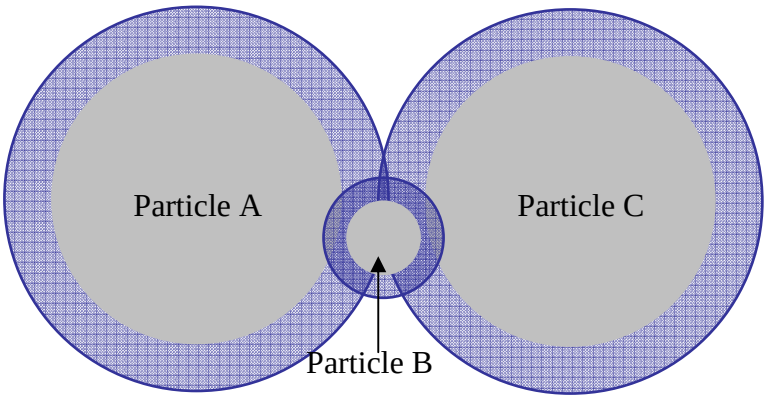

Figure 3.11 Particle *B* lies between particles *A* and *C*

By setting a value for contact radius multiplier that is appropriate for the range of particle sizes used (i.e. the greater the particle size distribution the lower the contact radius multiplier) particles are prevented from bonding beyond their closest neighbours without the need for a nearest neighbour limit. With this in mind it is recommended that the value of η should be kept in the range of 1.0 to 1.4 when dealing with high-density assemblies of similarly sized particles.

A higher contact radius multiplier means that more bonds will form in a given assembly. The more bonds that form, the stiffer the bond fabric becomes. As the stiffness of the individual bonds directly affects the bulk stiffness of the subject material, the higher the contact radius multiplier, the higher the bulk stiffness.

In the implementation of the EBPM in this study multiple bonds can be joined to any single particle. Although this may lead to an apparent overlap of the bond areas there is no penalty applied to the stiffness or strength of those bonds. This is because the bonds are a virtual representation of the interaction between particles rather than a physical cementitious substance. Characteristics such as radius are assigned so as to provide the basis for the strength and stiffness parameters of the interaction. By allowing multiple bonds to connect to each particle without penalty a dense network of bonds can be formed that represents the characteristics of a cementitious material.

When a bond is formed between two particles, the force displacement relationship is solved using the TBBM as described in Section 3.2.1 above. Some of the calculations in the TBBM, such as the determination of the stiffness matrix and failure criteria for each bond, only need to be completed once but their results must be referenced at every time step. To this end, a number of one-off calculations are conducted at the bond initialization time. At the end of the bond initialisation stage, all contact forces and overlaps (at both bonded and non-bonded contacts) are set to zero. This enforces an initial free stress state in the material. This is important to note, as a stress free state is not desired in all cases for example in excavation or tunnelling at depth the rock is often under an initial stress.

3.3.3 Calculation procedure of the EBPM implementation

The contact models within the EBPM are used to determine the internal forces arising from the two contact types: bonded and non-bonded. In order to demonstrate how the theory behind the TBBM has been implemented in the EBPM into EDEM, a single bonded contact will be considered; this contact consists of a single bond, the ends of which, points α and β, connect the centres of particles A and B as shown in Figure 3.12. The calculations executed by the EBPM once per bond per time step are outlined in a step-by-step manner in the flow chart shown in Figure 3.13.

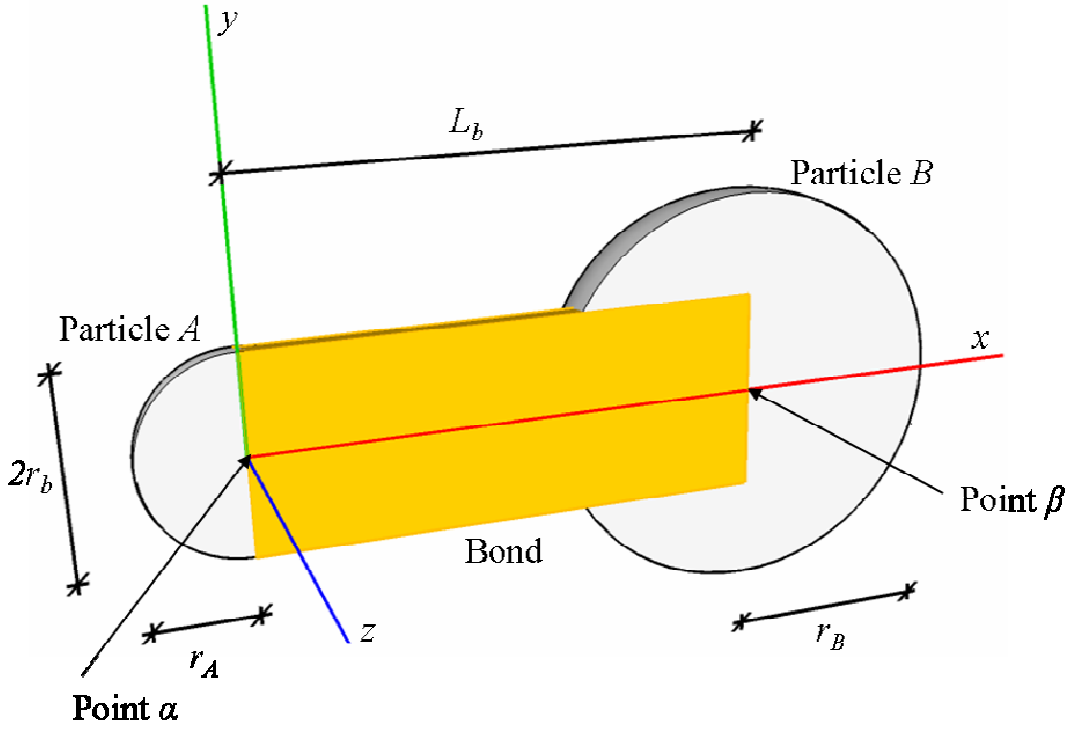

Figure 3.12 Longitudinal cross section (x-y plane at the neutral axis) of a single bond joining particles A and B - Reproduced from Figure 3.1(b)

The purpose of the bonded-contact model is to determine whether the connecting particles' load is sufficient to cause the bond to break. If not, then the model determines the total forces and moments that are returned to the two particles. What follows is a description of the calculation process:

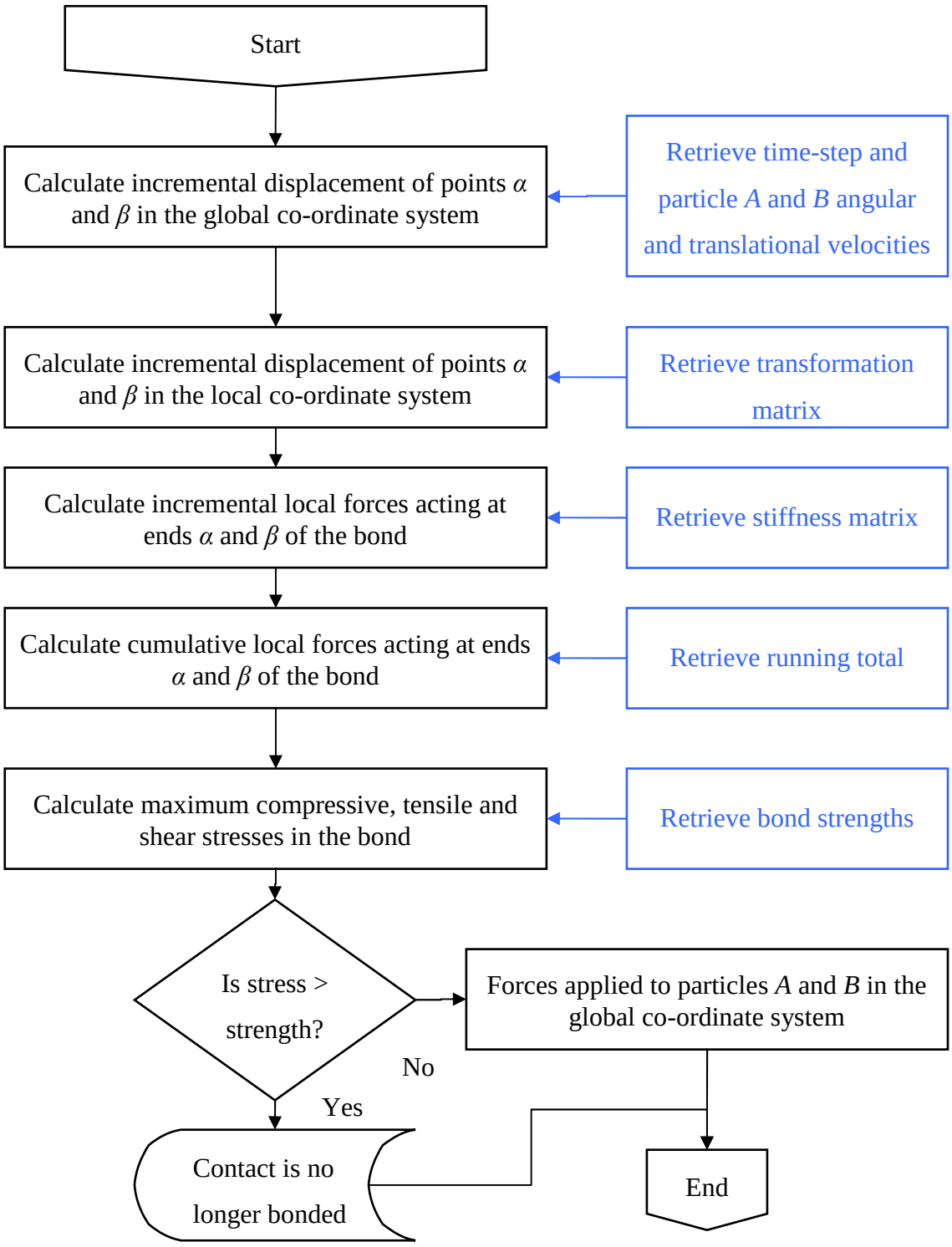

Figure 3.13 Flow chart outlining the calculation of the bonded contact model

Information such as translational and angular velocity is updated at each time step for each particle. These are presented as components of the three axes of the global co-ordinate system, *X*, *Y* and *Z*; this is the standard 3D Cartesian co-ordinate system in which data for the particles is available. Based on the time integration scheme used by EDEM, the incremental displacements and rotations of particles *A* and *B* are calculated by multiplying their velocities (translational and rotational) by the time step. In the DEM velocities and accelerations are considered to be constant over each time step (Cundall and Strack, 1979).

The bond end nodes α and β are always assumed to occupy the same positions in global space as the centres of the two particles *A* and *B*. Therefore, any global displacement and rotation of the particle centres is exactly equal to the global displacement and rotation of the corresponding node. At the considered time step, the translational velocity $\{V\}$ and angular velocity $\{\omega\}$ for the centre of each particle are known with components in the global directions *X*, *Y* and *Z*:

$$\{V_i\} = \begin{bmatrix} V_{iX} & V_{iY} & V_{iZ} \end{bmatrix}^T \quad i = A, B \tag{3.54}$$

$$\{\omega_i\} = \begin{bmatrix} \omega_{iX} & \omega_{iY} & \omega_{iZ} \end{bmatrix}^T \quad i = A, B \tag{3.55}$$

The global translational d_g and rotational displacement θ_g vectors for each particle are calculated by simply multiplying the velocity by the time step Δt:

$$\{d_{gi}\} = \begin{bmatrix} d_{giX} & d_{giY} & d_{giZ} \end{bmatrix}^T \quad i = A, B \tag{3.56}$$

$$\{\theta_{gi}\} = \begin{bmatrix} \theta_{giX} & \theta_{giY} & \theta_{giZ} \end{bmatrix}^T \quad i = A, B \tag{3.57}$$

where

$$d_{gij} = V_{ij} \cdot \Delta t \quad i = A, B \quad j = X, Y, Z \tag{3.58}$$

$$\theta_{gij} = \omega_{ij} \cdot \Delta t \quad i = A, B \quad j = X, Y, Z \tag{3.59}$$

As the ends of the bond on the neutral axis, noted as points α and β in Figure 3.12, connect the centres of particles A and B respectively, the incremental displacements of particles A and B correspond to the incremental displacements of points α and β in the global co-ordinate system. The incremental global displacement vector $\{u_g\}$ is:

$$\{u_g\} = \begin{Bmatrix} d_{g\alpha X} \\ d_{g\alpha Y} \\ d_{g\alpha Z} \\ \theta_{g\alpha X} \\ \theta_{g\alpha Y} \\ \theta_{g\alpha Z} \\ d_{g\beta X} \\ d_{g\beta Y} \\ d_{g\beta Z} \\ \theta_{g\beta X} \\ \theta_{g\beta Y} \\ \theta_{g\beta Z} \end{Bmatrix} = \begin{Bmatrix} d_{gAX} \\ d_{gAY} \\ d_{gAZ} \\ \theta_{gAX} \\ \theta_{gAY} \\ \theta_{gAZ} \\ d_{gBX} \\ d_{gBY} \\ d_{gBZ} \\ \theta_{gBX} \\ \theta_{gBY} \\ \theta_{gBZ} \end{Bmatrix} \tag{3.60}$$

The local incremental displacement vector $\{u\}$ can be determined by multiplying the incremental global displacement vector $\{u_g\}$ by the transformation matrix [γ], so that:

$$\{u\} = \begin{bmatrix} [\gamma] & & & \\ & [\gamma] & & \\ & & [\gamma] & \\ & & & [\gamma] \end{bmatrix} \cdot \{u_g\} \tag{3.61}$$

where

$$\{u\} = \begin{Bmatrix} d_{\alpha x} \\ d_{\alpha y} \\ d_{\alpha z} \\ \theta_{\alpha x} \\ \theta_{\alpha y} \\ \theta_{\alpha z} \\ d_{\beta x} \\ d_{\beta y} \\ d_{\beta z} \\ \theta_{\beta x} \\ \theta_{\beta y} \\ \theta_{\beta z} \end{Bmatrix} \tag{3.62}$$

The transformation matrix [γ] contains the nine directional cosines that existed between the axes of the two co-ordinate systems at the previous time step. The vectors from the previous time step are used because we want to determine the displacement of the bond between the previous and current time steps. The components of the transformation matrix are updated at each time step to take into

account the potential change in the position of the particles; the calculation of the transformation matrix is described in Section 3.2.3.

The incremental force values are calculated by multiplying the displacement vector by the stiffness matrix [*K*]:

$$\{\Delta F\} = [K] \cdot \{u\} \tag{3.63}$$

The incremental forces are then added to the running total, to provide the new total value of internal forces acting on the bond {*F*}:

$$\{F\} = \{F^{t-1}\} + \Delta F \tag{3.64}$$

The stresses generated by the sum of the forces at this time step are determined and compared against failure criteria, described in Section 3.2.2. If the bond stresses generated do not cause the bond to fail, then the internal forces and moments equal to $\{F_R\}$ as defined in Equation (3.65) are applied to the particles to resist the displacements and rotations; these forces are applied directly to particles *A* and *B*, and are considered in the summation of forces acting on these particles:

$$\{F_R\} = \begin{Bmatrix} F_{RAX} \\ F_{RAY} \\ F_{RAZ} \\ M_{RAX} \\ M_{RAY} \\ M_{RAZ} \\ F_{RBX} \\ F_{RBY} \\ F_{RBZ} \\ M_{RBX} \\ M_{RBY} \\ M_{RBZ} \end{Bmatrix} = \begin{bmatrix} [\gamma]^{-1} & & & \\ & [\gamma]^{-1} & & \\ & & [\gamma]^{-1} & \\ & & & [\gamma]^{-1} \end{bmatrix} \cdot - \begin{Bmatrix} F_{\alpha x} \\ F_{\alpha y} \\ F_{\alpha z} \\ M_{\alpha x} \\ M_{\alpha y} \\ M_{\alpha z} \\ F_{\beta x} \\ F_{\beta y} \\ F_{\beta z} \\ M_{\beta x} \\ M_{\beta y} \\ M_{\beta z} \end{Bmatrix} \tag{3.65}$$

3.3.4 Global damping

In real materials, kinetic energy is dissipated through microscopic actions such as internal friction and wave scattering (Potyondy and Cundall, 2004). When required, for example if frictional sliding does not represent the full damping effect seen in the real material, artificial damping can be introduced to reduce the kinetic energy and bring the simulation to a quasi static state.

In the EBPM, non-viscous damping is applied through the equations of motion so that energy is dissipated in every particle in the system. In essence this modifies the final forces acting on each particle so that the resulting particles acceleration is changed. As only the acceleration term is dampened stable motion is not affected, and elements with a fixed velocity will maintain that velocity. The damping used in the EBPM is based on the damping provided in the bonded particle model proposed by Potyondy and Cundall (2004). The damping forces and moments F_d and M_d are applied to each of the six degrees of freedom for each particle so that:

$$F_{di} = \frac{-\iota_d |F_i| V_i}{|V_i|} \quad i = X, Y, Z \tag{3.66}$$

$$M_{di} = \frac{-\iota_d |M_i| \omega_i}{|\omega_i|} \quad i = X, Y, Z \tag{3.67}$$

where F and M are the sum of the forces and moments acting on the particles, V and ω are the translational and angular velocity, X, Y and Z represent each degree of freedom and ι_d is a dimensionless constant which defines the magnitude of the damping. The range of values for this constant are zero to one, with zero providing no damping and one meaning the damping is equal in magnitude to the total forces. In Section 5.5.3 the influence of the damping coefficient on DEM simulations is discussed in more detail.

3.3.5 Time step

In order to ensure a stable explicit integration, the time step Δt used in the simulation should be a fraction of the critical time step Δt_{crit}. The critical time step is the largest time step for which a force is not transmitted beyond the nearest neighbors of a particle. The time step can be calculated such that:

$$\Delta t = \xi \, \Delta t_{crit} \tag{3.68}$$

where ζ is a factor which should be kept in the range of zero to one, although for real simulations it is suggested that values of 0.1 to 0.2 should be used (O'Sullivan and Bray, 2004). The critical time step is determined for both bonded contacts Δt_{Bcrit} and non-bonded contacts Δt_{Scrit}; the critical value is simply the lowest of these two values, such that:

$$\Delta t_{crit} = \min\left(\Delta t_{Bcrit}, \Delta t_{Scrit}\right) \tag{3.69}$$

For non-bonded contacts, the critical time step is determined using the Rayleigh time step, which is the time taken for a shear wave to propagate though a solid particle (DEM.Solutions, 2008). The critical spring time step is calculated such that:

$$\Delta t_{Scrit} = \frac{\pi r_p \left(\frac{\rho_p}{G_p}\right)^{0.5}}{\left(0.1631 v_p + 0.8766\right)} \tag{3.70}$$

If the particle density ρ_p, shear modulus G_p and Poisson's ratio v_p are constant for all particles in a simulation, then the critical spring time step is that for the smallest particle radius r_p.

The critical time step for bonded contacts is determined from an approximate solution based on a single degree of freedom in a mass spring system (O'Sullivan and Bray, 2004).

$$t_{Bcrit} = 2\sqrt{\frac{m}{K}} \tag{3.71}$$

Although the actual solution for a system of bonds and particles used when modelling cementitious materials is much more complex than the solution presented here this simplistic approach can be taken as a conservative fraction of the calculated critical time step is actually used in simulations. Normally this fraction is of the order of 0.1 to 0.2 (O'Sullivan and Bray, 2004).

3.4 Verification of the bonded particle model

Verifying the implementation of a numerical model is an important step to ensure that the mathematical descriptions in the programmed code match the theory underpinning the model. The advantage of using the Hertz-Mindlin Contact Model and EDEM is that both have already been verified, which simplifies this stage as only the TBBM and general EBPM formulations have to be tested. In order to verify each calculation stage of the TBBM, a series of benchmark tests were conducted.

In the first set of benchmark tests, a single bond was placed under a number of different loading actions (tensile, compression, shear, twisting and multiple bending configurations) by applying external forces to the particles connecting the bond. For each loading action, the orientation of the bond was varied so that the transformation matrix calculations could be verified. The results of these tests can be found in Appendix A. These benchmark tests proved that the TBBM is able to accurately predict the contact forces due to any single displacement loading action when the bond is orientated in any direction to the global co-ordinate system. The bond breakage stresses are also found to match the bond's failure criteria.

To verify the response of a bond under more complex loading actions, further benchmark tests were conducted. One such test was the loading of a simply-supported beam. The beam is formed by bonding between 3 and 31 particles in a line; an example with 5 particles is shown in Figure 3.14. The extreme left-hand particle is fixed so that no translational displacements can occur, but the particle can rotate freely; the extreme right hand particle is fixed against translational displacements, apart from in the axial direction, and can also rotate freely.

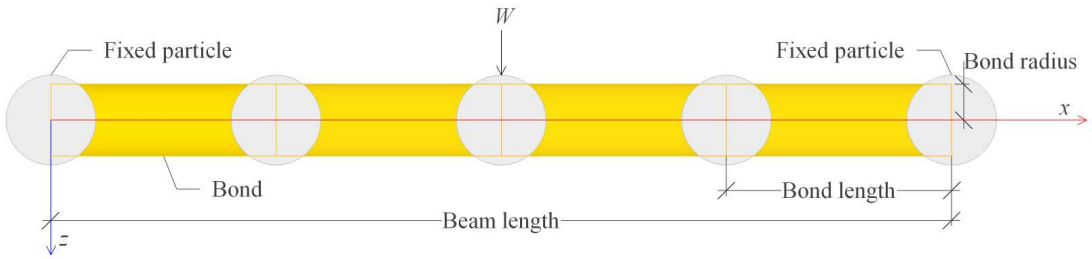

Figure 3.14 A beam of length L, made from connecting 5 particles with 4 bonds of length $L_{b,}$ in the x-z plane (not to scale)

Each bond was given the same material and geometrical properties, so the spacing or number of particles should not affect the response to a transverse load W being applied to the particle at mid-span. The transverse deflection δz and rotation dz/dx can be determined from the governing equations for a Timoshenko beam at any distance x from the left end fixed particle, such that:

$$\delta z = \frac{WL^3}{48EI}\left(\frac{x}{L}\right)\left(3-4\frac{x^2}{L^2}\right)+\frac{f_s W x}{2GA} \quad \left(0 \le x \le \frac{L}{2}\right) \tag{3.72}$$

$$\frac{dz}{dx} = \frac{WL}{16EI}\left(L^2-4x^2\right)+\frac{f_s W}{2GA} \quad \left(0 \le x \le \frac{L}{2}\right) \tag{3.73}$$

where L is the length of the beam, EI is the flexural rigidity and GA/f_s is the shear rigidity. It should be noted that determining deflection due to bending or shear can have boundary conditions which are incompatible. Using the shear deflection alone may not provide the correct rotation at the mid span, because the shear force changes stepwise with difference between the left and right equal to W; the equations are not of an order high enough to take this into account.

The theoretical mid-span deflection δ, for a simply supported beam subject to a central concentrated load W, can be calculated using (3.72) when $x = L/2$, so that:

$$\delta = \frac{WL^3}{48EI} + \frac{WLf_s}{4GA} \tag{3.74}$$

For the benchmark test, the material and geometric properties for the bonds and particles are described in Table 3.1.

Table 3.1 Beam material properties

Symbol	Description (units)	Value
E	Young's modulus (Pa)	2×10^{-11}
v	Poisson's ratio	0.3
L	Beam length (m)	6
r	Beam radius (m)	0.1
f_s	Form factor for shear	10/9

A central load W of 100,000 N is applied to the particle at the centre of the beam and the transverse deflection of that particle measured. Using Equation (3.74), the theoretical transverse mid-span deflection δ is 28.7169 mm. The mid-span deflections for beams made of between three and 31 particles is shown in Table 3.2.

Table 3.2 Predicted central deflection compared with theoretical solution

Number of particles	DEM predicted central deflection (mm)	error %
3	28.7151	0.0061
5	28.7144	0.0086
17	28.7142	0.0093
31	28.7142	0.0093

As can be seen from Table 3.2 there is a good agreement between the DEM predictions and the theoretical solution when any number of bonds are used to form the simply supported beam.

3.5 Summary

This chapter has outlined the development, implementation and verification of a new bonded particle model. Several weaknesses with the bond model that has been integrated within the EDEM software (the software to be used in this study) were discovered. In light of this a new bonded particle model was proposed which allows particles to be connected by bond elements which are treated as beams. In the new model the Timoshenko beam theory is used to determine the forces acting in each bond as this method is more suitable for beams of lower aspect ratio. The developed model has been implemented in the software EDEM and a verification procedure has been conducted in order to ensure that correct beam theory is being applied. The verification procedure proved that the developed model is capable of reproducing real beam behaviour. Although the primary objective is to model the behaviour of cementitious materials under quasi-static load the capabilities are not limited to cementitious materials and the modelling of structures is discussed later in this thesis.

Chapter 4 Parametric study: Part 1: reference case

4.1 Introduction

This chapter investigates the predictive capabilities of the Edinburgh Bonded Particle Model (EBPM) in producing the three dimensional response of cementitious materials under loading. In order to test this hypothesis, a series of Discrete Element Method (DEM) simulations are conducted mimicking physical tests of concrete cylinders under uni-axial compression. In this chapter the target bulk response is defined both quantitatively and qualitatively, before a set of input parameters are chosen to form the reference case. The effect of parameter variation on the bulk response will then be assessed in Chapter 5 relative to this reference case.

4.2 Bulk mechanical properties of concrete

The unconfined compression strength of concrete, a measure of the material's resistance to rupture, is widely regarded to be the material's most important property. As the strength of concrete increases, other properties, such as permeability, shrinkage, elasticity and creep, tend to improve (Akroyd, 1962). The strength of concrete comes from a hydrating chemical reaction between cement and water; this forms a cement paste which binds the aggregate together forming the finished material. Concrete, in its hardened state, can be considered a two phase material: the aggregate (coarse and larger fines) and the hardened cement paste (cement, water, smaller fines). The overall behaviour of concrete is not only governed by the properties of these two phases, but also by the interface between them. There is an area in the hardened cement paste immediately adjacent to the aggregate called the interfacial transition zone (ITZ). The thickness of the ITZ is between 10 μm and

50 μm and is dependent on the water-to-cement ratio rather than the aggregate size (Zheng et al., 2011). This area contains larger pores, a higher porosity and has a slightly higher water-to-cement ratio than the remainder of the cement paste which creates potentially weaker zones.

The strength of concrete can be measured in many ways depending on the application; the compressive strength is considered to be the principal engineering property of concrete (Kovler and Roussel, 2011) even though it is an empirical quantity (Jones, 1962). The compressive strength of a specimen of concrete is usually determined through destructive unconfined uni-axial compression tests of cylindrical specimens, such as the one shown in Figure 4.1 (a). In the parametric study presented here, DEM cylindrical specimens of bonded particles are loaded in uni-axial compression through the displacement of loading plates (In EDEM simulations loading plates are represented using geometries), as shown in Figure 4.1 (b). Bulk properties such as the compressive strength $f_c^{'}$ can be determined and used to describe the bulk response quantitatively. Using displacement-rate controlled loading allows the post-peak behaviour to be considered in the analysis, as discussed in more detail later in this section.

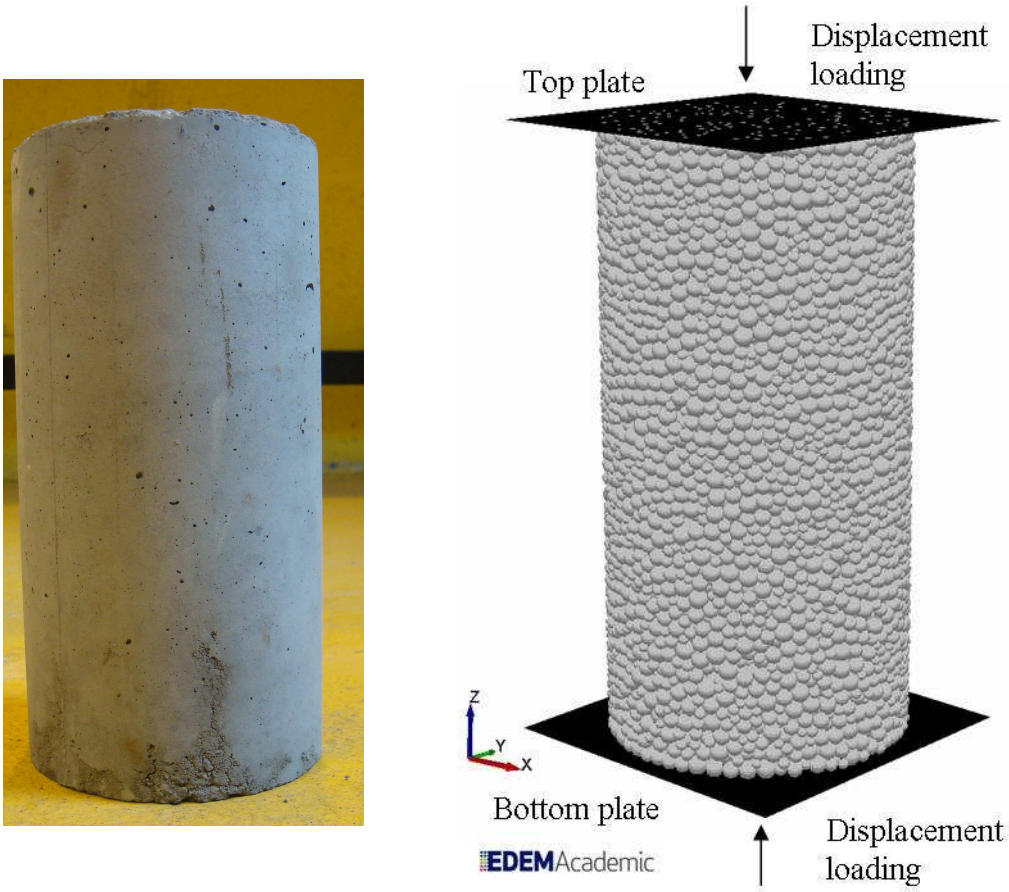

(a) Physical cylindrical specimen (b) DEM specimen

Figure 4.1 Physical specimen compared to DEM representation

As well as the ultimate compressive strength, the secant modulus of elasticity $E_{c(0.4)}$, the axial strain at failure ε_c and the Poisson's ratio $v_{c(0.4)}$ will also be recovered from each numerical specimen and used to describe the bulk response quantitatively. The subscript (0.4) denotes the fact that these properties are recovered at 40% of the ultimate strength. The definition of each bulk mechanical property and the method used to calculate them are described here:

The *ultimate compressive strength* $f_c^{'}$ is equal to the maximum compressive stress the specimen experiences during uni-axial loading. The compressive stress σ is determined from the compressive forces acting on the loading plates, such that:

$$\sigma = \frac{F_T}{A_T} = \frac{F_B}{A_B} \tag{4.1}$$

where F_T and F_B are the total compressive forces acting on the top and bottom loading plates respectively and A_T and A_B are the equivalent areas of the specimen in contact with the top and bottom loading plates respectively. These areas are assumed to be the same as the cross sectional area of the specimen. In the real world the forces in each plate should be the same so that (4.1) holds true. However, as this cannot be guaranteed in the numerical simulation the average force will be used when plotting the stress, so that:

$$\sigma = \frac{F_T + F_B}{A_T + A_B} \tag{4.2}$$

From the literature, the ultimate compressive strength for normal weight concrete can be estimated to fall in the range of 10 MPa to 70 MPa (Gere and Timoshenko, 1990); Mindess et al. (2003) suggested a typical value of 35 MPa.

The *axial strain at failure* ε_c is simply the value of axial strain corresponding to the ultimate compressive strength. The axial strain ε is determined from the full height of the specimen, such that:

$$\varepsilon = \frac{h_0 - h}{h_0} \tag{4.3}$$

where h is the height of the specimen and the subscript 0 denotes initial conditions; under compressive loading the specimen experiences axial contraction, noted as a poitive strain. The height of the specimen is defined as the maximum vertical

distance between the top and bottom surfaces of the specimen, as shown in Figure 4.2. This definition differs from assessing the axial strain from the positions of the loading plates, as it takes into consideration the overlap that develops between particles and the loading plates. This overlap represents the deformation of the specimen at the boundary.

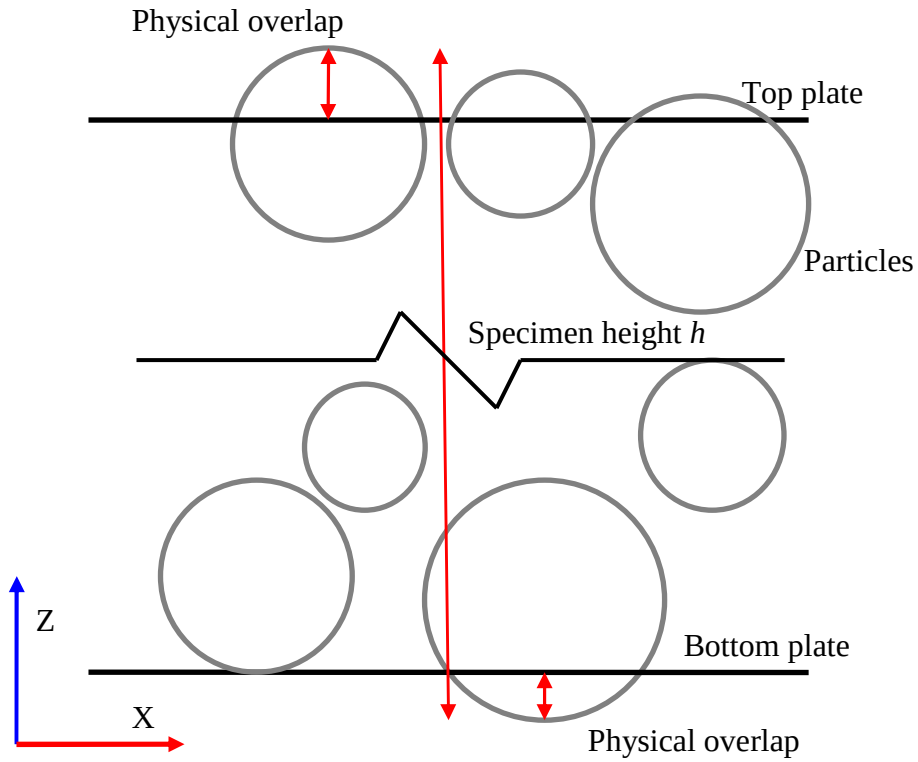

Figure 4.2 Calculation of the specimen height

The specimen height h is therefore calculated such that:

$$h = Z_T - Z_B + \max \delta_{pT} + \max \delta_{pB} \tag{4.4}$$

where Z_T and Z_B are the Z axis positions of the top and bottom loading plates respectively and δ_{pT} and δ_{pB} are the overlaps between particles and the top and

bottom loading plates respectively. Numerical stability of this equation leads to a gradual reduction in *h*, as this is reliant on quasi-static conditions such that the maximum overlaps do not change significantly between the time steps of the DEM implementation. The maximum overlap is taken into consideration when determining the height to remove the influence of the rough top surface. When the maximum overlap was not taken into consideration initial tests showed non-linear initial loading arising from the particles coming into contact with the loading plates. Although initial non-linear response is sometimes seen in physical tests the degree shown in the numerical response was unrealistic.

Mindess et al. (2003) suggest that the strain at peak stress falls in a range of 0.002 to 0.003 and generally increases with an increase in ultimate strength.

The *secant modulus of elasticity* E_c describes the secant value of the bulk stiffness of the specimen. As concrete is only partially elastic the secant modulus should be determined when loading is still in the near elastic range, up to approximately 30% to 40% of the ultimate strength (Bamforth et al., 2007), and is discussed in more detail later in this section. In this study the secant modulus of elasticity is determined using Equation (4.5) when loading is at 40 % of the ultimate strength, denoted by the subscript 0.4, the subscript 0 denotes the initial conditions:

$$E_{c(0.4)} = \frac{\Delta\sigma}{\Delta\varepsilon} = \frac{\sigma_{0.4} - \sigma_0}{\varepsilon_{0.4} - \varepsilon_0} \tag{4.5}$$

For concrete in compression, the secant modulus of elasticity can be estimated to fall in the range of 17 GPa to 31 GPa (Gere and Timoshenko, 1990). Mindess et al. (2003) suggested that for normal-weight concrete, the modulus of elasticity falls in a slightly wider range of 14 GPa to 42 GPa, with a typical value of 28 GPa.

From experimental observations the secant modulus of elasticity $E_{c(0.4)}$ has been related to the compressive strength f_c'. For normal-weight concrete the Eurocode (BS EN 1992-1-1, 2004) expresses this relationship as:

$$E_{c(0.4)} = 22000\sqrt[3]{(f_c'/10)} \tag{4.6}$$

It should be noted that the relationship shown in Equation (4.6) is only a general one; the literature shows that some factors do not comply with this relationship, such as: specimen age, aggregate modulus of elasticity and moisture condition (Neville and Brooks, 1987).

The *Poisson's ratio* v_c describes the ratio of the radial ε_r to axial ε strain. Like the secant modulus of elasticity, the Poisson's ratio is determined when the corresponding stress is at 40% of the ultimate compressive strength, such that:

$$v_{c(0.4)} = \frac{-\varepsilon_{r(0.4)}}{\varepsilon_{(0.4)}} \tag{4.7}$$

The axial strain is determined using Equation (4.3) and the radial strain ε_r is determined by tracking the transverse deflections of pairs of particles lying opposite to each other at the mid height of the exterior of the specimen, (see Figure 4.3).

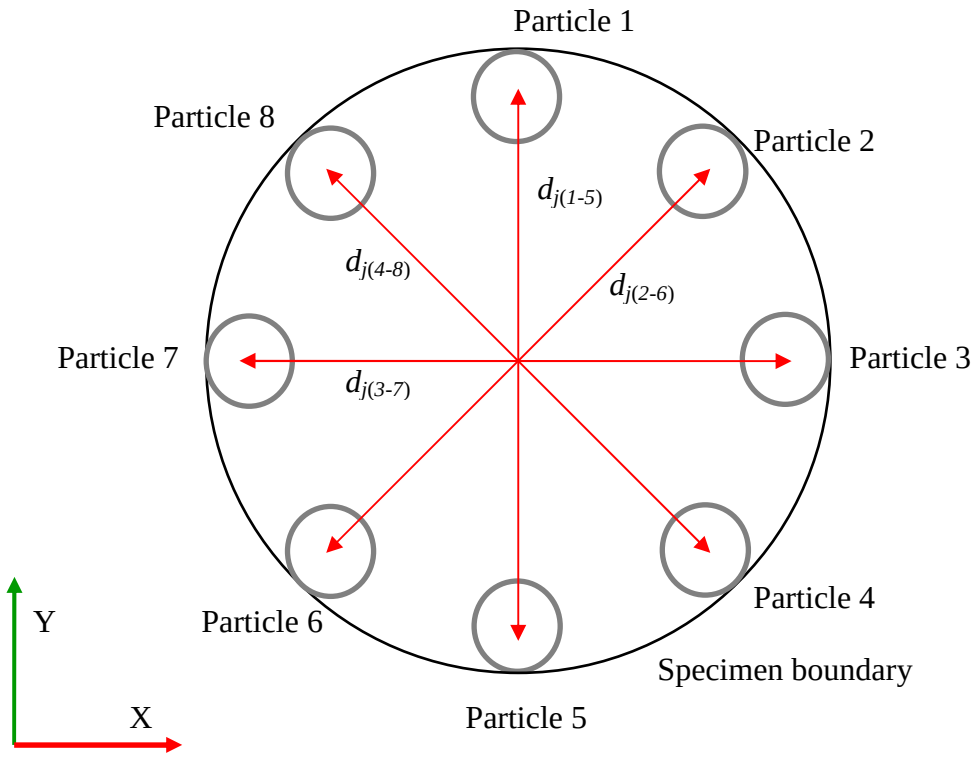

Figure 4.3 Diagrammatic representation of the determination of D

The radial strain is determined such that:

$$\varepsilon_r = \frac{D - D_0}{D_0} \tag{4.8}$$

where

$$D = \frac{1}{4}\sum_{j=1}^{4} d_j \tag{4.9}$$

where d_j is the distance between a pair of particles (as shown in Figure 4.3), and D is the average distance between all pairs. For the simulations in this thesis four pairs of particles are used. Because of the random initial particle arrangement there are not necessarily particles at the exact opposite boundaries to each other. The straight line between each pair of particles may not pass directly through the exact centre of the specimen.

Timoshenko and Gere (1984) suggest that the Poisson's ratio for concrete should fall in the range of 0.1 to 0.2; Mehta and Monterio (1993) and Neville and Brooks (1987) suggest a slightly narrower range of 0.15 to 0.20 when determined from strain measurements.

As well as using the quantitative measures of the bulk behaviour, the overall stress-strain response and post-peak behaviour will also be considered. Zhou and Wu (2012) presented a compilation of models which describe the compressive stress-strain relationship for concrete, including the Eurocode 2 (BS EN 1992-1-1, 2004) equation, which is reproduced in Equation (4.10):

$$\frac{\sigma}{f_c'} = \frac{1.05\frac{E_{c(0.4)}}{E_f}\frac{\varepsilon}{\varepsilon_c} - \left(\frac{\varepsilon}{\varepsilon_c}\right)^2}{1 + \left(1.05\frac{E_{c(0.4)}}{E_f} - 2\right)\left(\frac{\varepsilon}{\varepsilon_c}\right)} \tag{4.10}$$

where E_f is the secant modulus of elasticity at failure:

$$E_f = \frac{f_c'}{\varepsilon_c} \tag{4.11}$$

The normalised stress-strain curve shown in Figure 4.4 was plotted by substituting Equation (4.6) into Equation (4.10). The curve was divided into three zones; literature shows that the response of concrete to load differs slightly in these zones. Authors including Mindess et al. (2003) made similar divisions of the stress-strain curve and described the changing behaviour as the axial strain increased. It should be noted that although shown here as absolute regions, the boundaries of the zones should be considered more as guidelines:

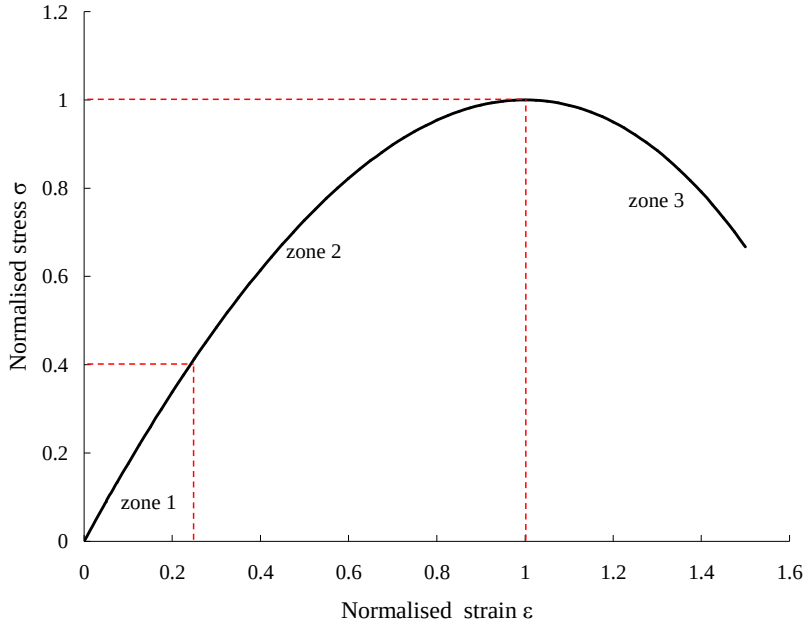

Figure 4.4 Theoretical stress-strain curve divided into three zones

Concrete is weaker and more inelastic than either mortar or aggregate (Buyukozturk et al., 1971). The failure mechanism of a concrete specimen under uni-axial compression and the shape of the corresponding axial stress-strain curve can be attributed to the initiation and propagation of a large number of cracks (when under direct tension the failure is caused by the propagation of a single crack). In its hardened state and before loading begins, concrete has naturally occurring internal flaws and micro-cracks (Du et al., 2013); these initial voids have been mapped using techniques such as X-radiography and microscopy by authors such as Dhir and

Sangha (1974), Nemati (1997), Diamond (2004) and Akçaoğlu et al.(2005). These voids are the result of segregation, bleeding and the incompatibility between the aggregate and hardened cement paste (different moduli of elasticity, coefficients of thermal expansion and responses to moisture) (Neville and Brooks, 1987) and/or simply due to inadequate compaction (Du et al., 2013). These voids form areas of weakness, which may not necessarily lead to failure on the macroscopic scale directly but may provide a starting point for larger cracks to propagate from as loading commences (Jones, 1962).

Under loads up to about 30% to 40% of the ultimate compressive strength (zone 1 in Figure 4.4), there is little additional micro-cracking observed between the aggregates and hardened cement paste (bond cracks); the stress-strain response is close to, but not quite, linear elastic (Dhir and Sangha, 1974; Mehta and Monterio, 1993).

As the loading is increased beyond approximately 40 % of the ultimate compressive strength (zone 2 in Figure 4.4) the number and size of the bond cracks increases as does the non-linearity of the stress-strain curve (Dhir and Sangha, 1974). The stress level at which new cracks begin to form is dependent on many factors including the grading of the aggregates used (concrete containing smooth natural gravel begins to crack at lower loads than comparable concretes containing crushed rocks, although their eventual compressive strengths are not significantly different) (Jones, 1962).

By 70% to 80% of the ultimate strength cracks form across the hardened cement paste (matrix cracks), bridging the bond cracks and forming a continuous crack network (Dhir and Sangha, 1974; Mehta and Monterio, 1993). This crack network forms largely parallel to the axis of loading, as shown by Jones (1962) using the ultrasonic pulse method and ultimately leads to the failure of the material. This in turn allows the unconfined material to expand in the radial directions which opens up the cracks further.

The eventual crack pattern visible at the macroscopic scale develops as the strain increases past that associated with the ultimate compressive strength (zone 3 in Figure 4.4). The failure pattern has been found to be significantly influenced by the

friction between the test specimen and the loading plates. The friction reduces the radial expansion, as described above, and causes the end regions of the specimen to be placed in tri-axial compression. Cracks in the centre of the specimen propagate vertically but those at the ends propagate at an incline leading to the formation of conical failure regions, as shown in Figure 4.5 (Mindess et al., 2003).

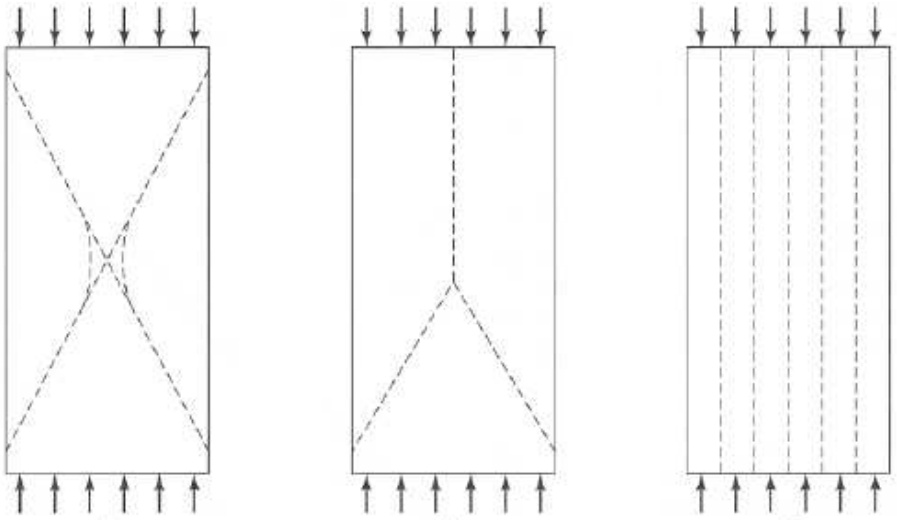

(a) confinement at both ends

(b) confinement at the bottom and no confinement at the top

(c) no confinement at both ends: splitting failure

Figure 4.5 Typical failure patterns for concrete cylinders under compression (after (Mindess et al., 2003) p.370)

4.3 Particle assembly and contact geometry

Initial tests highlighted the importance of generating a dense bond network. One way to achieve this is to ensure that the generated specimen has a high solid fraction. This has the advantage over using a more porous structure, compensating with a higher contact radius multiplier, as a high solid fraction ensures that there is sufficient load

carrying capacity through both bonded and non-bonded contacts (activated after bonded contacts break) to produce an acceptable loading stiffness.

Particle assemblies with high solid fractions couldn't be easily obtained with the generation techniques available in the EDEM software; the dynamic techniques used (gravitational deposition and compaction) led to unwanted anisotropy at the macroscopic scale and were computationally expensive, the constructive technique used (sequential inhibition model) could not produce a low enough porosity with the co-ordination numbers always being lower than desired. Instead a collective rearrangement technique using the software GiD (GiD, 2012) and developed by Labra et al. (2010) was used.

This generation technique works by randomly inserting particles of a predefined radius, taken from an imposed particle size distribution, with overlap allowed, into an appropriately sized "mould" until the porosity reaches approximately 20 % (in 3D). Through an iterative process particles are then rearranged depending on the branch vectors and overlaps of the surrounding particles so that a local equilibrium is reached. At the end of each iteration, particles with overlaps greater than a set limit are removed from the simulation. As this packing procedure continues the overlap limit is reduced, this process continues until the overlap limit reaches a predefined target. The generation technique described above was used in this study to generate cylindrical concrete specimens, of 100 mm diameter and 200 mm. For all specimens the target overlap was set at 2% of the particle radius.

For the generation of the reference case specimen the subject material was discretized into approximately 20,000 particles following a uniform particle size distribution with the maximum radius set to be as close to 3 mm as possible. In this manner, and as described in Section 3.1, particles do not represent individual grains but rather a proportion of the subject material. Therefore, the average particle size is greater than that of the grains found in the microstructure of concrete. The generated particle size distribution is shown in Figure 4.6; the minimum particle radius was 1.28 mm and the maximum 3.02 mm. In total the generated reference case specimen

has 20,561 spherical particles, the initial particle assembly is shown in Figure 4.7 and the assembly characteristics stated in Table 4.1.

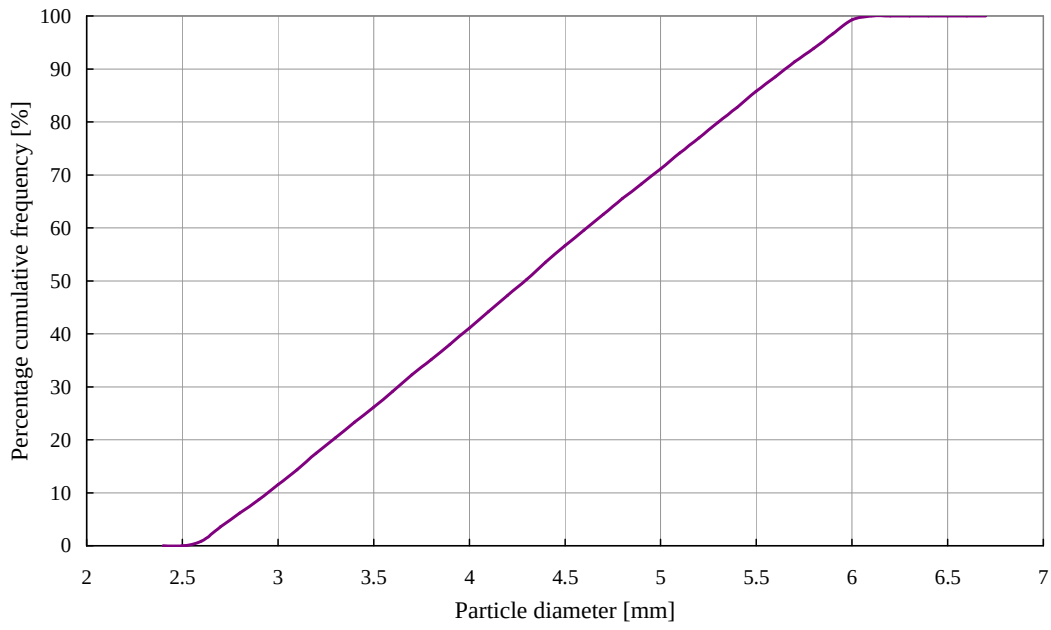

Figure 4.6 A cumulative frequency plot showing the particle size distribution of the reference case specimen

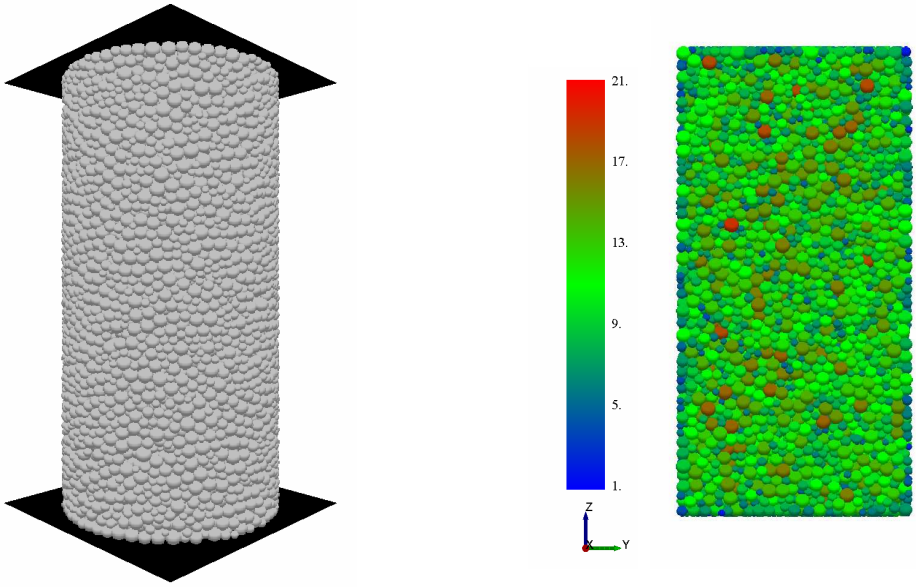

(a) particles and loading plates

(b) slice through the specimen showing the number of bonds per particle

Figure 4.7 The particle arrangement for the reference case specimen,

As can be seen Figure 4.7 (b) the particles on the boundary generally have the lowest number of bonds per particle and the largest particles generally have the higher numbers of bonds per particle. A dispersion factor d_f can be used to give a good indication of the variation in particle size within an arrangement (André et al., 2012). In this instance the dispersion factor is equal to 0.81 as calculated from Equation 4.12.

$$d_f = \frac{r_{\max} - r_{\min}}{r_{av}} \tag{4.12}$$

Table 4.1 Characterisation of the reference case specimen

Parameter	Description	Value
h_0	Initial specimen height (mm)	200
A_{ratio}	Aspect ratio – height to diameter	2:1
n_p	Total number of particles	20,561
r_{av}	Average particle radius (mm)	2.14
r_{min}	Minimum particle radius (mm)	1.28
r_{max}	Maximum particle radius (mm)	3.02
d_f	Dispersion factor	0.81
n	Porosity	0.37
ρ_p	Particle density (kg.m^{-3})	2700

As well as the reference case specimen two additional specimens are created. The difference between the specimens is that the particle size distribution has been shifted so that the dispersion factors are the same but the average particle size are different. A selection of parameters for these additional simulations are given in Table 4.2

Table 4.2 Characterization of the three specimens

Parameter	Description	Reference specimen	Specimen 2	Specimen 3
n_p	Total number of particles	20,561	10,202	28,982
r_{av}	Average particle radius (mm)	2.14	2.70	1.92
r_{min}	Minimum particle radius (mm)	1.28	1.61	1.15
r_{max}	Maximum particle radius (mm)	3.02	3.80	2.71
d_f	Dispersion factor	0.81	0.81	0.81
n	Porosity	0.37	0.38	0.37

As can be seen in Figure 4.8 the average particle size has no significant influence on the average number of bonds that are formed per particle. This is because the porosities of all three specimens are very similar. A greater influence is imposed by the contact radius multiplier η, as can be seen in Figure 4.9. The contact radius multiplier extends the contact search radius of each particle for the purposes of bonding particles that do not have a physical overlap. For the reference case, a contact radius multiplier of 1.2 was chosen, leading to an average number of bonds per particle of 9.58 with the distribution shown in Figure 4.10. The remaining parameter that defines the bond fabric is the bond radius multiplier λ, defined in chapter 3, which for the reference case was set at 1.0.

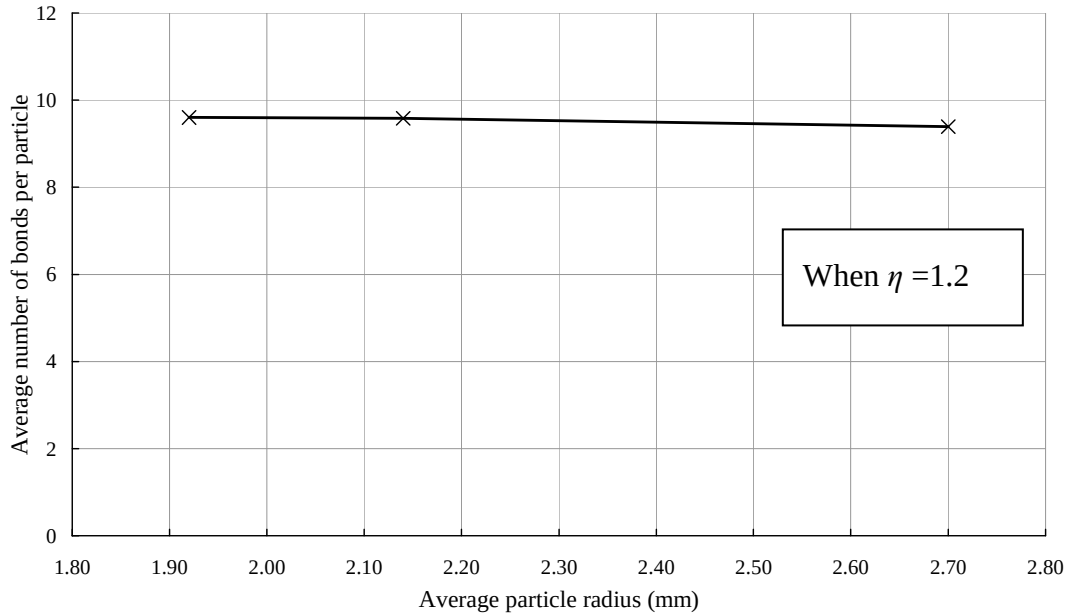

Figure 4.8 Average number of bonds per particle for varying particle radius

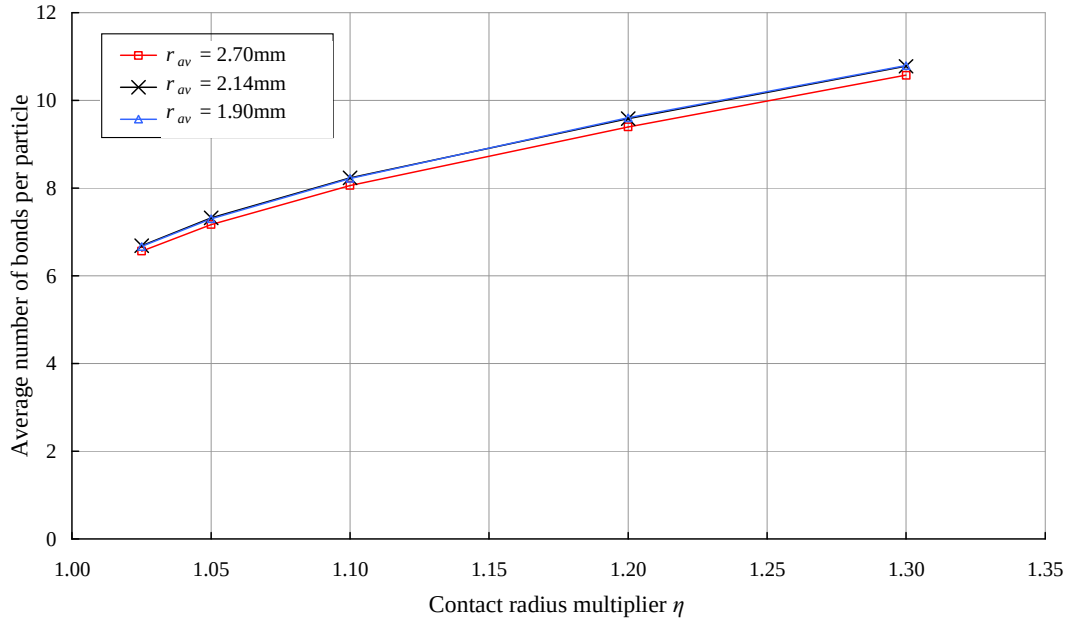

Figure 4.9 Average number of bonds per particle for varying contact radius multiplier for three different average particle radii

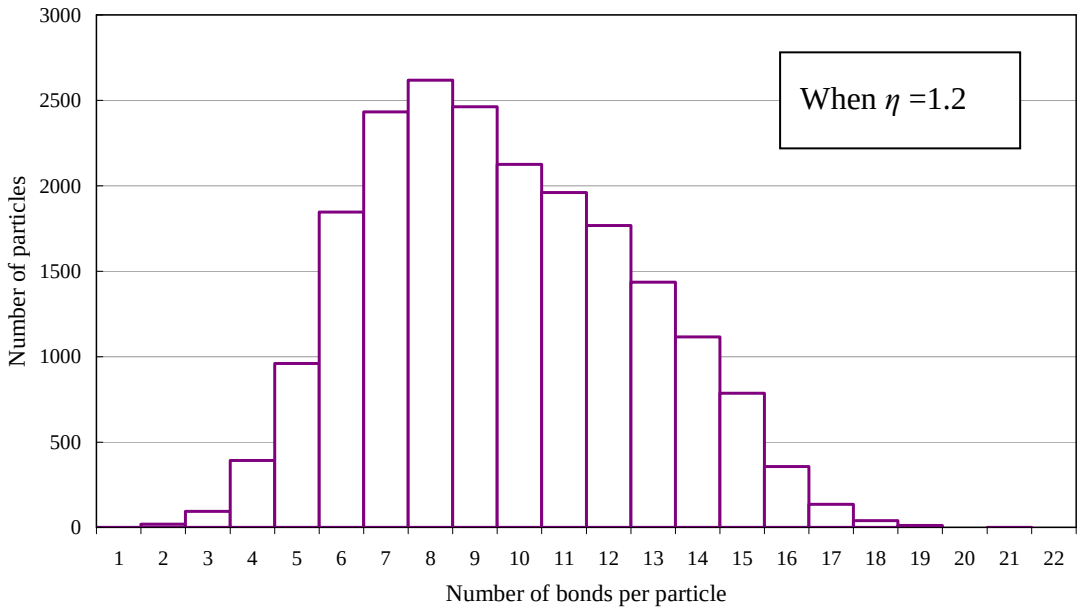

Figure 4.10 Distribution of the number of bonds per particle for the reference case

The contact orientation of the bond network can be assessed by observing the orientations of the bonds in the three orthogonal planes, as shown in Figure 4.11. As intended the contact network generated by the particle packing scheme is essentially isotropic, so any subsequent change in the distribution of the bond orientation will be a result of the loading of the specimen. Stress induced anisotropy has been observed in some granular materials where the contacts carrying the load change their orientation to be parallel with the loading direction.

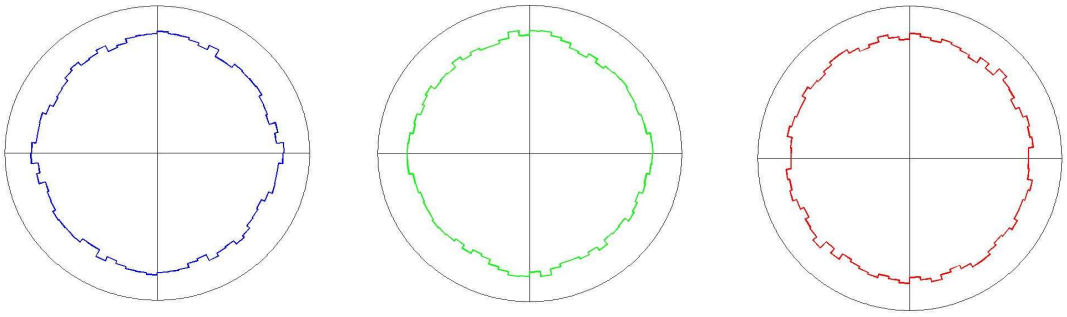

(a) X-Y plane (b) X-Z plane (c) Y-Z plane

Figure 4.11 Contact orientation of the bonds in the three planes

4.4 Contact model parameters for the reference case

The input parameters for the Hertz-Mindlin Contact Model for the reference case simulation are shown in Table 4.3. These values are determined through a heuristic approach and are of the same order of magnitude as values for aggregate.

Table 4.3 Particle and boundary model parameters for the reference case

Parameter	Description	Value
E_p	Particle Young's modulus (GPa)	40
ν_p	Particle Poisson's ratio	0.25
e_{rp}	Particle to particle coefficient of restitution	0.5
μ_{sp}	Particle to particle coefficient of static friction	1
μ_{rp}	Particle to particle coefficient of rolling friction	0
E_g	Plate Young's modulus (GPa)	200
ν_g	Plate Poisson's ratio	0.30
e_{rg}	Plate to particle coefficient of restitution	0.0001
μ_{sg}	Plate to particle coefficient of static friction	1
μ_{rg}	Plate to particle coefficient of rolling friction	0

Parameters describing properties of geometry are given the subscript *g* and the material characteristics are based on the assumption that the geometry is made from a material very similar to steel; appropriate material properties are taken from Gere and Timoshenko (1990).

Parameters relating to the particles themselves are given the subscript *p* and are kept in similar ranges for materials such as soft rock. Limestone has a Young's modulus in the range of 10 GPa to 70 GPa, and a Poisson's ratio for rock is approximately 0.2 to 0.3 (Gere and Timoshenko, 1990); for the reference case a value in the middle of

these ranges was chosen. The density of the particle material was kept constant in all simulations at 2700 $kg.m^{-3}$ since it is not expected to affect the simulation results.

There are other input parameters required for describing the particle-particle and particle-geometry interactions. These parameters are primarily coefficients of restitution, static friction, and rolling friction. No rolling friction is considered between either particle-particle or particle-geometry interactions. Although spherical particles were used, the bonded particles will resist particle rotation whilst the bonds are intact.

It is assumed that the bonds have stiffness properties similar to those for hardened cement paste, with appropriate values taken from Mindess et al. (2003). The values for the bond strength parameters appear to be very high when compared to the strength properties of hardened cement paste. Initial tests showed that when values closer to physical properties for hardened cement paste were used the resulting predicted bulk strength was far too low to be considered as being representative of concrete. It should be remembered that the bonds represent the interaction between portions of the subject material (represented as particles) therefore although physical properties can be used as a basis for bond properties the bonds do not directly represent the hardened cement paste. For simplicity the coefficient of variation of strength for all three strength parameters is kept the same, from experience a relatively high value of 0.8 was chosen as it has been shown to create a more ductile response. The full set of values for the bonded contact parameters can be found in Table 4.4.

Table 4.4 Bonded contact parameters for the reference case simulation

Parameter	Description	Value
E_b	Young's modulus (GPa)	35
ν_b	Poisson's ratio	0.20
S_C	Mean compressive strength (MPa)	500
ς_C	Coefficient of variation of compressive strength	0.8
S_T	Mean tensile strength (MPa)	60
ς_T	Coefficient of variation of tensile strength	0.8
S_S	Mean shear strength (MPa)	60
ς_S	Coefficient of variation of shear strength	0.8

4.5 Numerical implementation parameters

There are a number of additional simulation parameters that need to be considered when assessing the numerical stability of a simulation. These are principally the time step Δt, the global damping ι_d and the loading rate L_r. All three are parameters that are investigated further in this study. The numerical implementation parameters used for the reference case specimen are shown in Table 4.5. For all of the simulations in the parametric study the time-step used will be taken as approximately 5% of the critical time step (Δt_{crit}) which is 1×10^{-7} s for the reference case, the equations for the critical time step are given in Chapter 3. The global damping is set to zero in this study unless otherwise stated. The loading rate used in the simulations needs to be low enough to provide a static solution whist not requiring an unreasonable computational time. The rate for a displacement controlled machine in physical tests is usually around 0.02 mm.s^{-1}; in the numerical simulations a loading rate this low would be impractical as the computational time would be excessive. The loading rate used in the simulations will be 200 mm.s^{-1} (each plate displacing at 100 mm.s^{-1}) unless otherwise stated. For a numerical simulation this loading rate is acceptable as

a time step of 1×10^{-7} s means that 10,000 calculation steps need to be computed for the specimen to displace 1 mm; as a result, the dynamic effects are minimal (Cho et al., 2007).

Table 4.5 Numerical implementation parameters for the reference simulation case

Parameter	Description	Value
Δt	Time step (s)	1×10^{-7}
L_r	Loading rate (mm.s^{-1})	200
ι_d	Global damping	0

4.6 Computed bulk response

In total five DEM simulations were run using the reference case input parameters, the only difference between them being the random number used in the determination of the bond strengths in each simulation. The relevant stress-strain curves are shown in Figure 4.12 and the computed average bulk properties are given in Table 4.6.

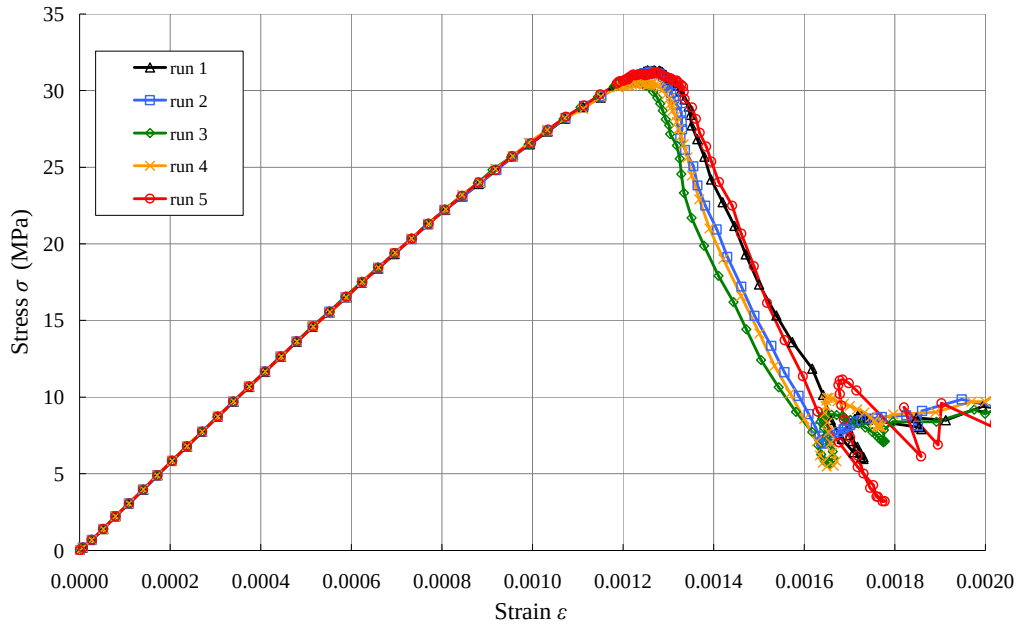

Figure 4.12 Stress-strain curves for the reference simulation cases

Table 4.6 Bulk properties computed from the five reference case simulations

Parameter	Description	Mean	Coefficient of Variation %
f_c	Ultimate strength (MPa)	30.95	1.28
ε_c	Axial strain at failure	0.001248	1.61
$E_{c(0.4)}$	Secant modulus of elasticity (GPa)	28.46	0.12
$\nu_{c(0.4)}$	Poisson's ratio	0.1959	0.67

From Figure 4.12 and Table 4.6 it can be seen that there is little difference in the stress-strain behaviour presented across the five simulations; the variation in the bulk parameters is also minimal. There is no significant difference in the projection of the ascending branches of the stress-strain curves; however, when approaching the peak stress and in the descending branches there is a slight dispersion of the curves. These

descending branches do all lie approximately parallel with each other and the residual strength is about 10 MPa for all specimens.

In Figure 4.12 an apparent reduction in strain can be seen at the end of the descending branch of the stress strain curve. This is a numerical effect caused by the rapidly changing maximum overlaps between particles and the loading plates. This strain reduction is discussed in more detail in the parametric study where certain numerical parameters, such as loading rate and damping, have a significant influence on this effect.

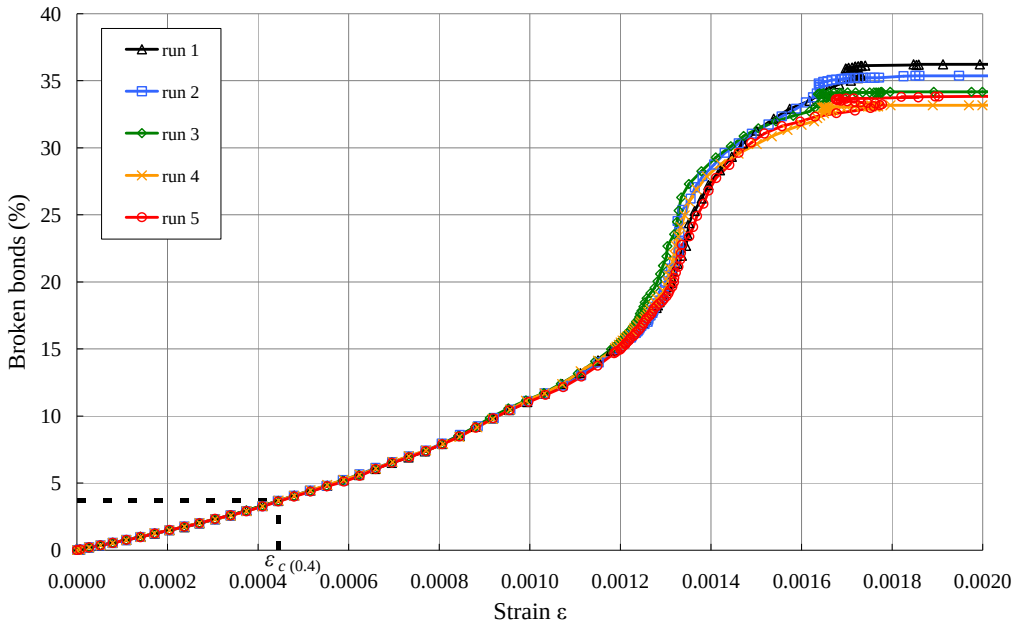

Figure 4.13 Broken bond curves for the reference simulation cases

The computed secant modulus of elasticity and Poisson's ratio have a particularly low variation; this is due to the fact that at the loading instant when these values are computed, at 40% of the ultimate compressive strength, very few bonds have broken as can be seen in Figure 4.13 (less than 4% for each of the five simulations). This means that the bulk response of the specimens will be very linear at this point.

As can be seen in Figure 4.13 for all specimens there is a gradual increase in broken bonds right from the beginning of loading. This is because with such a high

coefficient of variation of strength being used there are some bonds which are very weak. The breakage rate generally increases with strain, at ultimate strength there is a greater failure of bonds over a shorter strain before the rate then trails off. Approximately 18% of the total bonds have failed by the ultimate strength and eventually around 35% of the bonds fail by the time that there is no more significant breakage. The main failure pattern for all of the specimens is a preferential inclined plane; the development of this failure mechanism is discussed in more detail later in this section.

The slight variation in the ultimate strength and axial strain at failure is due to the fact that, although all five simulations used the same input parameters, the spatial distribution of bond strengths was different for each specimen due to the randomness introduced by the coefficient of variation of strength. As described in Chapter 3 the maximum compressive stress that a bond can resist before failing (its compressive stress limit) is dependent on the mean compressive strength, the coefficient of variation of compressive strength and a random number falling on a normal distribution; the same formulations are used to determine both tensile and shear stress limits. Due to the inclusions of random numbers two simulations using the same specimen and same input parameters will produce two different spatial distributions of strength i.e. the same bond in both simulations may not have the same stress limits. This means that a specimen with a greater number of weaker bonds lying on the eventual failure plane will fail earlier (at a lower strain) and have a lower strength. The fact that the variation seen in Figure 4.12 is minimal is probably due to the fact that there are almost 100,000 bonds in the initial fabric and so a relatively even distribution of weaker bonds is expected.

In order to ensure to verify that the variation in bulk properties, seen in Figure 4.12 and Table 4.6, was due to the spatial distribution of strength and not due to programming weaknesses three further tests were conducted (run 2b, run 2c and run 2d). These additional simulations have the same spatial distribution of strength as run 2, presented in Figure 4.12. The stress strain curves for these additional simulations can be seen in Figure 4.14.

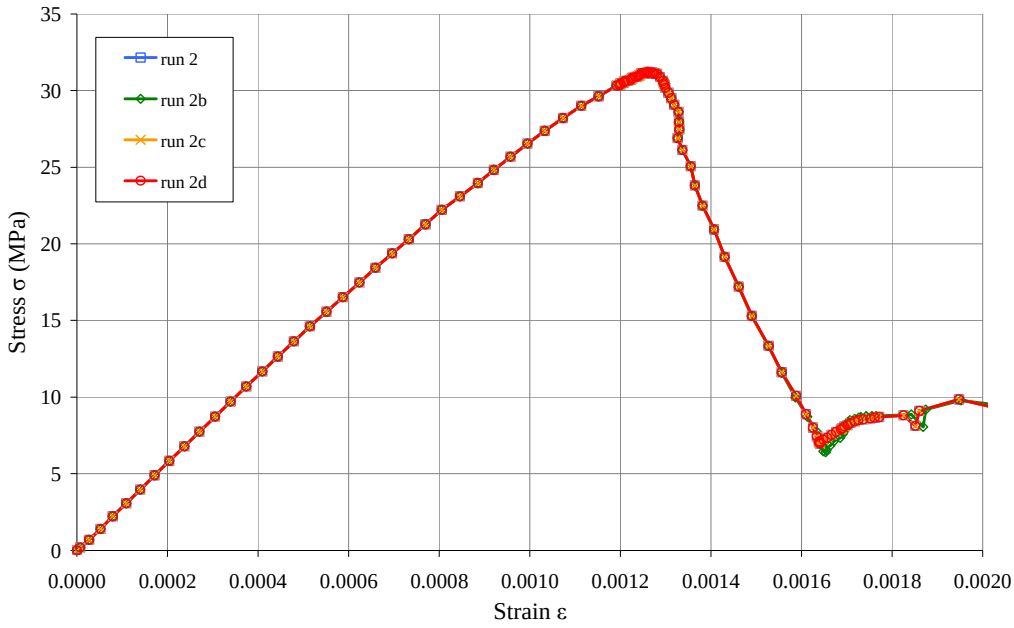

Figure 4.14 Four simulations with the same distribution of bond strengths

As can be seen from Figure 4.14 there is no significant variation in the computed results. This confirms that the variation seen in Figure 4.12 is due to the spatial distribution of bond strengths. It can be concluded that the spatial variation in bond strength, which arises from setting the coefficient of variation for each bond strength parameter, has no significant influence on the bulk properties or stress-strain behaviour. This means that in the parametric study, any change in the stress-strain curve seen beyond this slight variation will have been caused by the change in parameter.

The spatial variation in bond strength could be reduced by decreasing the coefficient of variation of bond strength; however this is seen as a key parameter that is expected to produce the non-linear stress-strain response which is closer to what is expected of a concrete specimen. The other option would be to implement a fixed seed so that all specimens would have the same spatial distribution of bond strengths; however, by using a random seed there is no predetermination of any bond strength and so a truly random distribution can be assured. As reported above there is no significant

difference in the predicted behaviour made when a different random number seed is used so this method will continue to be used in this study.

In order to compare the results from the reference simulation cases to further results from the parametric study and to empirical data one of the five runs from the reference simulation cases is used to represent the reference simulation cases. For this study the stress-strain response and bulk properties from run 3 are used. Accepted ranges for the bulk properties, as outlined in Section 4.2, are included in Table 4.7 for comparison against the simulated results. It should be noted that these ranges represent possible values rather than a specific values as may be known when considering a particular mix design.

Table 4.7 Bulk properties for the five reference case simulations

Parameter	Description	DEM Simulated	Accepted range
f_c'	Ultimate strength (MPa)	30.54	10-70
ε_c	Strain at maximum stress	0.00122	0.002-0.003
$E_{c(0.4)}$	Secant modulus of elasticity (GPa)	28.47	14-42
$\nu_{c(0.4)}$	Poisson's ratio	0.1956	0.15-0.20

From Table 4.7 it can be seen that all of the bulk properties for the reference case apart from the strain at failure fall within the accepted range. For the purposes of comparison with the Eurocode the DEM simulated strain at maximum stress will be used, but it is noted to be lower than desired.

An empirical stress-strain curve is generated using the Eurocode equation (BS EN 1992-1-1, 2004), the full relationship between stress and strain is shown in Equation (4.13) which is formed by substituting Equation (4.6) and Equation (4.11) into Equation (4.10):

$$\frac{\sigma}{f_c'} = \frac{23100\varepsilon\frac{\sqrt[3]{(f_c'/10)}}{f_c'} - \left(\frac{\varepsilon}{\varepsilon_c}\right)^2}{1+\left(23100\varepsilon_c\frac{\sqrt[3]{(f_c'/10)}}{f_c'} - 2\right)\left(\frac{\varepsilon}{\varepsilon_c}\right)} \qquad (4.13)$$

To produce the empirical curve from Equation (4.13) the strain at failure ε_c is set to 0.00122 and the value for ultimate strength f_c' is set at 30.54 MPa, the same as the values obtained from run 3 of the reference simulation case. The Eurocode 2 predicted stress-strain curve is compared against the DEM prediction using the reference simulation case results in Figure 4.15.

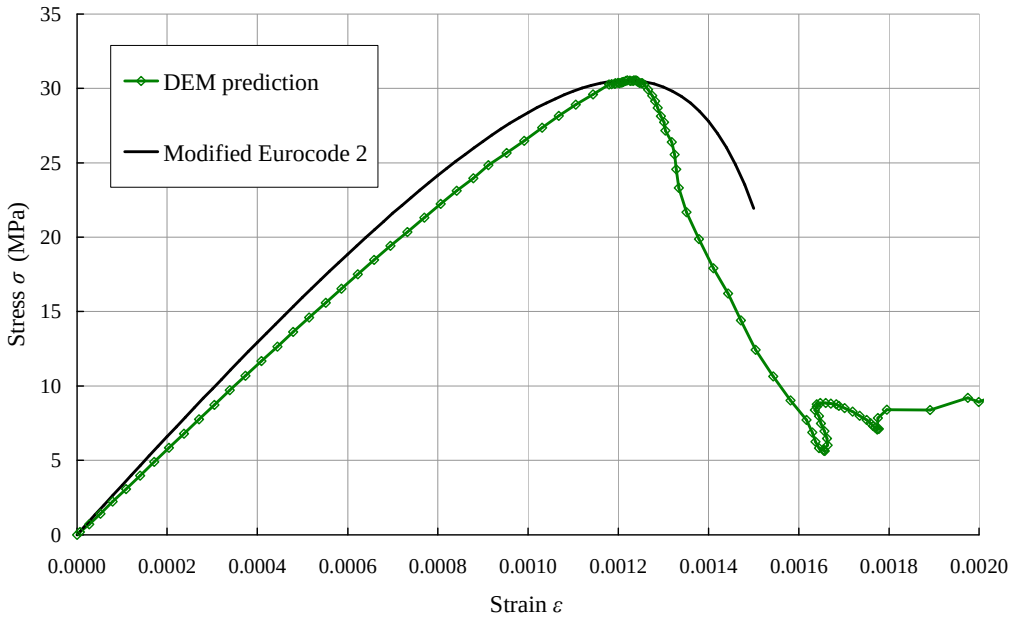

Figure 4.15 Comparison of DEM prediction to Eurocode curve

As can be seen in Figure 4.15, the DEM prediction does not show sufficient curvature in the pre-peak region. The secant modulus at 28.47 GPa is just over 10 % lower then that of the Eurocode curve – a value of 31.92 GPa. An indication of how the stiffness changes with strain is shown in Figure 4.16.

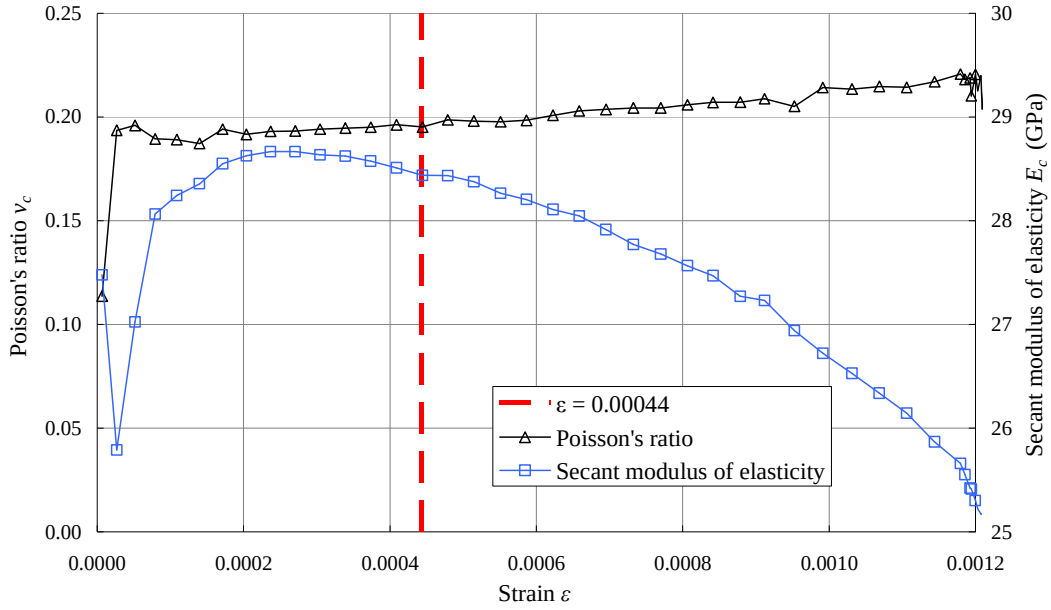

Figure 4.16 Secant modulus of elasticity and Poisson's ratio against strain

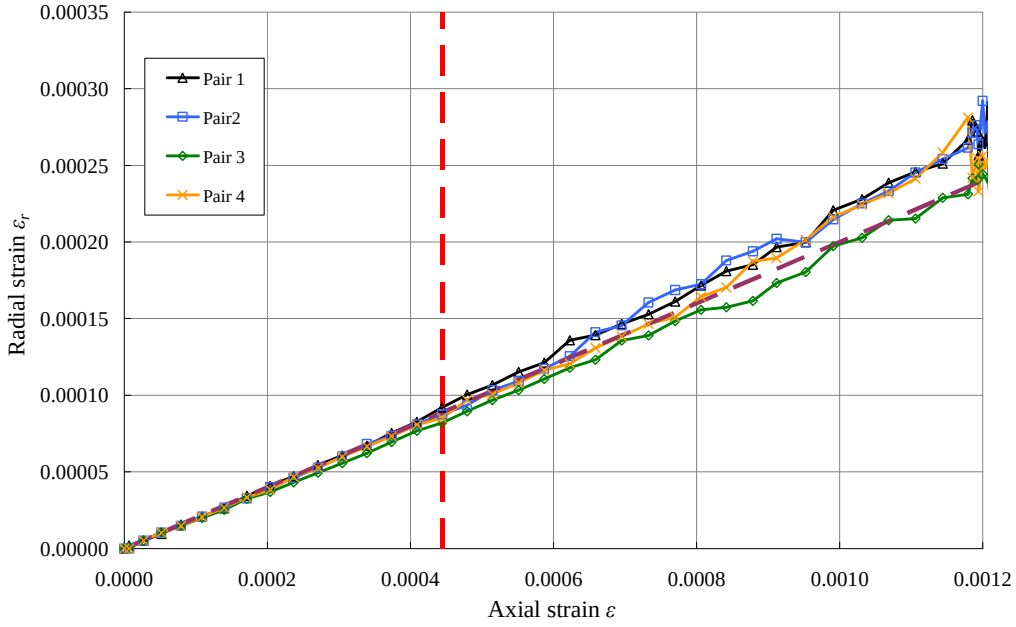

Figure 4.17 Variation in radial strain for the four sampling points

As can be seen from Figure 4.16 the Poisson's ratio remains relatively constant throughout loading. There is an initial rapid increase in Poisson's ratio from zero to approximately 0.2; the Poisson's ratio starts at zero because there is a delay between the beginning of loading and a recorded radial strain. The initial portion of Figure 4.16 is discussed in more detail below. A slight increase in Poisson's ratio is seen after loading reaches approximately 40% of the ultimate strength (indicated in Figure 4.16 and Figure 4.17 by the red dashed line). This is probably due to the exacerbation of the radial strain due to bond breakage, which is apparent in Figure 4.17 where the variation in radial strains determined for the four pairs of particles is shown. An increase in Poisson's ratio is similar to relations seen in experiments by Shah and Chandra (cited by Dhir and Sangha, 1974) where an increase in Poisson's ratio from 50-55% maximum stress was observed.

As can be seen from Figure 4.16 the secant modulus of elasticity reaches a peak at just after 0.0002 strain and then reduces with an increasing rate due to the increased breakage of bonds. This reduction in stiffness is not significant enough to match the non-linearity of the Eurocode prediction. Both the modulus of elasticity and Poisson's ratio vary significantly up until about 0.0002 strain. The variation in values of secant modulus of elasticity and Poisson's ratio up to a strain value of 0.0002 strain is explored further by retrieving more data points as shown in Figure 4.18.

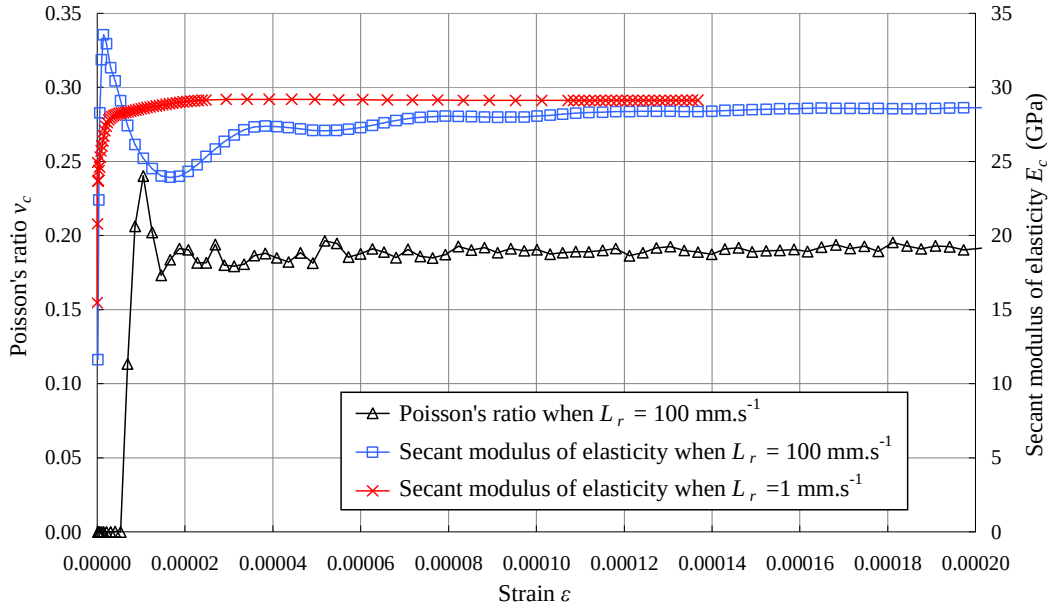

Figure 4.18 The initial modulus of elasticity and Poisson's ratio for varying loading rates (L_r)

When using the reference case value for loading rate (L_r) there is a fluctuation in the value of secant modulus of elasticity at small strains as can be seen in Figure 4.18. This fluctuation reduces as loading increases. This initial fluctuation is principally due to the introduction of dynamic effects caused by the relatively high loading rate as well as the packing structure at the boundaries, where the porosity is slightly higher than elsewhere in the specimen. As shown in Figure 4.18 by reducing the loading rate from 100 mm.s^{-1} to 1 mm.s^{-1} the initial fluctuation disappears. This initial variation does not affect the key macroscopic parameters computed from the results. The initial Poisson's ratio at very small strains is recorded as zero because there is a delay between the initial loading state and a time where there is any lateral deflection at the mid height which is where the Poisson's ratio is assessed.

In order to determine the mechanism through which the specimen fails a cross sectional slice, 10 mm thick, taken from the centre of the specimen is examined. The pattern of broken bonds at different strains is shown in Figure 4.19.

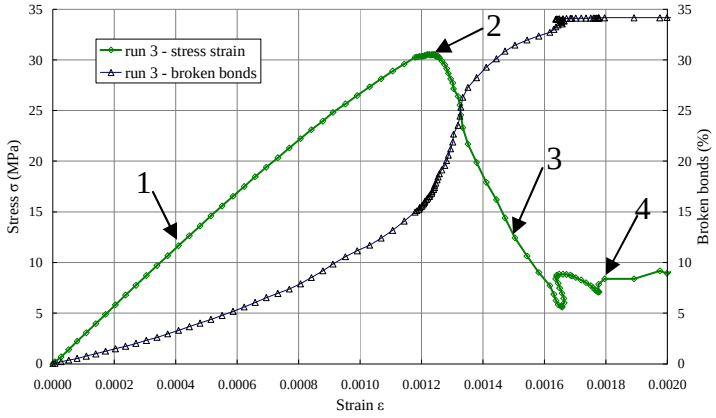

(a) stress-strain curve with sample points highlighted

(b) at 0.00041 strain

(c) at 0.00127 strain

(d) at 0.00150 strain

(e) at 0.00180 strain

Figure 4.19 Progression of failure mechanism with an increase in load

Crack propagation is on the scale of the particles, and one bond failure represents the crack propagation in the system. At the point at which the bulk stiffness and bulk Poisson's ratio are determined (Figure 4.19(b)) it can be seen that there are not many bonds that have failed; for run 3 this is only 3.7%. Even at the ultimate strength, where 16% of bonds have failed the eventual failure plane is not clear. However, on the descending branch of the stress-strain curve, and corresponding to a rapid increase on the broken bond curve, the main crack develops. By the end of the descending branch, Figure 4.19 (e), there is little additional cracking noted; the main crack widens slightly. In order to look in more detail at the progression of the failure plane that happens, the initiation and propagation of the failure plane, expressed as damage that develops in the specimen, is shown in Figure 4.20. The degree of local damage is calculated for each particle in the simulation using Equation (4.14). This is equivalent to continuum damage theory:

$$D_m = 1 - \frac{B}{B_0} \tag{4.14}$$

where D_m is the local damage, B is the number of bonds connected to that particle and B_0 denotes the number of bonds that were connected to that particle after the bonds had been first initialised.

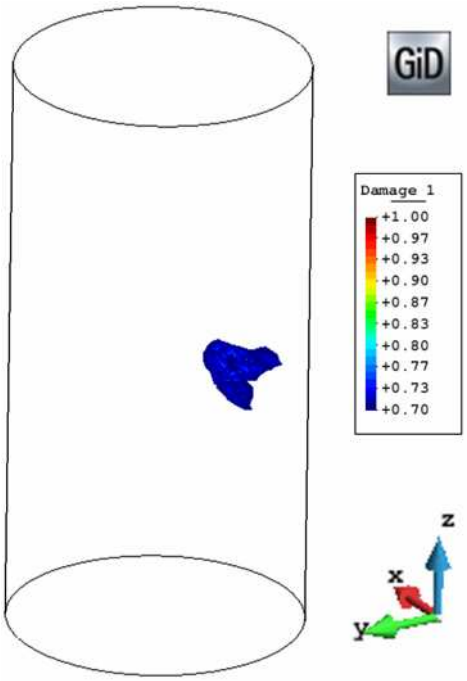

(a) at 0.00128 strain – 3D view

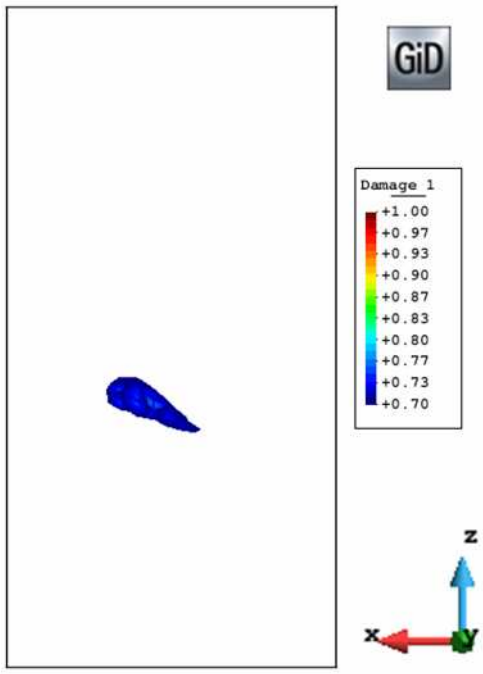

(b) at 0.00128 strain – side view

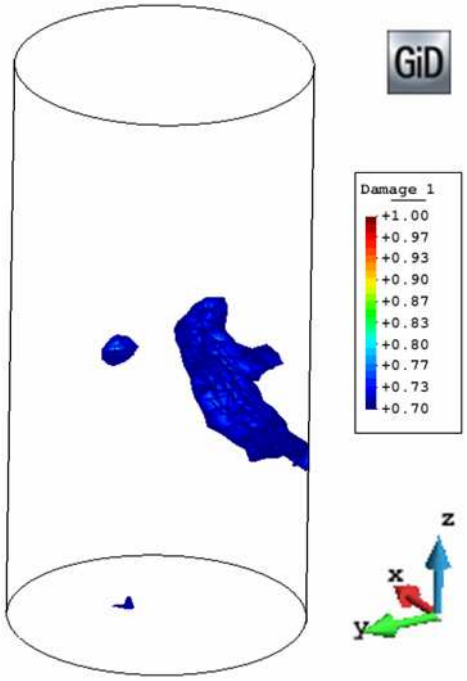

(c) at 0.00130 strain – 3D view

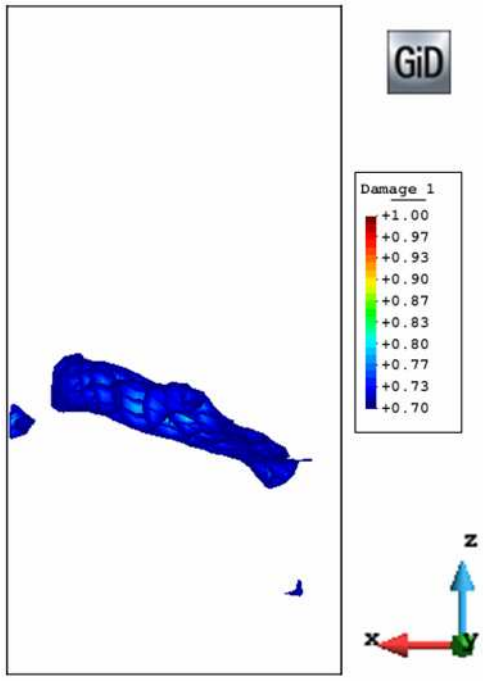

(d) at 0.00130 strain – side view

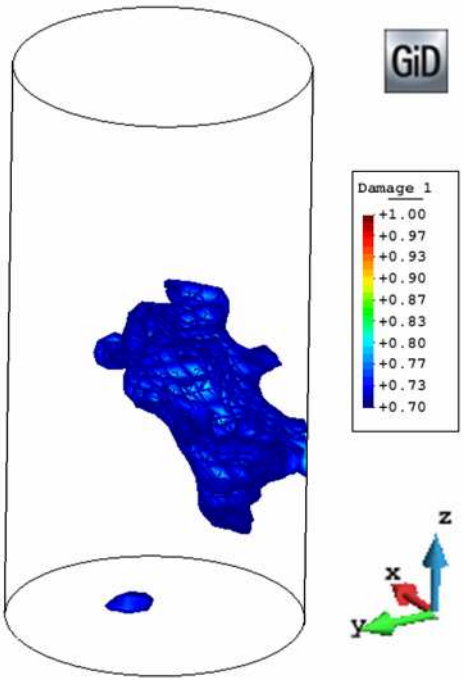

(e) at 0.00133 strain – 3D view

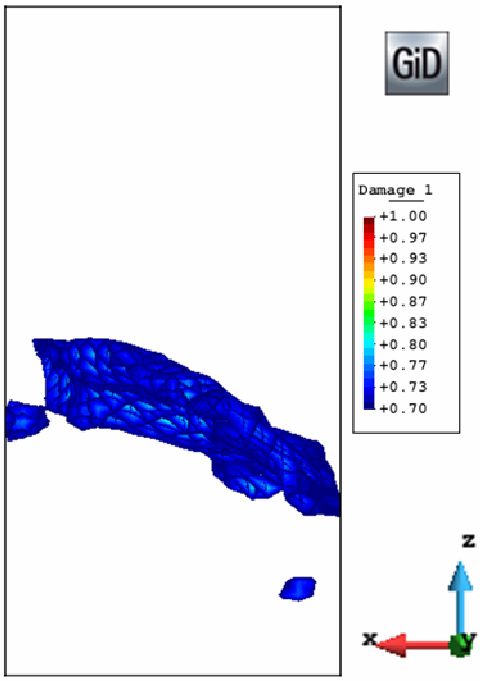

(f) at 0.00133 strain – side view

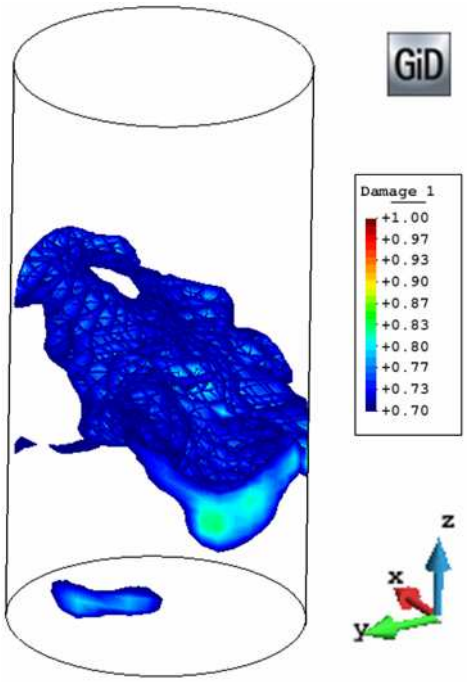

(g) at 0.00150 strain – 3D view

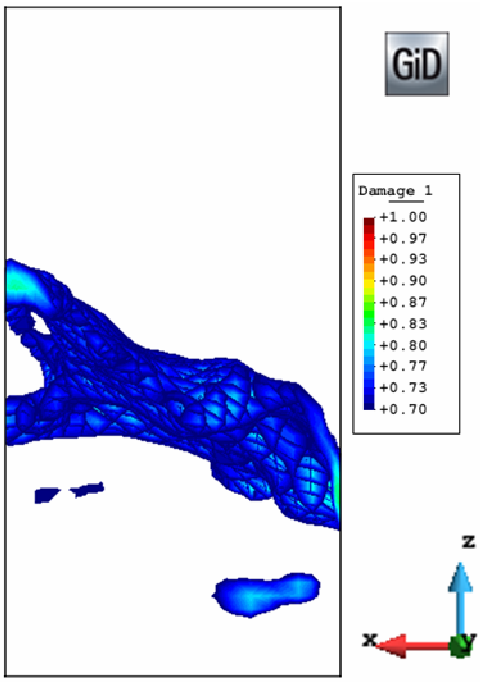

(h) at 0.00150 strain – side view

Figure 4.20 Progression of damage highlighting the primary crack

The damaged area in Figure 4.20 highlights the primary crack which propagates from one edge of the specimen to the other side of the specimen forming a preferential inclined plane. The cumulative number of bonds failing in compression, tension and shear during the axial loading is shown in Figure 4.21; this provides a better insight into the dominant failure mechanism responsible for failure.

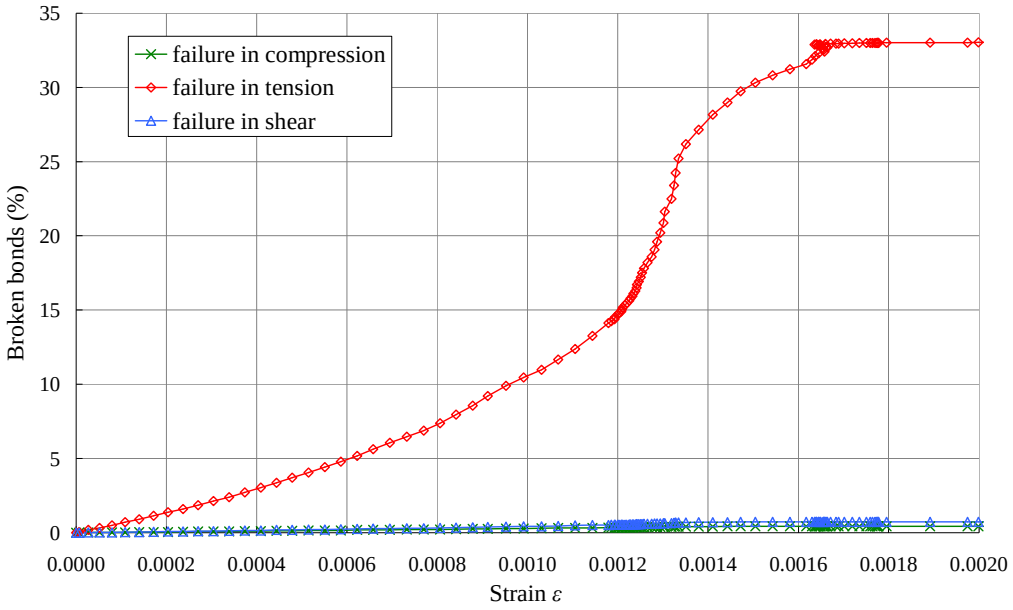

Figure 4.21 The number of bonds failing in each mode

It is evident from Figure 4.21 that the vast majority of the bonds fail in tension for this reference case, with very few bonds failing in either compression or shear. It can be seen that the total number of bonds failing increases steadily as the strain increases. Figure 4.22 compares the orientation of the bonds before loading and at the ultimate stress state to determine if the loading causes any change in the orientation.

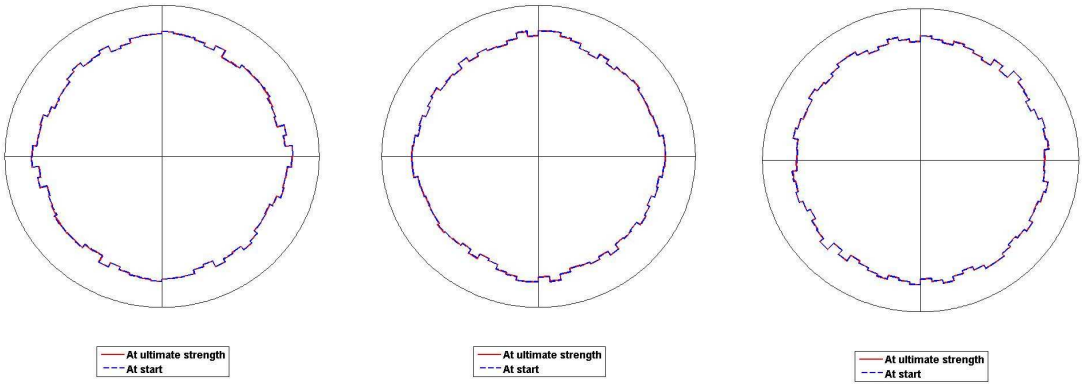

(a) X-Y plane (b) X-Z plane (c) Y-Z plane

Figure 4.22 Orientation of contacts before loading and at ultimate strength for the three planes

Figure 4.22 shows no noticeable changes in the contact orientation from the initial state. This is due to the fact that the particles are predominantly bonded together and the total deformation is relatively small, so no significant shift in the contact orientation can take place.

4.7 Summary of the reference case

The DEM simulation of a uniaxial compression of concrete cylinder to failure using a proposed set of reference input parameters has been discussed in detail. The results show a reasonable match between the predicted stress-strain behaviour and that using the Eurocode equation. The bulk properties for the reference case in terms of the compressive strength, the bulk stiffness and the Poisson's ratio have been evaluated from the DEM computations and found to fall within the range of values expected of typical concrete specimens. The strain at failure was a little low due to the lack of loss of stiffness shown. The set of parameters used has proved to be a good base for a full parametric investigation to be conducted which is presented in the next chapter.

Chapter 5 Parametric study: Part 2: influence of the input parameters

5.1 Introduction

This chapter presents a parametric study that investigates the influence of the model input parameters of the Edinburgh Bonded Particle Model (EBPM) on the DEM simulation of the uni-axial compression of a concrete specimen. The influence of each parameter will be explored whilst keeping the remaining parameters the same as those used for the reference simulation case. The background, justification and setup of the reference simulation case have been described in the preceding Chapter.

As described in Chapter 3 there are two contact models within the EBPM: the Hertz-Mindlin Contact Model (HMCM) and the Timoshenko Beam Bonded Contact Model (TBBM) which are used at non-bonded and bonded contacts respectively. Each of these contact models has a separate set of input parameters. With this in mind all of the parameters of interest in this study can be placed into one of the following four categories:

1) *Bonded contact parameters* characterise the constitutive behaviour at bonded contacts, and are used exclusively by the TBBM; these include bond Young's modulus, bond mean strength and coefficient of variation of strength.
2) *Non-bonded contact parameters* characterise the constitutive behaviour at non-bonded contacts, and are used exclusively by the HMCM; these include particle to particle coefficient of static friction and particle Young's modulus.
3) *Bond fabrication parameters* are numerical factors that characterise how the initial bond fabric and the bond geometry are formed; these include contact radius multiplier and bond radius multiplier.

4) *Other numerical parameters* which affect the behaviour of both bonded and non-bonded contacts but are not used in the contact models; they are global damping coefficient, computation time step and loading rate.

In the parametric study presented here the number of particles, the size of the particles and the size of the specimen are not changed. The only loading of the specimen comes from the displacement of the loading plates; there are no external actions on the specimen (e.g. gravity).

The predictive capability of the EBPM will be evaluated by inspecting four bulk response properties, which are generally considered to be the most important engineering properties. These are: the ultimate compressive strength, the secant modulus of elasticity, the axial strain at failure, and the Poisson's ratio. The exact methods for determining these parameters have been described in Chapter 4. All four bulk properties rely on the determination of at least one of the following: the bulk axial compressive stress, the bulk axial strain and/or radial strain. The compressive stress is determined by dividing the total force acting on the loading plates by the cross sectional area of the cylinder, the axial strain is effectively determined by tracking the vertical positions of the top and bottom particles in the specimen and the radial strain is determined by tracking the horizontal positions of particles at the mid-height of the specimen.

Along with these quantitative properties the overall stress-strain response including the post peak behaviour will also be considered. A normalised stress strain curve, produced using the Eurocode equation (BS EN 1992-1-1, 2004), is shown in Figure 5.1 (this is a replication of the same curve described in Section 4.2). The curve has been divided into three regions, in each of which the stress-strain behaviour is expected to be influenced by different variables.

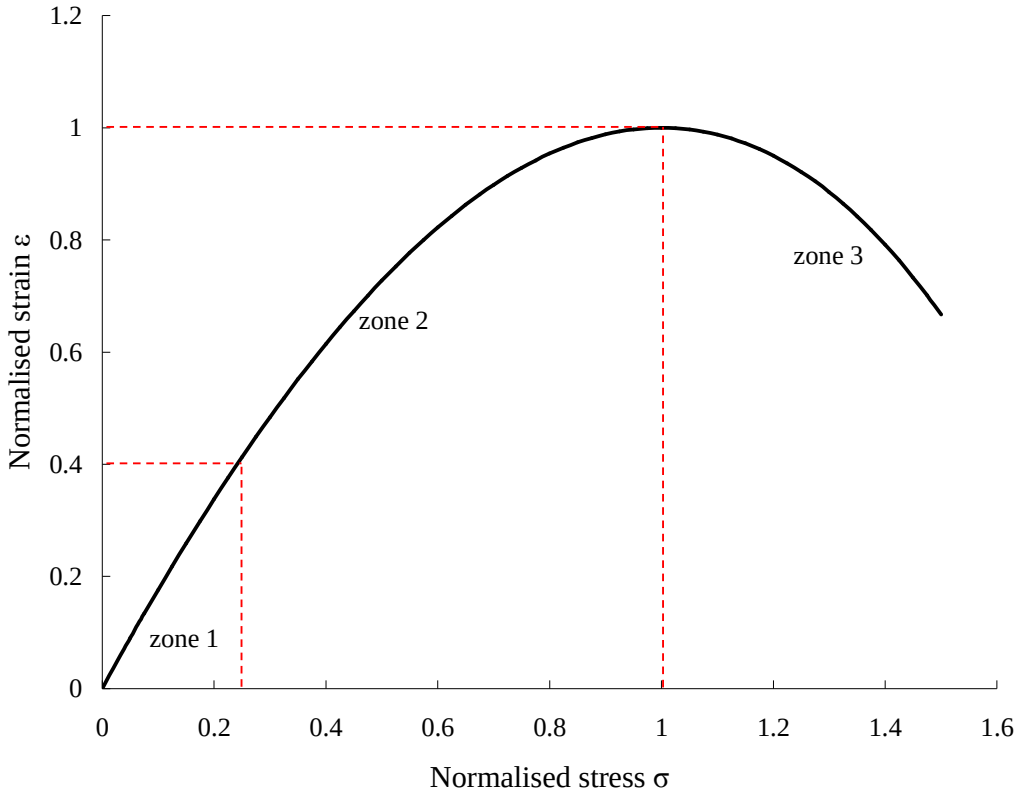

Figure 5.1 The stress-strain curve produced by the Eurocode equation highlighting the three zones in which there is a change in behaviour

It is expected that in the near elastic region of loading (zone 1 in Figure 5.1) very few bonds will fail as the stresses in each bond are likely to be well below their respective stress limits. This means that the stress-strain response will be predominantly influenced by bonded contact parameters (such as bond Young's modulus) rather than non-bonded contacts parameters (such as particles Young's modulus).

As loading continues and the strain increases (zone 2 in Figure 5.1) more bonds fail and new non-bonded contacts are formed, non-bonded contact parameters should begin to influence the behaviour. In the post peak region (zone 3 in Figure 5.1) any additional bond failure is likely to be governed by the particular failure mechanism

that forms. The bond fabrication parameters are likely to affect the initial stages of loading most as they influence the number and stiffness of the bonds in the specimen. The numerical implementation parameters are included to ensure the numerical stability of the simulations; their effect on the stress-strain behaviour is likely to be minimal when kept within specific bounds.

5.2 Influence of bonded contact input parameters

For a given initial bond fabric the EBPM has eight input parameters which describe the stiffness and strength characteristics of the bonds. Two of these parameters, the bonds' Young's modulus and bonds' Poisson's ratio, directly affect the stiffness characteristics for each bond. The other six parameters: the mean bond compressive strength, mean bond tensile strength, mean bond shear strength, and the corresponding three coefficients of variation, characterise the distribution of the compressive, tensile and shear stress limits for each bond.

The coefficient of variation of strength for each strength component has been kept the same, so that for the purposes of this study all three are covered by a single coefficient of variation of strength (CoV) ς. The range of values for the bonded contact parameters used in this parametric study is given in Table 5.1.

Table 5.1 Range of bonded contact parameters used

Parameter	Description	Reference	Min	Max
E_b	Young's modulus (GPa)	35	5	80
ν_b	Poisson's ratio	0.2	0	0.5
S_C	Mean bond compressive strength (MPa)	500	100	1000
S_T	Mean bond tensile strength (MPa)	60	40	80
S_S	Mean bond shear strength (MPa)	60	10	80
ς	Coefficient of variation of strength	0.8	0	1.0

5.2.1 Influence of the bond Young's modulus

The input value for the bond Young's modulus was investigated for a range between 5 GPa to 80 GPa. This is deemed an appropriate range for typical concrete material. The stress-strain response when using values of 10 GPa and 60 GPa are compared against the reference simulation case when E_b = 35 GPa, as shown in Figure 5.2.

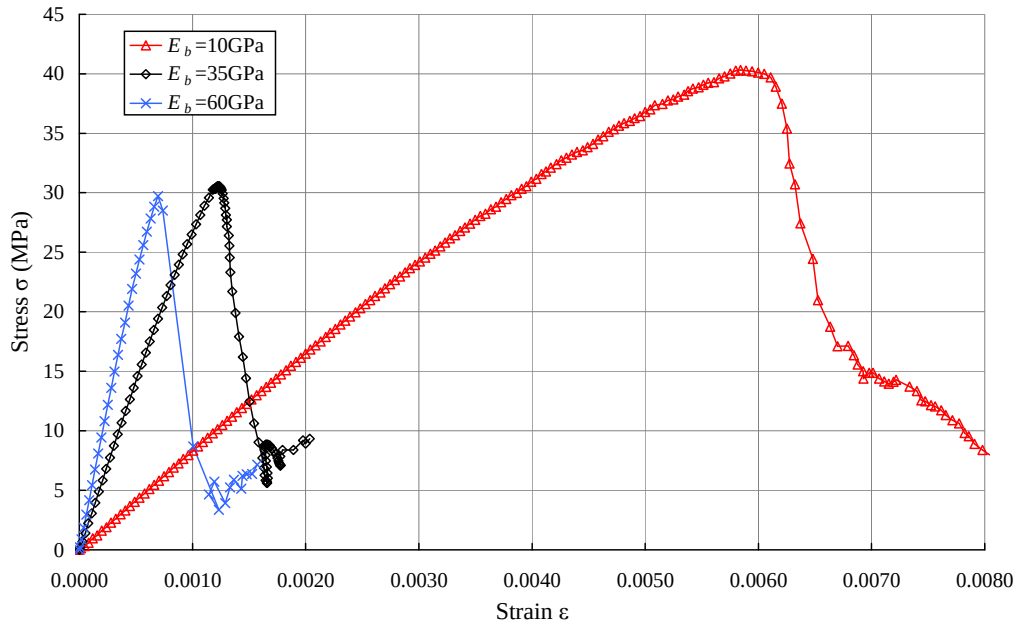

Figure 5.2 Influence of bond Young's modulus on the stress-strain response

As the bond's Young's modulus increases the bulk stiffness also increases and the strain at ultimate strength reduces, as would be expected. The bulk Poisson's ratio does not change but the ultimate strength is affected in a non-linear manner.

As expected, the predicted bulk stiffness rises as the bond modulus increases, this is because the bond's Young's modulus directly influences the stiffness of each bonded contact. The resulting bulk stiffness for the full range of bond modulus tested up to 80 GPa are plotted in Figure 5.3.

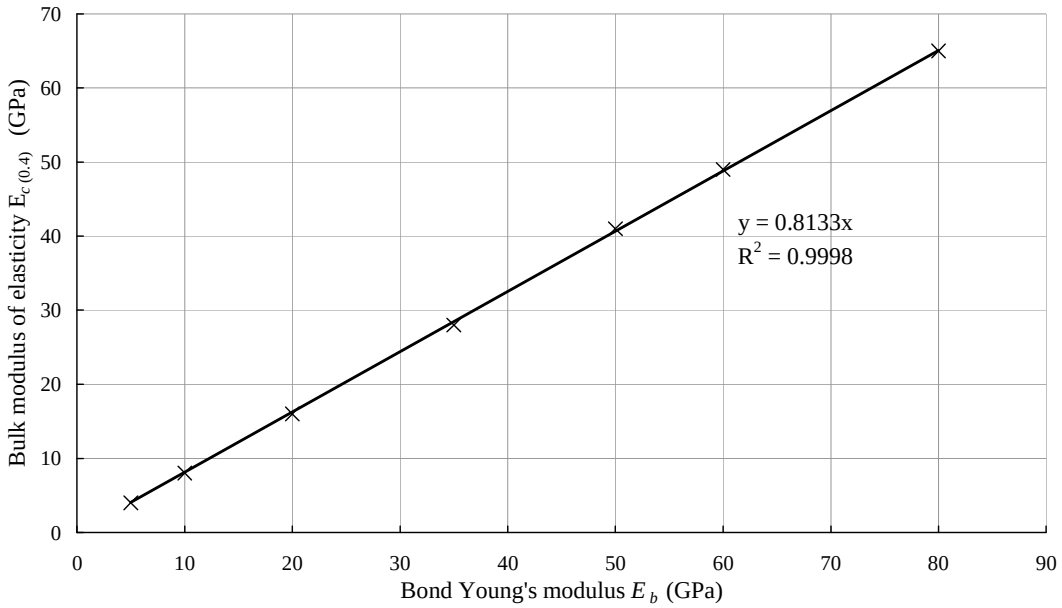

Figure 5.3 Influence of the bond Young's modulus on the bulk modulus

Figure 5.3 shows a linear relation between the bond Young's modulus and the bulk stiffness. At the loading instant when the bulk stiffness is determined (40% of the ultimate strength) very few bonds in any of the simulations have failed (between 3.1% and 4.7% for all values of E_b), so the bulk stiffness is very much dominated by the stiffness of the initial bond fabric, which is influenced by the stiffness of the individual bonds.

As the stiffness of the bond decreases, a larger deformation is required to create the same forces in each bond meaning that the strain at failure also increases, and this can be seen in Figure 5.4.

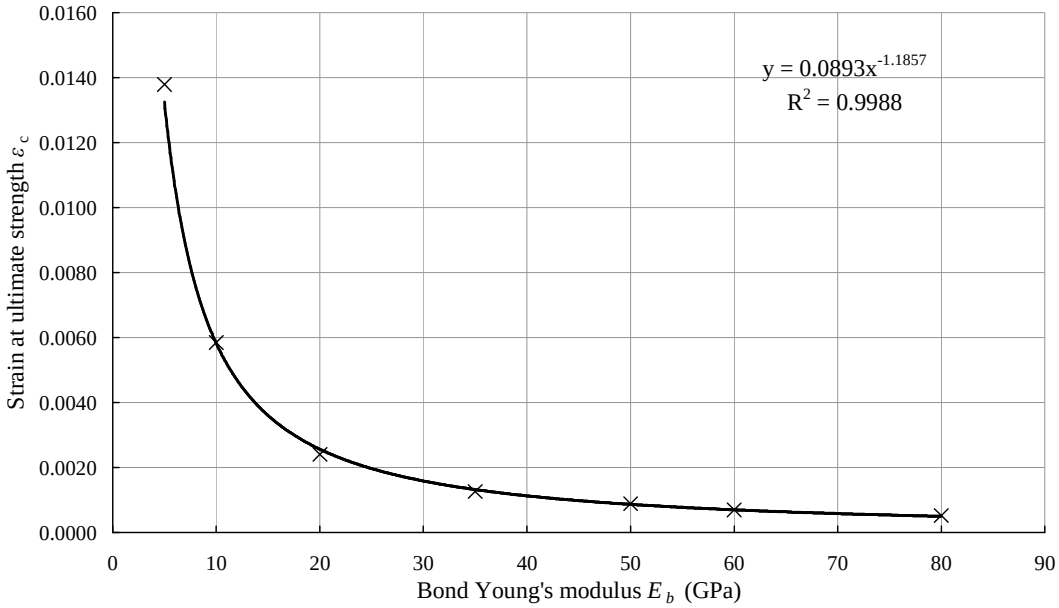

Figure 5.4 Influence of the bond Young's modulus on the strain at failure

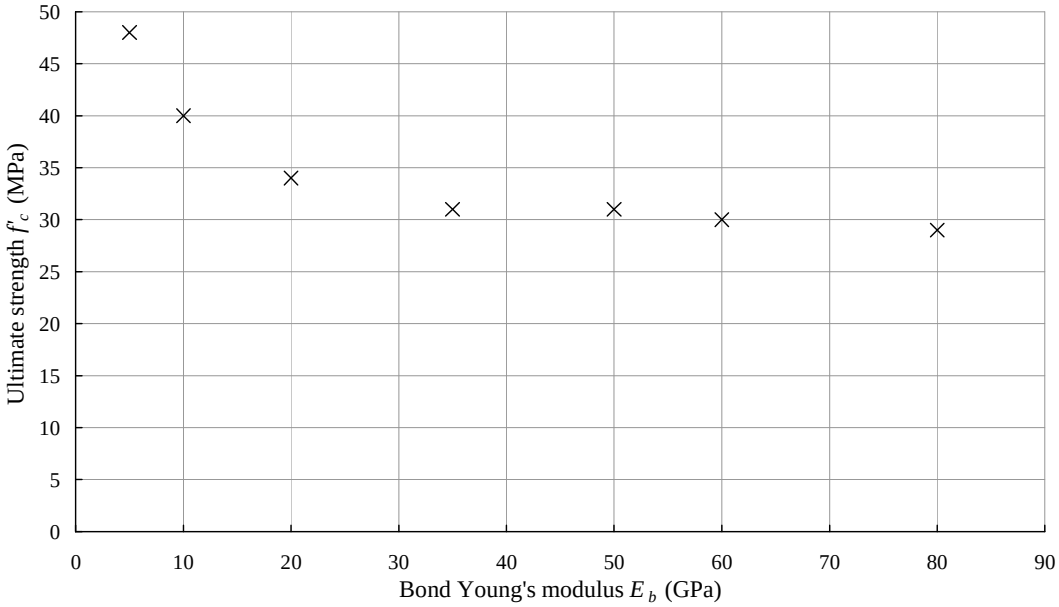

Figure 5.5 Influence of the bond Young's modulus on the ultimate strength

As shown in Figure 5.5 as the bond Young's modulus is reduced from 80 GPa to approximately 35 GPa the bulk strength increases slightly (approximately 7% over this range). However, as the bond stiffness is reduced further there is a more significant increase in strength.

This increase in strength comes from the fact that as the bond Young's modulus decreases the strain at failure increases. With increasing strain there is a larger deformation of the specimen meaning that more particles come into physical contact and so new non-bonded contacts are formed, this relationship is summarised in Table 5.2. These additional non-bonded contacts add additional load carrying capacity which ultimately increases the strength of the specimen. As can be seen in Table 5.2 the percentage of load carrying non-bonded contacts is much higher when the bond Young's modulus is less than 35 GPa. This is approximately the same point at which the significant strength increase is noted. It is suggested that the non linear relationships seen in Figure 5.4 and Figure 5.5 may be due to the complex relation between the strain and strength and the fact that the force-displacment law used in the Hertz-Mindlin Contact Model is non-linear; this means that for larger specimen deformations the force redistributed in the non-bonded contacts is much greater.

Table 5.2 Comparing the number of non-bonded contacts to broken bonds at failure

Bond Young's modulus of E_b (GPa)	Number of broken bonds at ultimate strength (a)	Number of load carrying contacts at ultimate strength (b)	Ratio of non-bonded contacts to broken bonds (a/b)
5	25477	7178	3.5
10	21289	4272	5.0
20	18207	1779	10.2
35	16848	617	27.3
50	17795	489	36.4
60	16300	247	66.0
80	16803	212	79.2

The bond stiffness has no significant influence over the failure mode which remains as a preferential inclined (shear) crack for all values, as seen in the reference case. The small change in post peak behaviour is caused by the change in the number of non-bonded contacts that are mobilised depending on the strain at failure.

5.2.2 Influence of the bond Poisson's ratio

One of the principal assumptions of the Timoshenko Beam Bonded Contact Model is that each bond behaves elastically up to the failure point. Therefore a bond's shear modulus G_b is related to its Young's modulus E_b and Poisson's ratio ν_b, such that:

$$G_b = \frac{E_b}{2(1+\nu_b)} \tag{5.1}$$

Values for Poisson's ratio of most materials fall in the range of 0.1 to 0.4. When investigating the influence of bond Poisson's ratio the bond Young's modulus is maintained at 35 GPa. Even if the Poisson's ratio of the bond material is investigated in the range 0.1 to 0.4 according to Equation (5.1) the shear modulus will only vary between 12.5 GPa and 15.9 GPa. It can be instantly seen that this is a much smaller range than that which the Young's modulus was investigated over (which was 5 GPa to 80 GPa); the response is being constrained by an elastic assumption. In the parametric study the Poisson's ratio is actually investigated over a range of 0 to 0.5; the influence of the bond Poisson's ratio on the stress-strain behaviour is shown in Figure 5.6. The key bulk parameters evaluated from the DEM computation are summarised in Table 5.3.

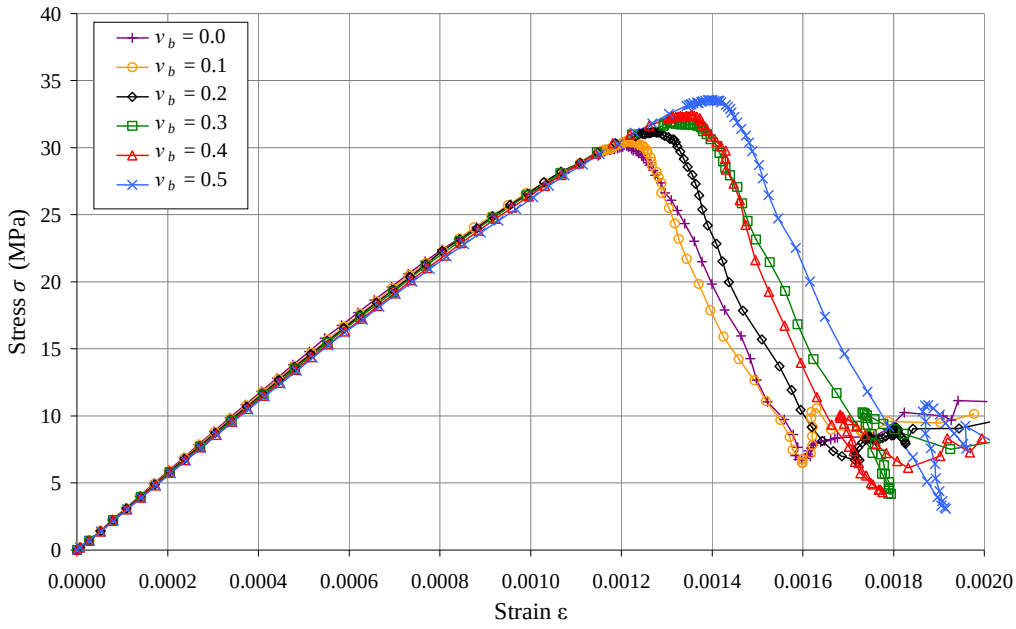

Figure 5.6 Influence of the bond Poisson's ratio on the stress-strain response

Table 5.3 Summary of influence of Poisson's ratio of bond material

Bond Poisson's ratio ν_b	Ultimate Strength (MPa) f_c'	Strain at failure ε_c	Secant modulus of elasticity (GPa) $E_{c(0.4)}$	Bulk Poisson's ratio $\nu_{c(0.4)}$
0.0	30.2	0.001205	29.1	0.189
0.1	30.5	0.001212	28.8	0.193
0.2	31.2	0.001275	28.4	0.197
0.3	31.9	0.001311	28.2	0.200
0.4	32.5	0.001356	27.9	0.203
0.5	33.6	0.001401	27.6	0.205

As the Poisson's ratio is increased from 0 to 0.5 the DEM model predicts a gradual increase in the ultimate strength f_c' (up approximately 10%), with a corresponding increase in the ultimate strain ε_c .The bulk Poisson's ratio $\nu_{c(0.4)}$ also increases by approximately 9% over this range. However the secant modulus of elasticity $E_{c(0.4)}$ decreases by about 5% . The relationships are shown in Figure 5.7, Figure 5.8 and Figure 5.9.

Increasing the bond Poisson's ratio reduces the bond shear modulus which in turn reduces the shear stiffness of the bonds, and this can be seen in the slight reduction in bulk secant modulus of elasticity, indicated in Figure 5.8. As the shear stiffness is constrained by the limits of the elastic relationship shown in Equation (5.1), there is no significant change in the initial loading portion of the stress-strain response meaning that the observable difference is negligible.

The apparent increase in ultimate strength caused by an increase in bond Poisson's ratio is still under investigation. There is no apparent change in the failure mode or in the number of bonds failing. It is suggested that the increase in strength is related to

the location of the failure. It appears that at higher Poisson's ratios the failure is at the mid-height and is a greater angled plane, whilst for lower Poisson's ratio the failure is closer to the base of the specimen. The additional strength probably arises from the additional frictional contacts that provide additional strength, as was seen for a reduction in bond Young's modulus above. However the increase in strength appears to be disproportionate to the change in bulk stiffness.

It is clear that the strain at failure is associated with a combination of bulk stiffness and ultimate strength. In this instance there is no significant difference in the bulk stiffness so the strain at failure will be linked with the ultimate strength, i.e. the higher the ultimate strength the higher the strain at ultimate strength.

This means that for the same bond forces a greater loading plate deflection is required. At higher deformations there are a greater number of non-bonded contacts that are able to carry load. This increases the bulk strength. In this instance the relationships between bond Poisson's ratio and strength and bulk stiffness appears to be linear as shown in Figure 5.7 and Figure 5.8 respectively. However this is due to the very small range of shear stiffness investigated.

As described in Chapter 4 the bulk modulus of elasticity gradually reduces and bulk Poisson's ratio gradually increases as the strain is increased. So as the predicted bulk Poisson's ratio for a varying bond Poisson ratio are taken at different actual strain points this could cause the change. On inspection when the bulk Poisson's ratio and secant modulus are taken at the same strains for all simulations the trends shown in Table 5.3 still exist. This suggests that some fundamental phenomenon in causing this change (i.e. it is not being caused by a change in the sampling point). However the range of values is not significant enough for bond Poisson's ratio to have a significant affect on the bulk Poisson's ratio or bulk modulus of elasticity.

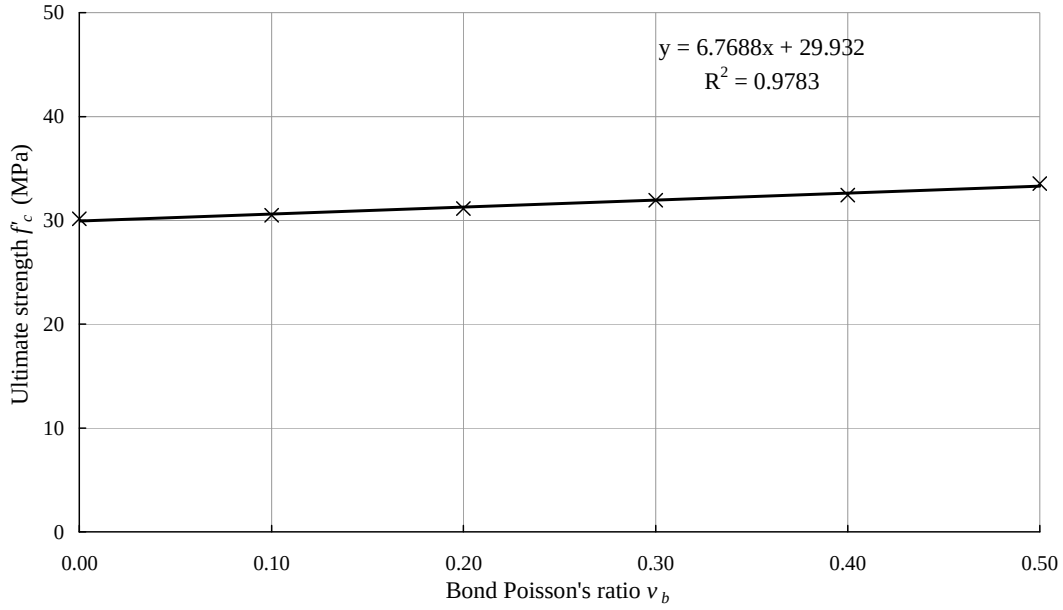

Figure 5.7 Influence of the bond Poisson's ratio on the ultimate strength

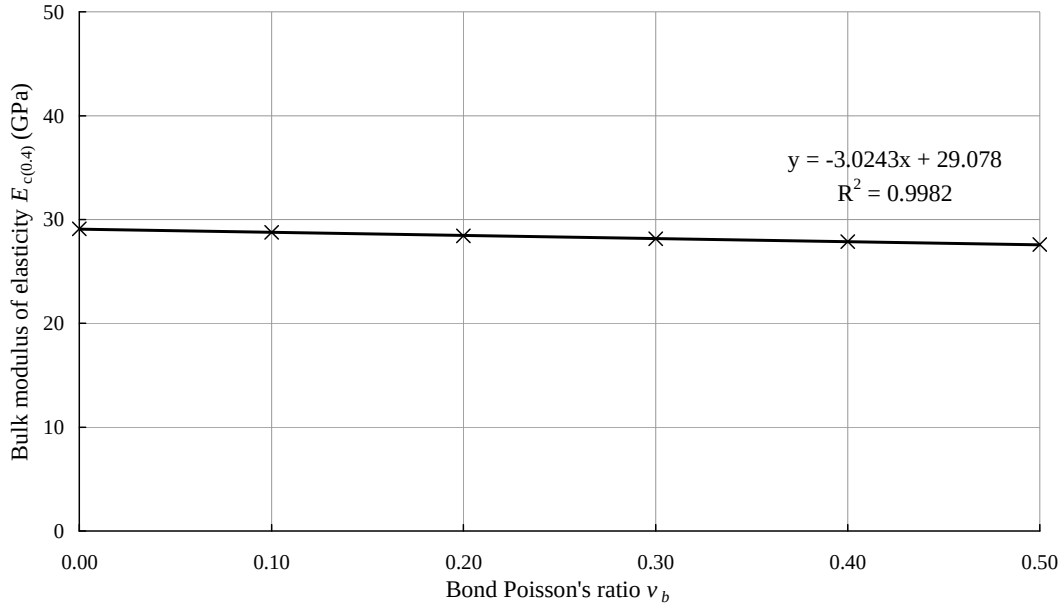

Figure 5.8 Influence of the bond Poisson's ratio on the bulk modulus of elasticity

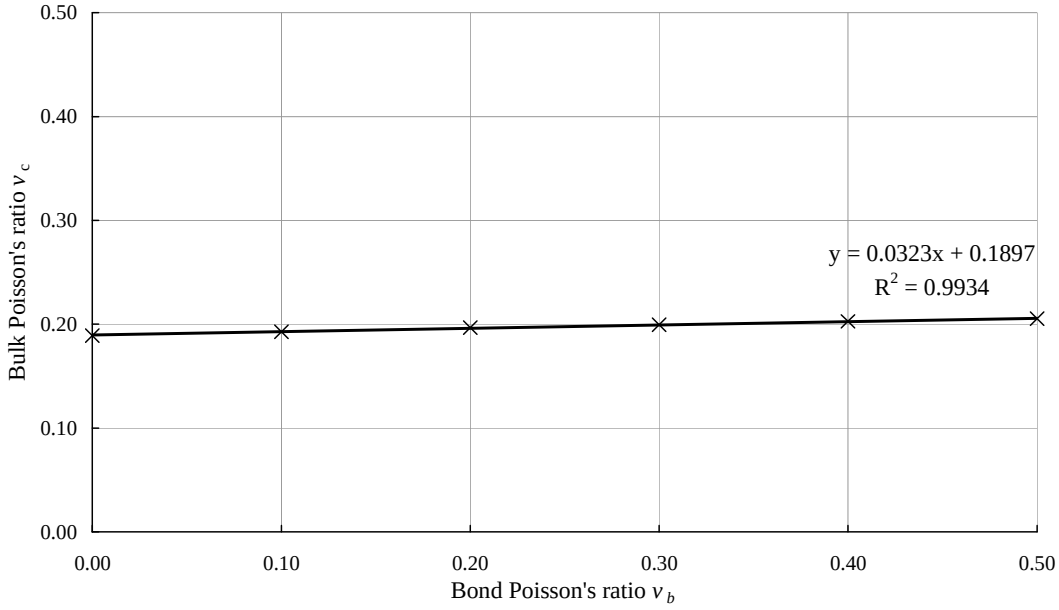

Figure 5.9 Influence of the bond Poisson's ratio on the bulk Poisson's ratio

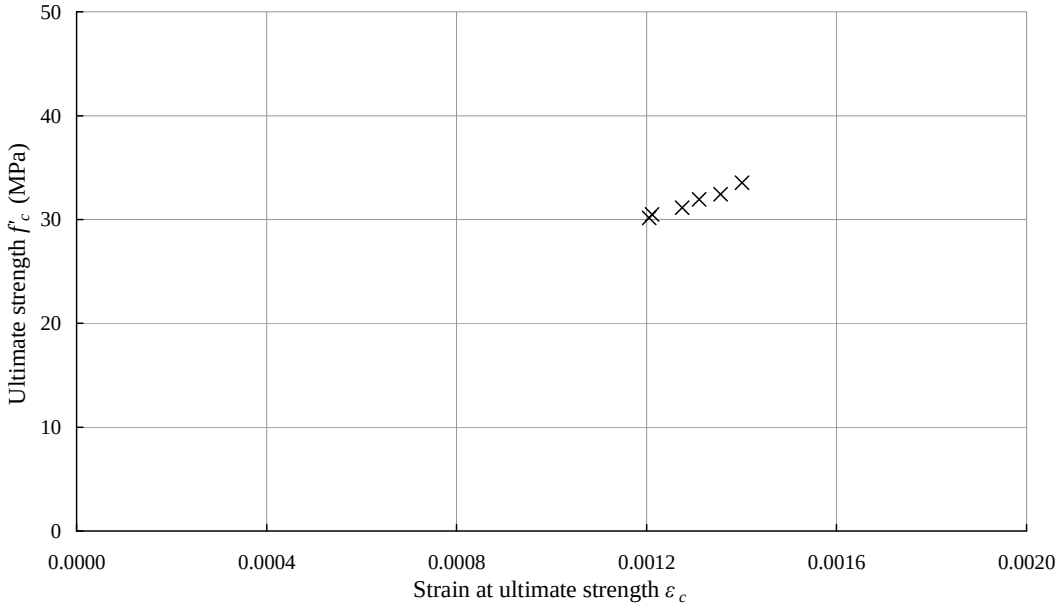

Figure 5.10 Relationship between strain at ultimate strength and ultimate strength for increasing values of Poisson's ratio

5.2.3 Influence of the compressive strength of the bonds

The compressive strength of the bonds is assumed to follow a Gaussian distribution. This distribution is defined by a mean and a standard deviation. Figure 5.11 shows the influence of the mean bond compressive strength on the stress-strain response. The influence of the standard deviation is discussed in Section 5.2.6 below.

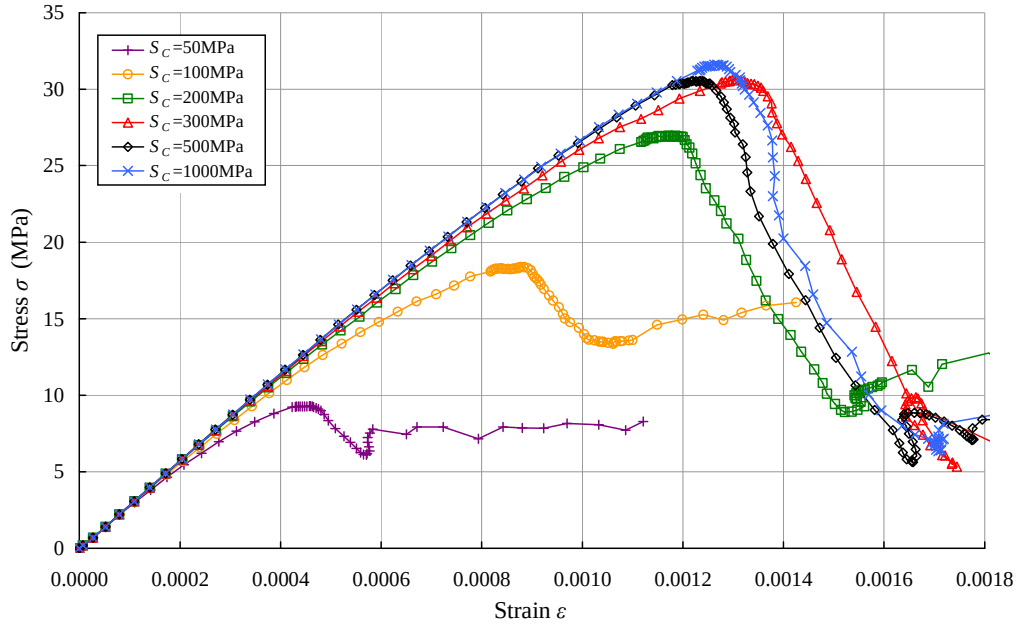

Figure 5.11 Influence of mean compressive bond strength on the stress-strain response

Of the four key bulk parameters the mean bond compressive strength only significantly affects the ultimate strength (and subsequently strain at failure); this relationship is asymptotic (shown in Figure 5.11). As the mean bond compressive strength is increased from 50 MPa to approximately 300 MPa the ultimate strength also increases; above this value there is no further increase in ultimate strength (shown in Figure 5.12). As the ultimate strength increases the strain at failure also increases; a strong positive trend can be seen between the two in Figure 5.13. It can be seen in Figure 5.11 that the lower the ultimate strength the lower the drop in stress post peak.

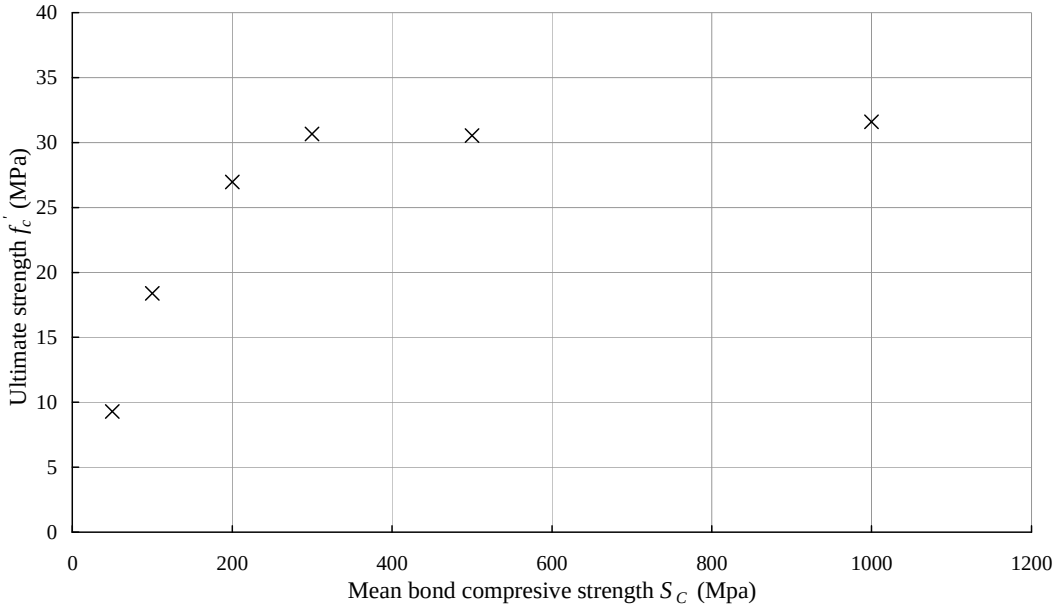

Figure 5.12 Influence of mean bond compressive strength on the ultimate strength

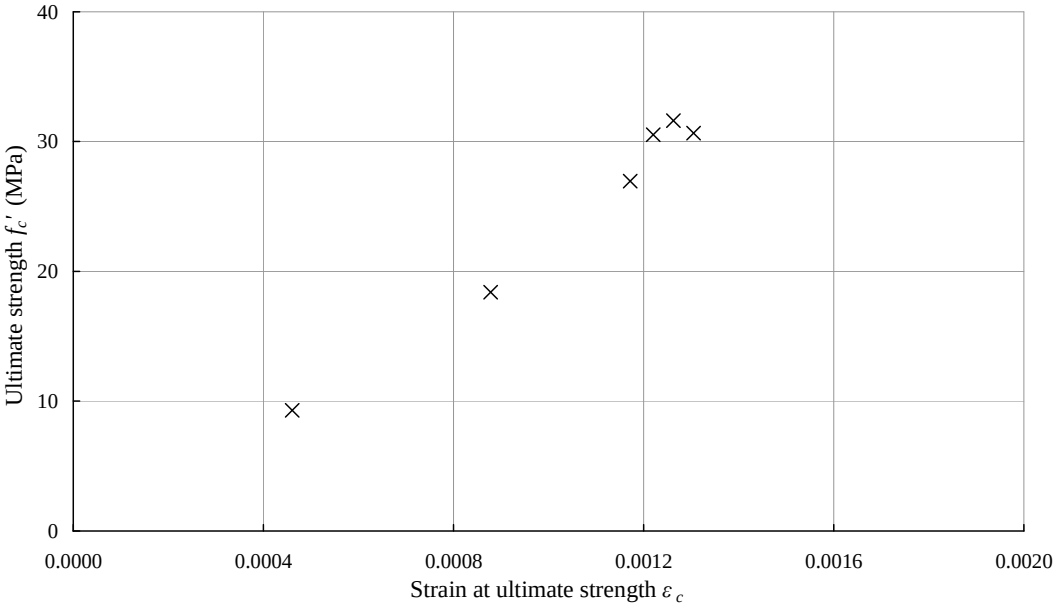

Figure 5.13 Relationship between strain at ultimate strength and ultimate strength for an increasing mean compressive bond strength

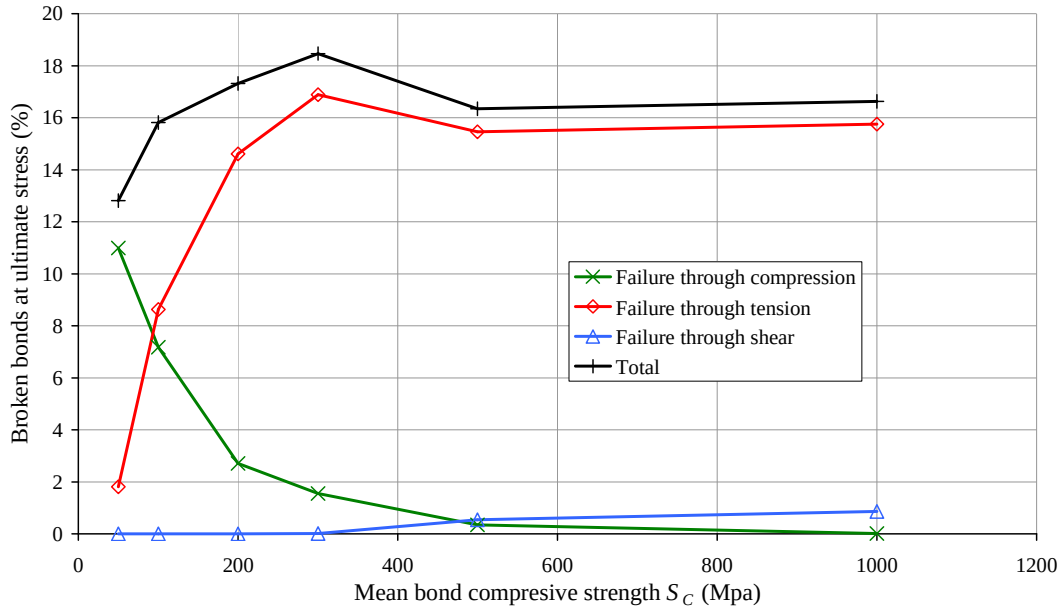

Figure 5.14 Influence of mean bond compressive strength on the failure mode

The reason for the asymptotic relationship between mean bond compressive strength and ultimate strength is because there is a change in the failure mode. At relatively high values of mean bond compressive strength (> 300 MPa) the ratio of bonds failing in tension to compression is of the order of 10. As the mean bond compressive strength is reduced (and the bonds become weaker in compression) compression becomes the dominant failure mode, from Figure 5.14 it can be seen that this change takes place when S_C < 100 MPa. As compression becomes the dominant failure mode the fracture mechanism in the specimen changes from a preferential inclined plane (shear crack), as seen for example in the reference case (Figure 5.15(a) where S_C= 500 MPa) to a thinner horizontal failure crack (Figure 5.15(b)) seen when S_C= 50 MPa. After a thin horizontal crack has formed the particles along the crack are not ejected from the specimen, they are locked in and are able to transfer load. This explains the high relative residual strengths seen in Figure 5.11; this is especially clear when S_C = 50 MPa.

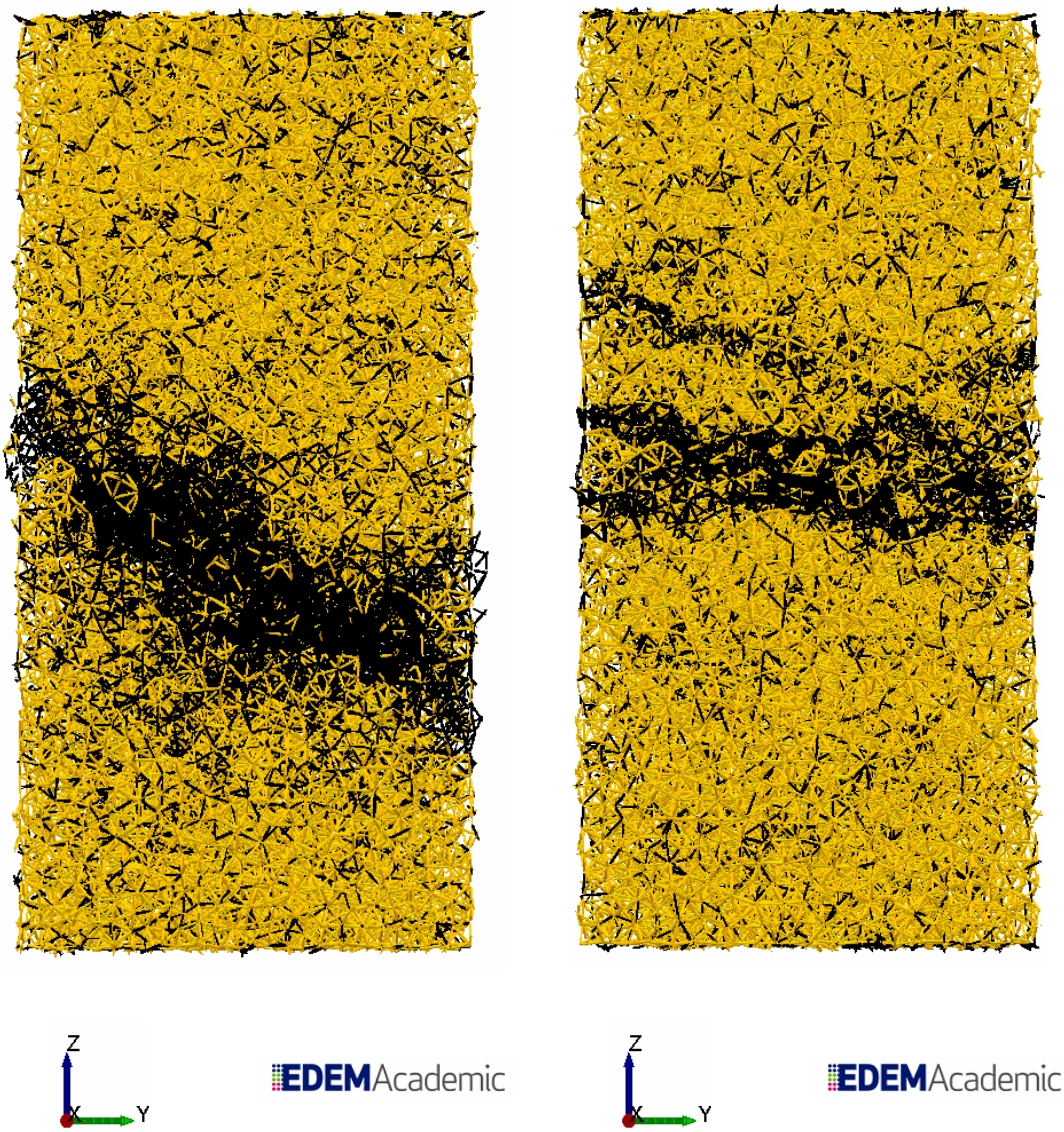

(a) S_C = 500 MPa, bonds tend to fail in tension

(b) S_C = 50 MPa bonds tend to fail in compression

Figure 5.15 Slices through the centre each specimen, intact bonds are shown in yellow and broken bonds are shown in black

It can also be noted that when the mean compressive strength is lower than in the reference case but compressive failure in not dominant, such as when S_C= 200 MPa, the strain at ultimate strength increases with no change in ultimate strength. The

stress-strain response is more ductile. This is due to the fact that there are more bonds failing in compression in the pre peak region.

The mean bond compressive strength has no influence on the bulk stiffness or bulk Poisson's ratio. This is because it has no influence on the stiffness characteristics of the bond fabric.

5.2.4 Influence of the tensile strength of the bond

The tensile strength of the bonds in the specimen follow a Gaussian distribution defined by a mean and standard deviation. The influence of the mean bond tensile strength on the stress-strain response is shown in Figure 5.16; the influence of the standard deviation is discussed in Section 5.2.6.

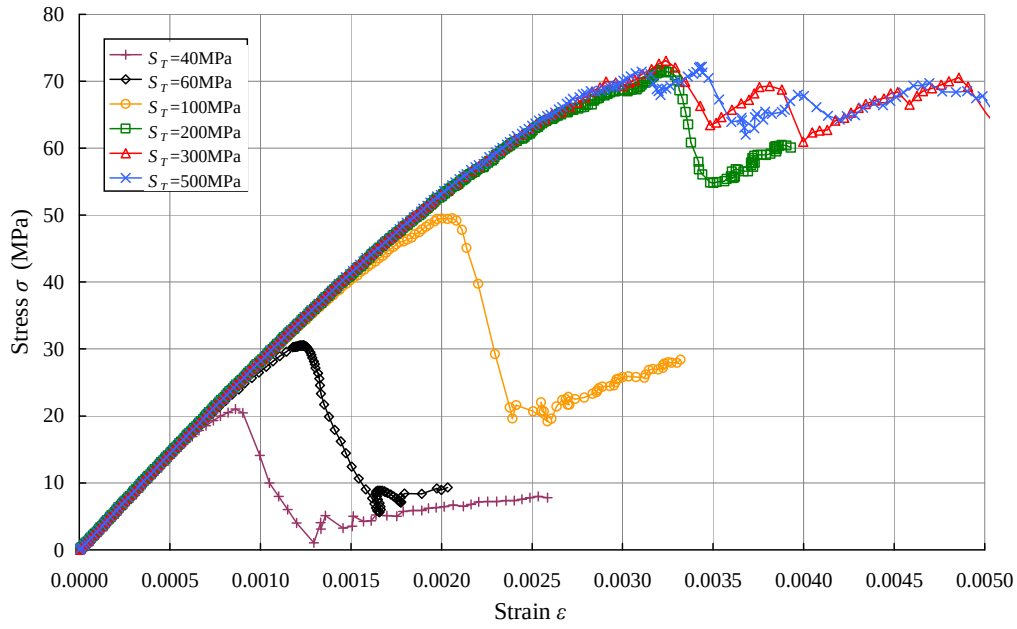

Figure 5.16 Influence of mean tensile strength on the stress-strain response

The mean bond tensile strength has no significant influence on the bulk Poisson's ratio or bulk stiffness. Generally as the mean bond tensile strength increases so does the ultimate strength; as shown in Figure 5.17 this relationship is asymptotic with the ultimate strength f_c' reaching 72 MPa when the mean bond tensile strength S_T

approaches approximately 200 MPa. The increase in strength leads to a complimentary increase in strain at ultimate strength as shown in Figure 5.18. There is also a significant increase in the relative residual strength as the tensile strength increases.

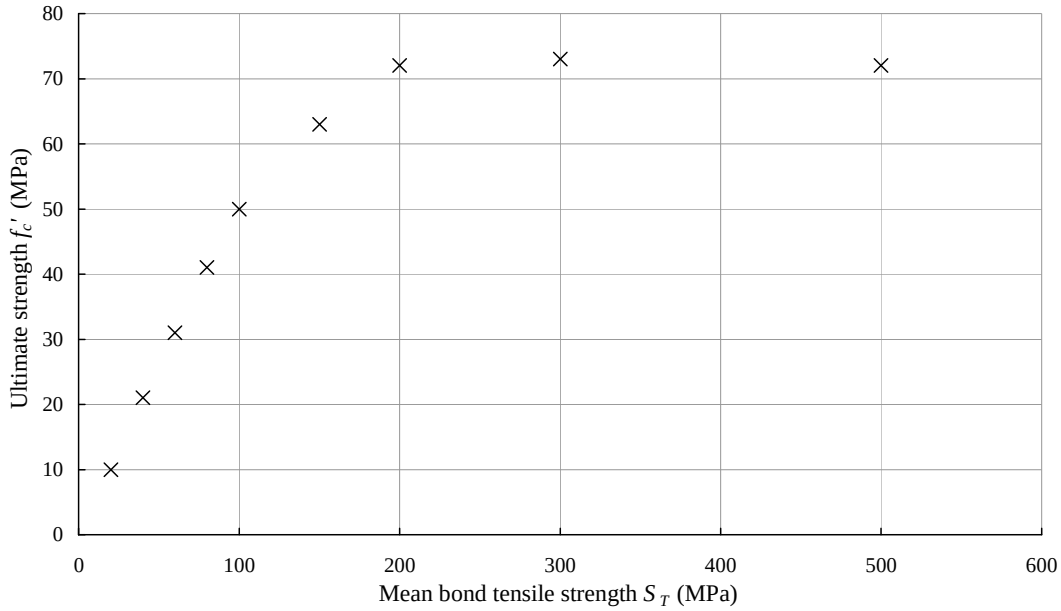

Figure 5.17 Influence of mean bond tensile strength on ultimate strength

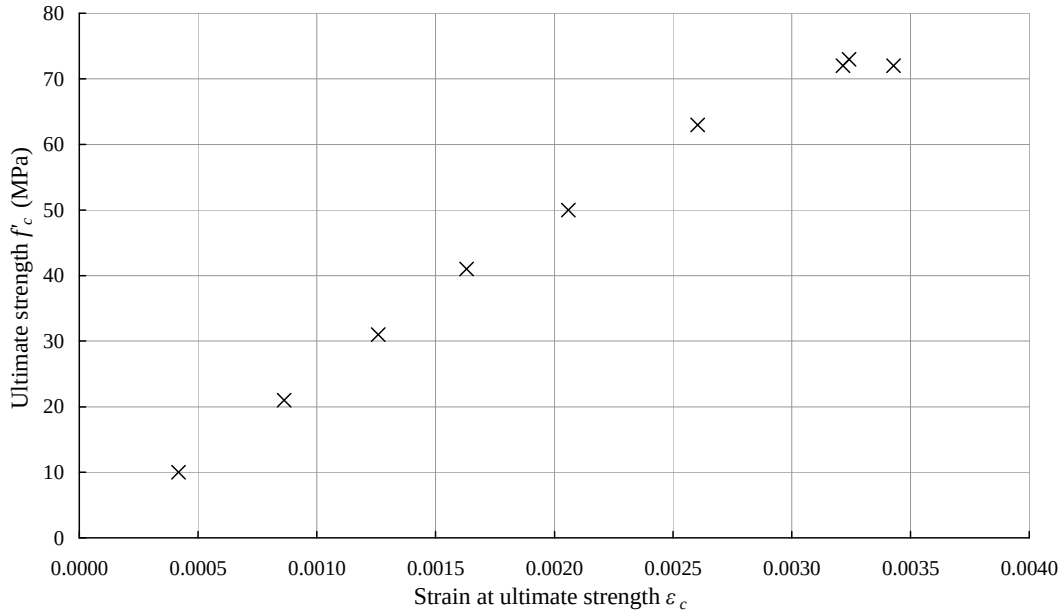

Figure 5.18 Relationship between strain at ultimate strength and ultimate strength

The reason for the asymptotic relationship between mean bond tensile strength and ultimate strength is due to a change in failure mode. At relatively low values of mean bond tensile strength the majority of bonds fail in tension. However, as the mean is increased the number of bonds failing in shear also increases (previous tests not included here showed that shear failure is more dominant than compressive failure) until eventually shear failure dominates; this change over is shown in Figure 5.19.

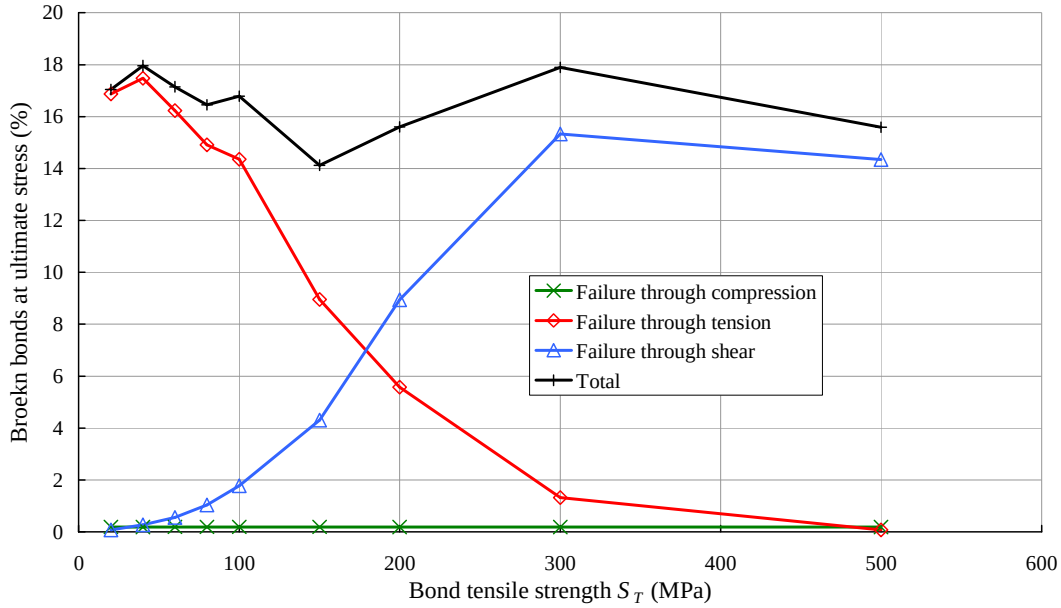

Figure 5.19 Influence of mean bond tensile strength on the type of dominant bond failure

As the failure mode changes from tension-dominant to shear-dominant the ductility of the post peak response is also affected and a different failure pattern develops. It should be remembered that there is friction between the end plates and the specimen providing a degree of confinement at both ends. When tension failure is dominant an inclined plane (shear crack) tends to form. This can be seen in Figure 5.20(a) when S_T = 60 MPa. As shear becomes the dominant failure mode the fracture mechanism in the specimen changes to a thinner horizontal crack as seen in Figure 5.20 (b) when S_T = 300 MPa. This has an influence on the residual strength because particles on a horizontal crack face cannot move past one another as easily as when there is an inclined crack face. The particles at the horizontal crack face are therefore more able to transfer load leading to higher residual strengths.

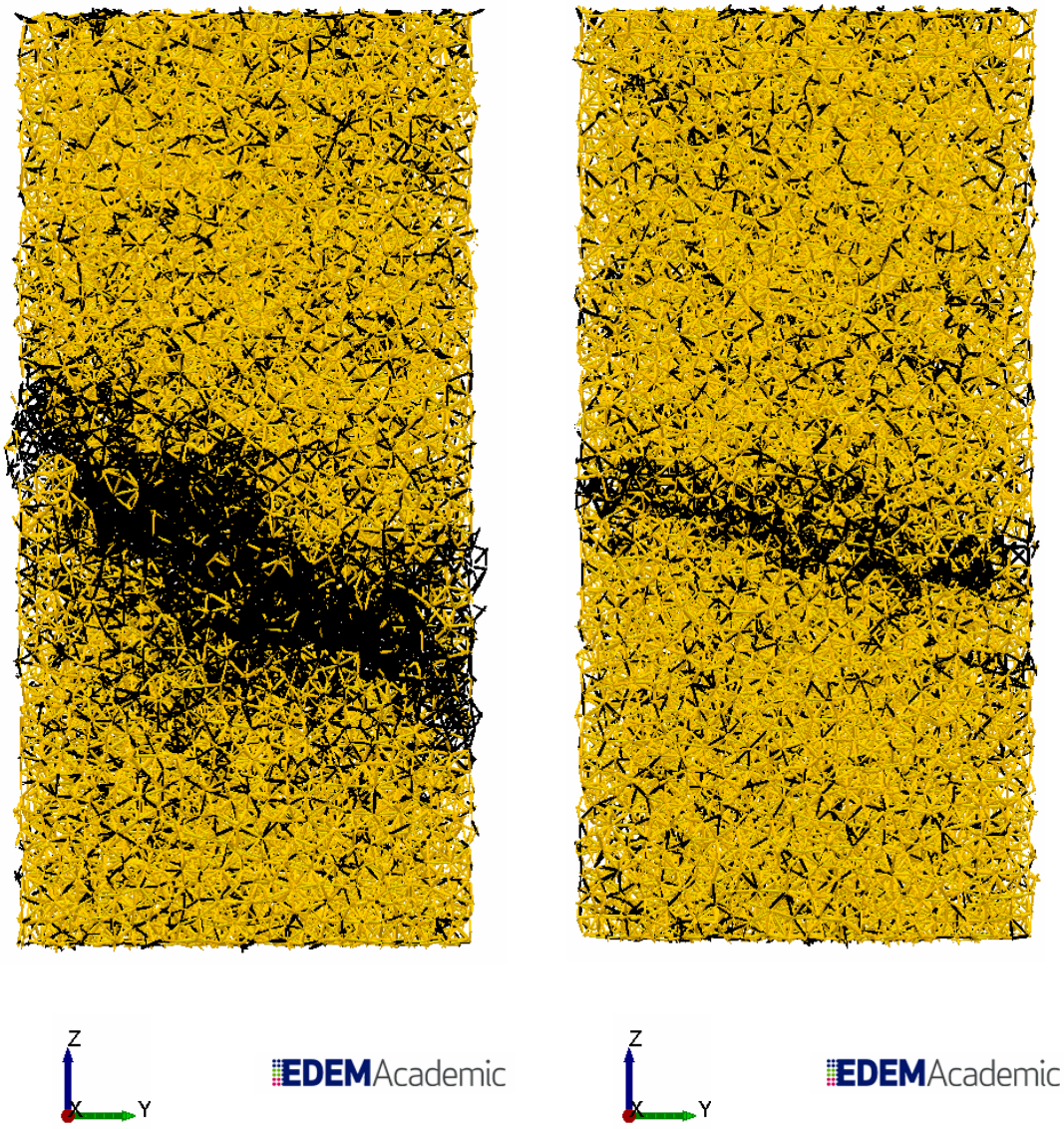

(a) S_T = 60 MPa, bonds tend to fail in tension

(b) S_T = 300 MPa, bonds tend to fail in shear

Figure 5.20 Slices through the centre each specimen, intact bonds are shown in yellow and broken bonds are shown in black

As can be seen in Figure 5.19 the total number of bonds that have broken by the ultimate strength stays roughly the same no matter what the value of mean bond

tensile strength. However Figure 5.21 shows that the eventual number of broken bonds decreases as the mean bond tensile strength increases.

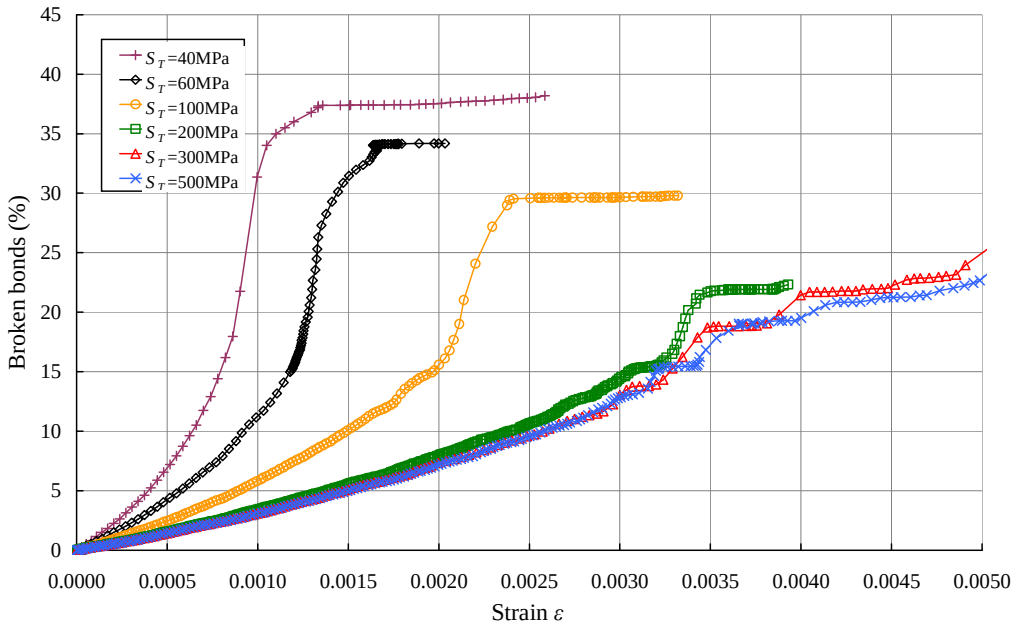

Figure 5.21 Influence of mean bond tensile strength on the breakage of bonds

The full reason and extent of this shift is still under investigation but it is suggested that the change in residual strength is due to a change in failure mode coupled with a strain at failure that is three times greater than that for the reference case.

5.2.5 Influence of the shear strength of the bonds

The shear strengths of the bonds in the specimen follow a Gaussian distribution defined by a mean and standard deviation. The influence of the mean shear strength on the stress-strain response is shown in Figure 5.22; the influence of the standard deviation is discussed in Section 5.2.6 below.

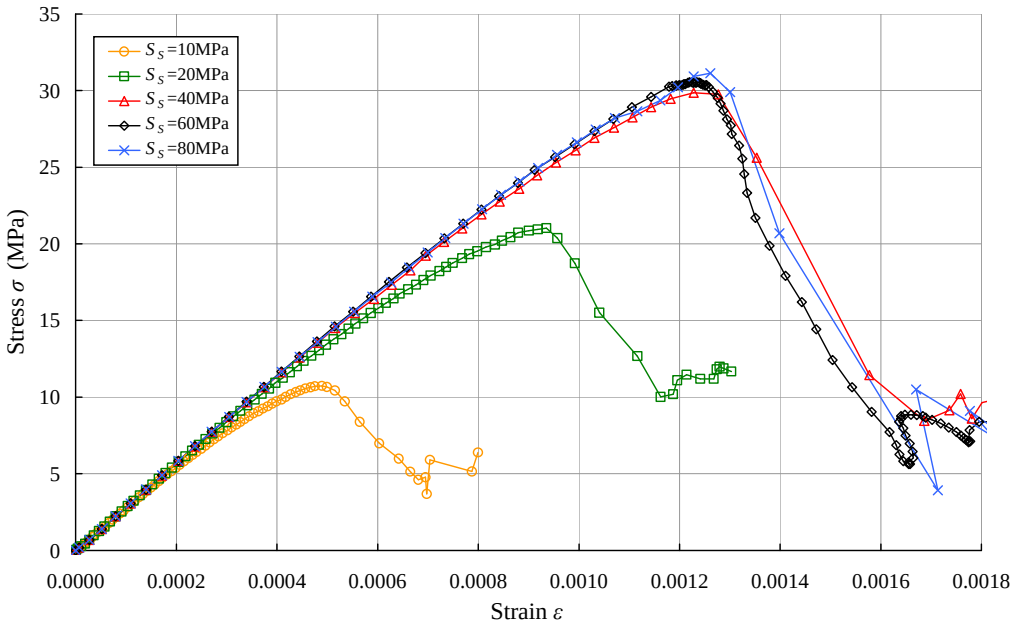

Figure 5.22 Influence of mean bond shear strength on the stress-strain response

The influence of the mean bond shear strength on the stress-strain response is very similar to the influence of mean bond compressive strength i.e. the mean bond shear strength only influences the ultimate strength (and the corresponding strain at failure). As the mean bond shear strength is reduced from approximately 40 MPa there is a decrease in ultimate strength, for values above 40 MPa no increase in ultimate strength is seen, this is shown in Figure 5.23.

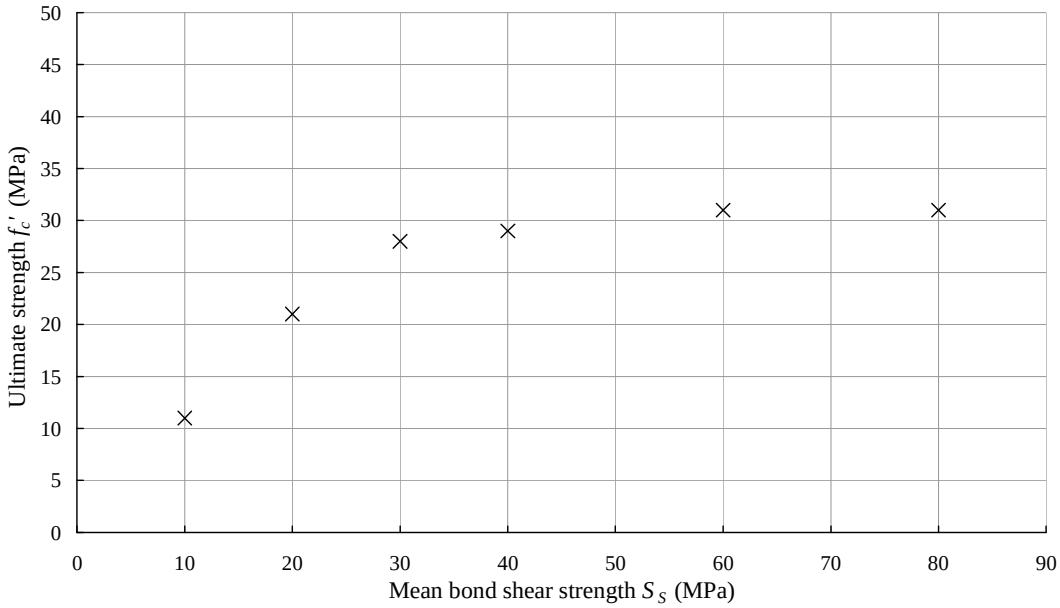

Figure 5.23 Influence of mean bond shear strength on ultimate strength

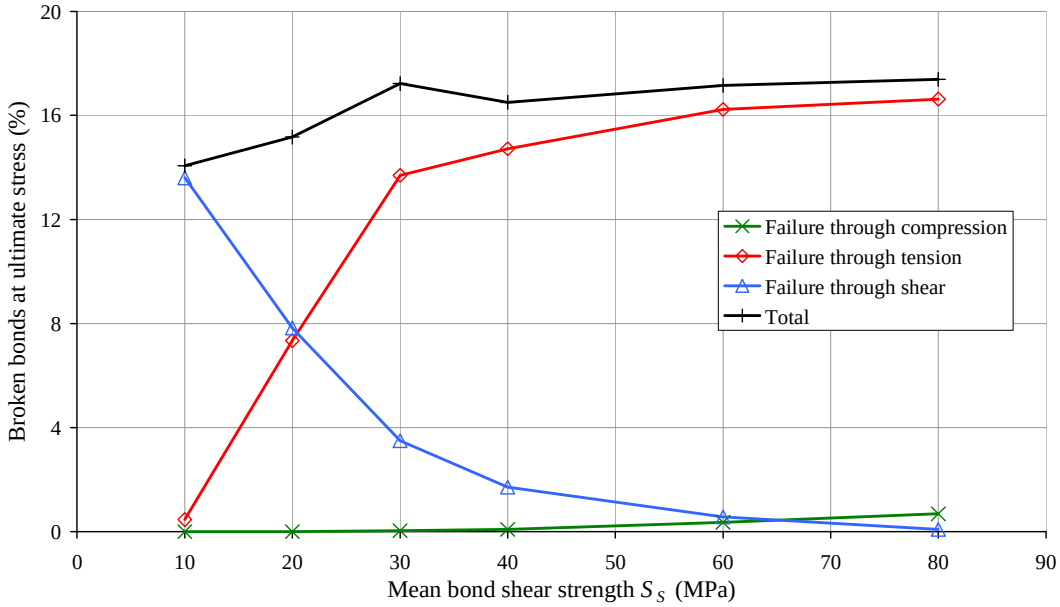

Figure 5.24 Influence of mean bond shear strength on the type of dominant bond failure

The reason for the reduction in ultimate strength seen when the mean bond shear strength is below approximately 40 MPa is because there is a change in the failure mode as can be seen in Figure 5.24. When the mean bond shear strength is approximately 20 MPa shear failure becomes dominant as can be seen in. The two failure modes produce similar but subtly different crack patterns, as shown in Figure 5.25 below, it should be remembered that there is friction between the end plates and the specimen providing a degree of confinement at both ends.

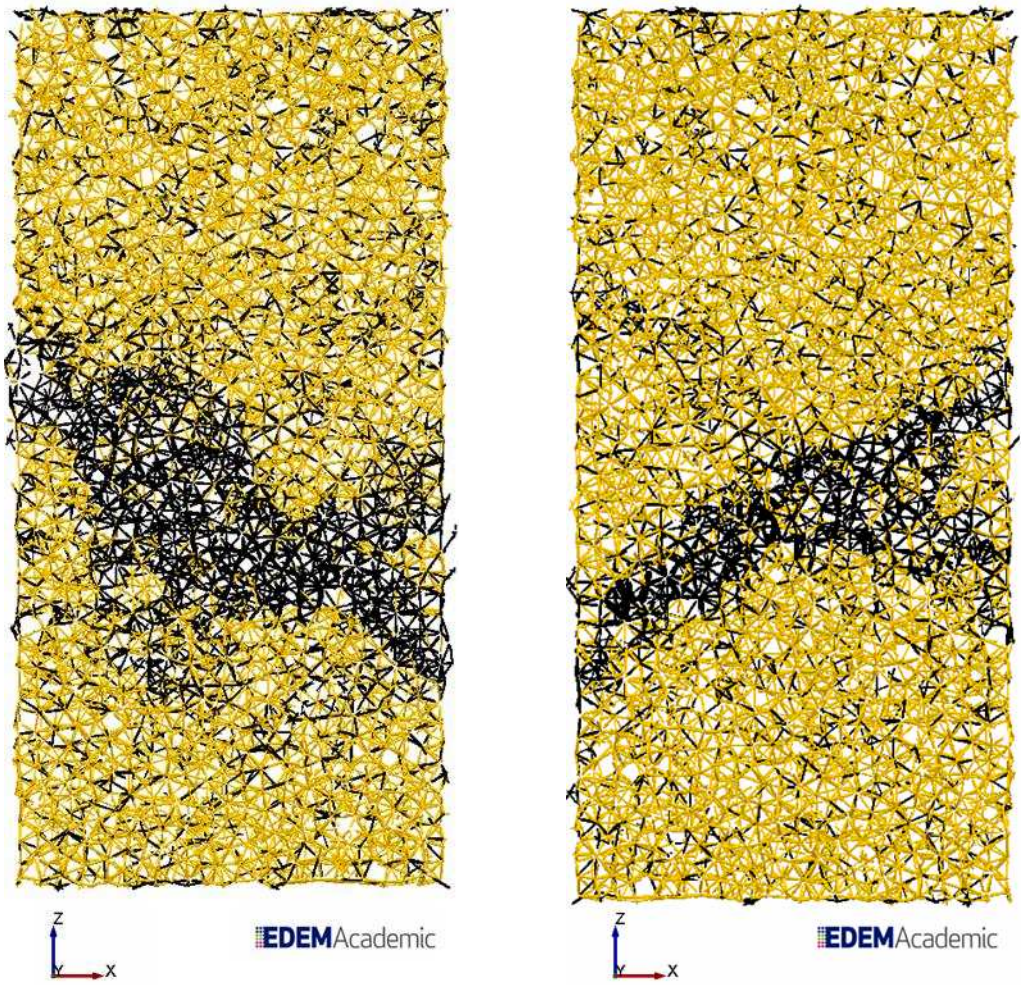

(a) when S_S = 60 MPa (b) when S_S = 20 MPa

Figure 5.25 Influence of mean bond shear strength on the failure mechanism

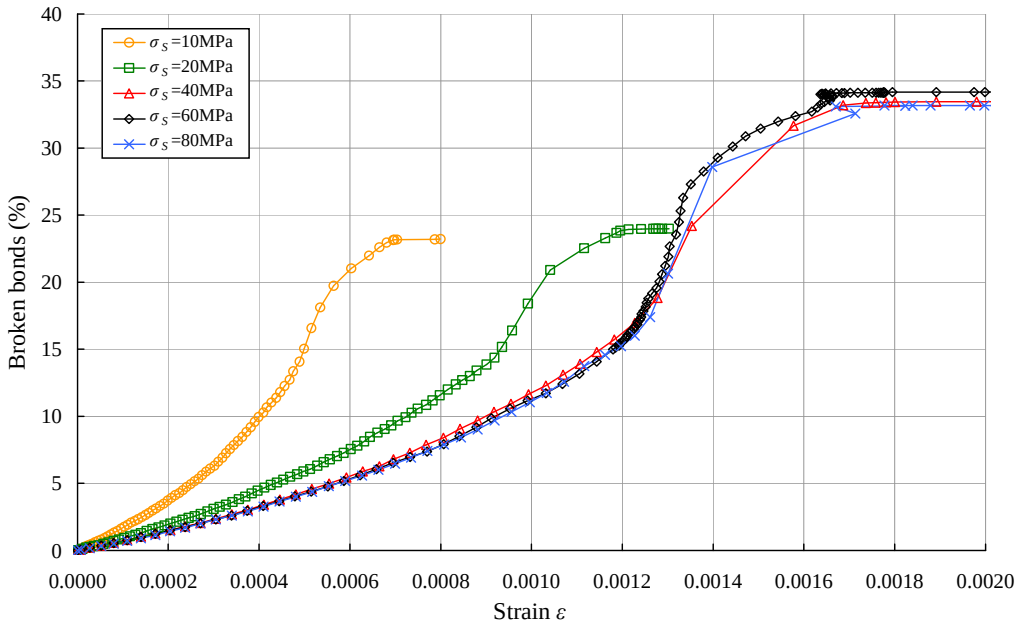

Figure 5.26 Influence of the mean bond shear strength on the progression of broken bonds

When shear has more influence on the failure mode, such as when S_S = 20 MPa, the crack pattern that develops still forms a plane at the same angle as the reference case (when S_S = 60 MPa) approximately 35°, as can be seen in Figure 5.25. When the failure mode is influenced more by shear, the crack that develops is thinner. This is confirmed by looking at the progression of broken bonds in Figure 5.26. Up until the peak load the total number of broken bonds is approximately the same for all simulations, these are the weaker bonds failing. When the failure mode is predominantly tension there is continued bond breakage after the ultimate strength has been reached (the number of bonds broken at failure represents halve of the total number of bonds that fail). When there is a mixture of shear and tension fewer bonds fail after the ultimate strength (the number of bonds broken at failure represents two thirds of the total number of bonds that fail). When shear has a greater influence the secondary crack is more visible, this secondary crack runs at 35° across the specimen too. The mean shear strength has no influence on the stiffness of the bond fabric so there is no change in the bulk stiffness.

5.2.6 Influence of the coefficient of variation of the strength parameters

The compressive, tensile and shear strengths of the bonds follow a truncated normal distribution controlled by a mean and standard deviation. The standard deviation can be calculated as the mean strength multiplied by the coefficient of variation (CoV), which are both used as input parameters for the model. The strength distribution is truncated between zero and double the mean strength. The influence of the coefficient of variation ς on the distribution of compressive strength is shown in Figure 5.27; the distributions for tension and shear are similarly represented.

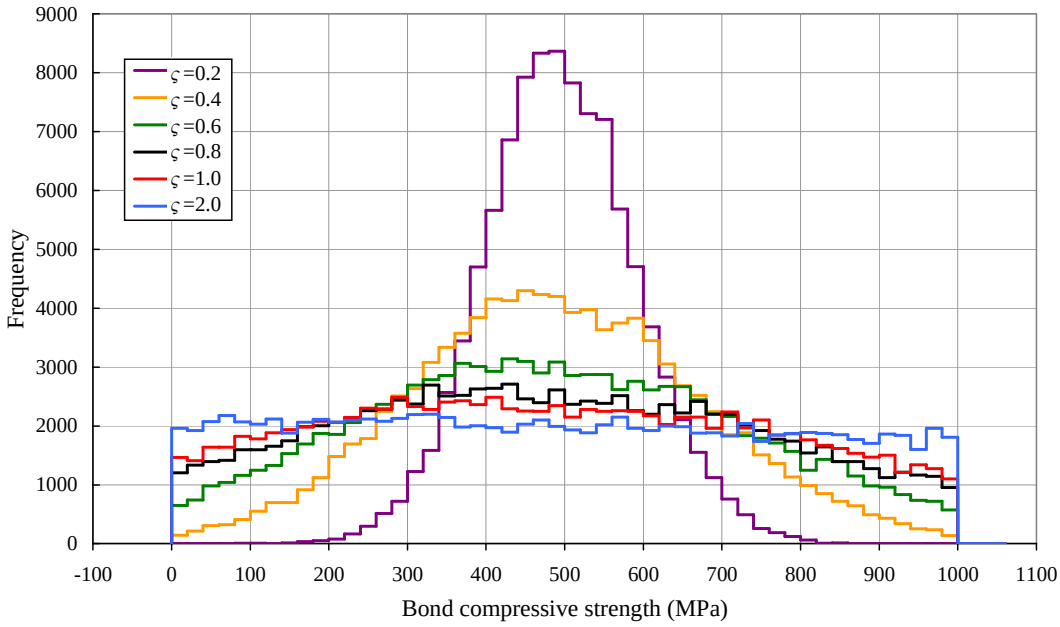

Figure 5.27 Distribution of compressive bond strengths for varying coefficients of variation, in this instance the mean strength is 500MPa – This figure is an expanded version of Figure 3.6

As can be seen in Figure 5.27 as the CoV is increased the strength distribution of bond strength becomes more uniform in nature and the relative impact on the distribution decreases i.e. there is a more significant impact on the distribution when the CoV is increased from 0.2 to 0.4 than when it is increased from 0.8 and 1.0.

To reduce the number of free parameters in the parametric study the CoV for all three strength components (compression, tension and shear) are assumed to be the same. The influence of the coefficient of variation on the stress-strain response is shown in Figure 5.28.

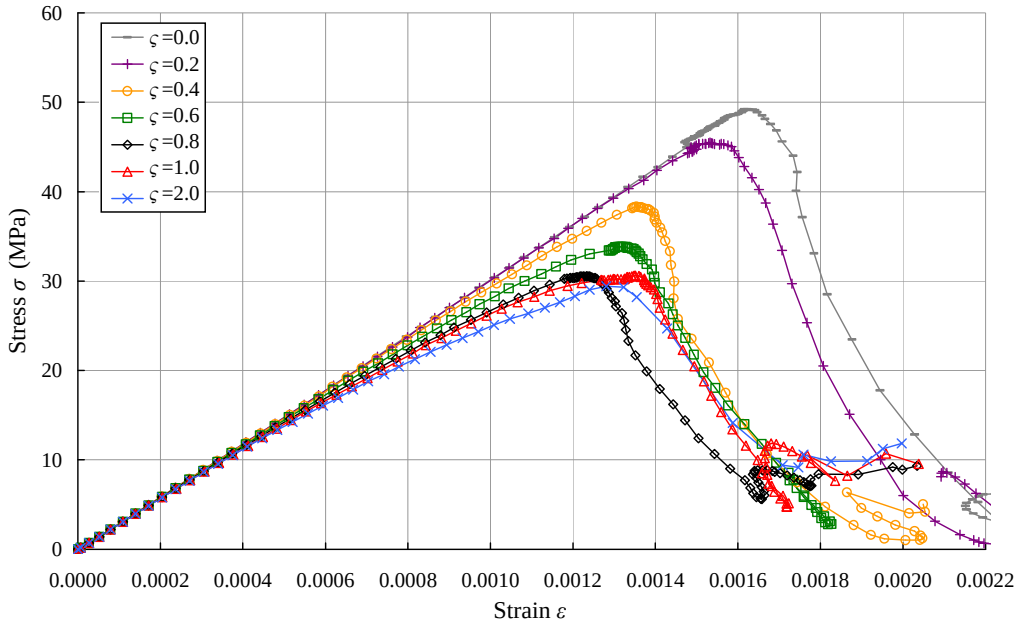

Figure 5.28 Influence of coefficient of strength variation on stress-strain response

As can be seen from Figure 5.28 as the coefficient of variation increases the ultimate strength reduces, this leads to a complimentary reduction in strain at ultimate strength. As the CoV is increased from 0.0 to 2.0 there is only a 2% increase in bulk Poisson's ratio and a 6% reduction in bulk stiffness, these are not significant. However, the loss of stiffness for each simulation does vary, this is highlighted in Figure 5.29 where the data from Figure 5.28 has been normalised against ultimate strength and strain at failure and compared with the Eurocode equation (BS EN 1992-1-1, 2004).

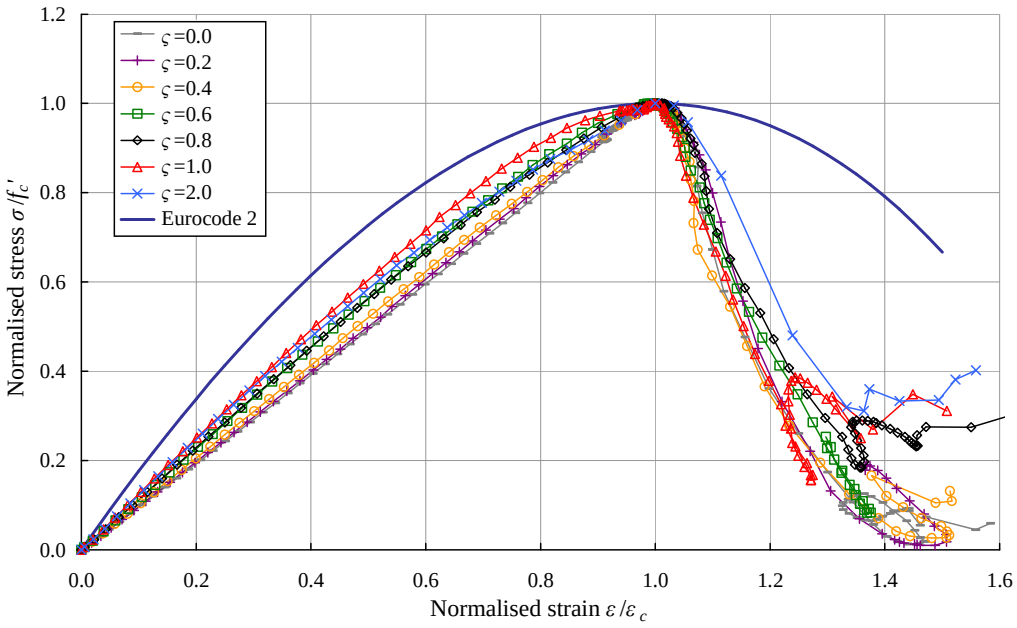

Figure 5.29 Normalised version of Figure 5.28 indicating the different levels of the loss of stiffness

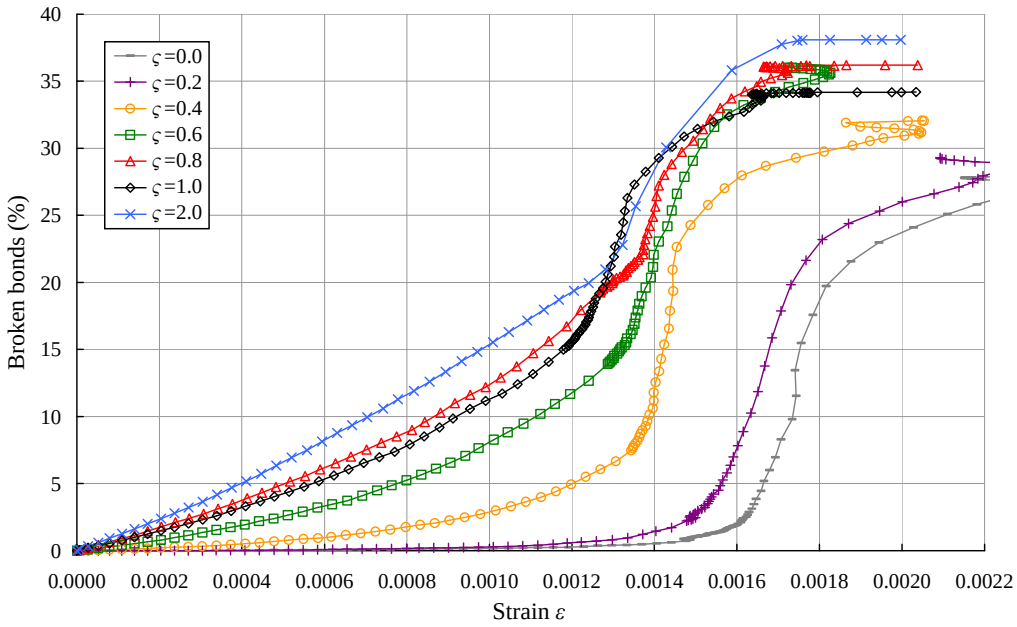

Figure 5.30 Influence of coefficient of variation on the progression of broken bonds

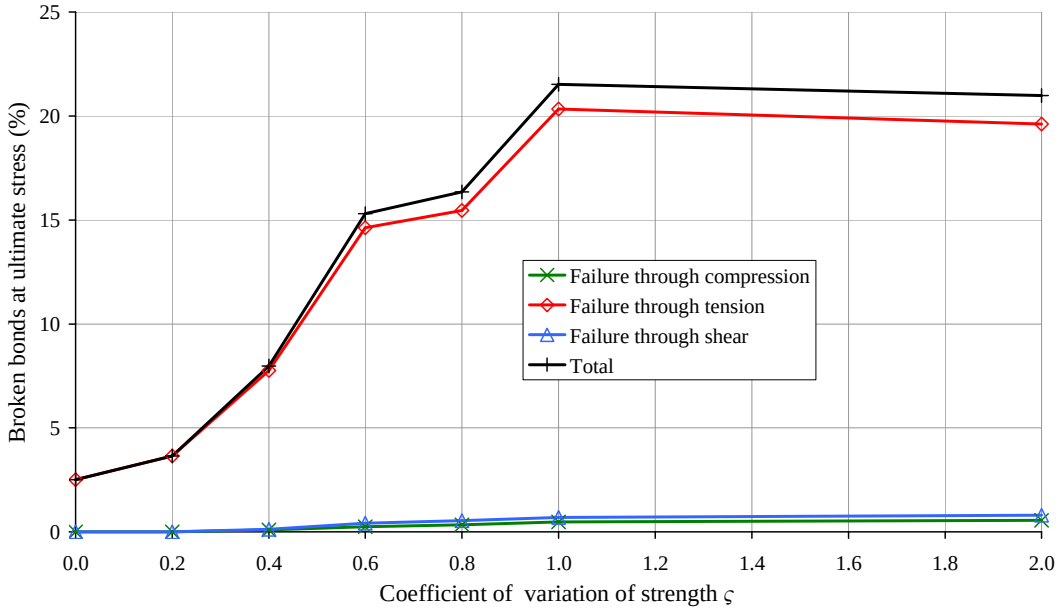

Figure 5.31 Influence of coefficient of variation on the failure mode

The reason for the change in ultimate strength and difference in the rate of loss of stiffness for different coefficient of variations is due to the fact that the higher the value of CoV above unity the more bonds there are with strength less than the mean, this relationship is shown in Figure 5.27. As can be seen from Figure 5.30 and Figure 5.31 the number of broken bonds failing in the pre-peak region is increased as the CoV is increased, from only 2.5% of the total when $\varsigma = 0$ to over 20% when $\varsigma \geq 1$. Although when the coefficient of variation is lower fewer bonds have failed by the ultimate strength, as shown in Figure 5.31, and it can be seen in Figure 5.30 that the total number of bonds failing increases so that there is less difference during post peak behaviour. When bonds break the bond fabric becomes softer and weaker, therefore it follows that those simulations with the most bond breakage in the initial stages of loading are the weakest and have the most loss of stiffness. As can be seen from Figure 5.32, the lower the CoV the fewer broken bonds appear away from the main crack.

From Figure 5.29 it is clear that the loss of bulk stiffness that is seen in real concrete under loading cannot be solely represented using a distribution of bond strengths.

(a) when CoV= 0.0

(b) when CoV= 0.2

(a) when CoV= 1.0

(b) when CoV= 2.0

Figure 5.32 Influence of CoV on the failure pattern

5.2.7 Summary of bonded contact parameters

All of the bonded contact parameters have an influence over one or more of the bulk properties as summarized in Table 5.4. The key bonded contact parameters are the bond Young's modulus, the mean bond tensile strength and shear strength, and the coefficient of variation of bond strength.

Given a value of mean bond compressive strength that is significantly higher than tensile strength i.e. it is not influential in the failure mode, then there is a relationship between the ultimate strength and the mean bond tensile to shear strength ratio, as shown in Figure 5.33.

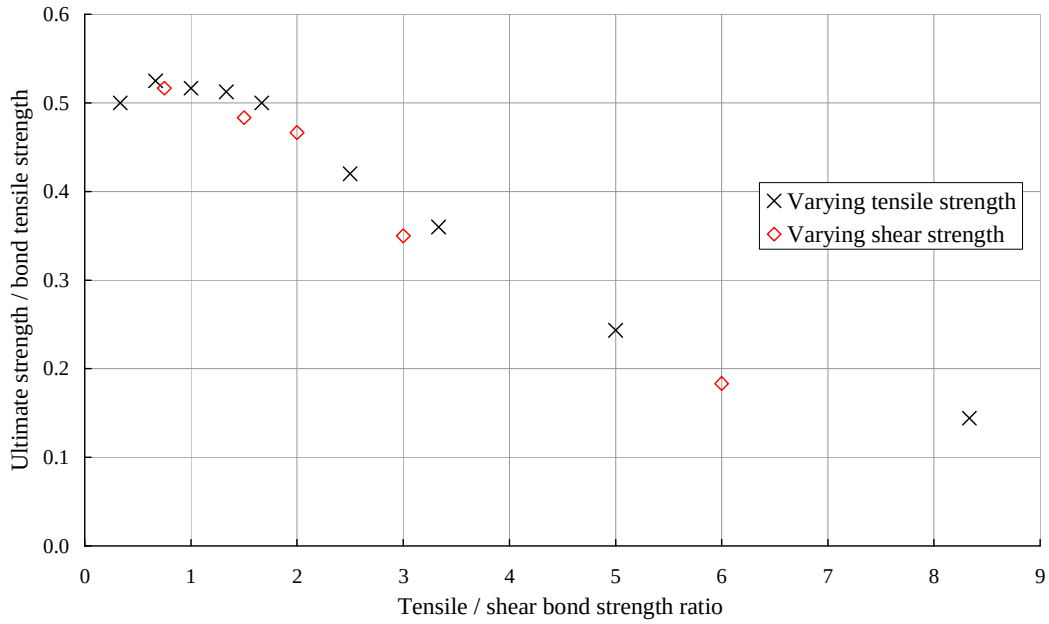

Figure 5.33 Relationship between ultimate strength and mean bond tensile to shear

At the macroscopic scale shear strength is greater than the tensile strength, but not by much. One might expect that a similar relationship exists at the microscopic scale. Therefore, the section of Figure 5.33 that is most relevant to concrete is when the value of tensile bond strength over shear bond strength is less than unity; within this range the value for ultimate strength over bond tensile strength is relatively stable

meaning that if all other factors remain as described in the reference case that the ultimate strength will be approximately double the mean bond tensile strength. The stable nature of this area is because tension failure dominates, while above this area the shear failure becomes more influential. Although Figure 5.33 is only directly relevant when the reference case input parameters are used it does indicate that a stable coefficient for the ratio between ultimate strength and mean bond tensile strength is probable when the mean bond tensile and shear strengths are approximately equal.

Whilst this study focuses on concrete there may be another material where the ratio is not as similar as that of concrete. If, for example, at the microscopic scale, the tensile strength is higher than the shear strength then the area on the curve above a ratio of 1.0 would be of more interest.

The Timoshenko Beam Bonded Contact Model is purely linear elastic which would have produced a purely linear response if there was no breakage of bonds. The results suggest that using CoV alone is not sufficient to mimic the loss of bulk stiffness seen in real concrete behaviour. In the model a reduction in local strength and stiffness occurs suddenly as the bond breaks. A more realistic representation may be to include bond plasticity as a softening function which is linked to local strain, bond stress or damage so that as the force increases the bond gets softer; the implementation of a softening technique is beyond the scope of this thesis.

Table 5.4 Summary of the influence of non-bonded contact parameters on bulk properties and broken bonds

Input parameter	Ultimate strength f_c'	Strain at failure ε_c	Bulk stiffness $E_{c(0.4)}$	Poisson's ratio $\nu_{c(0.4)}$	Total broken bonds
Young's modulus E_b	↓	↓	↑	✗	↓
Poisson's ratio ν_b	↑	↑	✗	✗	✗
Compressive Strength S_C	↑	↑	✗	✗	✓
Tensile Strength S_T	↑	↑	✗	✗	✓
Shear Strength S_S	↑	↑	✗	✗	✓
Coefficient of variation of strength ς	↓	↓	✗	✗	↑

Where ↑, ↓, ✗ and ✓ indicate an increase, decrease, no influence and an influence, respectively to the bulk property resulting from an increase in the input parameter.

5.3 Varying non-bonded contact parameters

For non-bonded contacts between particles or between particle and loading plate the Hertz-Mindlin Contact Model was used. Two of the non-bonded contact parameters that are expected to have the most influence are investigated in this parametric study. They are the stiffness and the static friction.

At the start of each simulation all inter particle contacts are bonded. Non-bonded contacts arise as specimen deformation begins; bonds break and particles are pushed together. Due to the need for deformation and bond breakage to occur before a significant number of non-bonded contacts form the non-bonded input parameters are unlikely to affect the bulk stiffness or Poisson's ratio. However, the ultimate compressive strength, the strain at failure and general stress-strain response, including post peak behaviour, may also be influenced. The ranges of values used in the parametric study are shown in Table 5.5. The particle Young's modulus is chosen as the parameter that defines the non-bonded contact stiffness.

Table 5.5 range of non-bonded contact parameters used

Parameter	Description	Reference	Minimum	Maximum
E_p	Particle Young's modulus (GPa)	40	10	70
μ_{sp}	particle-particle static friction	1.0	0.1	1.0
μ_{sg}	particle-geometry static friction	1.0	0.0	2.0

5.3.1 Influence of the Young's modulus of the particles

The input value for the particle Young's modulus E_p was investigated over a range of 10 GPa to 70 GPa, which is a realistic range for rock. Varying the value of particle Young's modulus was achieved by altering the particle shear modulus and maintaining the Poisson's ratio at $\nu_p = 0.25$. The influence of the particle Young's

modulus on the stress-strain response is show in Figure 5.34, a summary of the computed bulk properties is presented in Table 5.6.

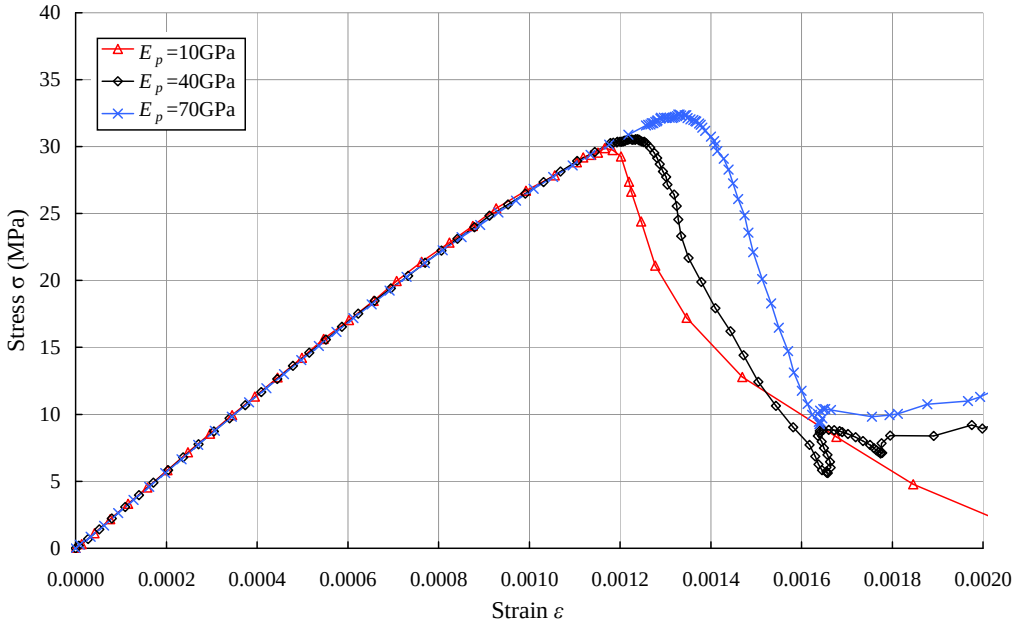

Figure 5.34 Influence of the particle Young's modulus on the stress-strain response

Table 5.6 Summary of computed bulk properties

Particle Young's modulus (GPa) E_p	Ultimate Strength (MPa) f_c'	Strain at failure ε_c	Bulk modulus of elasticity (GPa) $E_{c(0.4)}$	Poisson's ratio $\nu_{c(0.4)}$
10	29.9	0.001166	28.7	0.197
35	30.5	0.001220	28.5	0.196
70	32.4	0.001328	28.3	0.196

From Figure 5.34 and Table 5.6, it can be seen that the particle Young's modulus has no significant influence on the bulk stiffness or Poisson's ratio as expected. However, with an increase in particle Young's modulus, from 10 GPa to 70 GPa

there is an increase in ultimate strength of approximately 8%, with a corresponding increase in strain at ultimate strength. The post peak behaviour also changes slightly, with greater residual strengths predicted the higher the particle Young's modulus.

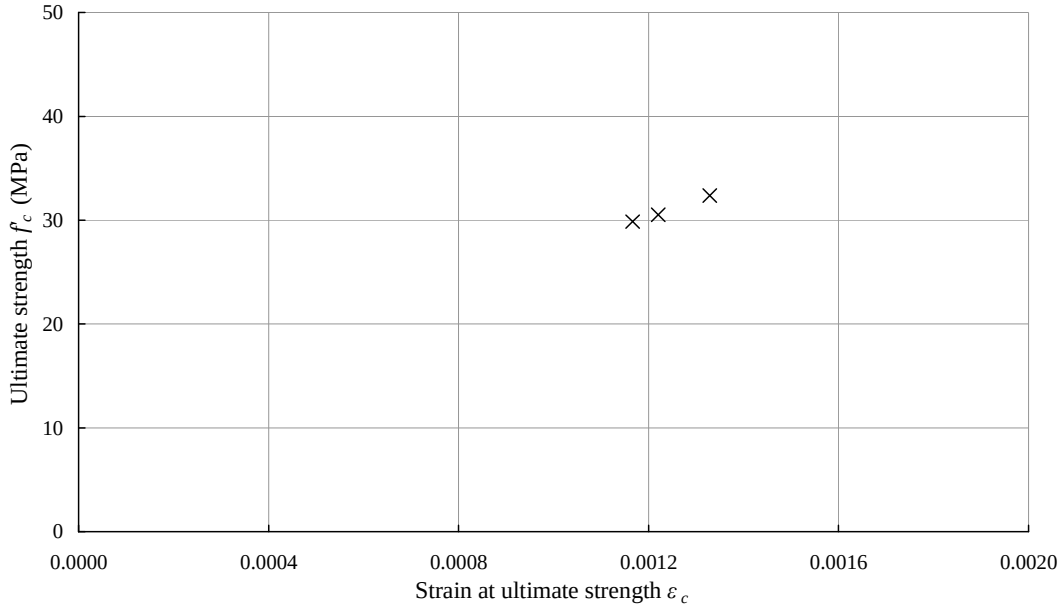

Figure 5.35 Relationship between ultimate strength and strain at ultimate strength for increasing values of particle stiffness

As the particle's Young's modulus increases the stiffness of non-bonded contacts also increases. A higher non-bonded contact stiffness means that for the same bulk deformation instant, a greater load can be transmitted through non-bonded contacts and therefore loading in bonded contacts is reduced. This means that the bonds require larger external load to fail and subsequently the ultimate strength is increased, this is shown in Figure 5.34. The higher ultimate strength also means that the strain at ultimate strength increases; the positive relationship between these two bulk properties is shown in Figure 5.35.

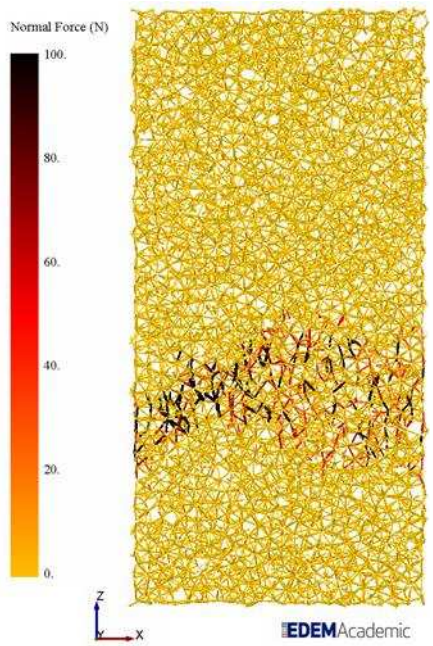

(a) Contact normal force when E_p = 10 GPa

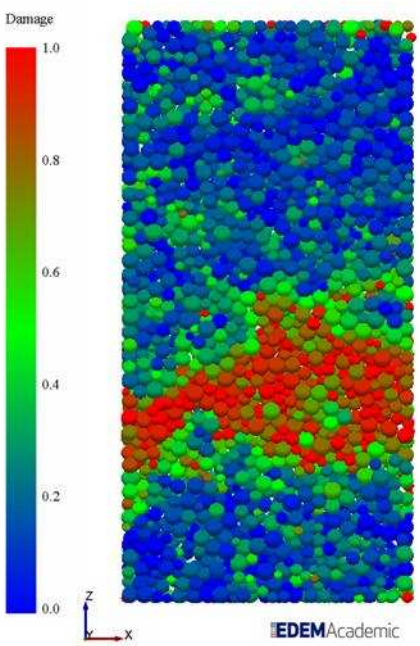

(b) Particle damage when E_p = 10 GPa

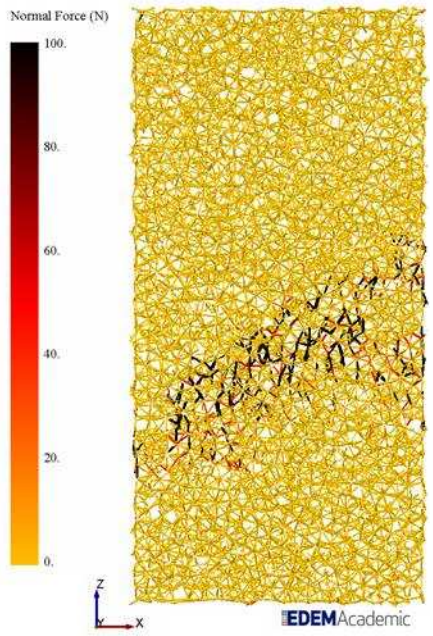

(c) Contact normal force when E_p = 70 GPa

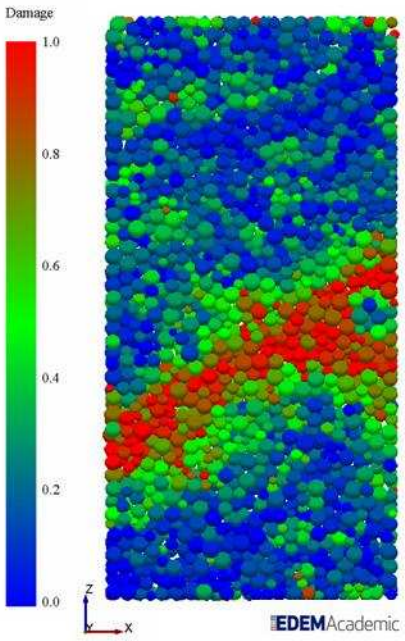

(d) Particle damage when E_p = 70 GPa

Figure 5.36 Slice through the centre of specimens with different particle stiffness, taken after the failure plane has developed

When the particle stiffness increases there is an increase in residual stress, seen after the softening zone. The change in residual strength is not due to a change in failure mode as seen in some cases above, and the failure mode is the same for all three specimens (shear crack). Bonds continue to break as the eventual macroscopic failure plane develops in the softening zone (immediately post-peak). There are no bonded contacts that bridge this plane; however there are non-bonded contacts. This can be seen in Figure 5.36 where the locations of the non-bonded contacts (identified as contacts which have a positive normal force) match up to the highly damaged areas i.e. the areas where there are no bonds. Stiffer non-bonded contacts transmit higher forces and so as loading continues and the loose material has not been expelled from the specimen, there are plenty of non bonded contacts that can transmit load. With the softer particles there is not much force transmission and so there is a larger drop in residual stress.

The particles' Young's modulus has no influence on the Poisson's ratio or bulk stiffness because at the point when these values are determined (at loads of 40% of the ultimate strength) there are very few non-bonded contacts. For the three cases shown in Figure 5.34 the number of bonds that have failed is all around 4% of the total number of bonds. For all three cases at this point there are approximately 200 non-bonded contacts of which only 50 transmit a load of over 1 N; this is a very small number of non-bonded contacts, this is less than 0.1% of the initial number of bonds.

5.3.2 Influence of the particle to particle coefficient of static friction

In the reference case, the inter-particle coefficient of static friction μ_{sp} was set at a value of 1, which is considered high. In the parametric study the inter-particle coefficient of static friction was assessed at two reduced intervals of 0.1 and 0.5. The resulting stress-strain curves are shown in Figure 5.37, a table summarising the computed bulk properties is presented in Table 5.7.

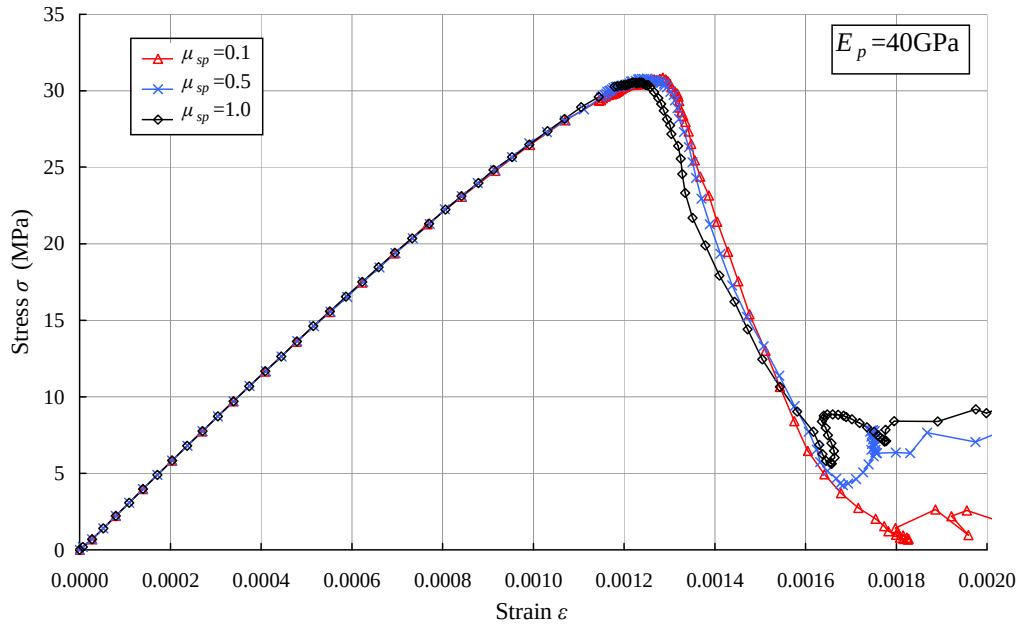

Figure 5.37 Influence of particle-particle static friction on the stress-strain response

Table 5.7 Computed bulk properties for changing particle-particle static friction

Particle-particle static friction	Ultimate Strength (MPa)	Strain at failure	Bulk modulus of elasticity (GPa)	Poisson's ratio
μ_{sp}	f_c'	ε_c	$E_{c(0.4)}$	$\nu_{c(0.4)}$
0.1	30.6	0.001184	28.4	0.194
0.5	30.6	0.001218	28.4	0.196
1.0	30.5	0.001220	28.5	0.196

From Figure 5.37 and Table 5.7 it can be clearly seen that there is no significant change to any of the measured bulk properties. However, there is a slight change in the residual strength. If a recording of residual strength is taken at 0.0018 strain then it can be seen that reducing the coefficient of particle-particle static friction from 1.0 to 0.5 reduces the stress by approximately 25%. A reduction in coefficient of

particle-particle static friction form 0.5 to 0.1 reduces the stress further by approximately 80%.

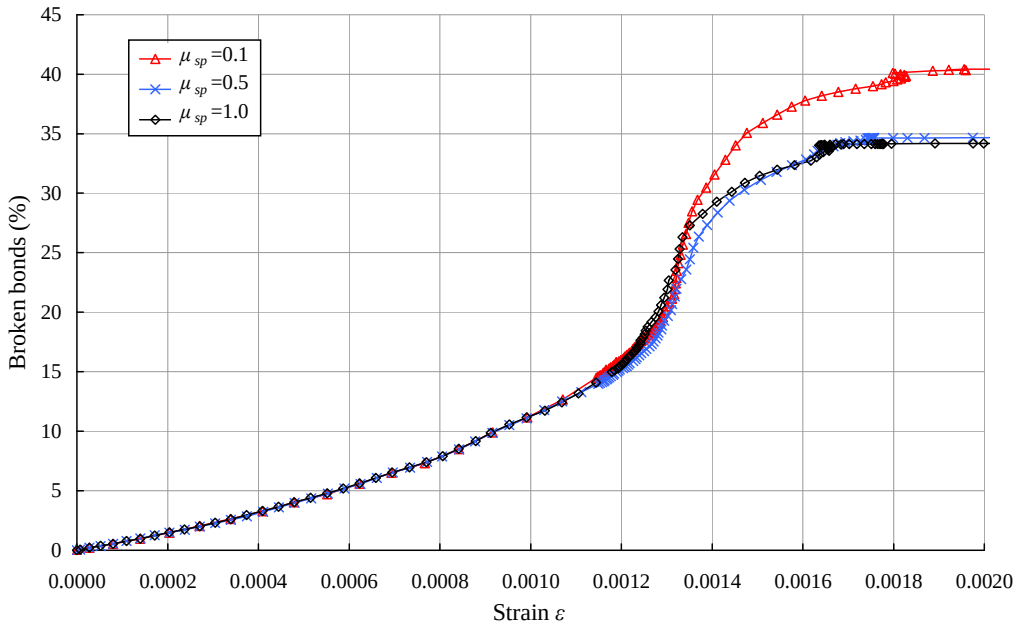

Figure 5.38 Influence of particle-particle static friction on the breakage of bonds

Although the number of bonds broken at the ultimate strength are approximately the same for all values of coefficient of particle-particle static friction (20% of the total number of bonds) the number of bonds that fail in the post peak region differs slightly. As can be seen in Figure 5.38 at the lowest coefficient of particle-particle static friction there is a significant increase in the number of broken bonds (approximately 15% at 0.0018 strain).

It is suggested that the reason for the change in residual strength is because the number of bonds breaking in the immediate post peak region increases when the coefficient of particle-particle static friction is reduced. The friction between particles is lower and so particles are able to slip past each other much easier. After the main failure plane has developed, what is seen is a much larger failure plane with a secondary crack forming a second pyramid. This large failure plane instantly reduces the residual strength, the failure pattern can be seen in Figure 5.39.

In the same way that changing the particles' Young's modulus of elasticity had no effect on the bulk stiffness or bulk Poisson's ratio the inter-particle coefficient of static friction also has no effect and for the same reasons, i.e. there is an insufficient number of non-bonded contacts at the instance that those properties are calculated and so there is minimal influence. As can be seen in Figure 5.37 there is minimal influence on the strength and strain at failure.

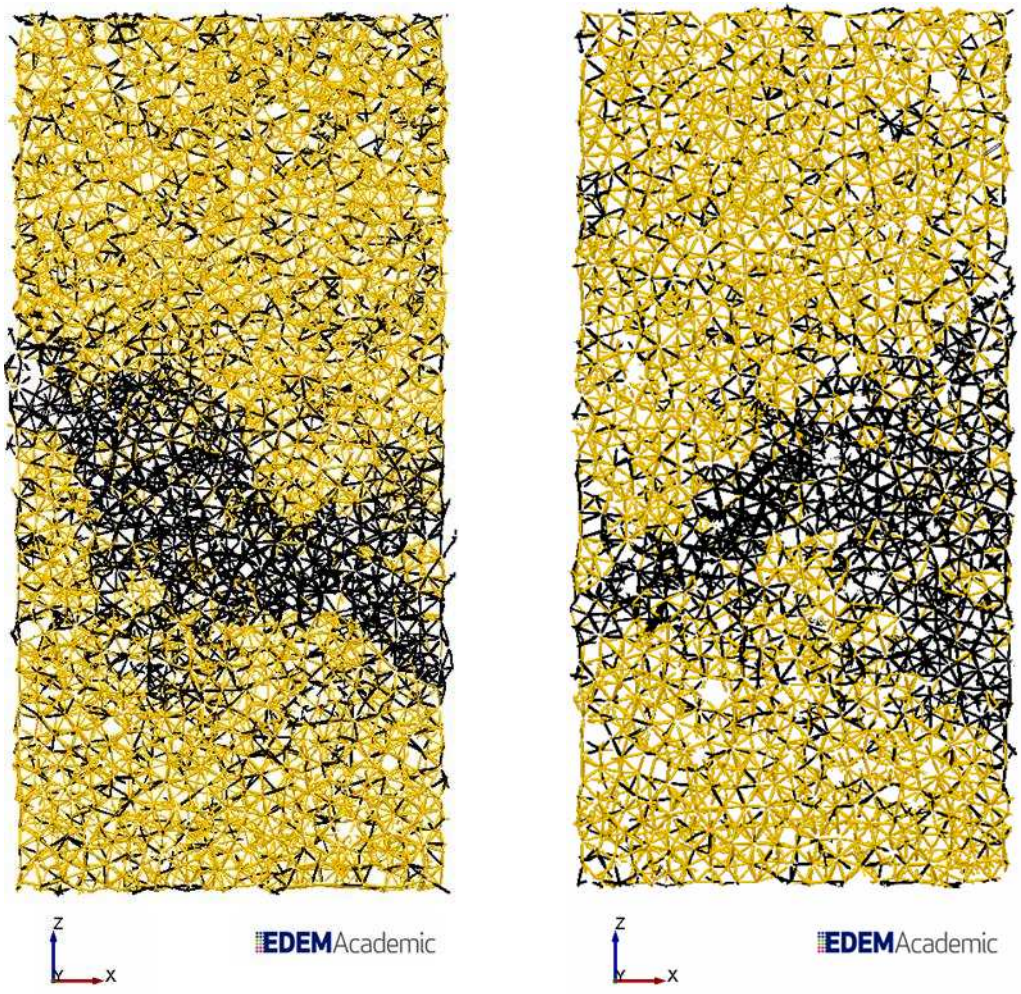

(a) when μ_{sp} = 1.0 (b) when μ_{sp} = 0.1

Figure 5.39 Influence of particle-particle static friction on the failure pattern

5.3.3 Influence of the particle to geometry coefficient of static friction

As mentioned above, in physical tests the friction between specimens and boundaries has an influence over the failure mechanism. In the parametric study the particle-geometry coefficient of static friction μ_{sg} was tested over a range of 0 to 1, with 1 being the value for the reference case simulation. A summary of the computed bulk properties for these simulations is shown in Table 5.8.

Table 5.8 Computed bulk properties for changing particle-geometry static friction

Particle-geometry static friction μ_{sg}	Ultimate Strength (MPa) f_c'	Strain at failure ε_c	Bulk modulus of elasticity (GPa) $E_{c(0.4)}$	Poisson's ratio $\nu_{c(0.4)}$
0.0	28.2	0.00110	28.2	0.187
0.1	31.0	0.00128	28.4	0.193
0.2	30.9	0.00125	28.4	0.194
0.3	30.9	0.00125	28.5	0.194
0.4	31.2	0.00127	28.4	0.196
0.5	31.8	0.00131	28.5	0.198
1.0	30.5	0.001220	28.5	0.196

As can be seen from Table 5.8 there is no significant difference between any of the computed bulk properties when $\mu_{sg} > 0.0$ (the stress-strain response is also near identical for these simulations). The noticeable difference can be seen when there is no static friction at the boundaries, then an approximate 9% drop in ultimate strength is noted and also a 3% fall in the bulk Poisson's ratio.

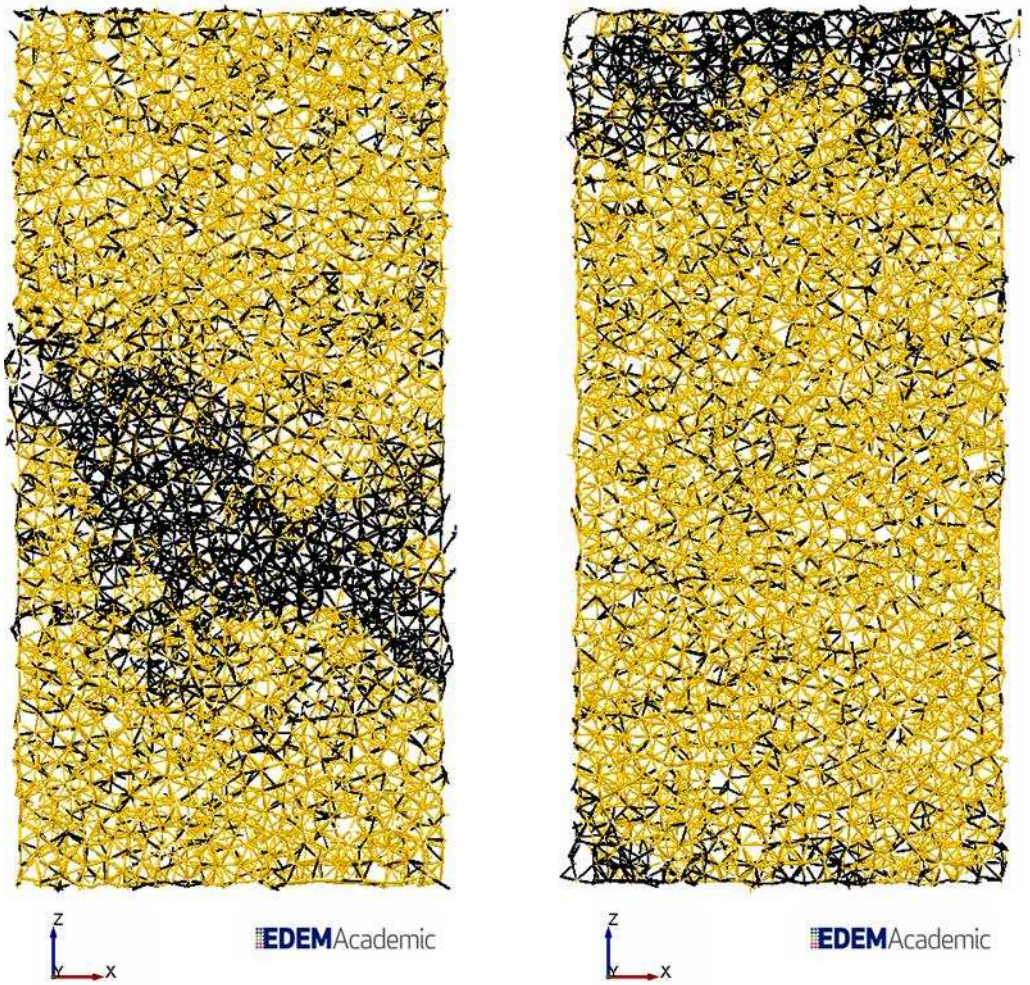

(a) when μ_{sg}=1.0 (b) when μ_{sg}=0.0

Figure 5.40 Influence of particle-geometry static friction on the failure pattern

Upon further investigation it was noted that the reason for the difference in bulk parameters is due to a significant change in the failure pattern. Figure 5.40(a) shows the preferential inclined failure plane (shear crack) noted when μ_{sg}> 0.0. However, when μ_{sg}= 0.0 the failure pattern changes and instead bond breakage (bonds still fail in tension) occurs at the boundaries with the top and bottom loading plate, as can be seen in Figure 5.40(b). The exact mechanism that occurs at this boundary is still under investigation. The recommendation is made that the friction at the boundaries should be greater than zero.

5.3.4 Summary of the influence of non-bonded contact parameters

The influence of the non-bonded contact parameters on the bulk stiffness and bulk Poisson's ratio was seen to be negligible. As mentioned above this is due to the fact that at the point at which these properties are calculated (at 40% of the failure strain) there are very few non-bonded contacts in the main body of the specimen. However around failure and in the post peak region the non-bonded contacts had more influence. The stiffness of the particles influences the ultimate strength and both the particle stiffness and particle-particle static friction have an influence over the post peak behaviour, including the residual strength. The influences of the non-bonded parameters tested on the bulk behaviour are summarized in Table 5.9.

Table 5.9 Summary of the influence of non-bonded contact parameters on bulk properties and broken bonds

Input parameter	Ultimate strength f_c'	Strain at failure ε_c	Bulk stiffness $E_{c(0.4)}$	Poisson's ratio $\nu_{c(0.4)}$	Total broken bonds
Particle Young's modulus E_p	↑	↑	×	×	↑
particle-particle static friction μ_{sp}	×	×	×	×	↑
particle-geometry static friction μ_{sg}	×	×	×	×	×

Where ↑, ↓ and × indicate an increase, decrease or no change respectively to the bulk property resulting from an increase in the input parameter.

5.4 Varying initial bond fabric parameters

The initial bond fabric of the specimen is controlled by the initial particle assembly and two numerical, dimensionless input parameters: the contact radius multiplier η and the bond radius multiplier λ. The influence of these two input parameters on the bulk response is discussed below.

5.4.1 Influence of the contact radius multiplier

If the value of contact radius multiplier η is set above 1 then the contact search radius of each particle is extended past its own physical radius; in this case particles which are not in physical contact may become eligible for bonding. For a given particle assembly the higher the contact radius multiplier is set the more bonds are formed, as shown in Figure 5.41. In this parametric study the value of η was investigated at values of 1.025, 1.05, 1.1, 1.3 and compared to the reference case (where η = 1.2). Although higher values are permissible this study limits bonds to nearest neighbours where possible.

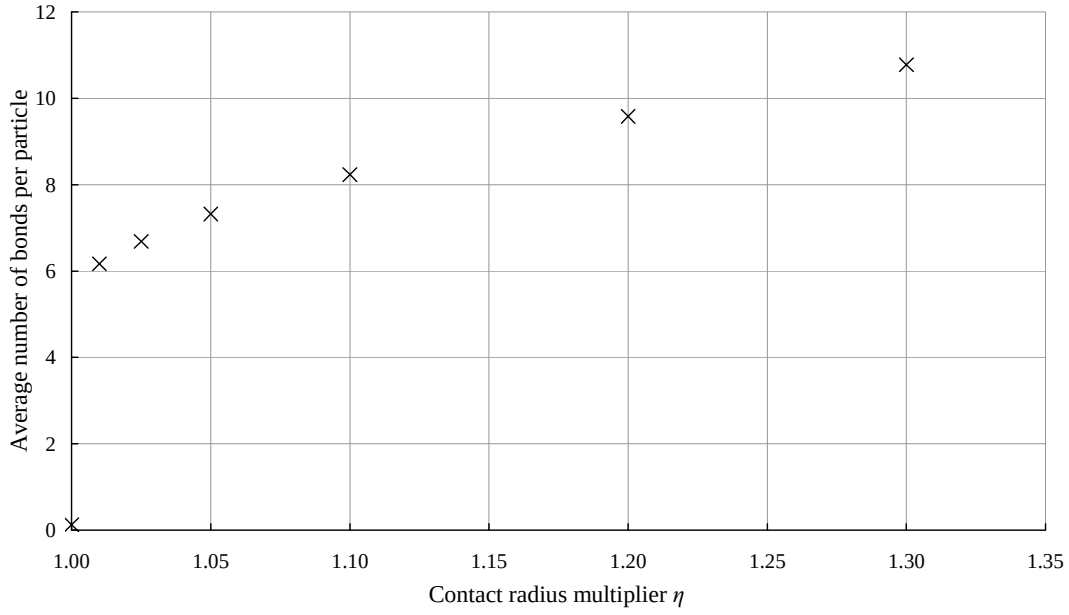

Figure 5.41 Influence of contact radius multiplier on number of bonds per particle

The influence of the contact radius multiplier on the stress-strain response is shown in Figure 5.42. The same stress strain response has been normalised against failure strain and ultimate strength in Figure 5.43.

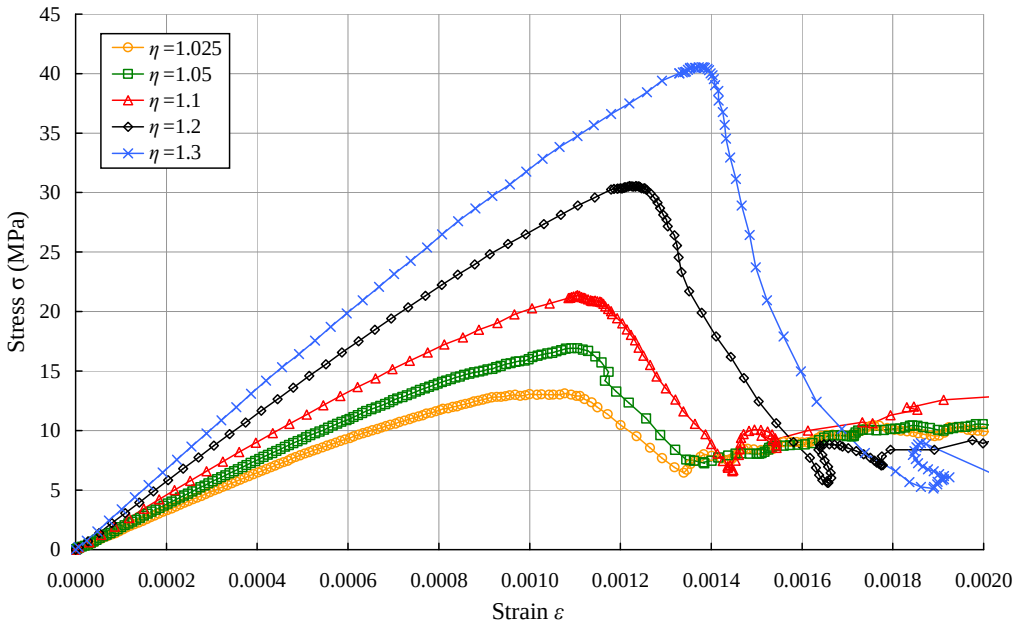

Figure 5.42 Influence of the contact radius multiplier η on the stress-strain response

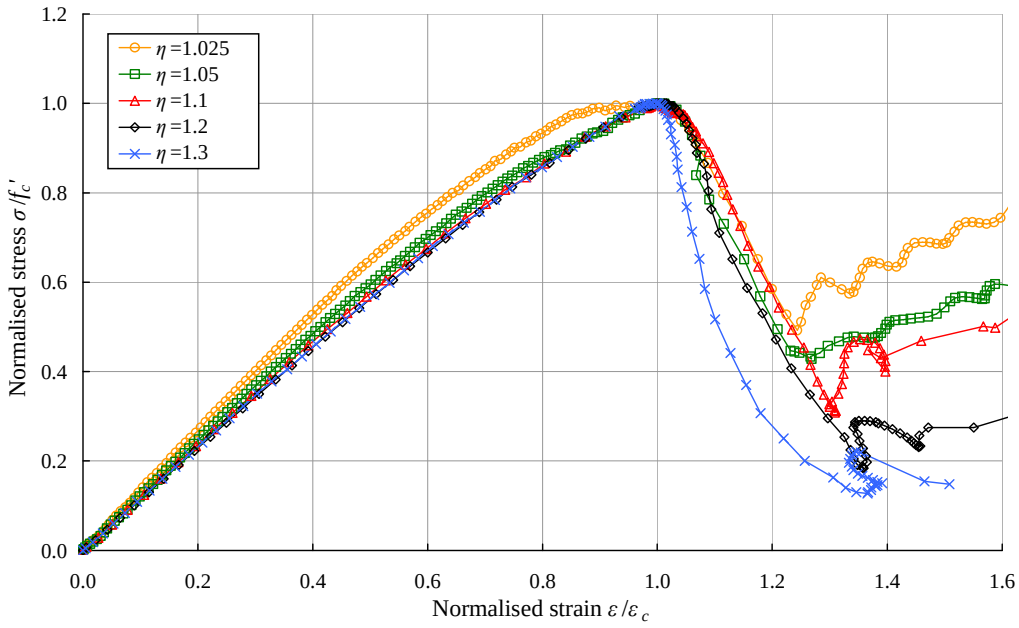

Figure 5.43 Normalised version of Figure 5.42

As can be seen in Figure 5.42, the contact radius multiplier has a significant influence on the stress-strain response. As the contact radius multiplier increases so does the bulk stiffness, the ultimate strength and the strain at ultimate strength. As can be seen in Figure 5.43 the lower the contact radius multiplier the more ductile the response. Figure 5.42 also shows that no matter the contact radius multiplier the residual strength is always approximately 10 MPa. It should be noted that no significant difference in Poisson's ratio was seen (with values computed in the range 0.190 to 0.193).

The post peak residual strength remains largely unchanged by the contact radius multiplier, it is suggested that this is because the residual strength is dominated by the failure mode as shown in the sections above, when the tension failure dominates then the residual strength seems to be set by factors such as the static friction an particle stiffness.

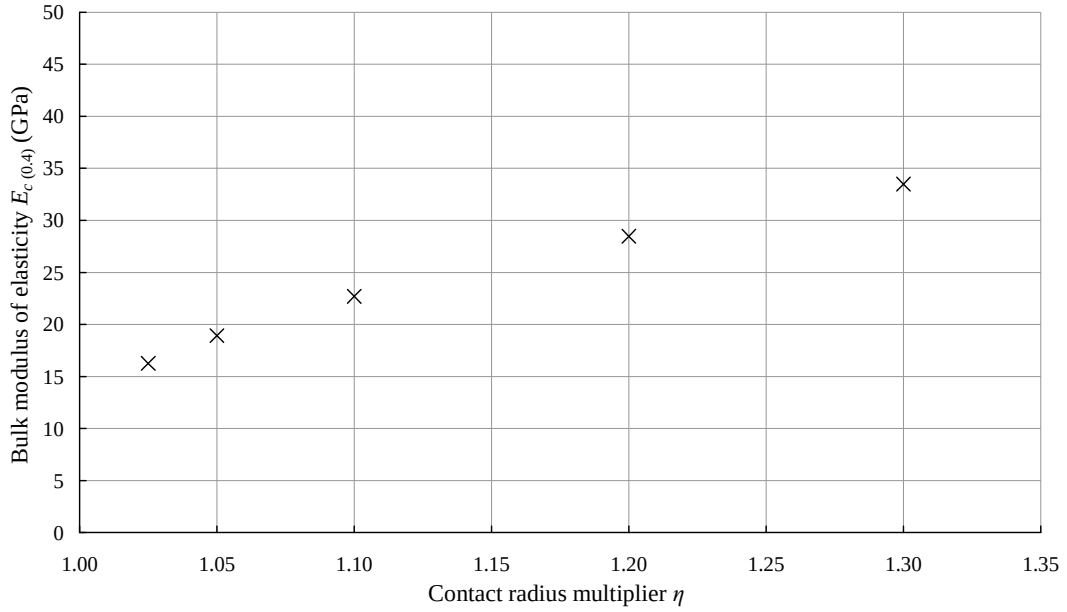

Figure 5.44 Influence of contact radius multiplier on the bulk modulus of elasticity

As can be seen in Figure 5.44 there is a strong positive relationship between the contact radius multiplier and the bulk stiffness. This is simply due to the fact that increasing the contact radius multiplier leads to a greater number of bonds in the initial fabric (as shown in Figure 5.41) meaning the overall bond fabric is stiffer. The relationship between contact radius multiplier and bulk stiffness is non-linear because the relationship between contact radius multiplier and the average number of bonds formed per particle is non-linear.

It should be noted that there is not a reduction in the strain at failure when there is an increase in the bulk stiffness as was seen when the bonds stiffness was increased. This is because there is also a significant increase in the ultimate strength which means a higher strain is required before failure, this is described in more detail below.

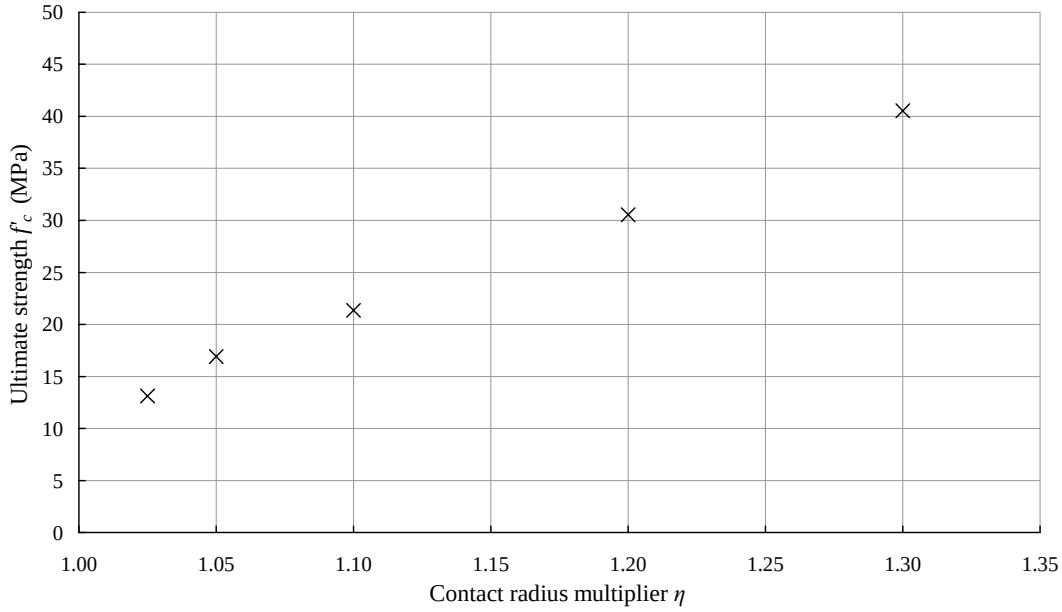

Figure 5.45 Influence of contact radius multiplier on ultimate strength

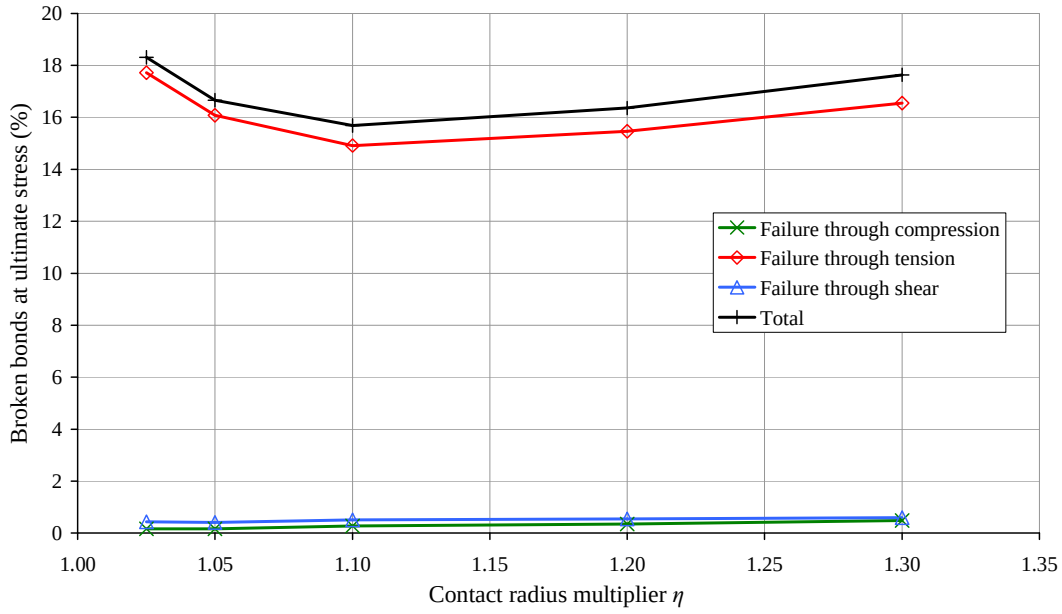

Figure 5.46 Influence of contact radius multiplier on the percentage of broken bonds at failure

As can be seen from Figure 5.45 there is a clear positive relation between contact radius multiplier and ultimate strength. This is because the more bonds that are included in the initial bond fabric the greater its total load carrying capacity and so the lower the force in each individual bond at any given loading instant. This means that a greater external load is required to cause failure in the specimen, although percentage-wise there is no additional breakage of bonds required (as shown in Figure 5.46). Like bulk stiffness the relationship between contact radius multiplier and ultimate strength is non-linear.

As mentioned above the relationships between the contact radius multiplier and both the ultimate strength and bulk stiffness are non linear because the relationship between contact radius multiplier and number of bonded contacts is also non-linear. However, the bulk stiffness can be plotted against the ultimate strength as shown in Figure 5.47.

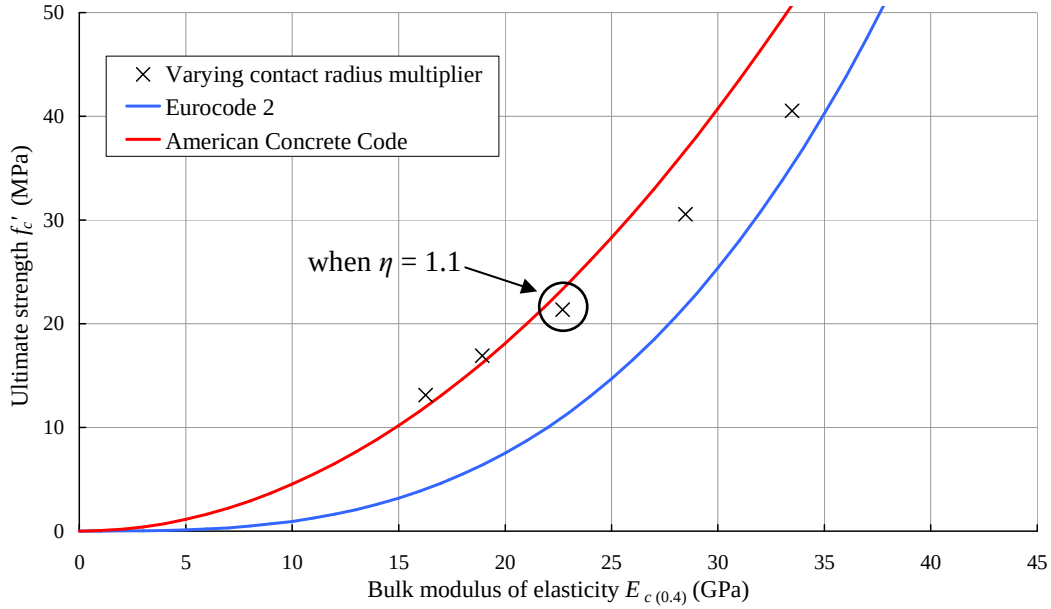

Figure 5.47 Relationship between bulk stiffness and strength for various contact radius multipliers

The relationship between bulk stiffness and ultimate strength has been compared with the empirical relationships provided by both the Eurocode (Bamforth et al., 2007) – which is a repetition of Equation (4.5) in Chapter 4 – and American Concrete Code ACI (Mostofinejad and Nozhatim, 2005).

$$E_{c(0.4)} = 22000\sqrt[3]{(f_c'/10)} \quad \text{(Eurocode2)} \tag{5.2}$$

$$E_{c(0.4)} = 4700\sqrt{f_c'} \quad \text{(ACI)} \tag{5.3}$$

As can be seen in Figure 5.47 the DEM prediction is of the right order as both of the design equations. It is suggested that a contact radius multiplier of 1.1 may make the model more closely mimic real concrete behaviour. This is in part due to the fact that a slightly more ductile response is noted when using a contact radius multiplier of 1.1.

5.4.2 Influence of the bond radius multiplier

The bond radius multiplier λ directly influences the radius of each bond (as described in Chapter 3). Although bonds do not occupy physical space in the specimen a high value of bond radius multiplier may mean that the theoretical volume occupied by the bonds exceeded the total volume of the specimen. To determine a theoretical maximum bond radius multiplier the maximum cross sectional area of a bond is equated to the equivalent local area of the specimen as described in Figure 5.48.

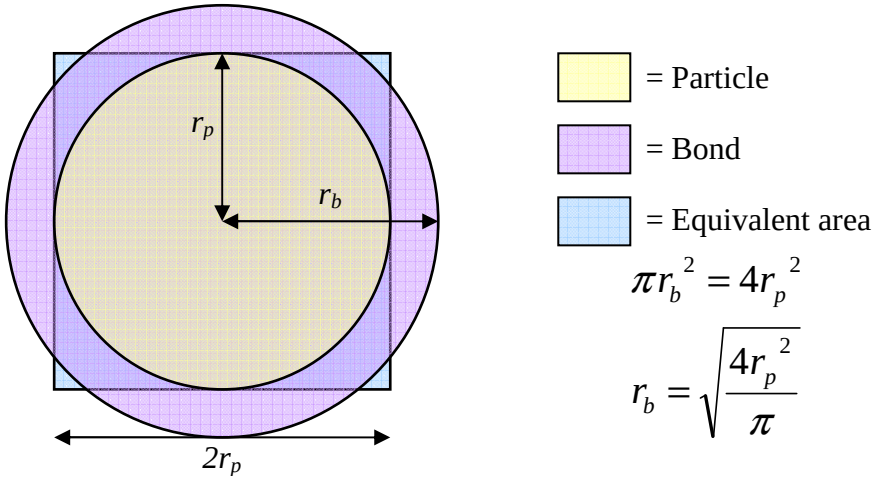

Figure 5.48 Equivalent cross sections of a bonded contact

The maximum theoretical bond radius multiplier $\lambda_{\max}$ can therefore be determined as:

$$\lambda_{\max} = \frac{r_b}{r_p} = \sqrt{\frac{4}{\pi}} = 1.128 \qquad (5.4)$$

where r_p is the radius of a particle and r_b is the radius of a bond. It should be noted that this is just a guideline and in fact the bond radius multiplier will be examined at a value of 1.2 to better understand the effects of the parameter.

As the same initial particle packing and contact radius multiplier are used the length and number of bonds in each simulation will remain the same. However, with an increase in bond radius multiplier the slenderness of each bond is reduced. The predicted stress-strain response is shown in Figure 5.49, and a summary of the computed bulk properties is shown in Table 5.10.

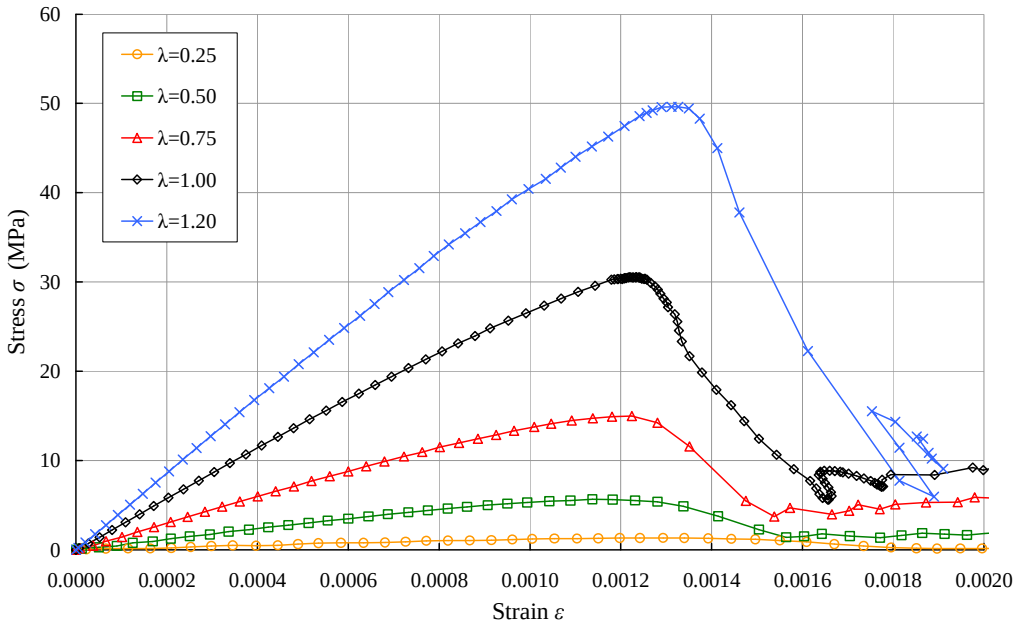

Figure 5.49 Influence of the bond radius multiplier on the stress-strain response

Table 5.10 Computed bulk properties for changing bond radius multiplier

Bond radius multiplier λ	Ultimate Strength (MPa) f_c'	Strain at failure ε_c	Bulk modulus of elasticity (GPa) $E_{c(0.4)}$	Poisson's ratio $\nu_{c(0.4)}$
0.25	1.3	0.00129	1.2	0.290
0.50	5.6	0.00114	5.9	0.237
0.75	15.0	0.00122	14.9	0.214
1.00	30.5	0.00122	28.5	0.196
1.20	49.6	0.00133	42.4	0.187

As the bond radius multiplier is increased both the ultimate strength and secant bulk stiffness increase as shown in Figure 5.50 and Figure 5.51 respectively, the Poisson's ratio reduces and the strain at failure remains relatively constant.

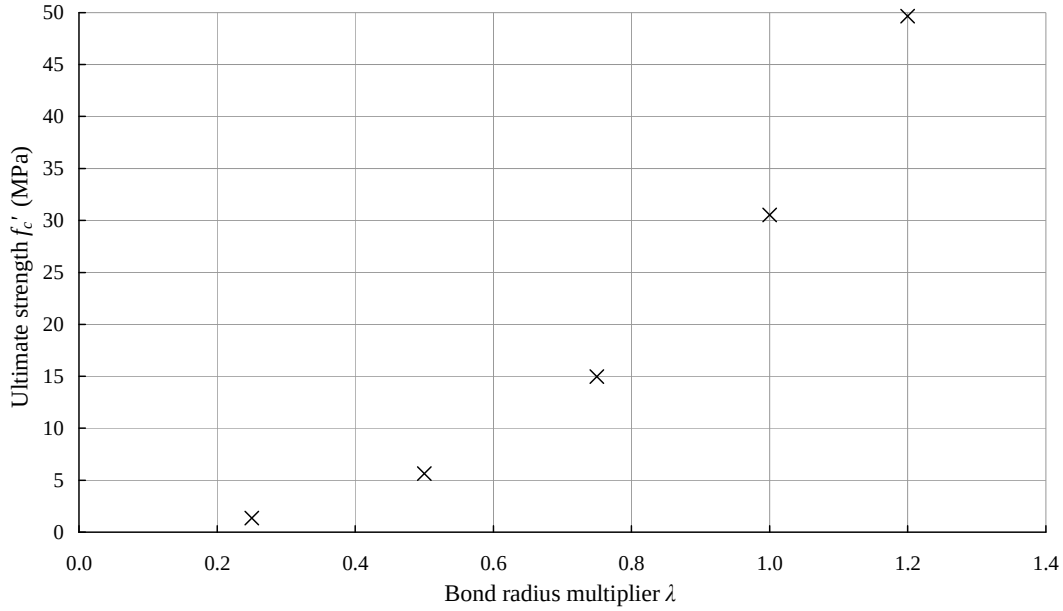

Figure 5.50 Influence of bond radius multiplier on ultimate strength

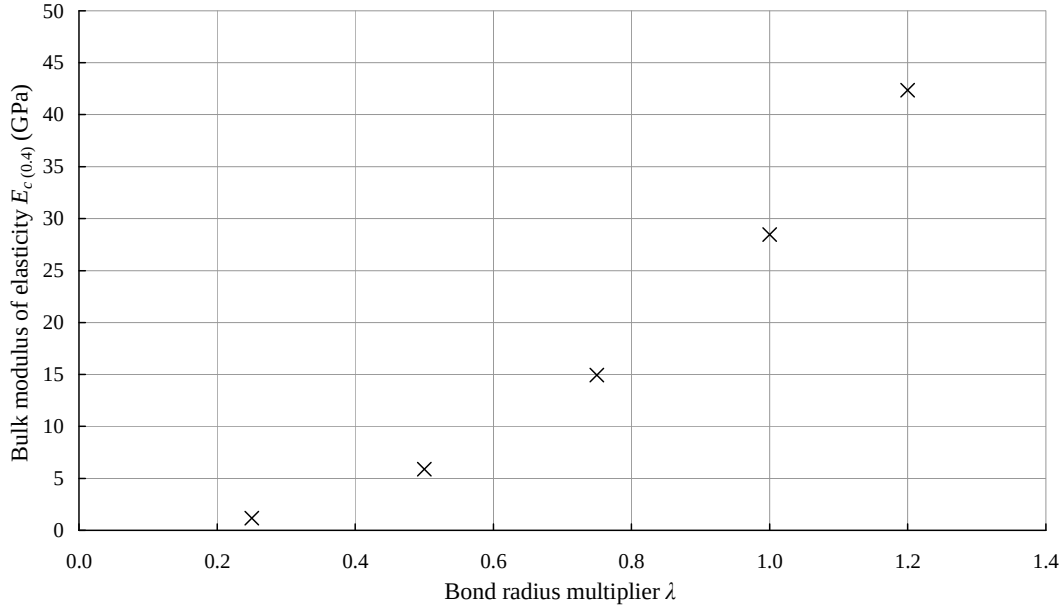

Figure 5.51 Influence of bond radius multiplier on the bulk modulus of elasticity

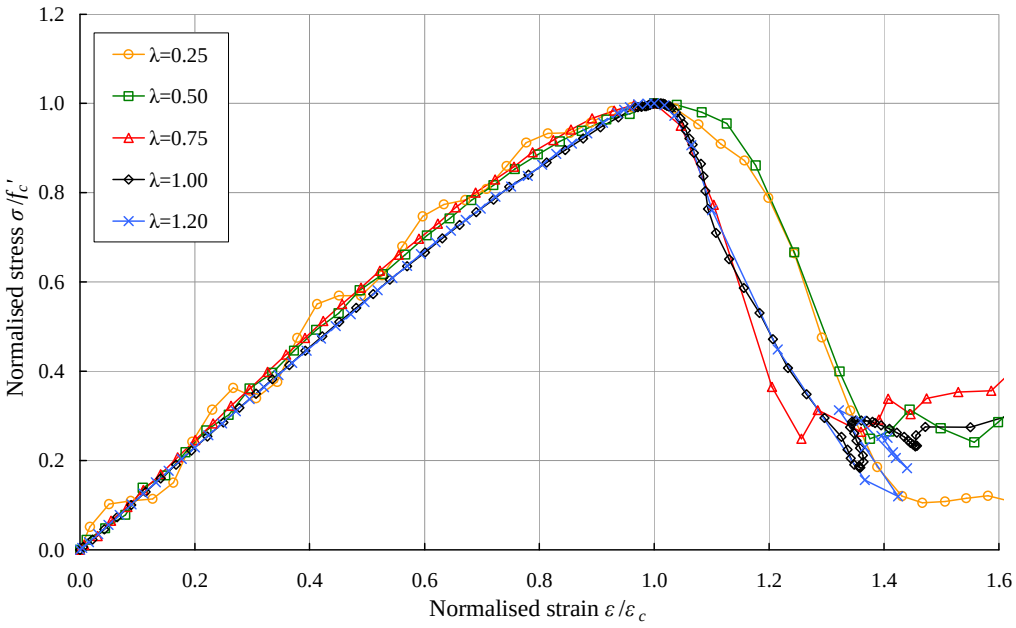

Figure 5.52 Normalised version of Figure 5.49

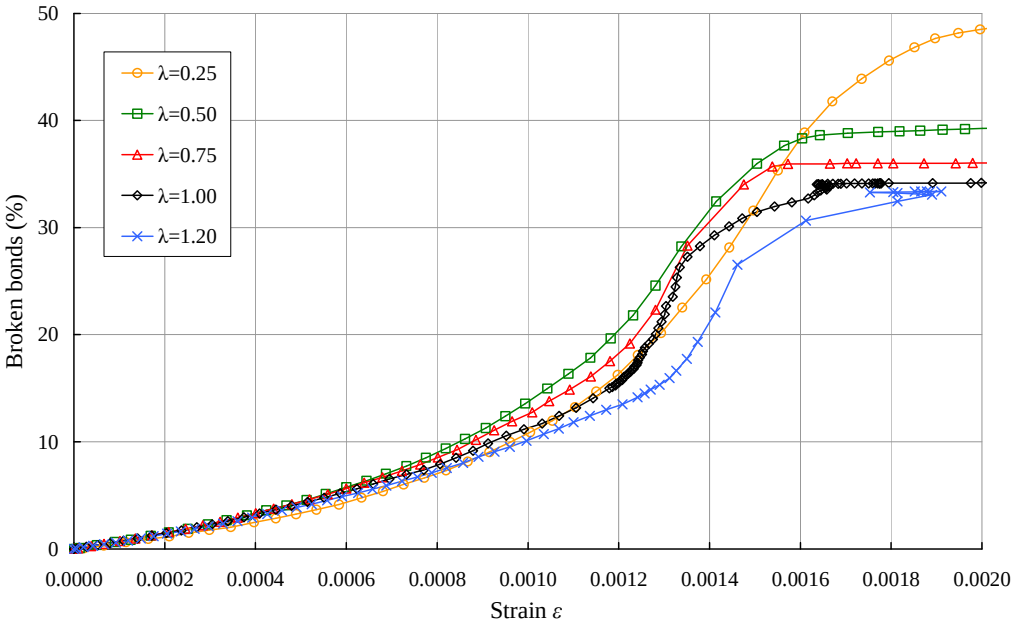

Figure 5.53 Influence of the bond radius multiplier on bond breakage

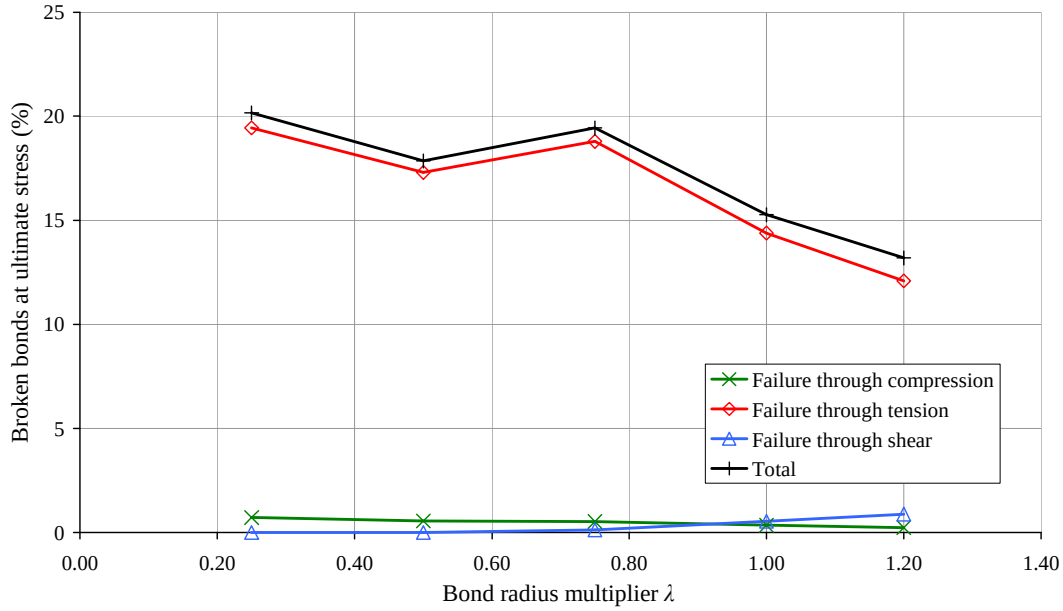

Figure 5.54 Influence of the bond radius multiplier on the bonds failure mode

As expected an increase in the bond radius multiplier leads to an increase in the bulk stiffness and also the bulk strength. As the bond radius is increased the bond becomes stiffer and stresses in the bond are reduced. The lower stresses mean that the fewer bonds fail for a given loading. These changes in the behaviour at the bond level lead to a more ductile response when the bond radius multiplier is decreased, as shown in Figure 5.52. However, at a bond radius multiplier of 0.25 the loading path can be seen to be very unstable.

From Figure 5.53 and Figure 5.54 it can be seen that as the bond radius multiplier increases the number of bonds failing both at the ultimate strength and in total also reduces. From Figure 5.54 it can be seen that as the bond radius multiplier is increased the percentage of bonds failing in shear increases slightly. As the bond radius multiplier is increased some of the shorter bonds will become wider than they are long and so shear becomes very important. The vast majority of bond failure is still through tension. If the radius of a bond is reduced (or the length increased) then the shear stresses generated are lower and so fewer bonds will fail in shear.

The same overall behaviour can be achieved using other parameters. To simplify the model it is suggested that the bond radius multiplier should be kept at a value of one, the bulk properties can be manipulated using other parameters.

5.4.3 Summary of the influence of bond fabric parameters

There are only two model input parameters that influence the initial bond fabric, they are contact radius multiplier and bond radius multiplier. They both influence the stiffness and strength of the bond fabric. However the same behavior can be achieved by varying other parameters. Therefore when it comes to forming a calibrated model these parameters should be kept within limits. This will simplify calibration significantly. The bond fabric parameters can be used to create a similar bond network for different particle packing. The influence of the bond fabric parameters on the bulk properties is summarized in Table 5.11 below.

Table 5.11 Summary of the influence of non-bonded contact parameters on bulk properties and broken bonds

Input parameter	Ultimate strength f_c'	Strain at failure ε_c	Bulk stiffness $E_{c(0.4)}$	Poisson's ratio $\nu_{c(0.4)}$	Total broken bonds
Contact radius multiplier	↑	↑	↑	×	↑
Bond radius multiplier	↑	×	↑	↓	↓

Where ↑, ↓ and × indicate an increase, decrease or no change respectively to the bulk property resulting from an increase in the input parameter.

5.5 Influence of numerical parameters

The primary aim of this thesis is to model cylindrical concrete specimens under quasi-static loading. The DEM is a dynamic calculation; therefore some of the numerical parameters must be treated with care. There are three parameters, used by the EBPM that affect the numerical stability of a simulation, they are: time-step, loading rate and global damping. The numerical stability of a simulation can be effectively improved by reducing the amount of motion that occurs between time steps; this can be achieved by either: reducing the time between calculation points, reducing the loading rate or introducing global damping which acts against particle acceleration. In the parametric study these three parameters are investigated in order to determine suitable values for use in future work that promote a stable simulation and do not lead to a loss of confidence in the results presented.

5.5.1 Influence of time step

For the parametric study the time step Δt was determined using the relevant equations described in Chapter 3. For all simulations the critical time step for bonded contacts was found to be lower than that for non-bonded contacts therefore using the solution based on a single degree of freedom in a mass spring system:

$$\Delta t = \xi \Delta t_{Bcrit} \tag{5.5}$$

where

$$\Delta t_{Bcrit} = \min 2\sqrt{\frac{m_i}{K_i}} \tag{5.6}$$

where Δt_{Bcrit} is the critical time step for the bonded contacts, K_i is the highest stiffness at a bonded contact, m_i is the smaller mass of a particle in that bonded contact and ξ is a numerical factor which in this instance was chosen to be 20. Although all terms in the stiffness matrix were considered the axial stiffness was always found to be the largest. The time step for the reference case, determined using Equation (5.5) and Equation (5.6), was rounded down to 1×10^{-7} s.

In the parametric study the time step was varied from five times smaller than that used in the reference case to five times larger. A summary of the influence of the time step on the bulk properties is shown in Table 5.12. The influence of the time step on the stress-strain response is shown in Figure 5.55. For clarity the stress-strain curves for two of the time steps used (2×10^{-7} s and 3×10^{-7} s) have been excluded from Figure 5.55; these responses were found to be very similar to that when $\Delta t = 1\times10^{-7}$ s. An additional simulation was run with a time step of 10×10^{-7} s (i.e. 10 times greater than the reference case). However, the simulation was too unstable and no meaningful data could be recorded.

Table 5.12 Summary of the influence of the time step on the bulk properties

Time step (s) Δt	Ultimate Strength (MPa) f_c'	Strain at failure ε_c	Bulk modulus of elasticity (GPa) $E_{c(0.4)}$	Poisson's ratio $\nu_{c(0.4)}$
2×10^{-8}s	30.2	0.001193	28.3	0.189
1×10^{-7}s	30.5	0.001220	28.5	0.196
2×10^{-7}s	31.3	0.001228	28.4	0.195
3×10^{-7}s	31.0	0.001258	28.4	0.196
5×10^{-7}s	29.7	0.001284	27.8	0.193

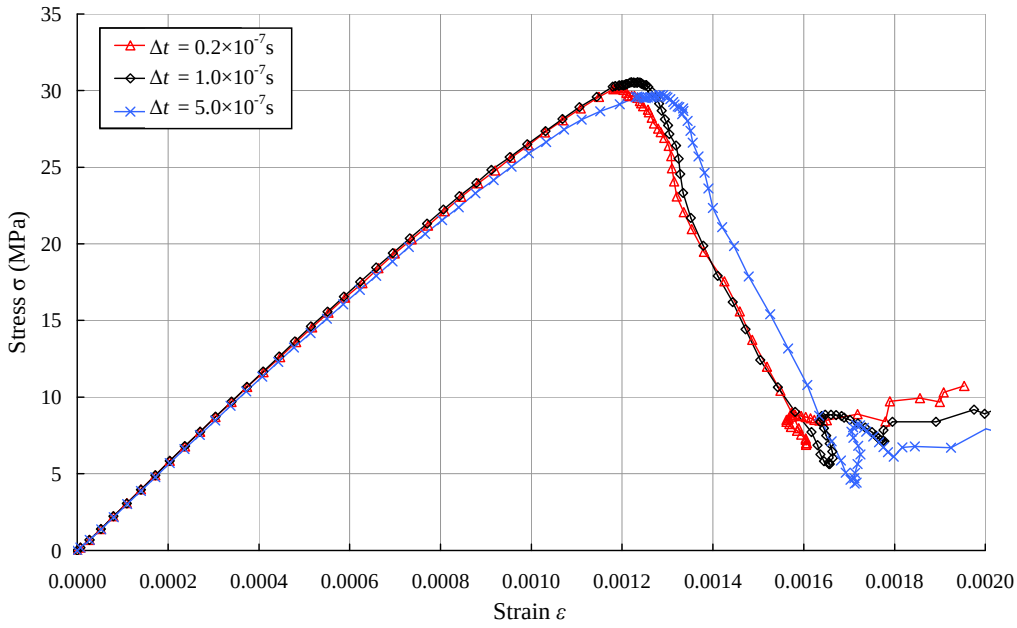

Figure 5.55 Influence of time step on stress-strain response

The lowest time step examined, and therefore theoretically most stable solution, was 2×10^{-8} s; from Figure 5.55 it can be seen that there is no significant change in the response when the time step is increased by five times to 1×10^{-7} s. However as the time step is increased by a further five times to 5×10^{-7} s there is a noticeable change in the response, with the bulk stiffness and strength both reducing.

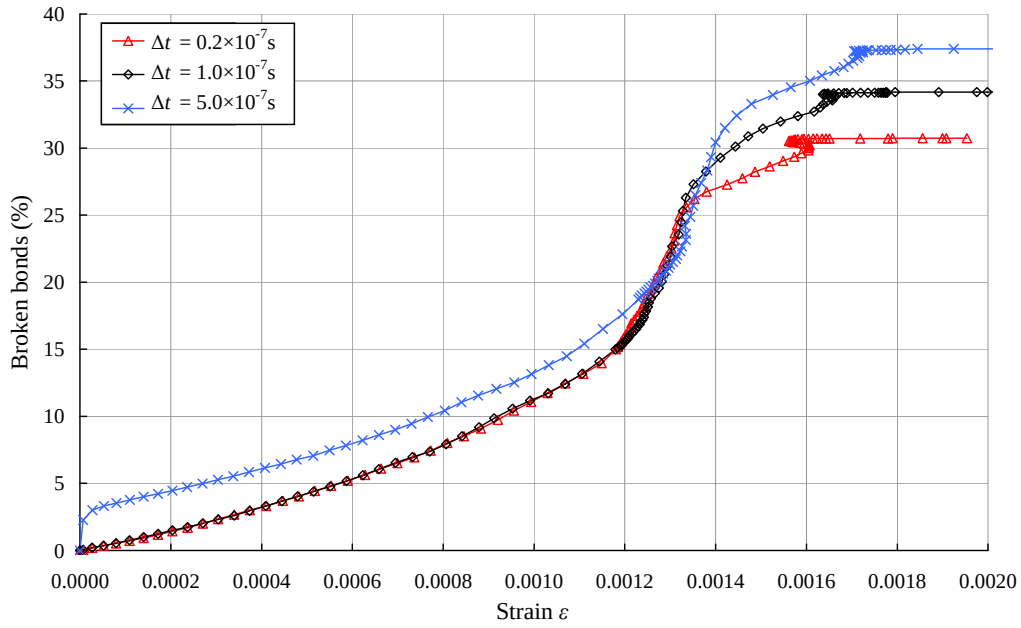

Figure 5.56 Influence of time step on the progression of broken bonds

The reason for the small reduction in ultimate strength and bulk stiffness seen when the time step was 5×10^{-7} s can be seen in Figure 5.56, a proportion of the bonds fail as loading commences. This reduces the stiffness and load carrying capability of the bond network causing the loss of stiffness and reduced strength. The reduction in stiffness and strength is not greater due to the fact that the bonds that fail initially are most likely to be the weaker bonds anyway; as can be seen in Figure 5.56 the gap in the number of broken bonds between the higher time step and the others reduces as the specimens approach failure. For the remainder of this thesis it is suggested that a time step of 1×10^{-7}s or less should be used.

5.5.2 Influence of the loading rate

For the reference case the displacement rate for each plate was set at 100 mm.s^{-1} meaning a loading rate of 1 strain per second (1 s^{-1}). In the parametric study loading rates of 0.01 s^{-1}, 0.1 s^{-1} and 10 s^{-1} were investigated; the stress-strain response for these simulations is shown in Figure 5.57.

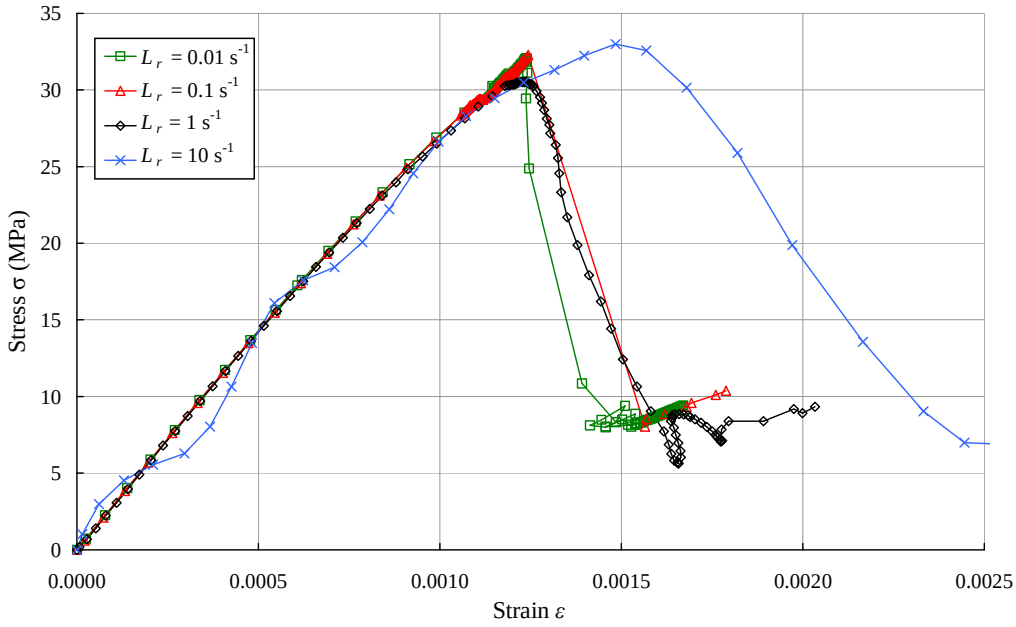

Figure 5.57 Influence of the loading rate on the stress-strain response

From Figure 5.57 it can be seen that the loading rate has no significant influence on the stress-strain behaviour when kept below 1 s^{-1}. However, when the loading rate is 10 s^{-1} the model predicts a somewhat erratic response, including a much softer post-peak behaviour. It is suggested that this may be due to numerical instability arising from high external displacements meaning equilibrium is harder to reach. For the remainder of this thesis it is suggested that a loading rate of 1 s^{-1} or less should be used.

5.5.3 Influence of global damping

The application of non-viscous damping in the EBPM is described in Chapter 3 and is known as global damping. The influence of global damping on the stress-strain behaviour is shown in Figure 5.58 with a summary of the computed bulk properties shown in Table 5.13.

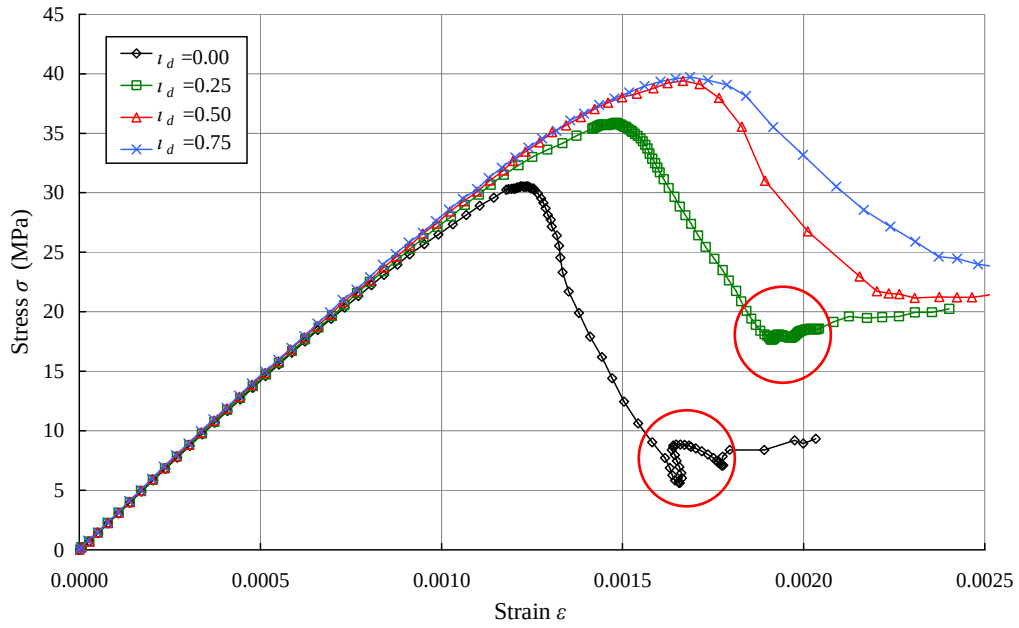

Figure 5.58 Influence of global damping on the stress-strain response

The red circles in Figure 5.58 highlight the difference in response at the end of the descending branch, after failure. The difference is indicative of different damping terms.

Table 5.13 Summary of influence of the global damping on the bulk parameters

Global damping	Ultimate Strength (MPa)	Strain at failure	Bulk modulus of elasticity (GPa)	Poisson's ratio
0.00	30.5	0.001220	28.5	0.196
0.25	35.7	0.001460	28.6	0.190
0.50	39.4	0.001667	28.9	0.192
0.75	39.7	0.001687	29.2	0.185

It can be seen from Figure 5.58 and Table 5.13 that the global damping has a significant impact on the ultimate strength and stress at large strains. There is no significant change to the bulk stiffness or bulk Poisson's ratio, any influence seen

may well disappear if a different initial particle packing is used. Overall the stress-strain response is very stable even when no global damping is used.

In a few instances the recorded strain appears to reduce, leading to unusual results as seen in the post elastic region, indicated by the red circles in Figure 5.58. This is not a real phenomenon but comes from the way in which the strain is calculated by considering the maximum overlap between the top particles and the loading plate. As failure begins and particles at the boundaries become loose the maximum overlap will begin to fluctuate. This is important to consider when examining stress-strain behaviour. However, as this region is not of primary interest any value for viscous damping can be used to achieve a numerically stable result and extract the bulk parameters of interest.

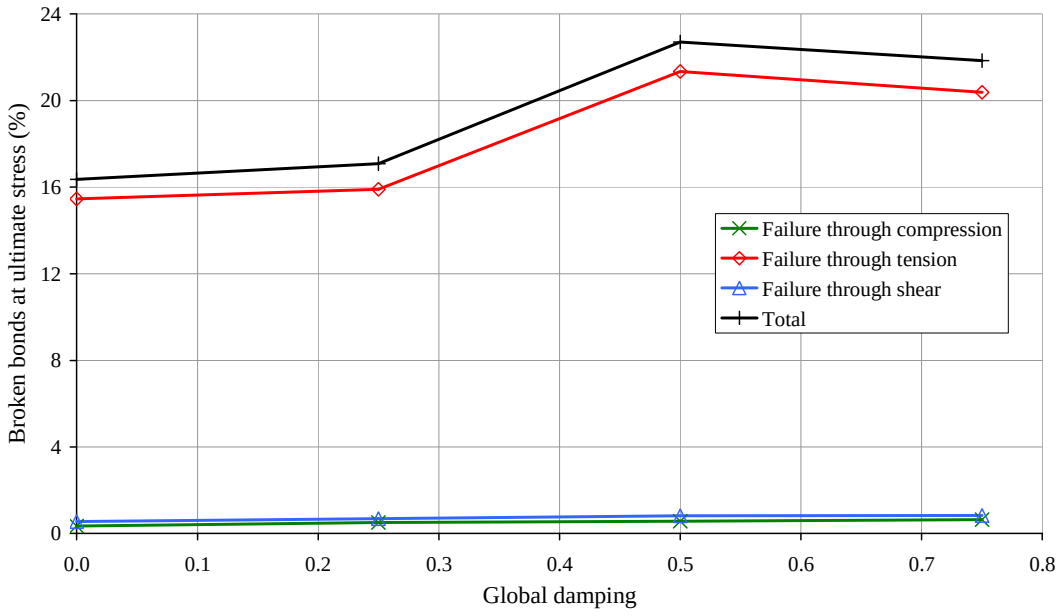

Figure 5.59 The influence of global damping on failure mode

The global damping is not a physical parameter, and therefore it should not have a significant influence on properties such as the ultimate strength. The increase in ultimate strength is not caused by an increase in the strength of the bonds, in fact from Figure 5.59 it can be seen that there is a slight increase in the number of bonds

that have failed in tension by the ultimate strength as the global damping increases. This suggests that the global damping influences the mobilisation of contact friction at non-bonded contacts. When a low coefficient of damping is used any fragments or individual particle that break away from the main body of the specimen, say along the failure plane, are able to move out of contact with their surrounding particles. In this case they do not contribute any load carrying and so a lower residual strength is noted.

As described in Chapter 3 alternative dynamic particle generation techniques were tested at the beginning of this project. Subsequently, global damping was introduced into the EBPM to help in achieving equilibrium and an initial stress free state in the system. With a further change in generation technique to the one used for the parametric study, also described in Chapter 3, the global damping was no longer required. Unless otherwise stated, global damping has been excluded from the simulations conducted in this thesis.

5.5.4 Summary of the numerical parameters

From the analysis above it is clear that it is critical to include the three numerical parameters mentioned: time step, loading rate and global damping when considering the numerical stability of the model. This is especially true for time step and loading rate, where it was found that these parameters must be kept below certain values for there to be no significant effect on the overall behaviour and to ensure numerical stability. It is also important to understand that these values should be kept as high as possible to reduce computational time. It is suggested that a time step of 1×10^{-7} s or less and a loading rate of 1 s^{-1} or less should be used.

The global damping parameter does not appear to be needed to improve numerical stability. However, a non-physical influence on the bulk properties was noted and so for the remainder of this project the global damping is not used unless specifically mentioned. There is however local contact damping which is active at non-bonded contacts.

5.6 Summary discussion of the parametric study

The parametric study has examined how the bonded contact parameters, non-bonded contact parameters, bond fabric parameters and numerical parameters influence the predicted behaviour of the cementitious solid. Each section has summarized which parameters have the most influence. The choice of values for these parameters to describe real materials will be examined further in the next chapter. A summary discussion of the relative importance of these parameters is presented here.

Due to the complexity of the model there are many parameters that could have an effect on the bulk behaviour. However provided the remaining parameters are kept within limits, this study has shown that the key parameters that are the most influential are:

- Bond Young's modulus
- Mean bond tensile and shear strength
- Coefficient of variation of tensile and shear strength
- Contact radius multiplier

What follows here is a discussion of how these key input parameters influence the characteristic bulk solid properties.

In general most model parameters appear to affect the bulk stiffness or the ultimate strength. These in turn affect the strain at failure. Logically, those that affect the stiffness of the bond fabric have most effect on the stiffness of the solid, while those that affect the strength of the bond fabric have most effect on the bulk strength of the cementitious solid. There are some exceptions that affect both; one such example is the Young's modulus of the bonds.

Most importantly the bond fabric factors such as the contact radius and the bond radius multiplier probably have the largest single affect, as they alter the bond network and basically change the affect of other model factors.

5.6.1 Parameters with a significant influence on bulk stiffness

Only a small minority of bonds have failed at the point at which the secant value of the bulk stiffness is determined (at 40% of the ultimate strength). The recorded value of the bulk stiffness is therefore primarily influenced by parameters which affect the stiffness of the bond fabric. The major model parameters that affect the bulk stiffness are:

- Bond Young's modulus
- Contact radius multiplier
- Bond radius multiplier

5.6.2 Parameters with a significant influence on the ultimate strength

In most simulations, in part due to the high coefficient of variation of strength used, a proportion of the bonds have broken resulting in a number of non-bonded contacts forming before failure. This means that the ultimate strength is influenced by both the interaction at bonded and non-bonded contacts. This implies that most parameters have some influence on the bulk strength. However the major model parameters that influence the bulk strength are:

- Contact radius multiplier
- Bond radius multiplier
- Mean tensile bond strength
- Mean shear bond strength
- Coefficient of variation of bond strength
- Bond Young's modulus

Nevertheless in the calibration procedure shown in Chapter 6 some of these parameters will be fixed to simplify the model. The most critical parameters are those that directly affect the strength of the bond fabric.

5.6.3 Parameters with a significant influence on the strain at failure

Creating a relationship between the strain at failure and the input parameters is very difficult. This is because the strain at failure is affected by the initial stiffness, the loss of stiffness and the ultimate strength. The process for calibration should therefore be to match bulk stiffness, loss of stiffness and ultimate strength allowing the strain at failure to reach the right magnitude.

5.6.4 Parameters with a significant influence on the Poisson's ratio

There are not many parameters that affect the Poisson's ratio, which is probably influenced most significantly by the initial particle packing. The ones that do have a slight influence (Bond Poisson's ratio, coefficient of variation of bond strength and global damping) are not significant enough to change the bulk Poisson's ratio.

5.6.5 Post peak behaviour and failure mode

The post peak behaviour, i.e. the descending branch of the stress strain curve after ultimate strength, can be characterized in two ways, the ductility and the residual strength. Accurate modelling of the post peak behaviour of cementitious materials is not the primary aim of this work. However, a brief comment on this element of the modelling is appropriate.

The residual strength and ductility are linked with the failure mode of the specimen as well as the mobilisation and significance of non-bonded contacts. More ductility is predicted when non-bonded contacts are more influential. This may be due to either an increased number of non-bonded contacts (caused by high specimen deformation) or the parameters that are chosen for their interaction.

Two common failure modes are noted, each of which has an influence on the predicted residual strength. An inclined crack is most often seen when bond tensile failure is dominant, as seen in Figure 5.15(a). The inclined nature of the crack allows for particles to slide past one another leading to less load transfer between un-bonded particles resulting in a lower residual strength. In this case the friction between

particles is seen to have an influence on the residual strength. In other cases, most notably when bond compression failure is dominant as seen in Figure 5.15(b), a horizontal crack forms. In this instance the loose material along the failure plane can be compressed against the specimen and is able to transmit load leading to a higher residual strength.

5.7 Conclusions

The summary in Section 5.6 has identified key parameters for modelling cementitious materials using the EBPM. The initial particle packing and bond network is sufficiently robust and redundant to enable a wide range of behaviours of cementitious materials to be modelled. Provided an appropriate particle packing is chosen and non-key parameters lie within the ranges explored above, then it is possible to assign values to the most influential parameters and hence to model a cementitious material with appropriate behaviour. Despite setting up a single bond fabric, this is sufficient to predict a wide spectrum of responses to failure. In Chapter 6 the modelling of a cementitious material is outlined using the principles discussed above.

Chapter 6 Application of the Edinburgh Bonded Particle Model to modelling cementitious materials

6.1 Introduction

In this chapter, a simple calibration procedure is presented in which the findings from the parametric study are used to produce a model capable of accurately predicting a wide range of cementitious material behaviour. It would be possible to conduct a full parameter optimisation procedure, such as the one presented by Johnstone (2010), but that is not the aim here. By providing appropriate values for parameters which have minimal influence on the bulk behaviour, the choice of model parameters to produce the intended computed bulk response is made much easier. This ultimately leads to a solution with the same predictive power but fewer input parameters.

6.2 Calibration procedure

The aim of the calibration procedure is to determine a workable relationship between key model input parameters and the model's predicted bulk response of a concrete cylinder under uni-axial compression. In this instance, these predictions are compared to those made for the same specimen using the Eurocode equations (BS EN 1992-1-1, 2004). The four properties used to characterise the quantitative response of the cylinder are: the ultimate strength f_c', the strain at ultimate strength ε_c, the secant bulk modulus $E_{c\,(0.4)}$ and the bulk Poisson's ratio $\nu_{c(0.4)}$. These properties were previously defined in Chapter 4.

The Eurocode (Table 3.1 in BS EN 1992-1-1:2004) provides empirical relationships between the ultimate cylinder strength f_c' of a physical specimen and both the bulk secant modulus and the strain at ultimate strength. These relationships are reproduced here as Equation (6.1) and Equation (6.2) respectively:

$$E_{c(0.4)} = 22\sqrt[3]{(f_c'/10)} \tag{6.1}$$

$$\varepsilon_c = 0.0007\,(f_c')^{0.31} \leq 0.0028 \tag{6.2}$$

It should be noted that Equation (6.1) has been used in Chapter 4. The Eurocode (BS EN 1992-1-1, 2004) also provides suggested strength classes for concrete; the minimum ultimate compressive cylinder strength given is 20 MPa and the maximum is 98 MPa. Generally, the ultimate strength is deemed to be the most important property to engineers and so will be the primary target property for the model calibration. For the purposes of this calibration study, the range of ultimate strength is extended so that the model is calibrated to predict cylinder strength over the range 10 MPa to 100 MPa. This allows the predictive capabilities of the model to be tested over an order of magnitude. Using Equation (6.1) and Equation (6.2), equivalent ranges for bulk modulus and strain at ultimate strength can be determined. The values representing the upper and lower limits for these ranges are shown in Table 6.1.

The parametric study showed that the model input parameters have limited influence on the bulk Poisson's ratio. It is suggested that there is more influence imposed by the initial arrangement of bonds and particles; this is currently under investigation. For the purposes of this calibration procedure, the bulk Poisson's ratio will be expected to lie in the range 0.1 to 0.3, with values suggested around 0.2.

Table 6.1 Ranges for bulk properties using the Eurocode

Property	Description	Min	Max
f_c'	Ultimate strength (MPa)	10	100
$E_{c\,(0.4)}$	Bulk secant modulus (GPa)	22.0	47.4
ε_c	Strain at ultimate strength	0.0014	0.0029

The parametric study found that there are a number of model parameters that have varying degrees of influence over the bulk properties. As mentioned above, it is the ultimate strength which is the main target property, followed by the bulk secant modulus and finally the strain at ultimate strength.

A model calibration procedure is described below; in it, a single initial particle packing is used. The majority of model input parameters are fixed whilst a few key parameters are determined from standard formulae so that the predicted bulk properties match the target bulk properties.

6.2.1 Setting the initial particle packing and bond fabric

The parametric study revealed that a fixed initial particle packing is versatile enough to produce a full spectrum of concrete behaviour. To simplify the model calibration, the initial particle packing is kept constant for all simulations. The particle packing is the same as that for the specimen produced for the parametric study. The initial bond fabric is characterised by the properties shown in Table 6.2.

Table 6.2 Characterisation of a reference DEM model

Parameter	Description	Value
h_i	Initial specimen height (mm)	200
A_{ratio}	Aspect ratio – height to diameter	2:1
n_p	Total number of particles	20,561
n	Porosity	0.37
r_{av}	Average particle radius (mm)	2.14
r_{min}	Minimum particle radius (mm)	1.28
r_{max}	Maximum particle radius (mm)	3.02
d_f	Dispersion factor	0.81

The initial bond fabric is defined by the initial particle packing structure and the bond fabric numerical parameters (contact radius multiplier η, and bond radius multiplier λ). The parametric study showed that both of these properties had a significant influence on the bulk response. However, it was determined that the bond radius multiplier should be excluded from the calibration and maintained at a value of 1 for all simulations. The contact radius multiplier has been set at 1.1. Using the results from the parametric study this contact radius multiplier should provide a slightly more ductile response than a higher contact radius multiplier whilst still maintaining a dense bond network. This means that there is an average of 8.23 bonds per particle.

6.2.2 Setting the additional non-key model input parameters

With the initial particle packing and bond fabric established the remaining parameters that must be selected are those that affect the numerical stability and those that affect the two contact models. It was determined that the numerical stability of the simulations is ensured when the time step and loading rate are kept

within certain bounds. In accordance with this in the calibration procedure the time step used was $\Delta t = 1\times10^{-7}$ s which was always at least 10% of the critical time step and the loading rate $L_r = 1\ s^{-1}$.

The parametric study showed that the non-bonded contact parameters have a limited influence on the bulk behaviour. However, a higher particle Young's modulus produced a more ductile response and a lower inter particle static friction enhanced the development of the failure plane, so suitable values have been chosen for the model calibration, the other non-bonded contact parameters are kept at the same values as in the reference case used above. As in the parametric study, no rolling friction is considered between particles. A summary of the non-bonded contact model input parameters used for all simulations in the model calibration procedure are shown in Table 6.3.

Table 6.3 Non-bonded contact parameters used in the calibration procedure

Parameter	Description	Value
ρ_p	Particle density (kg.m^{-3})	2700
E_p	Particle Young's modulus (GPa)	70
ν_p	Particle Poisson's ratio	0.25
μ_{sp}	Particle-particle static friction	0.5
μ_{sg}	Particle-geometry static friction	1
e_{rp}	Particle-particle restitution	0.5
e_{rg}	Particle-geometry restitution	0.0001

From the parametric study it was found that, for a given initial bond fabric, the bonded-contact parameters had the most influence on the bulk behaviour. As the parameters for bond fabric, numerical stability and non-bonded contact have been set

relationships can be established between the bonded-contact parameters and the predicted bulk response.

The bond Poisson's ratio was found to have a slight influence over the ultimate strength; however, as a greater influence was seen by varying the strength components of the bonds the bond Poisson's ratio has been set at 0.2 for the model calibration simulations. The coefficient of variation of strength was found to have a significant influence on the ductility of the response, being the property that affected the loss of stiffness through the progressive breakage of bonds. The coefficient of variation of strength for the model calibration is set at 0.8; the parametric study showed that this value provided the system with some plasticity without causing an excessive amount of bond failure in the near elastic region of loading. The parametric study also showed that tensile and shear bond failure was sufficient to produce the failure plane. Therefore, to further simplify the model calibration, the mean bond compressive strength will be set to five times that of the mean bond tensile strength; this high ratio was set so that bond failure through compression is unlikely. The coefficient of variation of compressive strength is set to zero. This leaves only a few key parameters which are used as the variables in the model calibration: bond Young's modulus, mean bond tensile strength and mean bond shear strength. In the parametric study a range of tensile to shear strengths was investigated. It was found that a satisfactory failure plane developed when the mean bond shear strength was equivalent to the mean bond tensile strength, as such this relationship will be maintained in the model calibration. The full influence of this ratio is still under investigation. A summary of the bonded contact model input parameters used for all simulations in the model calibration procedure are shown in Table 6.4.

Table 6.4 Bonded contact parameters used in the calibration procedure

Parameter	Description	Value
E_b	Bond Young's modulus (GPa)	variable
ν_b	Bond Poisson's ratio	0.2
S_C	Mean bond compressive strength (MPa)	$= 5 \times S_T$
S_T	Mean bond tensile strength (MPa)	variable
S_S	Mean bond shear strength (MPa)	$= S_T$
ς_C	Coefficient of variation of compressive strength	0.0
ς_T	Coefficient of variation of tensile strength	0.8
ς_S	Coefficient of variation of shear strength	0.8

The total number of free input parameters for the model calibration procedure has been reduced to two. It is proposed that this is enough to produce a wide range of concrete behaviour. The calibration procedure is discussed below.

6.2.3 Determining the relationship between material bulk stiffness and the bond Young's modulus

The ultimate strength is the most important bulk property for most practical applications. The parametric study has shown that there are many model input parameters that influence it including the bond Young's modulus. On the other hand the same parametric study has demonstrated that, for a given initial bond fabric, there are only two parameters that have a significant influence on the bulk stiffness. They are: the bond Young's modulus E_b, which directly influences the bulk stiffness, and the coefficient of variation of strength which influences the rate of loss of stiffness. The coefficient of variation of strength is kept constant in the model calibration as described above.

By using the model input parameters outlined above, and maintaining the tensile and shear strength so that $S_T = S_S =$ 60 MPa, the relationship between bond Young's modulus E_b and predicted bulk secant modulus $E_{b(0.4)}$ can be established. For this stage of the calibration any value for S_T could be used, however, using the results from the parametric study a value of 60 MPa should produce a typical response. As described above the strengths used in the model are much greater when compared against the strength properties for hardened cement paste. It must be remembered that the bonds are not supposed to match the characteristics of hardened cement paste as they are just a representation of the interaction between portions of the material. In total five simulations are run with bond Young's modulus increasing between 10 GPa and 70 GPa; The influence on predicted bulk modulus is shown in Figure 6.1.

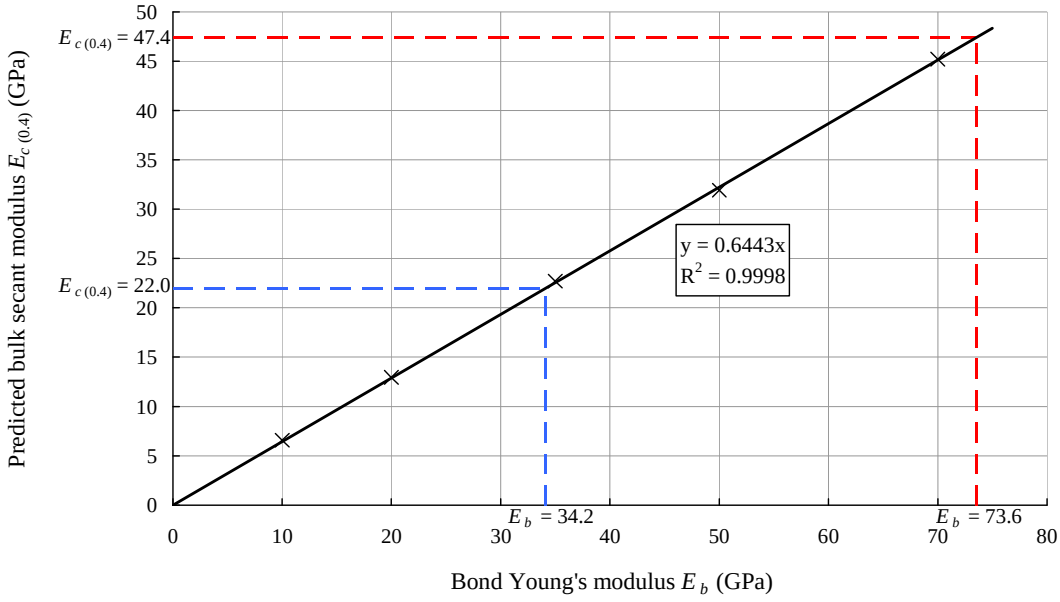

Figure 6.1 Relationship between bond Young's modulus and the bulk modulus

As can be seen in Figure 6.1 there is a strong linear relationship between the bond Young's modulus and the bulk secant modulus, this relationship can be described by the following equation:

$$E_b = 1.55E_{c(0.4)} \tag{6.3}$$

Using Equation (6.3) the bond Young's modulus can be determined for any desired bulk secant modulus. The two bond Young's modulus required to produce the minimum and maximum bulk secant modulus, as prescribed in Table 6.1, have been determined using Figure 6.1; these values have been marked on to Figure 6.1 as the minimum in blue and the maximum in red.

6.2.4 Determining the relationship between model input parameters and the bulk strength

The parametric study noted that a reduction in bond Young's modulus leads to an increase in ultimate strength. This is due to the fact that a greater specimen deformation is seen when the bond stiffness is lower, allowing an increasing engagement of non-bonded contacts which increases the bulk strength. With this in mind the bond Young's modulus should be taken into consideration when determining the relationship between the model input parameters and the bulk strength.

The other parameters that the parametric study showed had the most influence over the bulk strength are: mean bond tensile strength and coefficient of variation of strength, mean bond shear strength and coefficient of variation of strength, and particle Young's modulus. All of these parameters have been set, apart from the mean bond tensile and shear strengths.

If the mean tensile and shear strengths are related (in this case they are kept equal so that $S_T = S_S$), then for a known bond Young's modulus a relationship can be found between mean bond tensile strength S_T the mean bond shear strength S_S and the bulk strength f_c'. As this relationship depends on the bond Young's modulus a set of curves is generated relating the mean bond tensile and shear strength to the predicted

ultimate strength. The two curves shown in Figure 6.2 represent the upper and lower limits of bond Young's modulus determined from Figure 6.1.

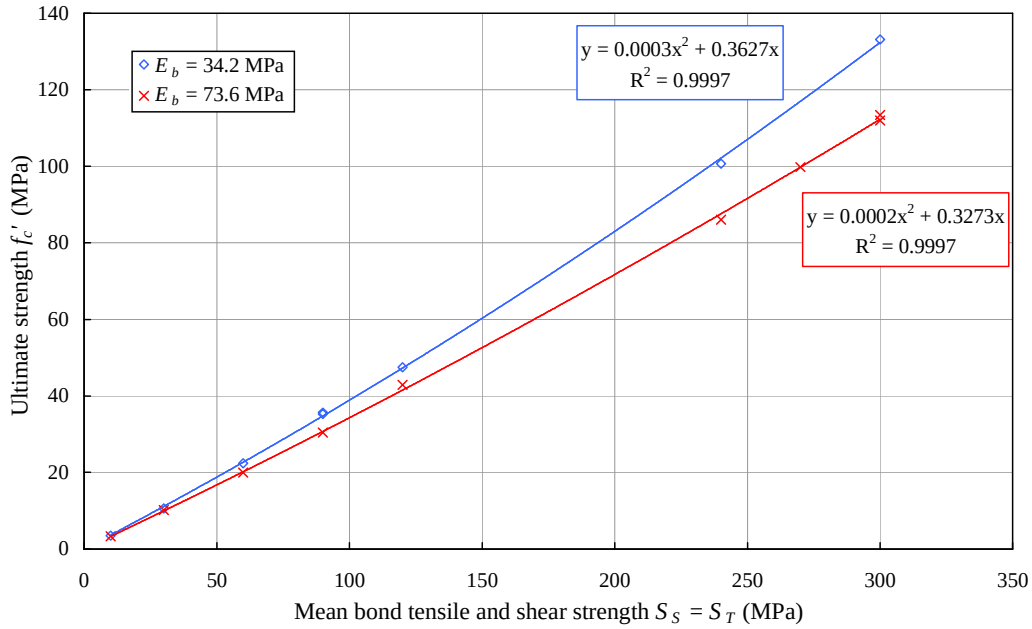

Figure 6.2 Relationship between mean bond strength and ultimate strength for varying values of bond Young's modulus

Therefore the relationship between mean bond tensile strength S_T and ultimate strength f_c', when E_b = 34.2 can be expressed as:

$$f_c' = 0.0003S_T^{\,2} + 0.3627S_T \tag{6.4}$$

And when E_b = 73.6 as:

$$f_c' = 0.0002S_T^{\,2} + 0.3273S_T \tag{6.5}$$

As can be seen in Figure 6.2 the difference in predicted ultimate strength increases as the bond strength is increased. This is due to the fact that at higher bond strengths a greater specimen deformation is required before failure which means that there are a greater number of non-bonded contacts which are able to transmit load.

6.3 Example simulations with comparisons to Eurocode

The relationships between key model input parameters and the bulk behaviour have been established for a given particle assembly. In order to assess the accuracy of these relationships three simulation cases were conducted, each of which had a target ultimate strength of either 10 MPa, 55 MPa or 100 MPa. The respective bulk secant modulus and strain at failure can be determined from empirical relationships given in the Eurocode (BS EN 1992-1-1, 2004), and reproduced as Equation (6.1) and Equation (6.2). The target bulk properties for these three cases are shown in Table 6.5.

Table 6.5 Target values for bulk properties

Property	Description	Case 1	Case 2	Case 3
f_c'	Ultimate strength (MPa)	10	55	100
$E_{c\,(0.4)}$	Bulk modulus of elasticity (GPa)	22.0	38.8	47.4
ε_c	Strain at ultimate strength	0.0014	0.0024	0.0029

Using the procedure outlined above the key model input parameters can be determined for each case. As ultimate strengths of 10 MPa and 100 MPa were both used as limits in part of the calibration procedure the key input parameters for these cases are known. What follows is the determination of the bond model input parameters for case 2 when the target strength is 55 MPa.

The target bulk stiffness for case 2 has been calculated as 38.8 GPa, using Equation (6.3) the required bond Young's modulus is found to be 60.3 GPa so

60 GPa will be used. To determine the mean bond tensile strength required a bond Young's modulus of 60.3 GPa is set as the target value in both Equation (6.4) and Equation (6.5), a goal seek operation is conducted in appropriate software (Microsoft Excel) to determine the bond strength to be used. This provides values for mean bond tensile strength of 136 MPa if the bond Young's modulus were 34.2 GPa and 154 MPa if the bond Young's modulus was 73.6 GPa. As the bond Young's modulus being used lies between 34 GPa and 74 GPa a linear interpolation is used to determine that the mean bond tensile and shear strength are set at 145 MPa. The stress-strain responses for the three target cases are shown in Figure 6.3, the predicted bulk properties are compared to the target properties in Table 6.4.

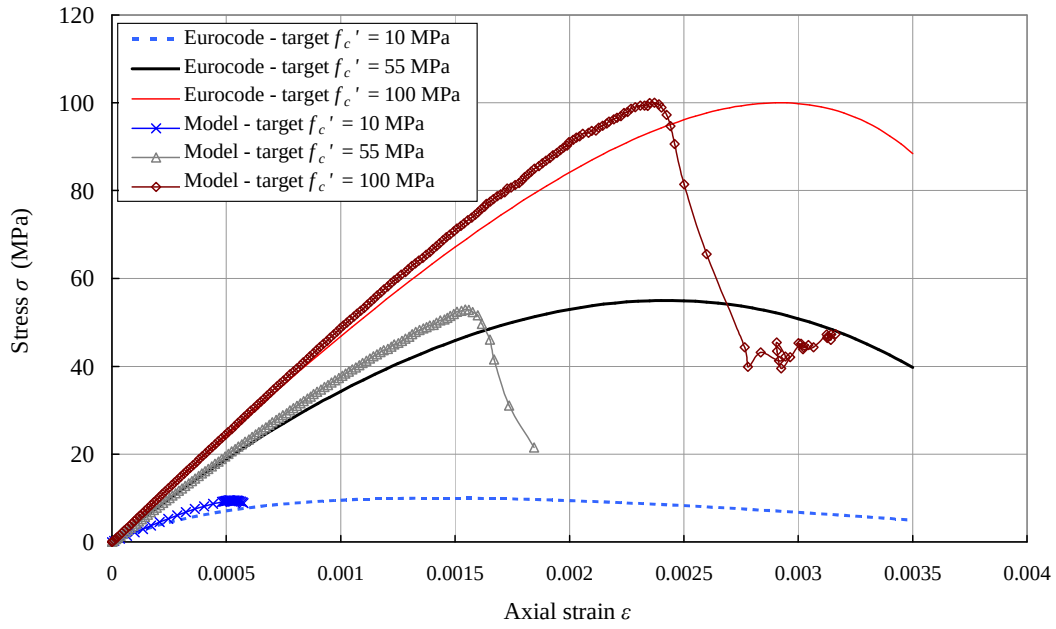

Figure 6.3 The stress-strain response for the three cases

Table 6.6 Comparison of target and predicted bulk properties

Case	Parameter	Target	Predicted	% error
1	Ultimate strength f_c' (MPa)	10.0	9.5	-5.0
	Bulk stiffness $E_{c\,(0.4)}$ (GPa)	22.0	21.8	-0.9
	Strain at ultimate strength ε_c	0.0014	0.0005	-64.3
	Bulk Poisson's ratio v_c	-	0.196	-
2	Ultimate strength f_c' (MPa)	55.0	53.0	-3.6
	Bulk stiffness $E_{c\,(0.4)}$ (GPa)	38.8	39.3	1.3
	Strain at ultimate strength ε_c	0.0024	0.0015	-37.5
	Bulk Poisson's ratio v_c	-	0.195	-
3	Ultimate strength f_c' (MPa)	100.0	100.0	0.0
	Bulk stiffness $E_{c\,(0.4)}$ (GPa)	47.4	48.8	3.0
	Strain at ultimate strength ε_c	0.0029	0.0024	-17.2
	Bulk Poisson's ratio v_c	-	0.201	-

From Table 6.6 it can be seen that in all three cases the models predicted ultimate strength and bulk stiffness are within 5% of the target values; the strain at ultimate strength however, is always underestimated. The predicted bulk Poisson's ratio is approximately 0.2 for all three cases, which is an appropriate value.

The percentage error between the model predicted and target ultimate strength reduces as the target strength is increased. At a target ultimate strength of 100 MPa there is no difference between the two. Initially for low target strengths the model under predicts the bulk stiffness, however as the target strength increases the model begins to over estimate the bulk stiffness.

The strain at ultimate strength is always under estimated by the model but with increasing target ultimate strength the percentage difference decreases. From Figure 6.3 it can be seen that the model generally predicts a more brittle response then that given by the Eurocode prediction. The primary bond failure mode for all three cases is through tension resulting in the failure patterns as shown in Figure 6.4. In each case a primary crack forms at the mid height of the specimen and branches towards the edges of the specimen.

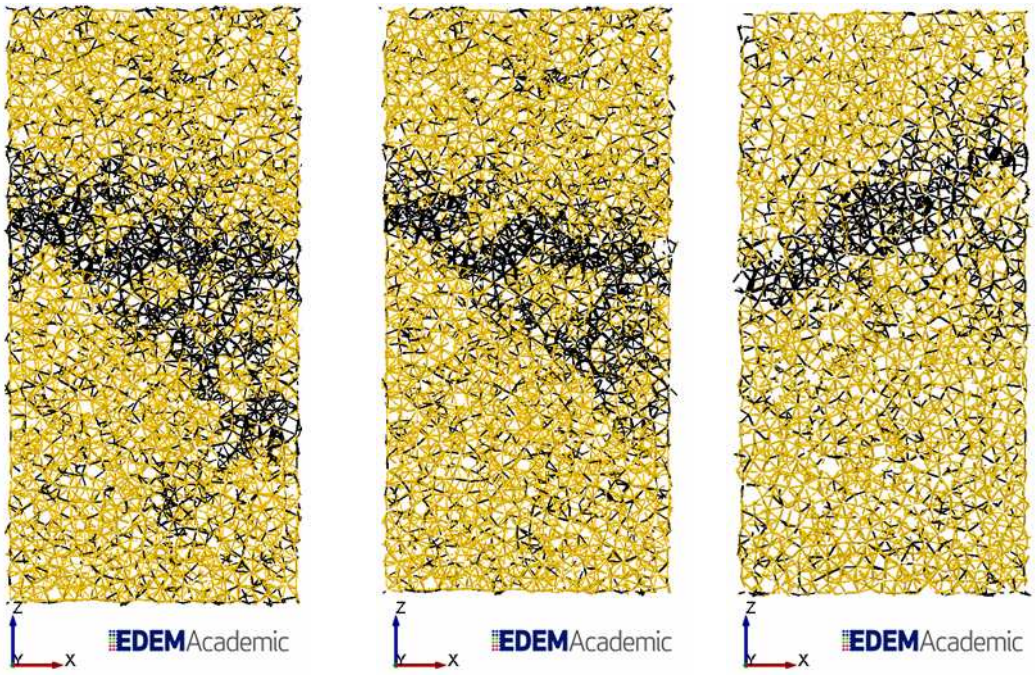

(a) for case 1 (b) for case 2 (c) for case 3

Figure 6.4 Slices through the centre of each case showing the intact bonds (yellow) and broken bonds (black)

6.4 Conclusions

A model calibration procedure has been described which uses only two parameters, bond Young's modulus, and mean bond strength (as mean bond tensile strength and

mean bond shear strength are set as equivalents), to produce a model for use with cementitious materials.

The model calibration was used so that the model was used to predict the bulk behaviour and achieve three target specimens which were using the empirical Eurocode equations.

The calibration procedure proved to be versatile enough so that the model provides a good predictor for the material in the elastic region. The ultimate strength and secant bulk stiffness were matched with a good degree of accuracy. However it is clear that the predicted behaviour from the Eurocode is not matched fully by the model. The model under predicts the loss of stiffness when compared with the Eurocode prediction. Although non-linear behaviour is seen in the model enhanced by the progression of broken bonds (introduced by the variation in bond strength) it is clear that this is not enough to show the same level of plasticity as the Eurocode equation.

It is suggested that using the model calibration presented above, and for a given particle packing arrangement, the model can predict the bulk stiffness and ultimate strength accurately. However, additional plasticity is required for the strain at failure to match the Eurocode prediction. It is suggested that this could be achieved either through the insertion of a softening term in the stiffness calculation or through the reduction of the shear or compressive strengths. An investigation in to the suitability of these methods for achieving greater softening behaviour is beyond the scope of this thesis but is an obvious next step in the development of the Edinburgh Bonded Particle Model.

Chapter 7 Further applications of the Edinburgh Bonded Particle Model

This chapter presents the application of the Edinburgh Bonded Particle Model (EBPM) to examples other than concrete cylinders. In the first section the EBPM is used to predict the response of structural elements to load. In the subsequent section a series of further simple applications are described, namely the modelling of the quasi-static loading of cubes in compression and cylinders in tension, the modelling of the dynamic loading of cementitious materials, and the interaction of fibre reinforced polymers (FRP) and concrete. These latter applications show the potential capabilities of the model, but an in depth study of each is not included here.

7.1 Application to simple structural elements

The theoretical solutions to the loading of simple structural elements are known and well understood. By utilising the fact that the bonded contact part of the EBPM is based on beam theory it is suggested that the model should be able to be conduct "conventional" structural analysis of beams, frames and plates. If the DEM predictions, made using the EBPM, provide an adequate match to the theoretical solutions then the EBPM will be validated for use in more complex structures. This section considers beams, frames, plates and rings all loaded within the elastic region. These structural elements can be modelled using the EBPM as they can all be constructed from a mesh of bonds, the constitutive behaviour of which is based on the Timoshenko beam theory. By ensuring the EBPM is suitable for simple structural analysis the potential for modelling both granular materials and structures within the same DEM framework is opened up. The reason simple structures such as rings and plates are of interest is that they could eventually be used for the basis of modelling

structural walls and the interaction between them and granular materials such as in the case of a silo or mechanised equipment.

7.1.1 Cantilever beams

A concentrated force P is applied horizontally at the free end of a fixed-free member AB as shown in Figure 7.1(a). The theoretical transverse deflection w and slope w' of the centroidal axis of the beam can be determined at any distance x from the fixed end using equations (7.1) and (7.2) derived from the governing equations, presented in chapter 3.

$$w = \frac{Px^2}{6EI}(3L - x) + \frac{Pxf_s}{GA} \tag{7.1}$$

$$w' = \frac{Px}{2EI}(2L - x) + \frac{Pf_s}{GA} \tag{7.2}$$

where L is the length of the member, EI its flexural rigidity, GA/f_s its shearing rigidity.

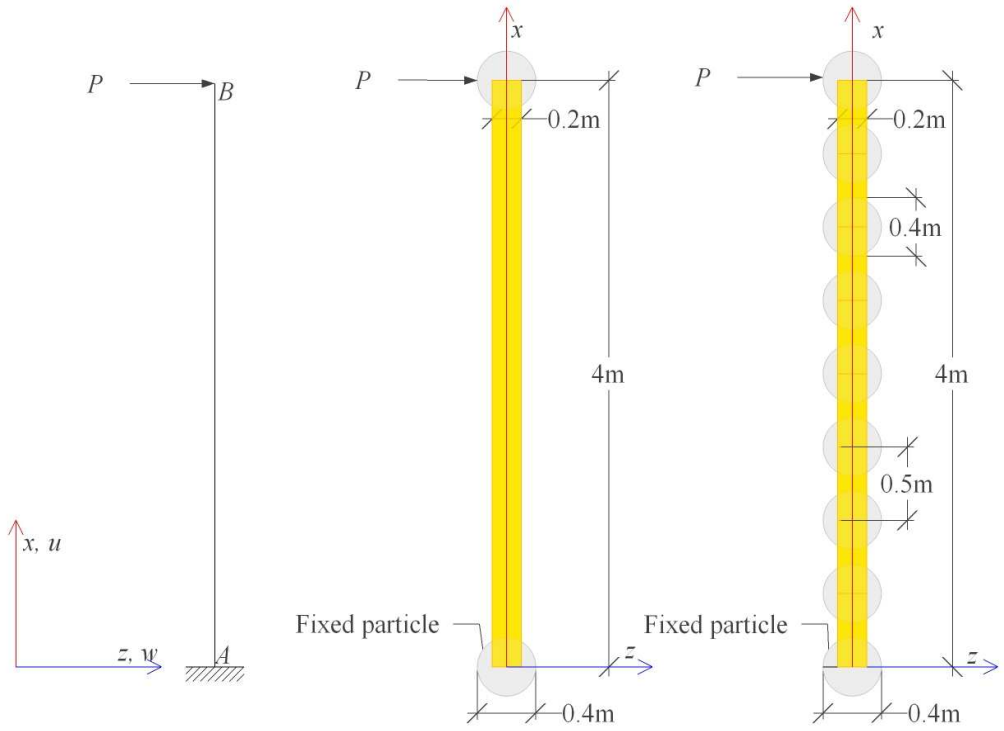

(a) schematic member *AB* (c) 2 particles, 1 bond (c) 9 particles, 8 bonds

Figure 7.1 A cantilever beam with two DEM representations

By substituting $x = L$ into equations (7.1) and (7.2) the tip deflection δ_B and rotation θ_B can be determined:

$$\delta_B = \frac{PL^3}{3EI} + \frac{PLf_s}{GA} \tag{7.3}$$

$$\theta_B = \frac{PL^2}{2EI} + \frac{Pf_s}{GA} \tag{7.4}$$

Four DEM representations of cantilever beams, all of four meters long, are created using between two and nine particles with bonds between them. One particle is restrained against all six degrees of freedom, representing the fixed support. Two

examples, using 2 and 9 particles, are shown in Figure 7.1(b) and Figure 7.1(c). The bonds in all four specimens have the same material properties and radius E_b = 200 GPa, ν_b = 0.3 and r_b = 0.1 m and are all considered to be not able to fail. An external load of 100 kN is applied horizontally to the free particle and the deflection of the particle recorded. A low computational time step is used and a relatively small global damping applied so that the system comes to rest; this is assumed to happen when the maximum particle velocity is below 1×10^{-6} mm.s^{-1}.

Using Equation (7.3) and Equation (7.4) the theoretical end deflection of the free particle and the end rotation are δ_B = 136.00 mm and θ_B = 2.9207 radians respectively. The DEM predictions of tip deflection and rotation from each test are recorded and compared against the theoretical values, as shown in Table 7.1.

Table 7.1 DEM predictions for a cantilever beam with end load P

Number of particles	Number of bonds	DEM predicted tip deflection (mm)	deflection % error	DEM predicted tip slope (rad)	rotation % error
2	1	135.89	0.07	2.9164	0.15
3	2	135.85	0.11	2.9155	0.18
5	4	138.88	0.09	2.9160	0.16
9	8	136.20	0.15	2.9214	0.02

The final positions and orientations of the particles in the DEM simulations are used to determine the deflection and rotation at points along the beam; they are found to match the theoretical values extremely well. It is not clear why the recorded errors shown in Table 7.1 are not monotonic; it is possible that as the magnitudes of the errors are so small numerical rounding errors could account for the variation. The DEM predictions for deflection and rotation, when using nine particles and eight bonds, are plotted against the theoretical solutions, determined from Equation (7.1) and Equation (7.2), in Figure 7.2 and Figure 7.3.

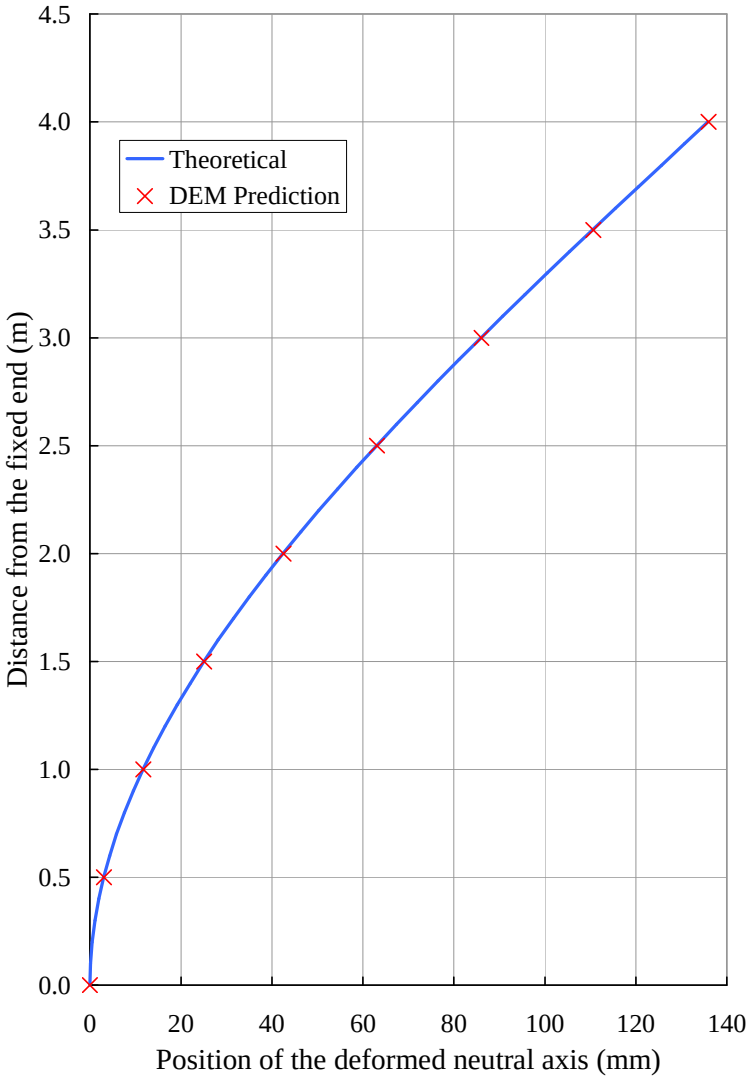

Figure 7.2 Nine particle DEM prediction and theoretical solution of the deformed position of a single column subject to end load

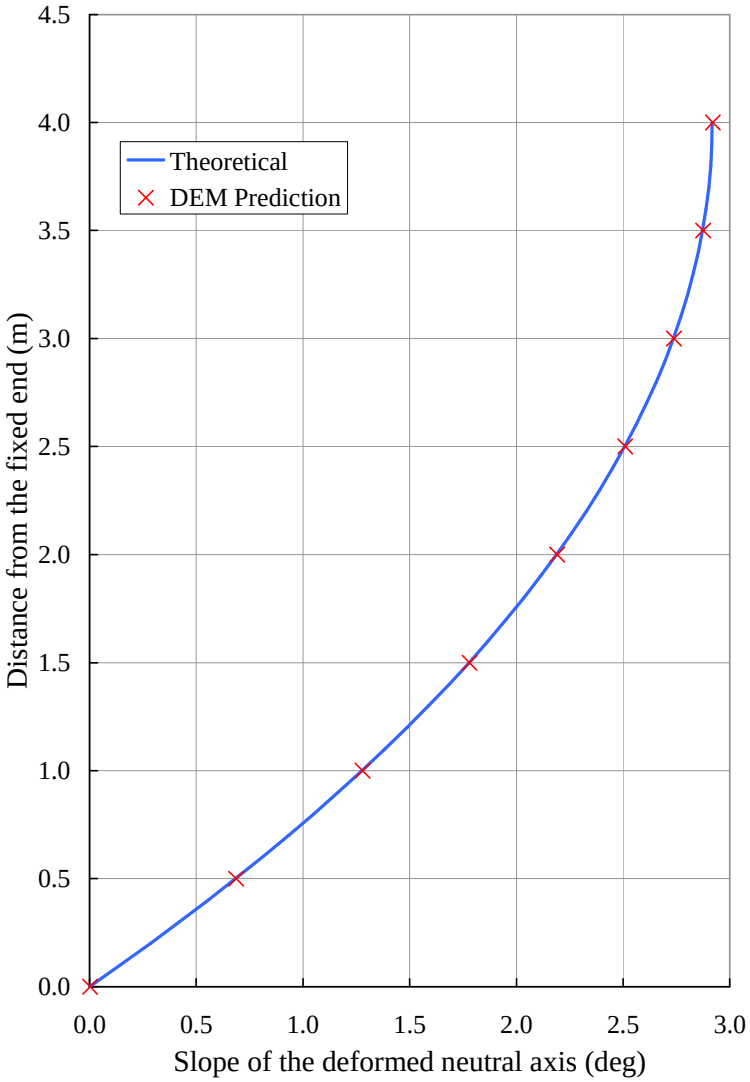

Figure 7.3 Nine particle DEM prediction and theoretical solution of the deformed slope of a single column subject to end load.

7.1.2 Single storey plane frames

In this example a simply plane frame structure consisting of three members connected at joints *A, B, C* and *D*, as shown in Figure 7.4, is considered; joints *A* and *D* are fixed and joints *B* and *C* are rigid.

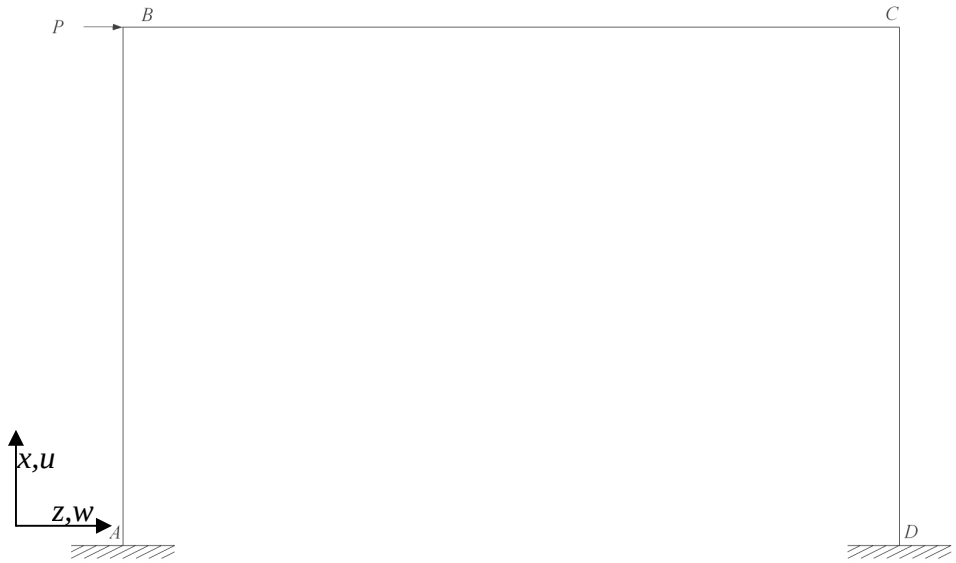

Figure 7.4 a single story single frame

A concentrated load *P* is applied horizontally at joint *B*; the force acting on the frame and the resulting translations are in the plane of the structure, so only in-plane deformations of the members are considered. If the flexural rigidity *EI* of member *BC* is significantly greater than that for the two column members then members *AB* and *CD* can be considered to act as fixed-fixed columns. Using this assumption the deflection δ_B and rotation θ_B at joint *B* in the global z direction can be described theoretically as:

$$\delta_B = \frac{PL^3(1+\Phi)}{24EI} \tag{7.5}$$

$$\theta_B \approx 0 \tag{7.6}$$

where L is the length of members AB and CD, and Φ is the Timoshenko shear coefficient of the member (Gere and Weaver, 1965). The stiffness at the joint is effectively double that for a single fixed-fixed column as both columns are resisting the load.

Using the EBPM the same frame can be created using four particles and three bonds as shown in Figure 7.5. All the bonds are given the same material properties, $E_b = 200$ GPa, $\nu_b = 0.3$ and shear form factor, while the geometric properties of the members differ, as shown in Figure 7.5.

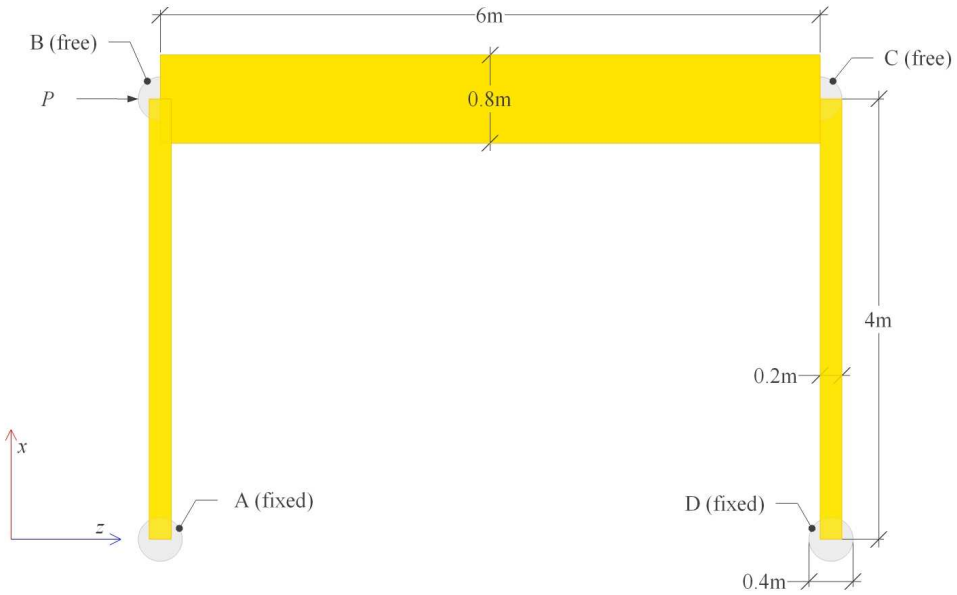

Figure 7.5 DEM representation of a single story frame structure, the two columns have the same geometrical properties

If an external horizontal force of 100 kN is applied to particle B, the DEM predicted deflection of particle B is 17.14 mm which is only 0.4% higher than the theoretical value of 17.07 mm, while the rotation of particle B is only 0.0018827 degrees, which is not significantly above zero.

The lateral displacement of node B decreases as the flexural stiffness of the bond between particles *B* and *C* representing the beam is increased, and the flexural stiffness of the other two bonds representing the columns remains constant. This is due to the fact that the behaviour changes from predominantly sway to predominantly beam bending and so the solution diverges from that of a fixed-free column to one in which the rotation at the top of the column is restrained to be zero, as can be seen in Figure 7.6.

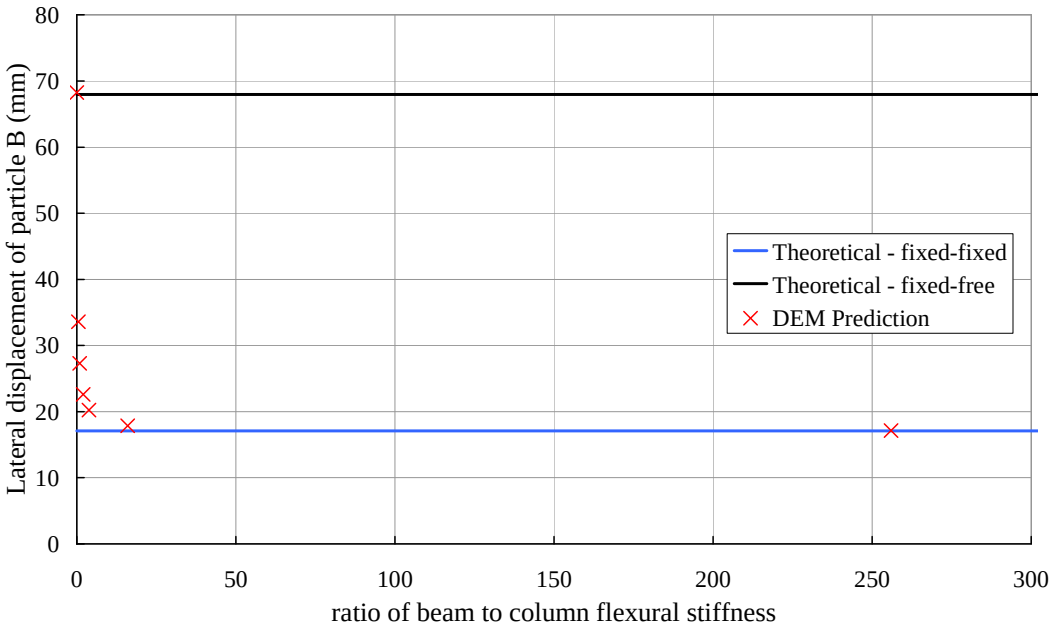

Figure 7.6 Lateral displacement of particle B, varying the ratio of beam to column flexural stiffness

Figure 7.7 shows the same results over a smaller range of beam to column flexural stiffness ratio to highlight that the combined mechanism is readily detected.

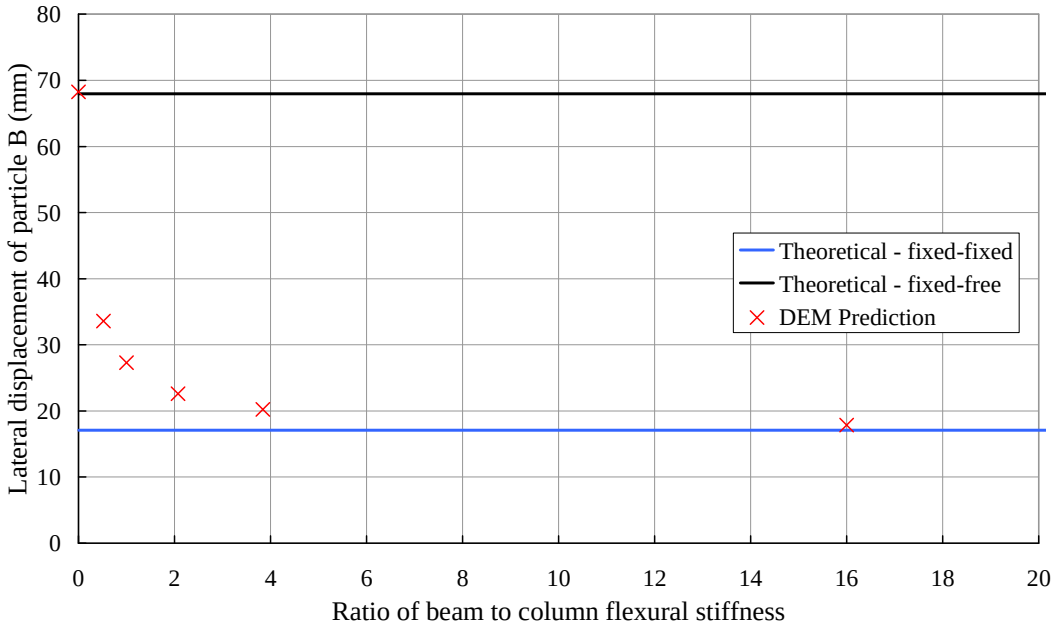

Figure 7.7 Lateral displacement of particle B, varying the ratio of beam to column flexural stiffness in the range zero to 20

7.1.3 Thin rectangular plates

Thin plates are structures for which one dimension (thickness) is much smaller than the other two dimensions (width and length). Plates are generally designed to resist distributed loads, applied normal to the plate surface, which cause transverse deflections; concentrated loads may lead to punching shear failure. Solutions, such as those compiled by Roark and Young (Young, 1989), can be used to determine the theoretical maximum deflection of plates under various loading conditions; the deflection is highly dependent on the boundary conditions imposed.

7.1.3.1 Representation of a plate

The EBPM which is based on a beam theory, cannot be used to directly reproduce the behaviour of a plate. Authors such as Yettram and Husain (1965) have shown that a plate can be represented as a grid of rectangular elements. In the representation

presented here a plate, of width a and length b, can be discretized into a grid of e_a by e_b elements each of length Δa and width Δb as shown in Figure 7.8(a). In the approximation using the EBPM the grid elements are replaced by a set of bonds which are rigidly connected by particles as shown in Figure 7.8(b).

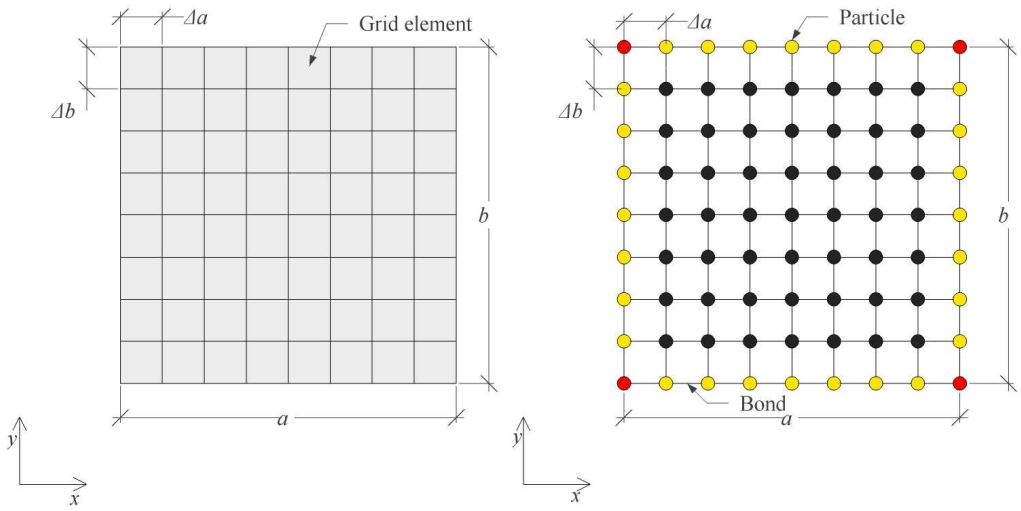

(a) A plate divided into e_a by e_b elements (b) DEM representation

Figure 7.8 Approximation of a plate using the EBPM

External forces can be applied to one or more particles (internal-unconstrained at boundaries, shown in black Figure 7.8(b)) to impose either a concentrated or distributed load. As the EBPM does not allow external forces to be applied to bonds; an even number of grid elements should be used when a single central point load is applied. Boundary conditions, such as fixed or simply supported, can be imposed by reducing the number of degrees of freedom the particles forming an edge or corner (yellow or red Figure 7.8(b)) have. The plates modelled in this study are all considered to be rectangular, of uniform thickness and isotropic.

In the EBPM approximation both the flexural rigidity and the axial stiffness of the bonds are matched to those for an equivalent span of the plate. For simplicity the grid

discretization will use square elements so that bonds running either parallel to the *x* or *y* axis will have the same properties. The flexural rigidity of the bonds can be determined so that for a single element of width Δb:

$$E_b I_b = \frac{E_b \pi r_b^4}{4} = \frac{E_{plate} t^3}{12\left(1-v_{plate}^{\ 2}\right)}\Delta b \tag{7.7}$$

Where E_b, I_b and r_b are the bond's Young's modulus, second moment of area and radius respectively and E_{plate}, v_{plate} and t are the plate's Young's modulus, Poisson's ratio and thickness respectively. The axial stiffness of the bond is also matched to that of the plate such that:

$$\frac{E_b \pi r_b^2}{L_b} = \frac{E_{plate} \cdot t \cdot \Delta b}{\Delta a} \tag{7.8}$$

Knowing that the bond length $L_b = \Delta b = \Delta a$ equation (7.8) can be simplified and rearranged in terms of E_b and then substituted into equation (7.7) to determine r_b, such that:

$$r_b = \sqrt{\frac{t^2}{3\left(1-v_{plate}^{\ 2}\right)}} \tag{7.9}$$

By substituting equation (7.9) into equation (7.8) E_b can be determined:

$$E_b = \frac{3E_{plate}\Delta b\left(1-\nu_{plate}{}^2\right)}{\pi t} \tag{7.10}$$

It can be seen from equation (7.9) that, unlike the bond's Young's modulus $E_{b,}$ the bond radius r_b is independent of the number of grid elements used.

7.1.3.2 Convergence test on a square fully fixed plate under central point load

A convergence test is conducted firstly to test the hypothesis that for a given loading and boundary conditions as the number of grid elements is increased the error between the DEM predicted and theoretical maximum deflection reduces. Secondly this enables the determination of a suitable number of elements required to provide a close approximation to the theoretical behaviour. It is unlikely that the DEM prediction will match the theoretical solution precisely as it does not include deflections due to shear; nevertheless a close approximation should be obtained. The convergence test uses a representation a fully fixed square plate subject to a central transverse load P. Using equations presented by Timoshenko and Woinowsky-Krieger (1959) the maximum theoretical displacement δ_{max} will occur at the centre of the plate, so that, assuming small deflections:

$$\delta_{\max} = \frac{kPb^2}{E_{plate}t^3} \tag{7.11}$$

where k is a numerical factor dependent on the ratio of the width to the length of the plate; in this instance k = 0.0611 for a square plate of a = b = 1 m. The parameters

plate are t = 0.005 m, E_{plate} = 20 GPa and v_{plate} = 0.3. When P = 50 N δ_{max}= 1.22 mm in the direction of the load.

The same plate is modelled using six different particle-bond configurations, each representing a different number of grid elements. Using equation (7.9) the r_b = 3.0261 mm for every bond in the simulation. The Poisson's ratio of the bonds v_b = 0.3 bond's Young's modulus, calculated using equation (7.10), varies depending on the number of grid elements used, the values are shown in Table 7.2.

Table 7.2 DEM predictions matching theory by increasing the number of element

Number of grid elements $e_a \times e_b$	Element length $\Delta a = \Delta b$ (mm)	Bond Young's modulus E_b (GPa)	DEM predicted deflection (mm)	Percentage error (%)
4×4	250.000	869	-1.3065	-6.92
8×8	125.000	435	-1.2925	-5.77
16×16	62.500	217	-1.2814	-4.86
20×20	50.000	174	-1.2796	-4.71
32×32	31.250	109	-1.2771	-4.51
64×64	15.625	54	-1.2753	-4.36

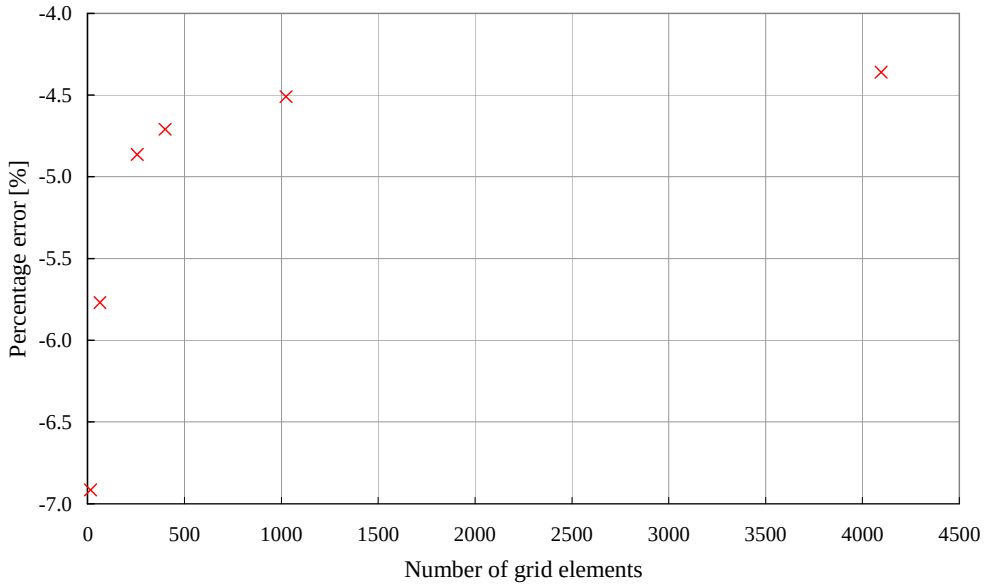

Figure 7.9 Percentage error between the DEM prediction and the chosen theoretical solution for increasing number of elements

Table 7.2 and Figure 7.9 show that as the number of elements in the DEM approximation is increased the percentage error between the EBPM prediction and the theoretical solution reduces. As the number of elements is increased in the model the stiffness of the model also increases, and deflections decrease. The resulting numerical solution still over-predicts the deflection due to assumptions made in the model. Using an element length of 31.25 mm for further study should allow a reasonable computational time without compromising accuracy.

7.1.3.3 Plates with different aspect ratios, boundary conditions and loading

The maximum displacement of a plate is highly influenced by loading and boundary conditions. In order to further test the EBPM approximation additional square and rectangular plates will be loaded either through either central concentrated load or a distributed load for combinations of fixed and simply supported edges.

Distributed loads acting on a plate cannot be directly modelled using the EBPM plate approximation method. Instead point loads of magnitude Q are applied to all of the free particles forming the plate, to represent a distributed load q acting on an area around each particle. Transverse deflections of edge particles are restricted, so no load will be applied to a small area around the edge of the plate.

$$Q = q \cdot \Delta a \cdot \Delta b \tag{7.12}$$

The ratio of the load being applied to the missing load can be determined, such that:

$$\frac{(e_a - 1)(e_b - 1)}{(e_a + e_b - 1)} \tag{7.13}$$

In the following set of tests when a square plate is considered (e_a = e_b = 32) the ratio of area loaded to unloaded is 15.25:1. This ratio increases to 18.44:1 when a rectangular plate is used (e_a= 48, e_b= 32). Rectangular plates used are usually restricted to a span ratio of no more than 1:1.5 as plate action is less efficient at higher ratios.

As in the convergence test, the plates used in these tests are considered to all be of uniform thickness and made of a homogeneous isotropic material. Fixed supports are created by restricting particles that form that edge so that they cannot rotate or displace. The particles representing a simply supported edge are allowed to rotate about the longitudinal axes of the edge. At corners the more severe boundary condition is applied – e.g. where a fixed edge meets a simply supported edge the particle at the corner is considered to be completely fixed. The theoretical solutions to the plate cases shown in Table 7.4 are taken from Young (1989) and Timoshenko and Woinowsky-Krieger (1959). Table 7.3 summarises the plate properties that are

being used in the theoretical solution. The DEM predicted maximum deflections and percentage errors from the theoretical results are shown in Table 7.3.

Table 7.3 Plate properties for theoretical solutions

Parameter	Description	Square plate	Rectangular plate
E_{plate}	Plate Young's modulus (GPa)	20	20
t	Plate thickness (m)	0.005	0.005
a	Plate width (m)	1	1.5
b	Plate length (m)	1	1
P	Concentrated central load (N)	-25	-25
q	Distributed load over whole plate (N/m^2)	-50	-50

Table 7.4 DEM predictions matched to theoretical solutions for a number of plate loading and support conditions

Plate shape and boundary conditions S = simply supported	Case No.	Loading conditions	Theoretical maximum deflection	DEM predicted deflection (mm)	Percentage error (%)
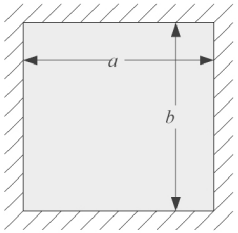	1a	P = -50N	$\delta_{\max} = \frac{0.0611 P b^2}{E_{plate} t^3}$	-1.28	-4.51
	1b	q = -100N/m^2	$\delta_{\max} = \frac{0.0138 q b^4}{E_{plate} t^3}$	-0.55	-5.42
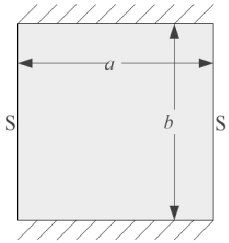	2a	P = -50N	$\delta_{\max} = \frac{0.07678 P b^2}{E_{plate} t^3}$	-1.58	-2.72
	2b	q = -100N/m^2	$\delta_{\max} = \frac{0.0210 \cdot q b^4}{E_{plate} t^3}$	-0.88	-4.15
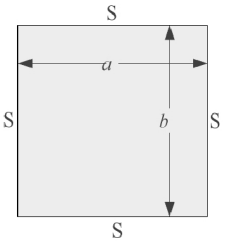	3a	P = -50N	$\delta_{\max} = \frac{0.1267 \cdot P b^2}{E_{plate} t^3}$	-2.35	7.11
	3b	q = -100N/m^2	$\delta_{\max} = \frac{0.0444 \cdot q b^4}{E_{plate} t^3}$	-1.72	3.41

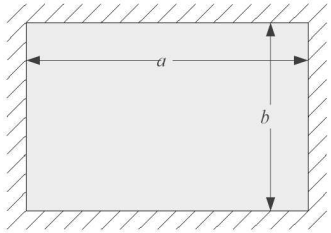	4a	P = -25N	$\delta_{\max} = \frac{0.07655\,Pb^2}{E_{plate}t^3}$	-0.80	-5.16
	4b	q = -50N/m^2	$\delta_{\max} = \frac{0.02385\,qb^4}{E_{plate}t^3}$	-0.50	-4.54
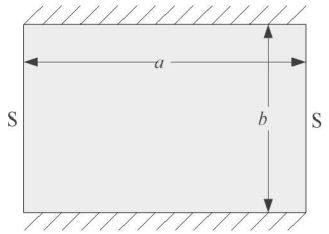	5a	P = -25N	$\delta_{\max} = \frac{0.07748Pb^2}{E_{plate}t^3}$	-0.83	-6.87
	5b	q = -50N/m^2	$\delta_{\max} = \frac{0.02675qb^4}{E_{plate}t^3}$	-0.56	-4.15
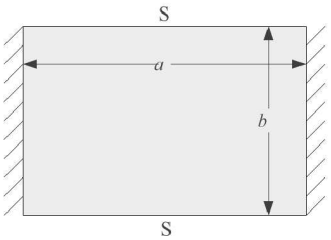	6a	P = -25N	$\delta_{\max} = \frac{0.06393Pa^2}{E_{plate}t^3}$ *	-1.40	-4.94
	6b	q = -50N/m^2	$\delta_{\max} = \frac{0.058\cdot qb^4}{E_{plate}t^3}$	-1.19	-2.76
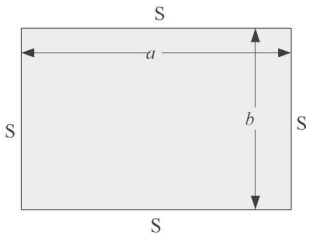	7a	P = -25N	$\delta_{\max} = \frac{0.1668\,Pb^2}{E_{plate}t^3}$	-1.66	0.70
	7b	q = -50N/m^2	$\delta_{\max} = \frac{0.0838\,qb^4}{E_{plate}t^3}$	-1.61	4.18

* This equation uses the width rather than length as it can be considered in a similar manner to case 5a but with the ratios switched.

The maximum deflection is always determined to be at the centre of the plate; static conditions are assumed to exist in the model when the largest particle velocity is 1×10^{-6} mm.s^{-1}. This ensures that no further deflection is likely to significantly affect the results. Considering all of the approximations that are made in the EBPM representation most of the results are below a 10% error to the theoretical solution. This shows that the EBPM can be used to approximate the behaviour of plate structures.

Further investigation could be conducted to include the additional benefit of using diagonal members to represent torsional behaviour. Further, this study has been restricted to comparison of the primary variable and the examination of the displacements of the plate and not the internal stresses.

7.1.4 Circular rings

Circular rings are important elements in various structures such as pipelines, tanks and silos. It is often important to know the deflections of rings under various loading and support conditions; theoretical solutions to these problems can be found in literature such as Young (1989).

The response of a circular ring to load can be modelled using the EBPM by bonding a series of particles together to form a closed loop. In the example shown in Figure 7.10, 64 particles are connected by 65 bonds forming a ring in the XY plane. External forces can be applied to particles in order to simulate loading conditions with the resulting displacements recorded.

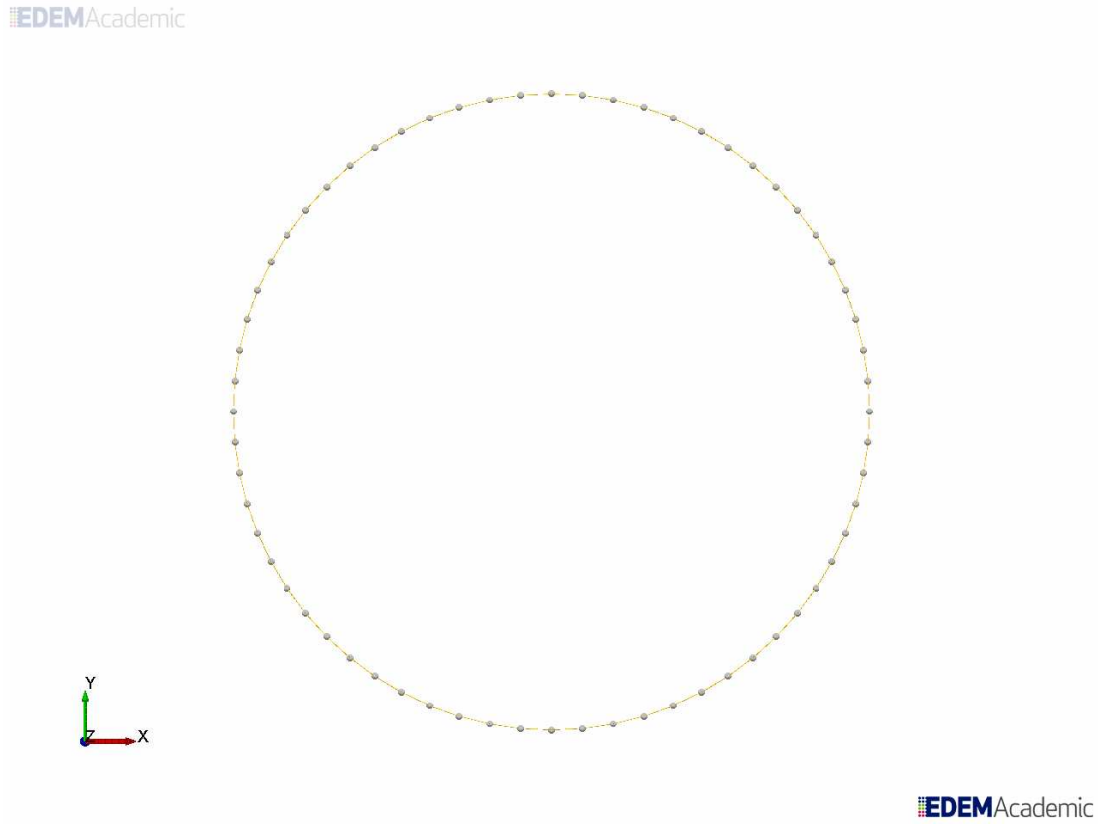

Figure 7.10 Using the EBPM to form a representation of a circular ring

The theoretical solution which describes the change in vertical and horizontal diameter of the ring, D_v and D_h respectively, caused by two loads of magnitude P acting on the surface of the ring, as shown in Figure 7.11, is presented in Young (1989), such that:

$$D_H = 0.1366 \frac{PR^3}{EI} \tag{7.14}$$

$$D_V = -0.1488 \frac{PR^3}{EI} \tag{7.15}$$

The horizontal diameter is taken as the distance between points D and B in Figure 7.11 and the vertical diameter is taken as the distance between points A and C in Figure 7.11. An increase in diameter is positive and a decrease negative.

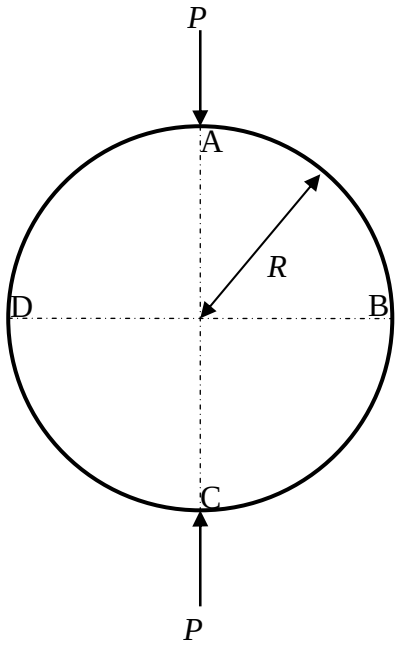

Figure 7.11 Loading configuration for a circular ring

The same loading conditions can be created using the EBPM and, unlike the modelling of plates (as shown in section 7.1.3), no modification of the bond stiffness is required as the ring can be assumed to have a circular cross section like the bonds. The ring created for this study consists of 64 particles connected by 65 bonds arranged on the XY plane so that the radius to the centroid of the cross section $R = 51$ mm. A relatively large number of particles are used to create the ring so as to reduce potential errors resulting in the fact that the bonds are straight and do not follow the curvature of the circle exactly. The bonds all have radius $r_b = 0.5$ mm, length $L_b = 5$ mm, Young's modulus $E_b = 200$ GPa, Poisson's ratio $\nu_b = 0.3$ and are assumed not to be able to fail. Equal and opposite external forces acting vertically are applied to the two particles forming the top and bottom apexes of the ring; the deformed positions of these particles and the particles that form the horizontal

diameter are used to determine the change in horizontal and vertical diameter and are compared against the theoretical values determined using (7.14) and (7.15). The results for five different external loads are shown in Table 7.5.

Table 7.5 DEM predictions and theoretical solutions for pinch loading over a ring under increasing loads

External load W (N)	Theoretical D_H (mm)	DEM predicted D_H (mm)	Percentage difference D_H (%)	Theoretical D_V (mm)	DEM predicted D_V (mm)	Percentage difference D_V (%)
0.2	0.3691	0.3692	-0.02	-0.4021	-0.4038	-0.42
0.4	0.7383	0.7402	-0.26	-0.8042	-0.8126	-1.04
0.6	1.1074	1.1124	-0.45	-1.2063	-1.2264	-1.66
0.8	1.4766	1.4862	-0.65	-1.6084	-1.6452	-2.29
1.0	1.8458	1.8614	-0.85	-2.0105	-2.0690	-2.91

As can be seen from Table 7.5, as the load is increased the percentage difference increases linearly. The error is also different for vertical and horizontal deflection. It is thought that the error may be caused by geometric non-linearity. When a small load is applied there is a small deflection. When a slightly larger load is applied a much greater deflection results, as the loading conditions are not the same.

These could be reduced by using more particles to reduce the beam length and decrease the misaligned beams. Instead of modelling a perfect circle the model is really creating a polygon with 65 sides, and by increasing the number of particles a closer representation of the circular ring would be obtained.

In order to highlight the deformed ring shape more clearly the displacement of the particles has been multiplied 5 times and plotted against the initial positions as shown in Figure 7.12. This is for a loading of 1.0 N.

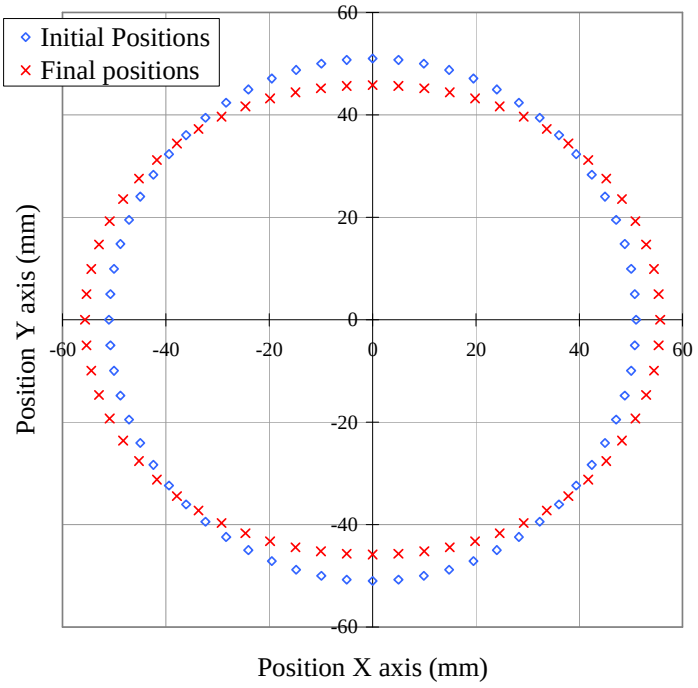

Figure 7.12 Comparison of initial and final positions of the particles making up the ring

This subchapter has highlighted that that the EBPM has the potential to model thin-walled shell structures and investigate bulk solids - structure interaction in detail. Demonstrating this further than that which has been described here is beyond the scope of this study but is clearly possible.

7.2 Application to additional cementitious material problems

In Chapter 6, the EBPM was successfully used to model the uni-axial compression of concrete cylinders and was shown above to be able to model the deformation of some simple structural elements in the elastic region within limits. This section presents the application of the EBPM for three further cases. They are modelling: the quasi-static loading of other concrete specimens, the dynamic loading of concrete specimens and finally the behaviour of composite materials, in this instance fibre reinforced polymer (FRP) strengthened concrete. These additional example

applications only show the potential capabilities of the EBPM, and again an in depth study is not included here.

7.2.1 Loading of concrete specimens

In Chapter 6 the EBPM was used to model the uni-axial compression of concrete cylinders. However, this is not the only way to determine the strength properties of concrete; in the United Kingdom the compressive strength is often determined through the uni-axial compression of cubes and the tensile strength is determined through tensile splitting tests of cylinders, both are described in The British Standards, (BS EN 12390-3, 2012; BS EN 12390-6, 2012). By simulating other loading tests the results can be compared to those for the uni-axial compression cylinder tests. Relationships exist relating the strengths determined from different tests e.g. in Elwell and Fu, (1995).

A 15 mm thin slice concrete cube has been constructed using 3 mm diameter particles connected by a dense network of bonds. The specimen is loaded uni-axially, this is only a pseudo 2D specimen so full 3D behaviour should not be expected. The development of the main crack that forms, as well as a number of perpendicular cracks that form are shown in Figure 7.13.

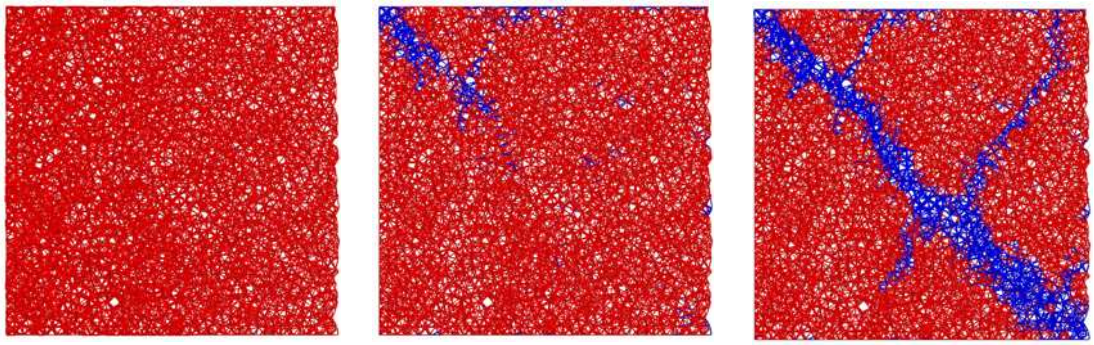

(a) initial bond network (b) crack initiation (c) final crack pattern

Figure 7.13 Modelling of uni-axial compression test of concrete cube, red lines are intact bonds and blue are broken bonds

The tensile strength of concrete is rarely determined directly, instead indirect methods, such as the tensile splitting test are used (BS EN 12390-6:2009), with relationships available to relate to the true tensile strength. Empirical relationships are available to link the compressive and tensile strengths for a given sample of concrete. In the example shown in Figure 7.14 a 15 mm thin slice cylinder has been assembled of 3 mm diameter mono-sized particles. Two plates load the specimen mimicking the physical test described in BS EN 12390-6:2009.

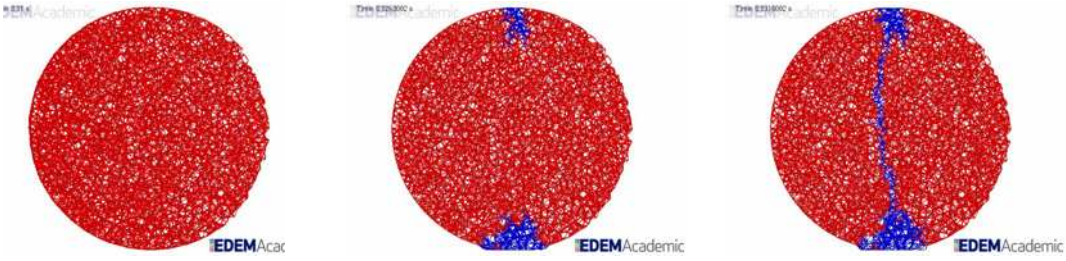

(a) initial bond network (b) crack initiation (c) final crack pattern

Figure 7.14 Modelling of tensile splitting test of concrete cylinder, looking through the cross section red lines are intact bonds and blue are broken bonds

As can be seen from Figure 7.14 there is a qualitative match between the crack pattern predicted by the model and that observed in practice.

7.2.2 Impact loading of cementitious materials

One potential application of the EBPM is for it to be used to investigate dynamic loading of cementitious materials. Various authors, such as Camborde et al., 2000; Donzé, et al., 2004; Qin and Zhang, 2011, have studied the dynamic loading of cementitious materials using DEM, however there is plenty of scope for improvement, especially in the modelling of the breakage of material. In industries such as mining and pharmaceuticals rocks or pills can be represented as an agglomerate of DEM particles forming a cluster particle. The breakage of these

cluster particles, either through impact with each other or another object, can be modelled, and the breakage studied. In the DEM simulations solid projectiles are impacted against concrete cylinders and the resulting damage and crack patterns recorded, a preliminary quantitative study shows how these crack patterns develop and are reliant on impact velocity. In the example shown in Figure 7.15 a steel ball is projected towards a concrete disk made by bonding together mono-size particles, the crack pattern that develop from the impact can be recorded.

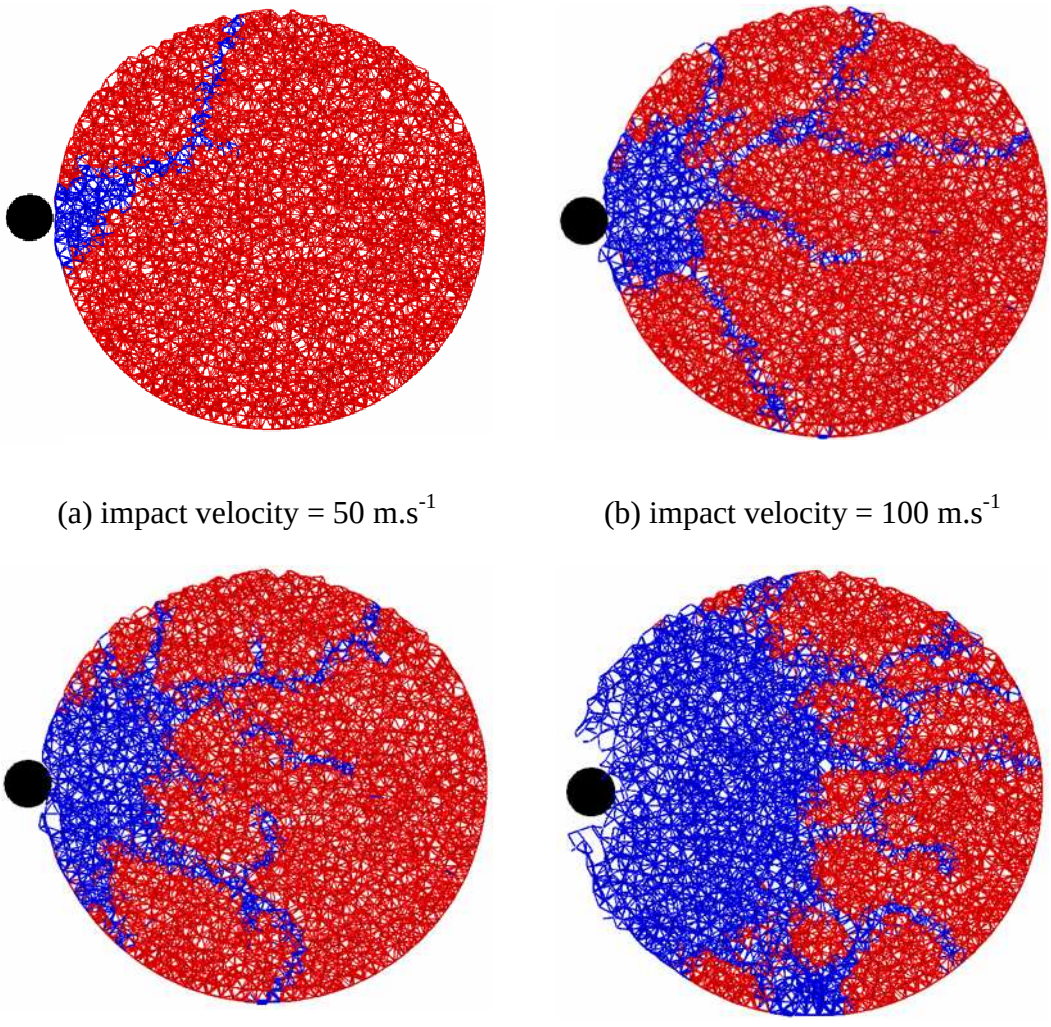

(a) impact velocity = 50 $m.s^{-1}$ (b) impact velocity = 100 $m.s^{-1}$

(c) impact velocity = 150 $m.s^{-1}$ (d) impact velocity = 500 $m.s^{-1}$

Figure 7.15 Influence of impact velocity on the breakage of bonds (red lines represent intact bonds and blue lines represent broken bonds)

As can be seen in Figure 7.15 as the impact velocity is increased the breakage of bonds becomes more severe. This example shows that there is significant potential for the EBMP to be used to model the impact loading.

7.2.3 Loading of Fibre Reinforced Polymers bonded to concrete

Fibre reinforced polymer (FRP) composites provide a relatively new and economical means of strengthening and repairing structures and has become a popular technique (Yao et al., 2005). Traditional studies of the behaviour of FRP reinforced concrete include using fracture mechanics analysis, finite element analysis and empirical models. One experimental test that is conducted for FRP-concrete composites is a near-end supported single shear test, such as presented by Yao et al. (2005). A representation of this test using the EBPM is shown in Figure 7.16.

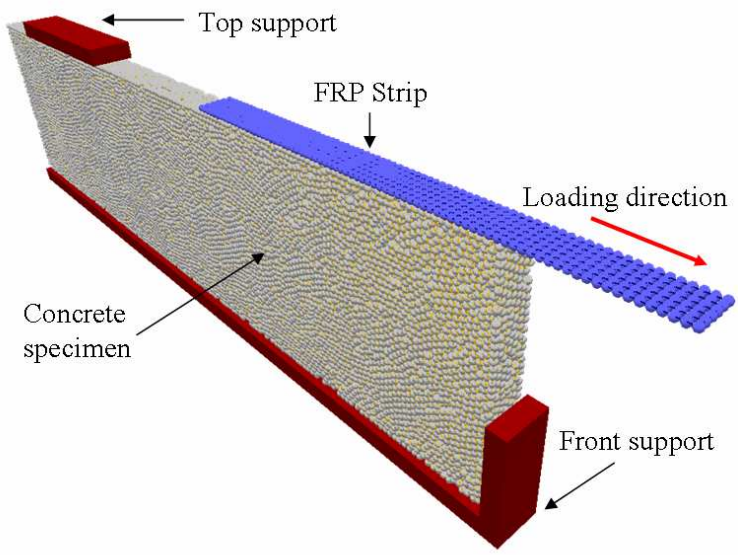

Figure 7.16 DEM representation of a near-end supported single shear test

The DEM representation shown in Figure 7.16 is only a thin slice of the full experimental test, this was done due to reduce the computational time required as the specimen already contains approximately 43,000 particles and almost 200,000 bonds.

In this simulation three types of bonds are considered: inter-FRP particle bonds, inter-concrete particle bonds and those between FRP and concrete particles. The recorded damage in one specimen is shown in Figure 7.17.

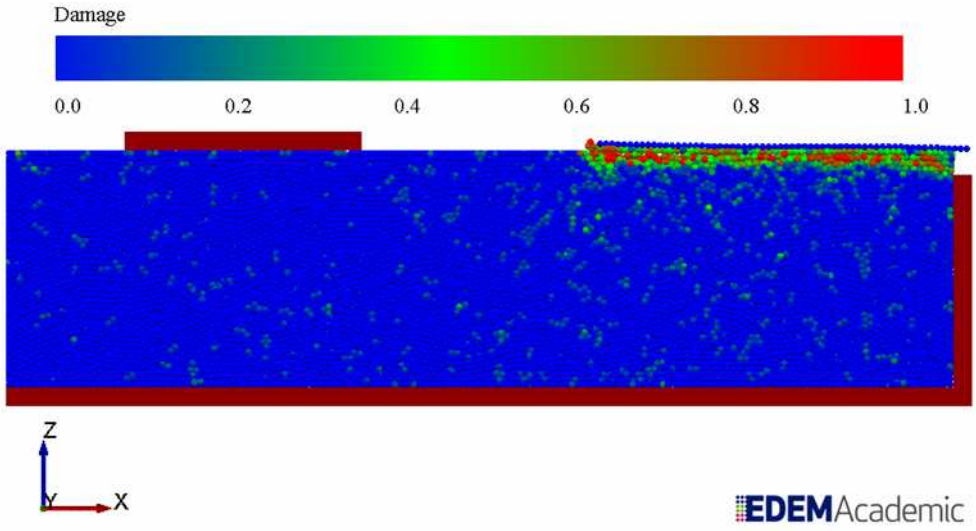

Figure 7.17 Damage to the top concrete layer

As can be seen in Figure 7.17 the failure of the system is the result of bond breakage in the top layer of concrete rather than at the bonds between the concrete and the FRP. This qualitatively matches one of the types of failure seen in physical experiments. This example shows the potential for the EBPM to be applied to the modelling of FRP composite concrete.

7.3 Summary

The first section of this chapter has shown that the EBPM can be used to model structural elements. The examples shown were in both two and three dimensions. Whilst the work was limited to the elastic region, whilst within this region a strong agreement was found between DEM predictions and classical solutions. The

modelling of cementitious materials beyond concrete cylinders has also been demonstrated, with DEM predictions matching known behaviour extremely well.

This chapter has shown that the DEM framework developed above can be applied to a range of problems. Further studies leading to the development of these methods is beyond the scope of this thesis. There is also the potential for modelling structures and interactions not shown here. The potential for modelling bulk solids-structure interaction can be improved by including a structure, such as a silo, at the same length scale as that of the material in the silo material.

Chapter 8 Conclusions and recommendations for future research

8.1 General

This thesis has presented the development, implementation, verification and validation of a novel bonded particle model that enables the study of cemented particulates and deformable structures using the Discrete Element Method (DEM) in three dimensions; the focus, however, is placed on modelling the behaviour of cementitious materials. The developed model, the Edinburgh Bonded Particle Model (EBPM), has been successfully implemented into the verified commercial software EDEM (DEM Solutions, 2008). The key element of the EBPM is the way in which inter-particle bonds are treated as Timoshenko beam elements to describe the behaviour at bonded contacts. This has been shown to be a successful method within an already successful DEM model which allows for the analysis of relatively complex materials and structures.

Existing DEM methods for modelling cementitious materials and their basis have been examined in Chapter 2, including a detailed investigation of the current bonded particle model in the EDEM code. The EDEM bonded model was found to be unsuitable for use in this study which led to the development of the EBPM model in this thesis.

The fundamentals of the theory underpinning the new EBPM model development are described in Chapter 3 along with the implementation of the model into the EDEM code. A thorough verification of the EBPM model and its implementation are given in Chapter 3. The model uses the Timoshenko Beam Bonded Contact Model (TBBM) to describe the behaviour for bonded contacts and the well used Hertz-Mindlin Contact Model (HMCM) to describe the behaviour for non-bonded contacts.

Along with the input parameters for both of these models there are additional parameters which influence the initial bond network for a given particle arrangement and also some that influence the numerical stability of the simulations. In order to determine the influence of these model parameters when modelling cementitious materials, a full parametric study was conducted. Chapter 4 presented the formulation of a reference case specimen and defined the bulk properties that were used to describe quantitatively the bulk behaviour of a cylindrical specimen of concrete under uni-axial compression; these included the ultimate strength, the strain at failure, the bulk secant modulus and the bulk Poisson's ratio. The bulk behaviour predicted by simulations using the reference case set of parameters showed a reasonable match to those using the Eurocode equation. This enabled the reference case to be used in a detailed and full parametric investigation which was presented in Chapter 5.

Overall the parameters that were considered in the parametric study could be divided into categories depending on what aspect of the model they affect: the TBBM calculations, the HMCM calculations, the initial bond fabric and the numerical stability of the model. The model has proved to be versatile enough so that a wide range of cementitious material behaviour can be predicted whilst only using a single initial particle packing and initial bond fabric. A relatively high level of confidence can be placed in the results as no numerical instability was noted during the parametric study. It was found that most of the model input parameters had an influence on the predicted ultimate strength or the predicted bulk secant modulus and these collectively affect the strain at failure. Changes in the predicted bulk stiffness were related to changes in the stiffness of the bond fabric, caused by the number of the bonds, the slenderness of the bonds and the stiffness properties such as Young's modulus. An increase in predicted ultimate strength was seen when either the strength of the bonds was increased, e.g. an increase in the mean bond tensile strength or when the stresses generated in the bonds were lower e.g. when there were more bonds in the fabric, the cross sectional area was greater or there was a higher load carrying contribution made by non-bonded contacts. No parameters appeared to

have a significant influence on the bulk Poisson's ratio, it was suggested that the value of this property arise from the initial particle assembly.

For most simulations the majority of bonds failed in tension, leading to an inclined failure plane (shear crack) forming. The only exception to this was when either the compressive or shear strength of the bonds was set relatively low when compared to the tensile strength. This normally led to a thin horizontal crack forming at the mid-height of the specimen. Overall the input parameters that were found to have the biggest influence on the bulk properties were the bond Young's modulus, the mean bond tensile and shear strength, the coefficient of variation of tensile and shear strength and the contact radius multiplier.

Chapters 6 and 7 demonstrate the application of the model to a sample of problems. In Chapter 6 the application is to cementitious materials, specifically a model calibration procedure for the uni-axial compression of a concrete cylinder in which the predicted bulk response of the model was matched to the behavioural prediction provided by the Eurocode. The parametric study determined that there are many parameters which have some influence on the bulk response. However, to simplify the model the value of the less influential parameters were kept constant in the calibration procedure. This meant that there was a consistent particle packing and initial bond fabric; the bulk behaviour was controlled only by the bond Young's modulus and the mean bond tensile strength, some of the remaining parameters were linked to these variables. In Chapter 6 it was proven that the model is capable of matching the prediction of ultimate strength and bulk secant modulus made by the Eurocode for a series of cylinders with increasing target strength of between 10 MPa and 100 MPa: this tested the model over an order of magnitude in the bulk strength prediction. Matching the strain at ultimate strength still presents a challenge as the model under predicts the rate of stiffness predicted by the Eurocode. This may be solved with the inclusion of a softening term for the bonds as discussed below.

In Chapter 7 the model is applied with some success to "conventional" structural analysis of beams, frames and plates. There is also a brief study of the use of the

method to the development of shell-like structures. While the analysis is restricted at this stage to elastic behaviour, the success of the method is quite clear. Some additional example applications are also included, such as impact loading, and the development of a model for simulating the interaction of fibre reinforced polymers with concrete. These example applications suggest that the model has applications beyond the quasi-static loading of cementitious materials.

8.2 Conclusions

A number of conclusions can be drawn from this study, these have been summarised below:

- A new bonded particle model has been developed which is based on sound engineering theory.
- The new model has been implemented in a verified commercial code.
- The key parameters that affect this model when used for modelling cementitious materials are examined.
- A random component in bond strength (coefficient of variation) has been introduced which leads to a more realistic stiffness response observed on the macroscopic scale.
- It has been demonstrated that by varying only four key parameters (whilst keeping the remaining parameters within limits), a significant spectrum of concrete bulk responses can be represented.
- This thesis has showed how this model could be used for predicting the behaviour of linear elastic structural elements.
- The model provides the framework for other applications including granular solid and structure interaction which can both be modelled in the same DEM framework.

8.3 Future Work

This thesis has shown the development, implementation, verification and validation of a new bonded particle model. The application of this model for studying both cementitious materials and simple structural elements has been demonstrated. However, there are several areas of further research which could enhance the model to reduce limitations, to improve its current capabilities or to add new capabilities.

When used to model cementitious materials, the EBPM tends to under-predict the loss of stiffness, even if there is progressive bond breakage induced by including a coefficient of variation of bond strength. As the bonds themselves are linear elastic when modelling structural elements only linear behaviour can be observed. To enhance the model's capabilities, it is suggested that a non-linear term is added to the stiffness calculation. In this manner the model may incorporate an element of material non-linearity for modelling the ductility of concrete more accurately. Examples of including non-linear stiffness terms can be found in the literature, e.g. Ergenzinger et al. (2011) and Schneider et al. (2010). The strength or stiffness of each bond can be changed depending on a number of factors, including the strain in the bond or the damage in the local area. Another option is to include bond fatigue whereby the maximum stress is remembered and the stiffness is altered accordingly.

The work on cementitious materials was limited to the uni-axial compression of a concrete cylinder. The developed model could be used to model other tests including Brazilian tension tests, or cube compression tests, in this manner the relationships between predicted strengths from these tests can be compared to those for physical specimens.

Although the parametric study investigated the majority of model parameters the specimen properties remained the same. The influence of particle packing properties such as particle size, dispersion factor and specimen size could all be considered and the influence noted. The parametric study presented in Chapter 5 did investigate how varying the number and size of bonds in the fabric influenced the bulk response. However, although relationships were found between the input parameters and bulk

response it would be interesting to investigate if this could be related to a physical property of the material.

One of the limitations of the developed model is the need for a relatively complex calibration procedure to determine the bond parameters to produce the desired behaviour for a given specimen. Although a method for determining these properties has been outlined there is the potential for this procedure to be simplified possibly through the elimination of parameters.

For the purposes of this study it was appropriate to model concrete as a single phase material with each particle representing a portion of its assembled constituent parts. It would be possible to use the developed model to further study the initiation and propagation of cracks at the interface between aggregate and hardened cement paste by representing both of these phases with particles.

There is also the potential for the range of applications of the model to be extended, especially for more complex structures (collapse of frames), more complex materials (cancellous bone) and the interaction between granular materials and structures (silos).

Chapter 9 References

Akçaoğlu, T., Tokyay, M., and Çelik, T. (2005). Assessing the ITZ microcracking via scanning electron microscope and its effect on the failure behavior of concrete. *Cement and Concrete Research*, *35*(2), 358–363. doi: 10.1016/j.cemconres.2004.05.042

Akroyd, T. N. W. (1962). *Concrete: Properties and Manufacture* (p. 336). Pergamon Press.

André, D., Iordanoff, I., Charles, J., and Néauport, J. (2012). Discrete element method to simulate continuous material by using the cohesive beam model. *Computer Methods in Applied Mechanics and Engineering*, *213-216*, 113–125. doi: 10.1016/j.cma.2011.12.002

Antonyuk, S., Khanal, M., Tomas, J., Heinrich, S., and Mörl, L. (2006). Impact breakage of spherical granules: Experimental study and DEM simulation. *Chemical Engineering and Processing: Process Intensification*, *45*(10), 838–856. doi: 10.1016/j.cep.2005.12.005

Azevedo, N. M., Lemos, J. V., and De Almeida, J. R. (2008). Influence of aggregate deformation and contact behaviour on discrete particle modelling of fracture of concrete. *Engineering Fracture Mechanics*, *75*(6), 1569–1586. doi: 10.1016/j.engfracmech.2007.06.008

Bagi, K. (2005). An algorithm to generate random dense arrangements for discrete element simulations of granular assemblies. *Granular Matter*, *7*(1), 31–43. doi: 10.1007/s10035-004-0187-5

Bamforth, P., Chisholm, D., Gibbs, J., and Harrison, T. (2007). *Properties of concrete for use in Eurocode2*. The Concrete Centre.

Bauchau, O., and Craig, J. (2009). Structural Analysis. (O. A. Bauchau and J. I. Craig, Eds.)*Solid Mechanics and Its Applications*, *163*, 173–221. Dordrecht: Springer Netherlands. doi: 10.1007/978-90-481-2516-6

Bažant, Z. P., Pang, S. D., Vorechovsky, M., Novak, D., and Pukl, R. (2004). Statistical size effect in quasibrittle materials: Computation and extreme value theory. *Fracture Mechanics of Concrete Structures* (Vol. 1, pp. 189–196).

Bažant, Z. P., Tabbara, M. R., Kazemi, M. T., and Pyaudier-cabot, G. (1991). Random particle model for fracture of aggregate or fiber composites. *Journal of Engineering Mechanics*, *116*(8).

Breugnot, A., Gotteland, P., and Villard, P. (2010). Numerical modelling of impacts on granular materials with a combined discrete – continuum approach. In Benz and Nordal (Eds.), *Numerical Methods in Geotechnical Engineering*. London: Taylor and Francis Group.

BS EN 12390-3. (2012). *Testing hardened concrete - Part 3: Compressive strength of test specimens*.

BS EN 12390-6. (2012). *Testing hardened concrete - Part 6: Tensile splitting strength of test specimens*.

BS EN 1992-1-1. (2004). *Eurocode 2: Design of concrete structures - Part 1-1: General rules and rules for buildings*.

Buyukozturk, O., Nilson, A., and Slate, F. (1971). Stress-strain response and fracture of a concrete model in biaxial loading. *ACI Journal*.

Caballero, A., López, C. M., and Carol, I. (2006). 3D meso-structural analysis of concrete specimens under uniaxial tension. *Computer Methods in Applied Mechanics and Engineering*, *195*(52), 7182–7195. doi: 10.1016/j.cma.2005.05.052

Camborde, F., Mariotti, C., and Donze, F. V. (2000). Numerical study of rock and concrete behaviour by discrete element modelling. *Computers and Geotechnics*, *27*.

Carmona, H. A., Wittel, F. K., Kun, F., and Herrmann, H. J. (2008). Fragmentation processes in impact of spheres. *Physical Review E*, *77*(5). Statistical Mechanics, . doi: 10.1103/PhysRevE.77.051302

Cho, N., Martin, C. D., and Sego, D. C. (2007). A clumped particle model for rock. *International Journal of Rock Mechanics and Mining Sciences*, *44*(7), 997–1010. doi: 10.1016/j.ijrmms.2007.02.002

Chung, Y. C., and Ooi, J. Y. (2011). Benchmark tests for verifying discrete element modelling codes at particle impact level. *Granular Matter*, *13*(5), 643–656. doi: 10.1007/s10035-011-0277-0

CIMNE. (2010). DEMpack. Retrieved from www.cimne.upc.edu/dempack

CIMNE. (2012). GiD. Engineering, International Center for Numerical Methods in Engineering. Retrieved from www.gidhome.com

Crisfield, M. A. (1997). *Non-linear finite element analysis of solids and structures, Volume 2* (p. 508). Wiley.

Cundall, P A. (1971). A Computer model for simulating progressive large scale movement in blocky rock systems. *Proceedings of the Symposium of the International Society of Rock Mechanics, Nancy, Fra*.

Cundall, P., and Strack, O. (1979). A discrete numerical model for granular assemblies. *Geotechnique*, *29*(1), 47–65.

Cundall, P.A., and Hart, R. D. (1992). Numerical Modelling of Discontinua. *Engineering Computations*, *9*(2), 101–113. MCB UP Ltd. doi: 10.1108/eb023851

D'Addetta, G. A., Kun, F., and Ramm, E. (2002). On the application of a discrete model to the fracture process of cohesive granular materials. *Granular Matter*, *4*(2), 77–90. doi: 10.1007/s10035-002-0103-9

D'Addetta, G. A., and Ramm, E. (2006). A Microstructure-based Simulation Environment on the Basis of an Interface Enhanced Particle Model. *Granular Matter*, *8*(3-4), 159–174. doi: 10.1007/s10035-006-0004-4

DEM.Solutions. (2008). EDEM 2.1 User Guide. DEM Solutions.

DEM.Solutions. (2010). EDEM 2.3. Edinburgh: DEM Solutions.

Dhir, R. K., and Sangha, R. M. (1974). Development and propagation of microcracks in plain concrete. *Matériaux et Constructions*, *7*(1), 17–23. doi: 10.1007/BF02482676

Diamond, S. (2004). The microstructure of cement paste and concrete—a visual primer. *Cement and Concrete Composites*, *26*(8), 919–933. doi: 10.1016/j.cemconcomp.2004.02.028

Dolado, J. S., and Van Breugel, K. (2011). Recent advances in modeling for cementitious materials. *Cement and Concrete Research*, *41*(7), 711–726. doi: 10.1016/j.cemconres.2011.03.014

Du, X., Jin, L., and Ma, G. (2013). Macroscopic effective mechanical properties of porous dry concrete. *Cement and Concrete Research*, *44*(0), 87–96. doi: http://dx.doi.org/10.1016/j.cemconres.2012.10.012

Elwell, D. J., and Fu, G. (1995). *Compression Testing of Concrete: Cylinders vs. Cubes*. New York.

Ergenzinger, C., Seifried, R., and Eberhard, P. (2011). A discrete element model to describe failure of strong rock in uniaxial compression. *Granular Matter*, *13*(4), 341–364. doi: 10.1007/s10035-010-0230-7

Gere, J. M., and Timoshenko, Stephen P. (1990). *Mechanics of materials* (3rd ed., p. 807). PWS-KENT Pub. Co.

Gere, J. M., and Weaver, W. (1965). *Analysis of framed structures* (p. 475). Van Nostrand.

Groh, U., Konietzky, H., Walter, K., and Herbst, M. (2011). Damage simulation of brittle heterogeneous materials at the grain size level. *Theoretical and Applied Fracture Mechanics*, *55*(1), 31–38. doi: 10.1016/j.tafmec.2011.03.001

He, H., Guo, Z., Stroeven, P., Stroeven, M., and Sluys, L. J. (2009). Characterization of the packing of aggregate in concrete by a discrete element approach. *Materials Characterization*, *60*(10), 1082–1087. doi: 10.1016/j.matchar.2009.02.012

Hentz, S., Daudeville, L., and Donzé, F.-V. (2004). Identification and Validation of a Discrete Element Model for Concrete. *Journal of Engineering Mechanics*, *130*(6), 709–719. doi: 10.1061/(ASCE)0733-9399(2004)130:6(709)

Hentz, S., Donzé, F. V., and Daudeville, L. (2004). Discrete element modelling of concrete submitted to dynamic loading at high strain rates. *Computers & Structures*, *82*(29-30), 2509–2524. doi: 10.1016/j.compstruc.2004.05.016

Hutchinson, J. R. (2001). Shear Coefficients for Timoshenko Beam Theory. *Journal of Applied Mechanics*, *68*(1), 87. doi: 10.1115/1.1349417

Ismail, Z. Z., and Al-Hashmi, E. A. (2008). Use of waste plastic in concrete mixture as aggregate replacement. *Waste management (New York, N.Y.)*, *28*(11), 2041–7. doi: 10.1016/j.wasman.2007.08.023

Itasca. (2001). PFC 2D. Minneapolis. Retrieved from http://www.itascacg.com/pfc3d/

Jerier, J.-F., Imbault, D., Donze, F.-V., and Doremus, P. (2009). A geometric algorithm based on tetrahedral meshes to generate a dense polydisperse sphere packing. *Granular Matter*, *11*(1), 43–52. doi: 10.1007/s10035-008-0116-0

Johnson, K. L. (1987). *Contact Mechanics* (p. 468). Cambridge University Press.

Johnstone, M. W. (2010). *Calibration of DEM models for granular materials using bulk physical tests*. *Philosophy*. The University of Edinburgh.

Jones, R. (1962). The development of microcracks in concrete. *Rheologica Acta*, *2*(1), 34–40. doi: 10.1007/BF01972552

Kaneko, T. (1978). An experimental study of the Timoshenko's shear coefficient for flexurally vibrating beams. *Journal of Physics D: Applied Physics*, *11*(14), 1979–1988. doi: 10.1088/0022-3727/11/14/010

Khanal, M., Schubert, W., and Tomas, J. (2005). DEM simulation of diametrical compression test on particle compounds. *Granular Matter*, *7*(2-3), 83–90. doi: 10.1007/s10035-005-0200-7

Kim, H., and Buttlar, W. G. (2009). Discrete fracture modeling of asphalt concrete. *International Journal of Solids and Structures*, *46*(13), 2593–2604. Elsevier Ltd. doi: 10.1016/j.ijsolstr.2009.02.006

Kovler, K., and Roussel, N. (2011). Properties of fresh and hardened concrete. *Cement and Concrete Research*, *41*(7), 775–792. Elsevier Ltd. doi: 10.1016/j.cemconres.2011.03.009

Kuhl, E., D'Addetta, Gian Antonio, Herrmann, Hans J., and Ramm, Ekkehard. (2000). A comparison of discrete granular material models with continuous microplane formulations. *Granular Matter*, *2*(3), 113–121. doi: 10.1007/s100350050003

Labra, C. (2012). *Advances in the development of the discrete element method for excavation processes*. Universitat Politecnica de Catalunya.

Labra, C., Escolano, E., and Pasenau, M. (2010). GiD features for discrete element simulations. *5th Conference on Advances and Applications of GiD*. Barcelona.

Labra, C., and Eugenio, O. (2009). High-density sphere packing for discrete element method simulations. *Online*, (November 2008), 837–849. doi: 10.1002/cnm

Langston P.A., Tuzun U., and Heyes D.M. (1995). Discrete element simulation of granular flow in 2D and 3D hoppers: dependence of discharge rate and wall stress on particle interactions. *Chemical Engineering Science*, *50*(6), 21. Elsevier.

Magnier, S. A., and Donze, F. V. (1998). Numerical simulations of impacts using a discrete element method, *276*(December 1996), 257–276.

Mehta, P. K., and Monterio, P. J. M. (1993). *Concrete: Structure, Properties and Materials*. Prentice Hall PTR.

Mindess, S., Young, J. F., and Darwin, D. (2003). *Concrete*. Prentice Hall.

Mindlin, R D. (1949). Compliance of Elastic Bodies in Contact. *J. of Appl. Mech.*, *16*.

Mindlin, R.D., and Deresiewicz, H. (1953). Elastic spheres in contact under varying oblique forces. *ASME*, *September*, 327–344.

Misra, A., and Cheung, J. (1999). Particle motion and energy distribution in tumbling ball mills. *Powder Technology*, *105*(1-3), 222–227. doi: 10.1016/S0032-5910(99)00141-2

Mostofinejad, D., and Nozhatim, M. (2005). Prediction of the modulus of elasticity of high strength concrete. *Iranian Journal of Science and Technology*, *29*.

Nemati, K. M. (1997). Fracture analysis of concrete using scanning electron microscopy. *Scanning*, *19*(6), 426–430. Wiley Periodicals, Inc. doi: 10.1002/sca.4950190605

Neville, A. M., and Brooks, J. J. (1987). *Concrete Technology*. Longman Scientific & Technical.

O'Sullivan, C., and Bray, J. D. (2004). Selecting a suitable time step for discrete element simulations that use the central difference time integration scheme. *Engineering Computations*, *21*(2/3/4), 278–303. doi: 10.1108/02644400410519794

Potapov, A. V., and Campbell, C. S. (1997). The two mechanisms of particle impact breakage and the velocity effect. *Powder Technology*, *93*(1), 13–21. doi: 10.1016/S0032-5910(97)03242-7

Potyondy, D. O., and Cundall, P.A. (2004). A bonded-particle model for rock. *International Journal of Rock Mechanics and Mining Sciences*, *41*(8), 1329–1364. doi: 10.1016/j.ijrmms.2004.09.011

Przemieniecki, J. S. (1968). *Theory of matrix structural analysis*. McGraw-Hill.

Qin, C., and Zhang, C. (2011). Numerical study of dynamic behavior of concrete by meso-scale particle element modeling. *International Journal of Impact Engineering*, *38*(12), 1011–1021. doi: 10.1016/j.ijimpeng.2011.07.004

Rojek, J., Labra, C., Su, O., and Oñate, E. (2012). Comparative study of different discrete element models and evaluation of equivalent micromechanical parameters. *International Journal of Solids and Structures*, *49*(13), 1497–1517. Elsevier Ltd. doi: 10.1016/j.ijsolstr.2012.02.032

Rotter, J. M., Holst, J. M. F. ., Ooi, J. Y., and Sanad, A. M. (1998). Silo pressure predictions using discrete-element and finite-element analyses. *Philosophical Transactions of the Royal Society A: Mathematical, Physical and Engineering Sciences*, *356*(1747), 2685–2712. doi: 10.1098/rsta.1998.0293

Sawamoto, Y., Tsubota, H., Kasai, Y., Koshika, N., and Morikawa, H. (1998). Analytical studies on local damage to reinforced concrete structures under impact loading by discrete element method. *Nuclear Engineering and Design*, *179*(2), 157–177. doi: 10.1016/S0029-5493(97)00268-9

Schneider, B., Bischoff, M., and Ramm, Ekkehard. (2010). Modeling of material failure by the discrete element method. *PAMM*, *10*(1), 685–688. doi: 10.1002/pamm.201010329

Stroeven, P., He, H., and Stroeven, M. (2011). Discrete element modelling approach to assessment of granular properties in concrete. *Journal of Zhejiang University SCIENCE A*, *12*(5), 335–344. doi: 10.1631/jzus.A1000223

Su, O., and Ali Akcin, N. (2011). Numerical simulation of rock cutting using the discrete element method. *International Journal of Rock Mechanics and Mining Sciences*, *48*(3), 434–442. doi: 10.1016/j.ijrmms.2010.08.012

Tavarez, F. A., and Plesha, M. E. (2007). Discrete element method for modelling solid and particulate materials. *International Journal for Numerical Methods in Engineering*, *70*(4), 379–404. doi: 10.1002/nme.1881

Timoshenko, S. P. (1921). LXVI. On the correction for shear of the differential equation for transverse vibrations of prismatic bars. *Philosophical Magazine Series 6*, *41*(245), 744–746. Taylor & Francis. doi: 10.1080/14786442108636264

Timoshenko, S., and Woinowsky-Krieger, S. (1959). *Theory of plates and shells* (2nd ed., p. 580). McGraw-Hill.

Timoshenko, Stephen P. (1922). X. On the transverse vibrations of bars of uniform cross-section. *Philosophical Magazine Series 6*, *43*(253), 125–131. Taylor & Francis. doi: 10.1080/14786442208633855

Tsuji, Y., Tanaka, T., and Ishida, T. (1992). Lagrangian numerical simulation of plug flow of cohesionless particles in a horizontal pipe. *Powder Technology*, *71*(3), 239–250.

Wang, C. M. (1995). Timoshenko Beam-Bending Solutions in Terms of Euler-Bernoulli Solutions. *Journal of Engineering Mechanics*, *121*(6), 763–765. American Society of Civil Engineers. doi: 10.1061/(ASCE)0733-9399(1995)121:6(763)

Wang, L. (2004). Characterization of asphalt concrete using X-ray tomography. In J. Ōtani and Y. Obara (Eds.), *X-ray CT for Geomaterials: Soils, Concrete, Rocks: Proceedings of the International Workshop on X-Ray CT for Geomaterials:* (p. 379). Lisse: Swets and Zeitlinger.

Xiao, J., Xie, H., and Yang, Z. (2012). Shear transfer across a crack in recycled aggregate concrete. *Cement and Concrete Research*, *42*(5), 700–709. doi: 10.1016/j.cemconres.2012.02.006

Yang, Z. ., Su, X. ., Chen, J.F, and Liu, G. . (2009). Monte Carlo simulation of complex cohesive fracture in random heterogeneous quasi-brittle materials. *International Journal of Solids and Structures*, *46*(17), 3222–3234. Elsevier Ltd. doi: 10.1016/j.ijsolstr.2009.04.013

Yang, Z., and Frank Xu, X. (2008). A heterogeneous cohesive model for quasi-brittle materials considering spatially varying random fracture properties. *Computer Methods in Applied Mechanics and Engineering*, *197*(45-48), 4027–4039. doi: 10.1016/j.cma.2008.03.027

Yao, J., Teng, J. G., and Chen, J.F. (2005). Experimental study on FRP-to-concrete bonded joints. *Composites Part B: Engineering*, *36*(2), 99–113. doi: 10.1016/j.compositesb.2004.06.001

Yettram, A. L., and Husain, H. H. (1965). Grid-Framework method for plates in flexure. *Journal of the Engineering Mechanics division, Proceedings of the American Society of Civil Engineers*, (June), 53–64.

Young, W. C. (1989). *Roark's Formulas for Stress and Strain* (6th ed., p. 763). McGraw-Hill.

Zheng, J., Zhou, X., Wu, Z., and Jin, X. (2011). Numerical Method for Predicting Young ' s Modulus of Concrete with Aggregate Shape Effect. *Journal of Materials*, (December), 1609–1615. doi: 10.1061/(ASCE)MT.1943-5533.0000334.

Zhou, Y.-W., and Wu, Y.-F. (2012). General model for constitutive relationships of concrete and its composite structures. *Composite Structures*, *94*(2), 580–592. doi: 10.1016/j.compstruct.2011.08.022

Zienkiewicz, O. C., Taylor, R. L., and Zhu, J. Z. (2005). *The Finite Element Method: Its Basis and Fundamentals: Its Basis and Fundamentals* (p. 752). Butterworth-Heinemann.

AppendixA Verification examples

A.1 Introduction

In order to have full confidence that the developed model, the Edinburgh Bonded Particle Model (EBPM), had been implemented into EDEM (DEM Solutions, 2008) correctly an extensive verification procedure was carried out. The EBPM contains two contact models, one for bonded contacts, the Timoshenko Beam Bonded Contact Model (TBBM) and one for non-bonded contacts, the Hertz-Mindlin Contact Model (HMCM). EDEM supports a fully implemented version of the HMCM code which has previously been verified by authors including Johnstone (2010). Therefore after a brief verification of the HMCM where the benchmark tests described by Chung and Ooi (2011) are satisfied the focus is placed on verification of the TBBM. This is the new contact model, developed for this study, which deals with bonded contacts. As such the verification of this model is based on the fact that a single bond between two particles is considered to behave like a Timoshenko beam. The core parts of the TBBM that need to be verified using single bond tests are the transformation matrix and the stiffness matrix. A great number of verification simulations were conducted, these can be categorised as either being single bond tests or multiple bond tests. A selection of single bond tests are included here, the multiple bond tests included the creation of beams which were tested both statically and dynamically. One of the static beam tests is included in Chapter 3 which then formed the basis of the structural analysis shown in Chapter 7.

A.2 Single bond between two particles

The major focus of the verification procedure is placed on the loading of a single bond which is considered to exist between two particles. A single bond of length L= 0.02 m and radius r= 0.005 m is formed between two particles A and B each of radius $r_A = r_B$ = 0.001 m as shown in Figure A.1. The bond and both particles are made of aluminum, the relevant material properties of which are shown in Table A.1.

The bond has a cross sectional area $A = 7.85\text{x}10^{-5}\,\text{m}^2$, second moment of area $I = 4.91\text{x}10^{10}\,\text{m}^4$ and Timoshenko shear coefficient $\Phi = 0.5625$. By applying external forces and moments to the two particles and setting different support conditions the simulated bond can be subjected to a number of different loading actions. The bond response can be compared to theoretical solutions in order to verify the components of the stiffness matrix. A selection of the loading action responses are presented below.

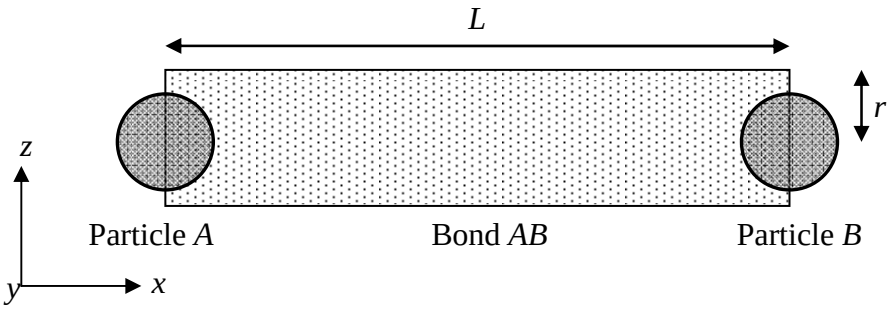

Figure A.1 A single bond between particles *A* and *B*

Table A.1 Material properties for particles and bonds

Parameter	Description	Value
E	Young's Modulus (Pa)	$70.2\ \text{x}10^{10}$
v	Poisson's Ratio	0.35
ρ	Density	2700

In the single bond loading scenarios discussed below only small deflections are allowed. In order to ensure that the transformation matrix used in the TBBM always places the displacement loading into the correct local co-ordinate system, as described in Chapter 3, the orientation of the bond relative to the global axes will be changed in each loading condition; the bond orientation should not influence the behavior of the bond. The orientations used are with the bonds centroid axis being:

parallel to the global *X* axis, perpendicular to the global *X* axis and lastly arbitrarily orientated in space.

A.3 Single bond under a tensile loading action

To ensure that the axial stiffness component of the stiffness matrix has been implemented correctly an external axial force *P* of 1 kN is applied to particle *B*, as shown in Figure A.2(a) which causes an axial displacement $d_{\beta x}$, as shown in Figure A.2(b). Particle *A* is fixed so that no rotations or displacements are allowed; particle *B* has a full six degrees of freedom.

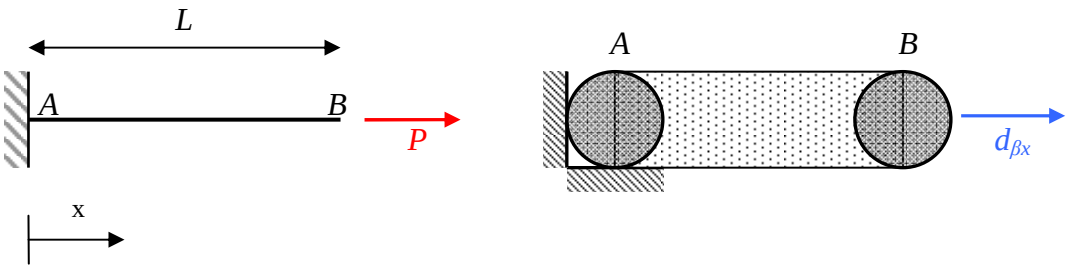

(a) axial force acting on the bond (b) displacement of bond AB

Figure A.2 Testing a single bond under axial loading

The only forces in the bond caused by the displacement $d_{\beta x}$ are $F_{\alpha x}$ and $F_{\beta x}$ which are related by the axial stiffness term such that:

$$F_{\beta x} = -F_{\alpha x} = P = \frac{EA}{L} d_{\beta x} \tag{A.1}$$

$$\therefore d_{\beta x} = \frac{PL}{EA} \tag{A.2}$$

Theoretically the axial force term $F_{\beta x}$ = 1000 N and $d_{\beta x}$ = 0.003627 mm. The measured bond forces and particle displacements for all orientations of bonds were found to match the theoretical response to four significant figures.

A.4 Single bond under a twisting loading action

The twisting component of the stiffness matrix is verified by applying a twisting moment M_o of 1 kN.m to the right hand end of a bond with end constraints as shown in Figure A.3(a). This causes an axial rotation $\theta_{\beta x}$ of the bond. As particle *A* cannot displace or rotate the stiffness of the beam restricts the rotation of particle *B*.

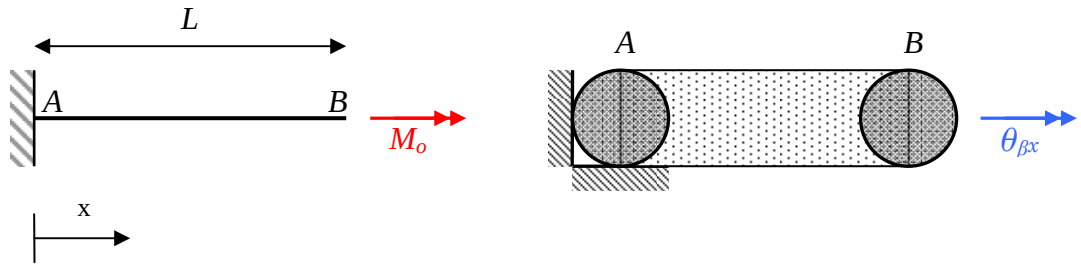

(a) twisting moments acting on the bond (b) displacement of bond AB

Figure A.3 Testing a single bond under a twisting loading action

The only moments in the bond caused by the displacement $\theta_{\beta x}$ are $M_{\alpha x}$ and $M_{\beta x}$ which are related by the torsional stiffness term such that:

$$M_{\beta x} = -M_{\alpha x} = M_o = \frac{2GI}{L}\theta_{\beta x} \tag{A.3}$$

$$\therefore \theta_{\beta x} = \frac{M_o L}{2GI} \tag{A.4}$$

The DEM predicted rotation at all orientations matched the theoretical rotation $\theta_{\beta x}$ of 0.7835 radians to four significant figures.

A.5 Single bond under bending loading action

An external moment M_o of 1 kN is applied to a pinned particle *B* which is bonded to a fixed particle *A*, as seen in Figure A.3(b). The rotation caused by the external moment induces two shear forces $F_{\alpha z}$ and $F_{\beta z}$, and two bending moments $M_{\alpha y}$ and $M_{\beta y}$ in the bond. As the external forces and internal forces on the particle must equate the final rotation θ_B of particle *B* can be determined.

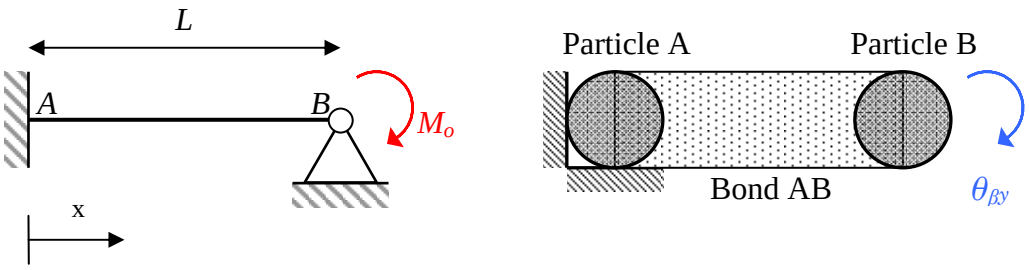

(a) a single beam under a bending loading action

(b) single bond representation

FigureA.4 Bending moment acting about *B*

As the ends of the beam are restrained from translational displacement the rotation at particle *B* can be related to the applied moment such that:

$$M_{\beta y} = M_o = \frac{(4+\Phi)EI}{L(1+\Phi)}\theta_{\beta y} \qquad \text{(A.5)}$$

The DEM predicted rotation at particle *B* matches the theoretical rotation θ_B of 0.7835 radians to four significant figures for all orientations.